Bruno Pighinelli Cambria

Numerical and experimental active control for a vibration system using advanced beam elements

São Paulo

2018

Bruno Pighinelli Cambria

Numerical and experimental active control for a vibration system using advanced beam elements

Undergraduate Thesis presented as a requisite to obtain the Mechatronic Engineering Bachelor Degree at Escola Politécnica da Universidade de São Paulo.

Escola Politécnica da Universidade de São Paulo (USP)

Departamento de Engenharia Mecatrônica e de Sistemas Mecânicos (PMR)

Mechatronic Engineering Bachelor Degree

Supervisor: Prof. Dr. Emílio Carlos Nelli Silva

São Paulo
2018

Bruno Pighinelli Cambria
Numerical and experimental active control for a vibration system using advanced beam elements/ Bruno Pighinelli Cambria. – São Paulo, 2018-
164 p.

Bachelor Thesis (Mechatronic Engineering) – Escola Politécnica da Universidade de São Paulo (USP), Departamento de Engenharia Mecatrônica e de Sistemas Mecânicos (PMR), 2018.

1. Active vibration control. 2. Piezoelectric. 3. PID. I. Universidade de São Paulo. Escola Politécnica. II. t.

To my beloved family and friends,
who always supported me along this journey.

Acknowledgements

First, I would like to thank my supervisor Prof. Dr. Emílio C. N. Silva from the Mechatronics Engineering Department (PMR) at Escola Politécnica da USP. Prof. Emílio and the researchers oriented by him, specially Ruben Andres Salas, were always very helpful when I ran into trouble in this project, from the first to the last day of development and writing. They allowed me to propose my own solutions to the problems along the work, while steering me always to the right direction.

I would also like to acklowledge Prof. Erasmo Carrera from the Aerospace Engineering Department at Politecnico di Torino, the owner of the formulation used in this project who surpervised me during my Laurea Magistrale thesis in Italy with the help of his research group MUL2.

I am also grateful for everyone who helped me along the experimental implementation of the project with advices and instruments without which the completeness of this work would not be possible: everyone from the LMR, LUS and GMSIE laboratories, specially Prof. Dr. Flávio Buiochi.

Furthermore, thanks to all the professors I had in my academic life. Without their instruction I would not be able to develop a detailed academic work that I was proud to own.

At last, I must express my deep gratitude to my family, partner and friends. Their support and encouragement was essential to accomplish my objective to research and write this thesis, and to finally obtain my second engineering degree. Thank you.

"I have been impressed with the urgency of doing.
Knowing is not enough; we must apply.
Being willing is not enough; we must do."
Leonardo da Vinci

Abstract

The purpose of this study is the active vibration control of an aluminum plate both experimentally and numerically. Piezoceramic patches are used as sensor and actuator for the system's characterization and to implement the closed loop control. The numerical model is based on the Carrera Unified Formulation (CUF), which decently approximates a 2D structure through advanced beam elements and bidimensional cross-section expansions. The numerical model is adjusted according to the experimental frequency response curve obtained from 3 manufactured prototypes. PD controllers are designed from a reduced order model. It is implemented in the real system as an analog PD, with the aid of operational amplifiers, and in the numerical model as a discrete PD in a loop that simulates the structural dynamics through a generalization of the Newmark method. The anticipated outcome of this project is the successful control of the second and third vibration modes of the structure in the experimental and numerical implementations. It can be concluded that the adjusted numerical model represents well the real system.

Key-words: Active Control, Finite Element Method, Piezoelectric, PID

List of Figures

Figure 1 – Example of a stable damped (negative exponential) and an unstable (positive exponential) sinusoidal vibration. 24
Figure 2 – Oscillations amplitude as function of input frequency (OGATA, 2005). 25
Figure 3 – Tacoma Narrows Bridge collapsing (James Bashford / The News Tribune, 1940) (BUSH, 2015). 26
Figure 4 – Example of fundamental structures. 27
Figure 5 – Example SISO and MIMO mass-spring-damper systems. 27
Figure 6 – Open loop control. 28
Figure 7 – Closed loop control. 28
Figure 8 – Sampling and quantization of an analog signal. 29
Figure 9 – Sinusoidal signal with period 0.052 $t.u.$ sampled with a sampling period of 0.05 $t.u.$ 30
Figure 10 – Piezoelectric material property according to electric polarization. (VATANSEVER; SIORES; SHAH, 2012). 31
Figure 11 – Piezoceramic patches (CERAMTEC, 2018). 31
Figure 12 – MUL2 logo. 36
Figure 13 – World's first jetliner: de Havilland Comet (CARDINAL, 2012). 37
Figure 14 – Block diagram of the state-space continuous time representation. 42
Figure 15 – Graphical representation of the 1D element shape functions N_i and N_j (left) and the 2D cross-section expansion functions F_τ and F_s (right). (CARRERA et al., 2014), page 60. 46
Figure 16 – Global matrix assembly for a 1D element. (CARRERA et al., 2014), page 63. 46
Figure 17 – Euler-Bernoulli beam model. (CARRERA et al., 2014), page 107. . . . 47
Figure 18 – Timoshenko beam model. (CARRERA et al., 2014), page 109. 48
Figure 19 – Actual and normalized L4 element. (CARRERA et al., 2014), page 154. 51
Figure 20 – Actual and normalized L3, L6 and L9 elements. (CARRERA et al., 2014), page 155. 52
Figure 21 – Cross-section taken from example found in (CARRERA et al., 2014), page 174. 53
Figure 22 – Cross-section discretizations: (a) 8 L9; (b) 9 L9; (c) 11 L9, as in (CARRERA et al., 2014), page 175. 53
Figure 23 – Piezoelectric cross-section with 4 L4 elements. Blue elements are part of a piezo patch and red elements are purely mechanical. 57
Figure 24 – Underdamped harmonic oscillation with exponential envelope functions for $U_0 = 1$ m, $\phi = 0$, $\zeta = 0.05$, $\omega_n = 200\pi$ rad/s. 60

Figure 25 – Definition of half-power bandwidth. (CHOPRA, 2012), page 83 61
Figure 26 – Block diagram of the closed loop control system of a structure using output feedback control. 66
Figure 27 – PID block diagram. 68
Figure 28 – Graphical user interface for *pidTuner* function. 69
Figure 29 – Graphical user interface for *sisotool* function. 70
Figure 30 – RLC series circuit. 72
Figure 31 – Ideal operational amplifier equivalent circuit (WIKIMEDIA, 2009). . . 73
Figure 32 – Inverting adder circuit. 74
Figure 33 – Inverting differentiator circuit. 75
Figure 34 – Low-pass RC passive filters with one or two stages. 75
Figure 35 – Block diagram of an open loop system of a structure with piezo-patches. 79
Figure 36 – Prototype blueprint. 82
Figure 37 – Top: Aluminum substrate for one of the prototypes after cutting and sanding processes. Bottom: Piezoceramic patches before attached to the substrate. 83
Figure 38 – Graphical representation of considered measurements: A) plate length; B) plate width; C) piezoceramic thickness; D) epoxy layer thickness; E) aluminum sheet thickness; F) distance between clamp and piezoceramic. 84
Figure 39 – Finished prototypes. 85
Figure 40 – Experimental characterization diagram. 86
Figure 41 – Terminal block BNC 2110, National Instruments. 87
Figure 42 – Set composed by power supply, amplifier and transformers connected to both output channels. 87
Figure 43 – Polytec OFV-5000 laser vibrometer. 88
Figure 44 – Alignment preparation before vibrometer measurement. 89
Figure 45 – Shaker and laser head positioned for a measurement. 89
Figure 46 – Schematics for Zener diodes protection circuit. 90
Figure 47 – Structure to be controlled. 95
Figure 48 – Mesh representation as a GMSH 3D model. 96
Figure 49 – First bending modal shape of the model. 97
Figure 50 – Second bending modal shape of the model. 97
Figure 51 – Third bending modal shape of the model. 97
Figure 52 – Resultant structural static deformation due to the application of 1V to the actuator. 98
Figure 53 – Frequency response for the actuator/sensor system from the numerical FEM model. 99
Figure 54 – Experimental frequency response for the sensor voltage/shaker voltage disturbance system (V_{sen}/V_d) for prototype 2 used for correction. 101

Figure 55 – Experimental frequency response for the base displacement/shaker voltage disturbance system (u_b/V_d) for each prototype used for normalization. 102
Figure 56 – Experimental frequency response for the free extremity displacement/shaker voltage disturbance system (u_e/V_d) for each prototype. 102
Figure 57 – Numerical and experimental frequency response for the actuator/sensor system (V_{sen}/V_{act}) for each prototype. 103
Figure 58 – Complex electrical impedance around the first mode for the three prototypes. 107
Figure 59 – Complex electrical impedance around the second mode for the three prototypes. 108
Figure 60 – Complex electrical impedance around the third mode for the three prototypes. 108
Figure 61 – Frequency response for the adjusted numerical model. 109
Figure 62 – Magnitude Bode diagram comparison between experimental data and estimations. 110
Figure 63 – Eighth order RLC circuit representing the structural system. 112
Figure 64 – Unit step response for the eighth order transfer function G_{est} and the equivalent RLC system G_{RLC}. 113
Figure 65 – Stability margins for the reduced order model $G_{est}(s)$. 114
Figure 66 – Sensitivity function $S(s)$ Bode diagram. 115
Figure 67 – Nyquist plot and robustness margins for each sensitivity peak. 115
Figure 68 – Control loop for the plant transfer function $G_p(S)$ and the controller transfer function $G_c(s)$ with inputs from the reference r and disturbance d. 117
Figure 69 – Output transient response for disturbance step input for different controllers. 117
Figure 70 – Bode diagram for open loop, P, D and PD control systems. 118
Figure 71 – Output response for unit step disturbance with an ideal high gain PD controller and the respective P, D and PD actuation signals. 119
Figure 72 – Bode diagram comparison between the open loop and the ideal high gain PD control system. 119
Figure 73 – PD controller implemented on LTSpice. 121
Figure 74 – Output transient response for disturbance step input for different controllers implemented in LTSpice. 122
Figure 75 – Decoupled signals for each RLC circuit equivalent to a vibration mode. 123
Figure 76 – Fast Fourier transform for the disturbance step with P, D and PD control. 123
Figure 77 – Disturbance step response comparison between $G_c(s)$ and $G'_c(s)$ controllers implemented in LTSpice. 124

Figure 78 – Fast Fourier transform for the disturbance step control for controllers G_c and G'_c. 125
Figure 79 – Resonance peaks damping for the harmonic control of the first mode. . 127
Figure 80 – Resonance peaks damping for the harmonic control of the second mode. 128
Figure 81 – Resonance peaks damping for the harmonic control of the third mode. . 129
Figure 82 – Prototype 1: sensor voltage, tip displacement and control effort for open loop system and closed loop systems with P, D and PD control. 132
Figure 83 – Prototype 2: sensor voltage, tip displacement and control effort for open loop system and closed loop systems with P, D and PD control. 133
Figure 84 – Prototype 3: sensor voltage, tip displacement and control effort for open loop system and closed loop systems with P, D and PD control. 134
Figure 85 – Filtered tip displacement signals for the three prototypes. 135
Figure 86 – Prototype 1: FFT for the second and third resonance peaks in the sensor voltage and extremity displacement signals. 136
Figure 87 – Prototype 2: FFT for the second and third resonance peaks in the sensor voltage and extremity displacement signals. 137
Figure 88 – Prototype 3: FFT for the second and third resonance peaks in the sensor voltage and extremity displacement signals. 138
Figure 89 – Resulting filtered voltage signal when a step signal is sent to the modal shaker. 140
Figure 90 – Free extremity motion comparison between controlled and uncontrolled system for a shaker disturbance. 141
Figure 91 – Signal containing 500Hz and 10kHz frequencies filtered by first order low pass discrete filter. 142
Figure 92 – Numerical implementation of the designed controllers: sensor voltage and tip displacement (original and filtered) for open loop system and closed loop systems with P, D and PD control. 144
Figure 93 – FFT for the second and third modes using controllers designed in LTSpice. 145
Figure 94 – Numerical implementation of the controllers obtained experimentally: sensor voltage and tip displacement (original and filtered) for open loop system and closed loop systems with P, D and PD control. 146
Figure 95 – FFT for the second and third modes using controllers obtained experimentally. 147
Figure 96 – Filtered tip displacement Time response comparison between numerical model and experiments executed with each prototype. 150
Figure 97 – Tip displacement FFT comparison between numerical model and experiments executed with each prototype. 151

Figure 98 – Experimental open-loop vs. closed-loop vibration response of beam (b); (RAHMAN; ALAM, 2012). 152
Figure 99 – Free vibration response of the open-(OL) and closed-loop (CL) systems and control voltage with filtered velocity feedback control; (VASQUES; RODRIGUES, 2007). 153
Figure 100 – Sensor voltage for the first two bending modes: (a) without control; (b) PD control; (QIU et al., 2006). 154

List of Tables

Table 1 – Loaded point vertical displacement for different models. (CARRERA et al., 2014), page 175. 54
Table 2 – Ziegler-Nichols tuning parameters. 68
Table 3 – PZT-5H orthotropic properties (SALAS et al., 2017). 80
Table 4 – Isotropic aluminum alloy properties (SALAS, 2017). 81
Table 5 – Mean value of measured lengths in milimeters by prototype for each measurement from figure 38 and mean between prototypes. 84
Table 6 – Three first natural frequencies associated to bending of the FEM model obtained through MUL2 and MATLAB codes. 98
Table 7 – Resonance frequencies estimated for each prototype before acquiring experimental data. 100
Table 8 – Boundary conditions adjustment impact on natural frequencies. 104
Table 9 – Quality factor Q_i and damping ratio ζ_i estimation for the first three natural bending frequencies f_i of each prototype. Obtained from the harmonic response curves. 105
Table 10 – Decay exponent $a_i = 2\pi f_i \zeta_i$ and damping ratio ζ_i estimation for the first three natural bending frequencies f_i of each prototype. Obtained from the transient response curves. 106
Table 11 – Rayleigh damping coefficients α_M and β_K estimated by each kind of analysis for each prototype. 106
Table 12 – Quality metrics for estimated transfer functions with 6, 8 and 10 poles for each prototype experimental data. 111
Table 13 – Residues r, resonance frequencies ω_n, and damping ratios ζ for the four pair of poles of G_{est}. 111
Table 14 – Sensitivity peaks characteristics. 116
Table 15 – Controller parameters implemented in LTSpice. 122
Table 16 – New controller parameters implemented in LTSpice. 125
Table 17 – Harmonic control results for the sensor voltage signal. Comparison between the uncontrolled system parameters (ζ_i, f_i and $|H|$) and the controlled ones (ζ_i', f_i' and $|H'|$). 130
Table 18 – Harmonic control results for the extremity displacement signal. Comparison between the uncontrolled system parameters (ζ_i, f_i and $|H|$) and the controlled ones (ζ_i', f_i' and $|H'|$). 130
Table 19 – Controller parameters with best results for each prototype. 131
Table 20 – Peak magnitude $|H|$, damping ratio ζ and frequency f for the second and third resonance of the sensor voltage signal. 136

Table 21 – Peak magnitude $|H|$, damping ratio ζ and frequency f for the second and third resonance of the free extremity displacement. 137
Table 22 – Time domain quality metrics for each transient control experiment. 139
Table 23 – Shaker disturbance: gain magnitude for the first peak of the transient response FFT in open and closed loop systems. 141
Table 24 – Mesh comparison for: static analysis with 1V applied to the actuator (extremity displacement u_e), modal analysis (frequencies f_i), and step response dynamic analysis for 400 time steps (execution time t_{run}). 142
Table 25 – Frequency domain quality metrics for the second and third resonance modes for the controllers designed in LTSpice. 145
Table 26 – Frequency domain quality metrics for the second and third resonance modes for the controllers obtained experimentally. 147
Table 27 – Time domain quality metrics for the controllers designed in LTSpice (*Design*) and obtained experimentally (*Exper.*). 148

Contents

1 INTRODUCTION . . . 23

1.1 Background . . . 23

1.1.1 Vibration . . . 23

1.1.2 Structures . . . 25

1.1.3 Control theory . . . 26

1.1.4 Piezoelectricity . . . 30

1.2 Literature Review and State of the Art . . . 32

1.3 Problem Statement . . . 34

1.3.1 Objective and Requirements . . . 34

1.3.2 Scientific Contribution . . . 35

1.4 Motivations . . . 36

1.4.1 Human Exposure Limits: . . . 36

1.4.2 Mechanical Fatigue Failure: . . . 36

2 METHODOLOGY . . . 39

2.1 Governing Equation . . . 39

2.1.1 Static . . . 39

2.1.2 Free Vibration . . . 40

2.1.3 Dynamic . . . 41

2.1.3.1 State-Space Representation . . . 41

2.1.3.2 HHT-α and Newmark-β integration methods . . . 42

2.2 Mathematical Model . . . 43

2.2.1 3D Elasticity . . . 43

2.2.2 Carrera Unified Formulation (CUF) . . . 44

2.2.3 Classical Cross-Section Models . . . 47

2.2.3.1 Euler-Bernoulli Beam Theory (EBBT) . . . 47

2.2.3.2 Timoshenko Beam Theory (TBT) . . . 48

2.2.4 Taylor Expansion Class . . . 48

2.2.5 Lagrange Expansion Class . . . 50

2.2.6 Piezoelectricity Formulation . . . 54

2.2.7 Damping Matrix . . . 59

2.3 Active Vibration Control . . . 61

2.3.1 Frequency Response . . . 62

2.3.2 Model Order Reduction . . . 64

2.3.3 Feedback Control Loop . . . 66

2.3.4 PID Design . . . 68
2.3.5 Analog Electronic Implementation . . . 72
2.3.5.1 Equivalent RLC . . . 72
2.3.5.2 Operational Amplifier PID Circuit . . . 74
2.4 Numerical Implementation . . . 76
2.4.1 MUL2 Fortran Application . . . 76
2.4.2 MATLAB . . . 78
2.5 Prototypes . . . 79
2.5.1 Design . . . 80
2.5.2 Manufacturing . . . 82
2.6 Experimental Characterization . . . 85
2.6.1 Signals Acquisition . . . 86
2.6.2 Experimental Curves . . . 91
2.6.2.1 Transient Response (Time Domain) . . . 91
2.6.2.2 Harmonic Response (Frequency Domain) . . . 92

3 RESULTS AND DISCUSSION . . . 95
3.1 Finite Element Model . . . 96
3.2 Frequency Response . . . 99
3.2.1 Numerical Curve . . . 99
3.2.2 Experimental Curves . . . 100
3.3 Numerical Model Adjustment . . . 104
3.3.1 Boundary Conditions . . . 104
3.3.2 Rayleigh Damping Coefficients . . . 105
3.3.3 Additional Considerations . . . 106
3.4 Model Order Reduction . . . 110
3.4.1 Transfer Function . . . 110
3.4.2 Equivalent RLC . . . 111
3.5 Controller Design . . . 113
3.6 Control Loop Implementation . . . 120
3.6.1 LTSpice Control . . . 120
3.6.2 Experimental Control . . . 126
3.6.2.1 Harmonic Control . . . 126
3.6.2.2 Transient Control . . . 130
3.6.2.3 Shaker Disturbance Control . . . 139
3.6.3 Numerical Model Control . . . 141

4 FINAL CONSIDERATIONS . . . 149
4.1 Conclusions . . . 149
4.2 Suggestions for Future Works . . . 154

BIBLIOGRAPHY **157**

1 Introduction

The main focus of this thesis is to actively control the first controllable vibration modes of a plate using piezoceramic patches as sensor and actuator. To achieve this objective, a Finite Element Method (FEM) formulation will be used to model a real prototype, that will later be manufactured and experimentally controlled with a low cost analog circuit.

This monograph will initially present a background theory to subjects related to the project, followed by the *Literature Review and State of the Art*, that will clarify the progress and the current scientific state regarding the fields of study of this thesis. Then the problem statement, its objectives, requirements, scientific contributions and motivations will be presented, concluding the introductory chapter.

The next chapter that will present all the fundamental theories and methods, as well as the methodology used to obtain a feasible solution to the stated problem. Finally, the results and discussion will be shown, followed by the final considerations, divided in the conclusions of the work and suggestions for possible continuations.

1.1 Background

1.1.1 Vibration

The mechanical phenomenon of oscillations of an element around a static equilibrium point is called vibration (PALAZZOLO, 2016).

In some cases, vibration can be desired and purposely generated, but in most situations it is an undesired motion, that wastes energy, generate unwanted sounds and damages structures. The motion of a vibrating point may have different transient and steady-state responses in the time domain according to its excitation and the dynamics associated to its system, that can be either stable or unstable, as shown in figure 1. A vibration can be also classified as marginally stable if the signal is bounded: it does not converge to the equilibrium point, but does not diverge too.

The amplitude of the vibration motion depends on its frequency: usually for too high excitation frequencies, a system will not oscillate with high amplitudes, because the system is too slow and will not have enough time to overcome the inertia when the excitation changes direction; for too low excitation frequencies, a system will behave closer to a steady motion, because the variation of the input is too slow for the system. It is not possible to determine if a frequency is too low or too high if not compared to a reference

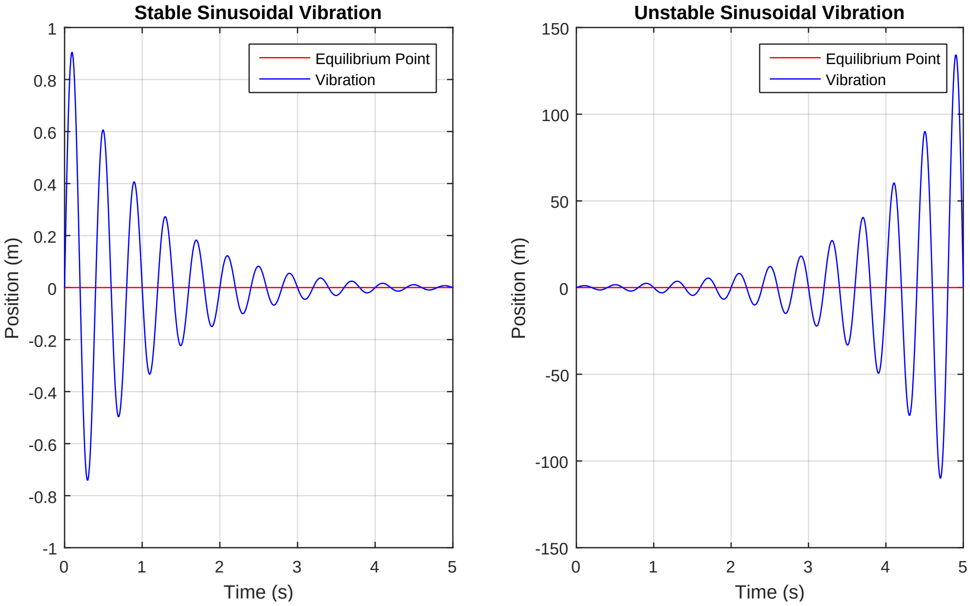

Figure 1 – Example of a stable damped (negative exponential) and an unstable (positive exponential) sinusoidal vibration.

value, associated to the concerned system. Usually, for an electrical system, the reference frequencies are going to be higher than for a mechanical system, it means that a low frequency for the first may be a high frequency for the second. This reference is based in the resonance (natural) frequencies of the system (figure 2), that exist for each degrees of freedom. The resonance occurs in the easiest frequency for the system to convert potential to kinetic energy, so they are the critical points in the vibration amplitudes, generating the modal shapes, and must be avoided for the safety of the system (OGATA, 2005).

A classic example of trouble caused by reaching the resonance frequency of a mechanical system that has been widely used in engineering textbooks from the past few decades, was the tragic collapse of the Tacoma Narrows Bridge in 1940. This bridge, built in the state of Washington, US, was opened to traffic on July 1, 1940 as the third longest suspension bridge in the world. In November 7 of the same year, it was said that strong winds excited it in its torsional vibration mode, causing unstable oscillations to multiple degrees of freedom. Not even the control strategies used due to prior vertical oscillations were enough to avoid the collapse (figure 3). Unlike this very simple explanation to the problem that was well accepted some years after the catastrophe, newer scientific researches proved that the collapse was uncorrelated to the resonance phenomena, but to self-excitation of the bridge, called "negative damping" by Billah and Scanlan (BILLAH; SCANIAN, 1990). They explained that as the bridge moved torsionally, it changed the wind above and below to the opposite direction, causing the vibration to increase monotonically with the wind speed.

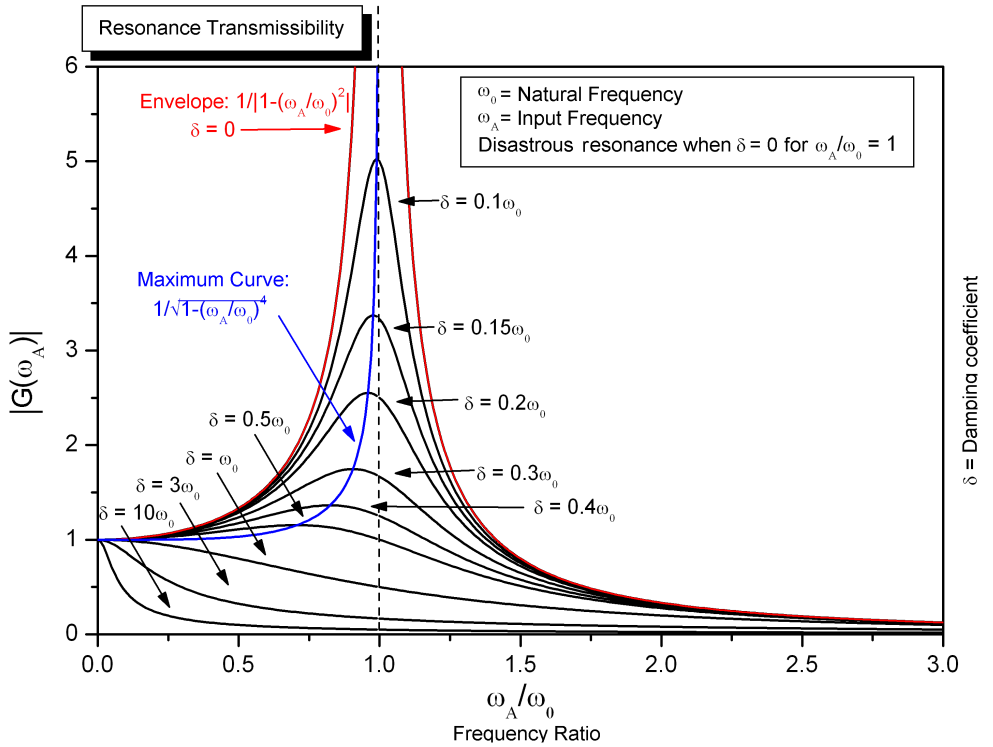

Figure 2 – Oscillations amplitude as function of input frequency (OGATA, 2005).

Mathematically, the natural frequencies are associated to the eigenvalues and the modal shapes to the eigenvectors of the problem. Each frequency is associated to a certain deformation of the structure, among which may be bending, torsion, axial deformation.

1.1.2 Structures

There are some different kinds of fundamental structures that can be classified in the structural mechanics field, as in figure 4:

1. **Beam (1D):** The beam (or bar) is a structure which length is much higher that the other two dimensions, so it can be modelled as unidimensional (line). In the truss theory, the structures are composed as a set of bars that transmit only axial forces, which is the simplest structural element we can model. A more complex beam analysis takes into account shear forces and bending moments as well.

2. **Panel, Plate, Shell or Membrane (2D):** In this case, two of the dimensions are in the same order of magnitude and the third one is a lot smaller, so we can consider this as a bidimensional structure (surface). A plate is usually associated to a plane structure, while a shell is usually a curved structure. A panel may be either a plate or a shell.

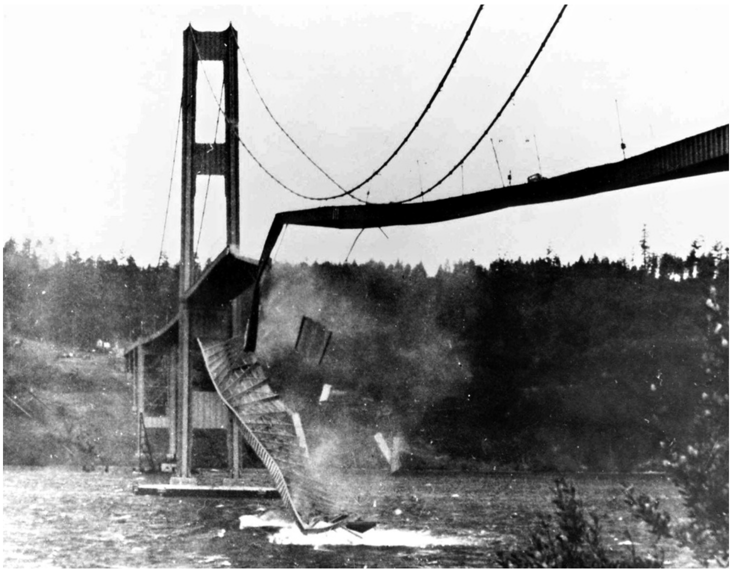

Figure 3 – Tacoma Narrows Bridge collapsing (James Bashford / The News Tribune, 1940) (BUSH, 2015).

3. **Solid (3D):** If all three dimensions are significant in our structure (all with same order of magnitude), we have to use the approaches of a tridimensional structure (solid), that is the most complex we can reach.

It is clear that one may perform bidimensional analysis in a beam or tridimensional analysis in a beam or a plate, but depending on the application, the algorithm complexity and computational costs involved in solving the equations may be too high compared to the low results improvements it would provide. The feasibility of modeling a problem as a chosen fundamental model depends not only on the physical structure to be analyzed, but also in the type of analysis to be performed. A model may originate accurate results when performing a static structural analysis, but not in a dynamic or kinematic analysis, for instance. Fortunately, with the formulation used in this work, we can even use beam elements to model plates with a decent precision in a significant large number of situations, as will be explained in a future chapter.

1.1.3 Control theory

Control theory is a branch of the engineering that aims to set variables to a desired value, compensating the dynamics of the system and the disturbances associated to it. In some applications, a **passive control** may exist, that is basically changing the system dynamics before using it, by adding dampers, springs or mass to a structure or changing its material, for instance. In the other hand, the **active control** acts on the system while it is working by means of sensors and actuators, that are driven by the controllers.

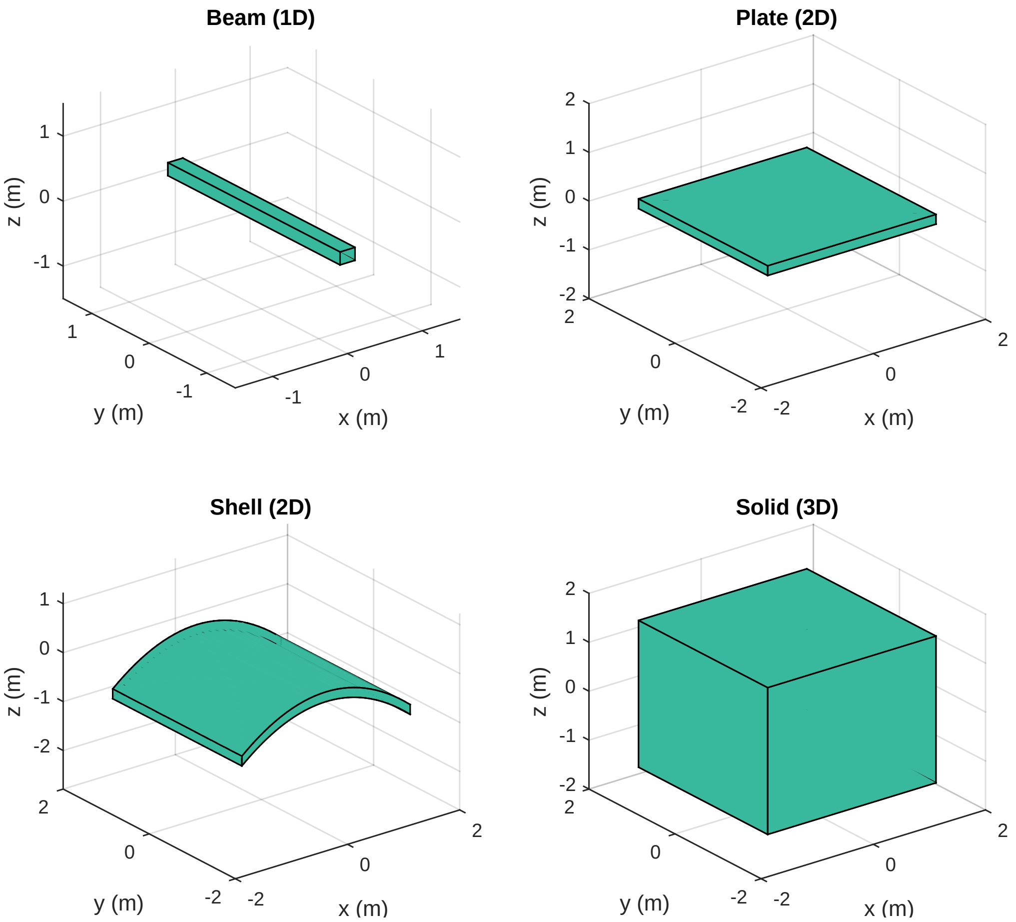

Figure 4 – Example of fundamental structures.

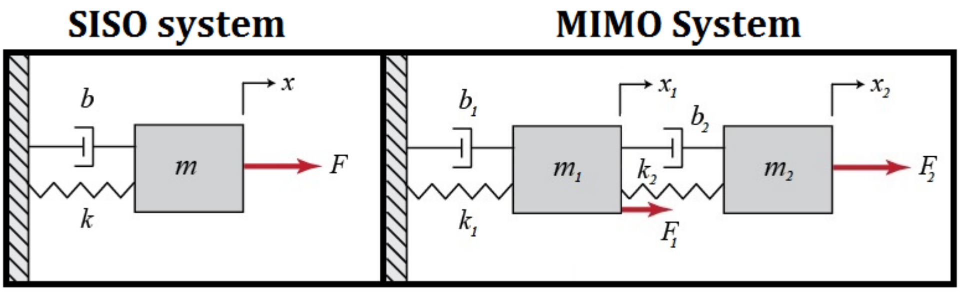

Figure 5 – Example SISO and MIMO mass-spring-damper systems.

The systems are divided in SISO (Single-Input and Single-Output) and MIMO (Multiple-Inputs and Multiple-Outputs), depending on the number of input and output variables considered in the model. A SISO system could be the motion of a mass-spring-damper system due to the application of a force, while a MIMO system could be the motion of two coupled mass-spring-damper in a system due to the application of a force in each mass (figure 5). Just like the systems, controllers can also be classified as SISO or MIMO.

Besides that, two different types of control are considered regarding the output measurability:

- **Open Loop:** The control is executed without knowing exactly what is happening to the output. Because of this, an open loop is only efficient if the variables behave similarly to what is expected. It is much simpler to design an open loop controller, but any disturbance not taken into account may change completely the output we desire to control. In figure 6 a general open loop control system is schematized.

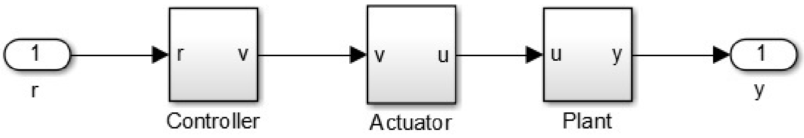

Figure 6 – Open loop control.

- **Closed Loop:** The control is executed with sensors, composing a feedback that closes the loop, so the system is able to follow the motion of the output variables and set them to a desired value. This control is more complex to design than an open loop controller, but it is clearly a lot more efficient and robust, because it compensates the effects of outside agents not considered in the model of our system (plant). In figure 7 a general closed loop control system is shown.

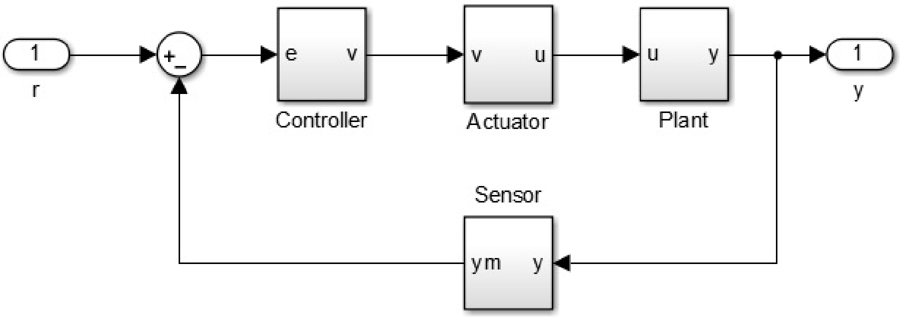

Figure 7 – Closed loop control.

Imagine you are driving a car in an empty road you know really well, which you could remember the exact distance between each curve and how tight they are. Even with all this information, would you be able to drive with closed eyes as well as you would with open eyes? Surely you would not, because you would not receive any feedback of your velocity and position, that could be changing according to a small angle you were not expecting in the steering wheel, to the imperfections in the road surface or to the small deviations between the approximated distance to the next curve you kept in your mind and its real value, for instance. Just by opening your eyes, you could drive safely even with other vehicles in the road that could not be predicted if you did not see them. That is why the feedback is so important for a control loop and should be implemented when trying to control a variable with a minimum possibility to not follow strict predictions we can make.

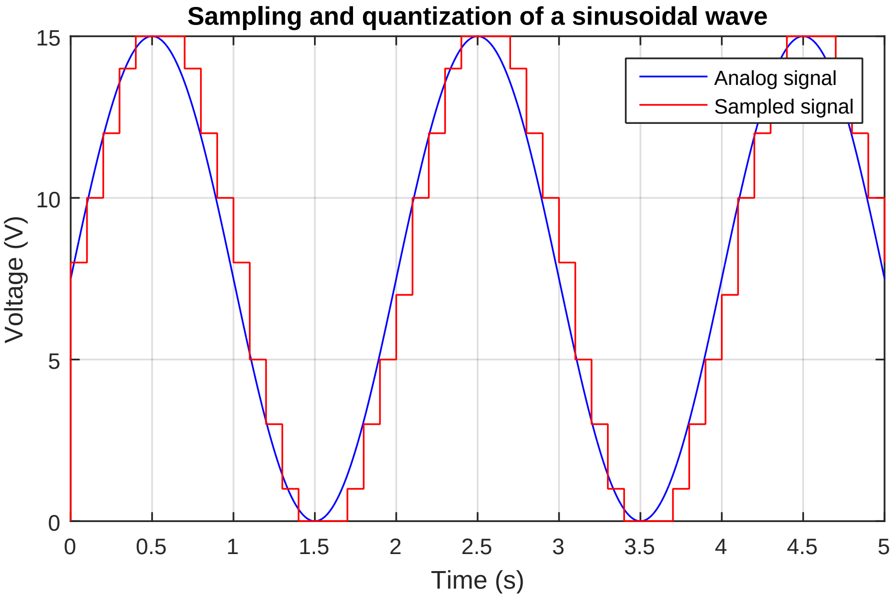

Figure 8 – Sampling and quantization of an analog signal.

When talking about control it is relevant to define the type of signal we are dealing with. It may be either an **analog** or a **digital** signal. An analog signal is a continuous-time signal, which means that it may change for any time instant you pick, in the other hand, a digital signal is a discrete-time signal generated by an electronic device. In the real world, the physical quantities have continuous-time behavior, so to work with them in the discrete-time, that is how computers and microcontrollers work, it is needed to convert the analog signal to a digital signal, sampling and quantizing it: a sampling time T_s is fixed and, after every T_s, the analog signal is read and its value is converted to one of the discrete amplitude values it can be stored with, which is called quantization. In figure 8 a sinusoidal wave was sampled with $T_s = 0.1$ s and with 4 bits, which gives a quantization of 1V in a range of 15V ($2^N - 1$ levels).

In the interface between continuous and discrete-time signals Analog-to-Digital (A/D) and Digital-to-Analog (D/A) converters are used. The sample time must be wisely chosen to avoid the aliasing effect, which may cause the processed signal to become indistinguishable. The lowest sampling frequency that can be used is called Nyquist frequency, that is half of the highest frequency that composes the original signal, but usually it is safe to use a sampling frequency at least five times this value to assure a proper accuracy in the output of the converter. Figure 9 illustrates the effect of undersampling, where a signal with a period of 0.052 t.u. (time units) was sampled with a sampling time of 0.05 t.u.

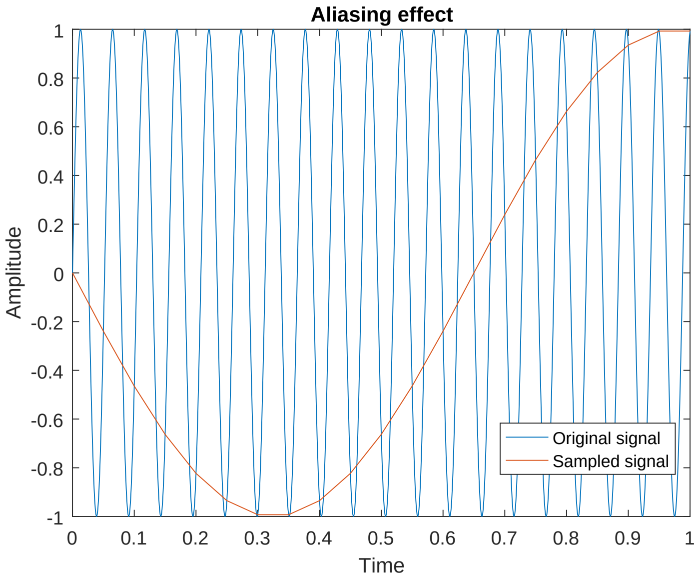

Figure 9 – Sinusoidal signal with period 0.052 $t.u.$ sampled with a sampling period of 0.05 $t.u.$

The concept of continuous and discrete signals can be generalized to our systems and, consequently, to the controllers designed. Continuous-time systems are modelled through the Laplace transform and discrete-time systems through the Z transform resulting in what we call a **transfer function**, that may be continuous or discrete, as explained in (OGATA, 2010; OGATA, 1995):

- **Laplace transform:**

$$F(s) = \mathcal{L}[f(t)] = \int_0^{\infty} f(t)e^{-st}dt \tag{1.1}$$

- **Z transform:**

$$F(z) = \mathcal{Z}[f(t)] = \mathcal{Z}[f(kT_s)] = \sum_{k=0}^{\infty} = f(kT_s)z^{-k} \tag{1.2}$$

1.1.4 Piezoelectricity

Piezoelectricity is the reversible capability of certain materials in which the application of an electrical field causes mechanical stresses and straining, called the direct effect, and the application of mechanical stresses produces an electric potential, which is called the reverse effect 10. It is derived from the greek *piezein* that is the word for "press". Due to this process, piezoelectric materials have been commonly used as sensors and actuators in mechanical structures, where they may be embedded or bonded to its surface, creating the called "smart structures" (CARRERA; ZAPPINO; LI, 2017). In active vibration control, piezoelectric patch transducers 11 are commonly used as both sensors and actuators: electric potential accumulated in the sensor transducers are measured and compared to the desired voltage, which is a function of the desired position of the patch, then this difference is processed by one or more controllers that generate the input voltage signals for the transducers used as actuators, in order to compensate the position error of the sensors. One of the most used piezoelectric material is the ceramic lead zirconate titanate ($Pb[Zr_xTi_{1\text{-}x}]O_3$, $0 \leq x \leq 1$), also called PZT.

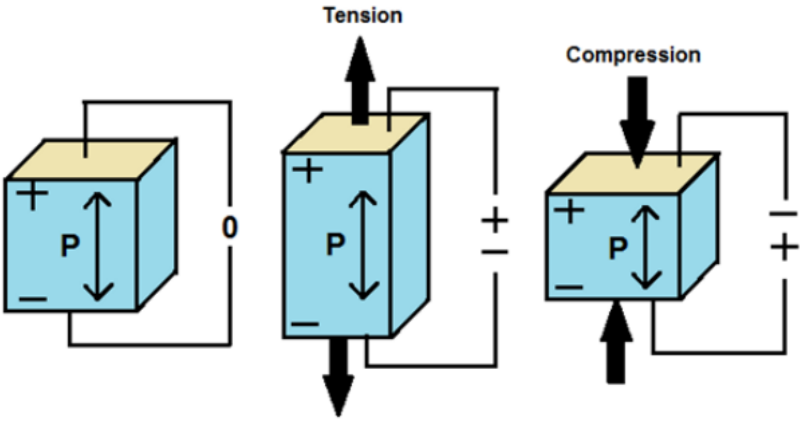

Figure 10 – Piezoelectric material property according to electric polarization. (VATANSEVER; SIORES; SHAH, 2012).

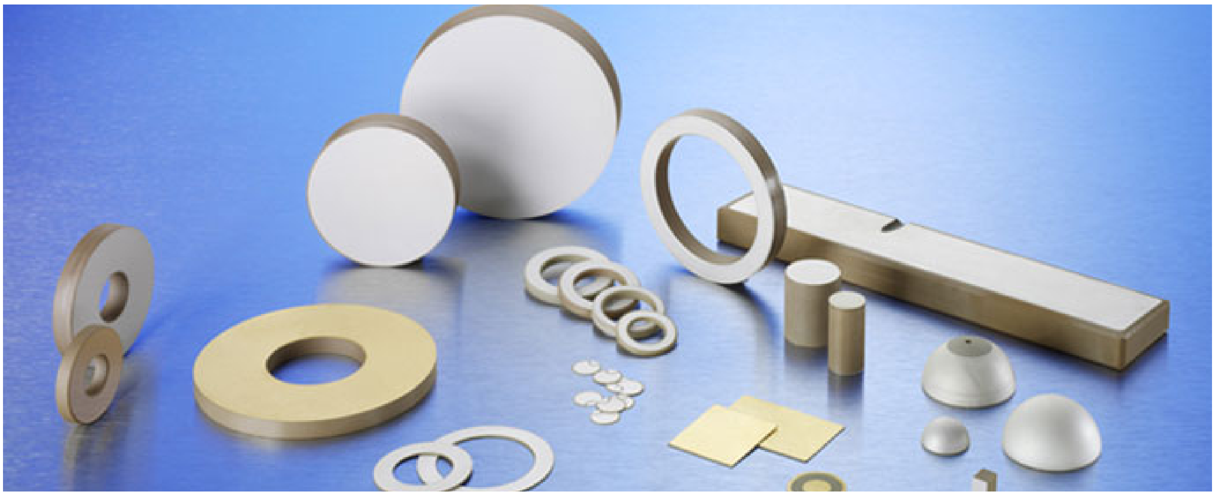

Figure 11 – Piezoceramic patches (CERAMTEC, 2018).

1.2 Literature Review and State of the Art

The vibration problem has been known in engineering for quite some time. Timoshenko brought together several technical problems and applications in his *Vibration Problems in Engineering* (TIMOSHENKO, 1937) after developing the theory of vibration, releasing later with Gere, in *Mechanics of Materials* (TIMOSHENKO; GERE, 1991), where formulations for the mechanics were presented.

Some of the first studies based on finite elements formulation in the academic history were in structural analyses of elasticity and vibration in civil and aeronautical engineering. Among the pioneers of the method, are Hrennikoff (HRENNIKOFF, 1941) and Courant (COURANT, 1943). A good base textbook focused in the analytical and numerical solutions of solid mechanics FEM problems was released by Zienkiewicz and Taylor (ZIENKIEWICZ; TAYLOR, 2000).

The Carrera Unified Formulation (CARRERA, 2002) was proposed as a new methodology for modeling unidimensional and bidimensional structures as 3D, enriching the models along the directions that would be disconsidered. This is achieved by discretizing the remaining dimensions with cross-section (for beams) and thickness (for plates and shells) series and expansions. A detailed discussion about the Taylor series and Lagrange expansions usage with the CUF and the formulation based on the *fundamental nuclei* can be found in (CARRERA et al., 2014). Equivalent Single Layer and Layer-wise models based theories, in the framework of CUF, were presented in (CINEFRA; VALVANO; CARRERA, 2015) and (CINEFRA; VALVANO, 2016).

Some of the early works about models accounting electromechanical responses of smart structures are (TIERSTEN, 1969), (TZOU; GADRE, 1989), (AHMAD; UPADHYAY; VENKATESAN, 2006), and (ROGACHEVA, 1994), discussing about linear piezoelectric plate vibrations, analysis of a multi-layered shell with piezoelectric actuators, thermo-piezo-elastic analysis using classical beam models, and the theory of piezoelectric 2D structures, respectively. More recent articles, such as (ROBBINS; REDDY, 1991), (HEYLIGER; RAMIREZ; SARAVANOS, 1994), and (BEHESHTI-AVAL et al., 2011), report refined 1D elements, to capture the interaction between the piezoelectric materials in the structure and the substrate, which is essential for understanding the relations of the voltage in the actuator and sensor piezo-patches to the displacements of the mesh nodes. Crawley and De Luis (CRAWLEY; LUIS, 1987) and Crawley and Anderson (CRAWLEY; ANDERSON, 1990) developed models for bonded and embedded piezoelectric actuators in beams. The debonding effects of a piezoelectric actuator in smart composite laminates was modelled in this study (HUANG; KIM; YOON, 2015), showing the behavior in the time and frequency domain of the structures due to problems caused during the manufacturing process.

Prof. Emílio C. N. Silva, the supervisor of this project, leads several studies in the field of piezocomposites and topology optimization, including (SALAS et al., 2018), that characterizes the an optimized design of a piezocomposite actuator considering the fiber orientation of the layers. Reports by the MUL2 research group in the field of electromechanical FEM models, making possible the matrix assembly of the FEM matrices with piezoelectric materials, include (CARRERA; FAGIANO, 2007), (CARRERA; BÜTTNER; NALI, 2010), and (CARRERA; ROBALDO, 2010). Zappino and Carrera (ZAPPINO; CARRERA, 2017) presented an analysis of piezoceramic actuators with a refined 1D model and another (CARRERA; ZAPPINO; LI, 2017) with piezo-patches by node-dependent kinematic.

In the field of FEM dynamics, Stoykov (STOYKOV; MARGENOV, 2016) studied the plates dynamic response with 2D elements. For the time domain integration of the structural equations, Gavin (GAVIN, 2016) released a review of algorithms to solve the forced time response of structures at Duke University, containing explicit and implicit methods, among which are Newmark (NEWMARK, 1959) and Hilber-Hughes-Taylor-α (HHTα) method (HILBER; HUGHES; TAYLOR, 1977), a generalization of the Newmark-β. An example of Hilber-Hughes-Taylor method for multibody dynamics was studied in (NEGRUT et al., 2006). Torii and Machado (TORII; MACHADO, 2012) implemented a generalized FEM for a time domain structural dynamic analysis for bars and trusses. As an evolution of the HHTα method, the Generalized-α method was introduced (CHUNG; HULBERT, 1993). This algorithm improves the numerical dissipation when compared to its predecessors: it dissipates high-frequency and minimizes unwanted low-frequency dissipation.

Depending on the control approach for the active control of the system, a less complex model than the one modeled by the FEM is needed for the controllers design. Model Order Reduction (MOR) is the name of the study that is responsible for simplifying the system, involving several different techniques, as the method of proper orthogonal decomposition, with some reports and studies released in (KERSCHEN et al., 2005), and spectral decomposition, simultaneous gradient error reduction and balancing, as described by Colgren (COLGREN, 2010). For projection-based order reduction, the stability preservation concept to this technique was addressed in (SELGA; LOHMANN; EID, 2012).

Control theory dates from the 19th century, drastically evolving since then. The studies of stability, controllability and observability were essential for the evolution of this field. An important author about control theory is Ogata (OGATA, 2010; OGATA, 1995; OGATA, 2005), releasing theoretical explanations for classical and modern control, in continuous and discrete time. The active vibration control is based on the control theory studies to perform oscillations suppression in structures.

Zuo and Wong (ZUO; WONG, 2016) and Alkhatib and Golnaraghi (ALKHATIB;

GOLNARAGHI, 2003) reported reviews about recent control techniques for active vibration control, passing through PID, pole placement, sliding mode, nonlinear and positive feedback controllers, including the control in Micro-Electro-Mechanical structures. A book from Palazzolo (PALAZZOLO, 2016) about structural vibration, including numeric methods and active control, was also an important base for this thesis development.

Positive results in the vibration active control were reported in (SHUNQI; XIANSHENG, 2015) and (LIN, 2007), using PID and PD control, (TRINDADE; BENJEDDOU; OHAYON, 2001), controlling damped sandwich beams, (BALAMURUGAN; NARAYANAN, 2001), using LQR in composite 2D structures, (ZHANG; SHEN, 2007), using laminated plates reinforced with piezoelectric fibers, (LUO S. XIE, 2008), controlling a honeycomb sandwich panel, and (HE, 2002), proposing a control scheme within a finite element framework of curved functionally graded material shells.

Other studies focus more on optimization for the control, which is the case of NASA (NASA, 2011), that used point sensor and actuator for an efficient vibration control system, (QIU et al., 2006) and (KUMAR; NARAYANAN, 2008), that focused in optimal piezo-patch placement, (TEO; FLEMING, 2014), which focused on optimal integral force feedback to introduce active damping in the structure, and (VASQUES; RODRIGUES, 2006) and (HANAGUD; OBAL; CALISE, 1992), that compared classical and optimal control strategies in the active vibration control field. An analysis on the influence of the patches location with the aid of ANSYS was performed in (XIAOJIN et al., 2010), (BAILEY; UBBARD, 1985) worked on the control using piezoelectric-polymer, and (ALMA et al., 2012), which based on H-infinity feedforward compensators for the control.

Experimental characterization of smart structures containing piezoelectric materials are usually performed for energy-harvesting applications, such as (GOLDSCHMIDTBOEING; WOIAS, 2008), (ERTURK; INMAN, 2009) and (SALAS, 2017). In the literature is also found the characterization for vibration control, as in (VASQUES; RODRIGUES, 2007), in which the actuation signal is proportional directly to the tip velocity of a cantilever beam. Positive experimental active control have also been presented by (RAHMAN; ALAM, 2012) and (JOVANOVIC et al., 2013), both based on digital PID controllers.

1.3 Problem Statement

1.3.1 Objective and Requirements

As stated in the beginning of this chapter, the main objective of this project is to physically implement a functional system that attenuates the vibration of the first resonance frequency of a metallic bidimensional structure using piezoceramic patches as sensors and actuators. The project will be divided in two main parts: the first will focus on the modeling and numerical simulations of the problem in a computer, while the second will aim the experimental implementation of the problem and the active control loop that will solve it.

For the numerical modeling and simulation in the first section of the project, the equations that rule the motion of the structure are going to be derived using the Principle of Virtual Displacement (PVD) and solved through the Finite Element Method (FEM), with elements coming from the innovative Carrera Unified Formulation (CUF).

The experimental section will be composed by the designing and manufacturing of the prototype, the experimental characterization for the solution, the comparison between the prototype to the numerical model created in the previous section dinamically and, finally, the implementation of the control system electronically.

The scope of the work is limited to the attenuation of the first vibration mode of the designed prototype and the analysis of using the control system that solves this problem to reduce forced vibrations in other frequencies. The attenuation will not be optimized using difficult techniques, the requisite of the problem is satisfied as long as a reduction in the first vibration mode of the structure is clearly achieved.

This work is an extension of a previous project developed at Politécnico di Torino, in Italy, supervised by Prof. Erasmo Carrera during a Double Degree program, which was focused in the usage of the CUF for developing numerical analyses for passive and active control fields of unidimensional structures. This formulation was first introduced to the academic community by Prof. Carrera and, for this reason, was named after him.

1.3.2 Scientific Contribution

Among the motivations to develop this thesis is the gap in the knowledge of vibration control concerning structures with two significant dimensions. According to the literature review, several studies have been made in the vibration control field concerning beam structures and involving piezoelectricity. The main difference of this thesis to other papers is the utilization of the CUF to solve the FEM equations with multivariable active control techniques in the vibration field and the experimental implementation of it. Another important point to highlight in this work is the usage of dynamic condensation of matrices to simulate state-space systems in MATLAB, allowing an uncoupled manipulation of the mechanical and electrical displacements.

Works based in the CUF have been and currently are still being developed by the MUL2 research group (MUL2, 2018), leaded by Prof. Erasmo Carrera at Politecnico di Torino. The MUL2 projects are focused in advanced structural models for multilayered structures in different applications: aeroelasticity, spacecraft design, biomechanics, composites, damage and failure, meshless methods, etc. On the other side, Prof. Emílio Carlos

Figure 12 – MUL2 logo.

Nelli Silva leads researches mainly focused in piezoelectrics, energy harvesting, composite materials and topology optimization in the structural and fluid mechanics fields at Escola Politécnica da Universidade de São Paulo.

1.4 Motivations

As stated in (PALAZZOLO, 2016), there is a large number of harmful effects of the vibration. Listing some of these effects, we have the human exposure limits and the mechanical fatigue failure, which will be introduced next.

1.4.1 Human Exposure Limits:

According to the Standard ISO 2631: "Mechanical vibration and shock – Evaluation of human exposure to whole-body vibration" (ISO, 1997; ISO, 2003), the vibration may be quantitatively measurable to classify how intense it is to human health. This quantity is called Vibration Dose Value (VDV), and is calculated by the fourth power vibration dose method:

$$VDV = \left[\int_0^T a^4(t) dt \right]^{1/4} \tag{1.3}$$

where $a(t)$ is the instantaneous vibration acceleration and T is the stardard duration of the measurement, both in the International System of Units (SI). The caution zone is when VDV is between 8.5 m/s$^{1.75}$ and 17 m/s$^{1.75}$ and above it, there is health risk that may cause discomfort, disorder of the joints, cardiovascular and respiratory changes, muscular fatigue and stiffness, etc. For vibration in buildings, where there is a continuous exposition, a limit between 0.1 m/s$^{1.75}$ and 0.8 m/s$^{1.75}$ is set, depending on the type of building.

1.4.2 Mechanical Fatigue Failure:

Fatigue is the process of weakening a material and crack initiation under cyclic loads applied. The number of cycles that may cause fatigue failure to a structure will depend on its materials, geometry, manufacturing processes, temperature, on the loads applied, and other factors. In aerospace structures, that are usually light and highly stressed due to vibration, the problem of high-cycle fatigue (HFC) failure is quite significant.

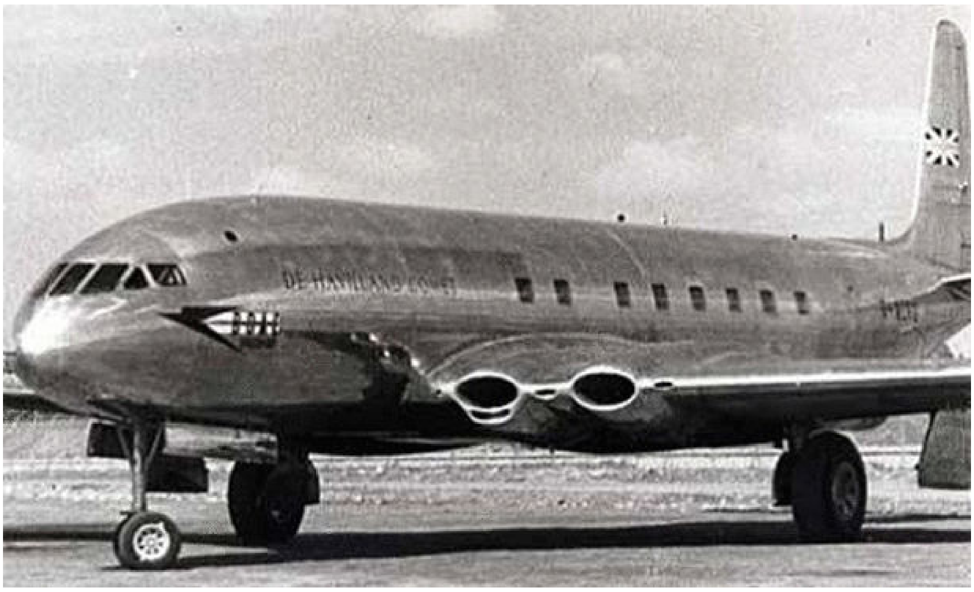

Figure 13 – World's first jetliner: de Havilland Comet (CARDINAL, 2012).

A well known airplane that exemplifies this importance is the de Havilland DH 106 Comet (PUSHKAR, 2002) (figure 13): the world's first commercial jetliner, first introduced in May 1952. After one year of its debut, some accidents started to happen due to fatigue failures mainly in the fuselage and in the airframe, with one of the most famous ones being British Overseas Airways Corporation (BOAC) Flight 781 on 10 January 1954 (ASN, 2018). The aircraft suffered an explosive decompression about 20 minutes after taking off from Ciampino Airport, in Rome, killing 29 passengers, 6 crew members and leaving no survivors. It is considered the worst air crash of all time in Italy. After intense investigations, two of the accidents, including Flight 781, were found to be caused due to metal fatigue failure, resulting from the severe weather applying high cyclical loads in the aircraft's body. The main structural flaw was in the design of the windows, which were squared instead of round. This minor change could have avoided the stress concentration and, therefore, the cracks initiation and spreading in the windows' vertices.

2 Methodology

The simulations of this project could be performed using any FEM software that is out in the market, but it was decided not to use any of them in favor of the flexibility and computational costs. Instead, the problems will be simulated with system matrices generated by a Fortran FEM application based on CUF developed by MUL2, which will be manipulated with MATLAB, where it is possible to work directly on the matrices and design suitable controllers, given the wide range of possibilities and freedom this software offers.

2.1 Governing Equation

The general second order matrix differential equation that governs the vibration system is:

$$\mathbf{M}\ddot{\mathbf{u}} + \mathbf{D}\dot{\mathbf{u}} + \mathbf{K}\mathbf{u} = \mathbf{F} \tag{2.1}$$

where $\mathbf{M}$ is the mass matrix, $\mathbf{D}$ is the damping matrix, $\mathbf{K}$ is the stiffness matrix, F is the external force vector, $\mathbf{u}$ is the displacement vector, $\dot{\mathbf{u}} = \frac{d\mathbf{u}}{dt}$ is the velocity vector and $\ddot{\mathbf{u}} = \frac{d^2\mathbf{u}}{dt^2}$ is the acceleration vector. This equation is originated from the Principle of the Virtual Displacement, which states through the work balance that:

$$\delta L_{ine} + \delta L_{int} = \delta L_{ext} \tag{2.2}$$

where δL_{ine} is the inertial contribution, δL_{int} is the internal and δL_{ext} the external.

From the second order vibration equation, three different kind of analysis may be performed. Each of them is going to be detailed in the following subsections.

2.1.1 Static

This analysis is used to calculate the deformation in the equilibrium configuration of the structure given a constant input load vector applied. As it is static, the vector of displacement is constant, so $\dot{\mathbf{u}} = 0$ and $\ddot{\mathbf{u}} = 0$. Hence, the simplified equation becomes:

$$\mathbf{K}\mathbf{u} = \mathbf{F} \tag{2.3}$$

which solution can be obtained using an algorithm for solving linear equations, once that inverting the stiffness matrix is not always a simple task in terms of computational cost:

$$\mathbf{u} = \mathbf{K}^{-1}\mathbf{F} \tag{2.4}$$

The calculated displacement vector will give the deformations of each degree of freedom of the system for the given constant input.

2.1.2 Free Vibration

This analysis, also known as Modal Analysis, is used to study the frequencies associated to the system. Unlike the static analysis, the answer of the problem is not given by a single configuration. Instead, n different vibration modes are found for a structure with n non constrained degrees of freedom. For each of this modes there is a frequency and a displacement vector associated, which are called natural or resonance frequency and modal shape or configuration, respectively. The study is performed without any external force applied and with no damping, so $\mathbf{F} = \mathbf{0}$ and $\mathbf{D} = \mathbf{0}$:

$$\mathbf{M\ddot{u}} + \mathbf{Ku} = \mathbf{0} \tag{2.5}$$

Without damping, the time response of the vibrating structure may be written as:

$$\mathbf{u_i} = \mathbf{x_{mod,i}} e^{j\omega_i t} \tag{2.6}$$

for the i-th vibration mode, the $\mathbf{x_{mod,i}}$ modal configuration and the ω_i natural frequency are given ($j = \sqrt{-1}$). Replacing $\mathbf{u}$ by $\mathbf{u_i}$ from equation 2.6 to equation 2.5 and simplifying:

$$(\mathbf{K} - \mathbf{M}\omega_i^2)\mathbf{x_{mod,i}} = 0 \tag{2.7}$$

transforming $\mathbf{A} = \mathbf{M}^{-1}\mathbf{K}$, $\lambda_i = \omega_i^2$ and $\mathbf{v_i} = \mathbf{x_{mod,i}}$, the equation becomes an eigen problem:

$$\mathbf{Av_i} = \lambda_i \mathbf{v_i} \tag{2.8}$$

After finding the eigenvalues and eigenvectors of $\mathbf{A}$, the analysis is solved. The natural frequencies of the system are going to be $\omega_i = \sqrt{\lambda_i}$ and the modal shapes $\mathbf{x_{mod,i}} = \mathbf{v_i}$. Therefore, any forced vibration of the structure may be translated as a linear combination of its natural modes. For piezoelectric materials, the forced response of a structure is not proportional only to its mechanical modes, but also to the electrical terms that depend on the boundary conditions of the problem (GUO; CAWLEY; HITCHINGS, 1992). The high modal density and modal coupling effects makes this analysis not elementary (GUO; CAWLEY, 1991).

2.1.3 Dynamic

This is the generic analysis of the problem, with non-null terms in equation 2.1 and the input load as a function of time. It is possible to solve this equation analytically just for a few F inputs, so most of the times we must use numerical methods for ordinary differential equations to obtain the solution for $\mathbf{u}(t)$.

2.1.3.1 State-Space Representation

If we convert the system equation in a continuous time state-space system, we have:

$$\begin{cases} \dot{\mathbf{x}}(t) = \mathbf{A_{ss}}\mathbf{x}(t) + \mathbf{B_{ss}}\mathbf{F}(t) \\ \mathbf{y}(t) = \mathbf{C_{ss}}\mathbf{x}(t) + \mathbf{D_{ss}}\mathbf{F}(t) \end{cases} \tag{2.9}$$

the states are represented by vector $\mathbf{x}(t) = \begin{bmatrix} \mathbf{u}(t) \\ \dot{\mathbf{u}}(t) \end{bmatrix}$, the input of the system is the vector $\mathbf{F}(t)$ and the output is $\mathbf{y}(t) = \mathbf{u}(t)$. The LTI (Linear Time-Invariant) state-space (SS) system matrices are:

$$\begin{cases} \mathbf{A_{ss}} = \begin{bmatrix} \mathbf{0} & \mathbf{I} \\ -\mathbf{M}^{-1}\mathbf{K} & -\mathbf{M}^{-1}\mathbf{D} \end{bmatrix} \\ \mathbf{B_{ss}} = \begin{bmatrix} \mathbf{0} \\ \mathbf{M}^{-1} \end{bmatrix} \\ \mathbf{C_{ss}} = \begin{bmatrix} \mathbf{I} & \mathbf{0} \end{bmatrix} \\ \mathbf{D_{ss}} = \mathbf{0} \end{cases} \tag{2.10}$$

where I is the identity matrix and 0 is the null matrix. The algorithm to simulate the system in continuous time is given by the block diagram in figure 14.

The solution for the displacement vector in a static analysis matches the steady-state response of a dynamic analysis with a step load vector input, because $\dot{\mathbf{u}} \to \mathbf{0}$, $\ddot{\mathbf{u}} \to \mathbf{0}$ and $\mathbf{F}$ is time invariant. It is also convenient to emphasize that all dynamic response is composed by the superposition of the modes obtained by the free vibration analysis.

Besides the state-space approach, we can find numerous numeric methods to solve the system of differential equations concerned in the Computational Mechanics field. Among them, are the Runge-Kutta (RK) methods, the finite difference methods, the Newmark-β method and the Hilber-Hughes-Taylor (HHT-α) method.

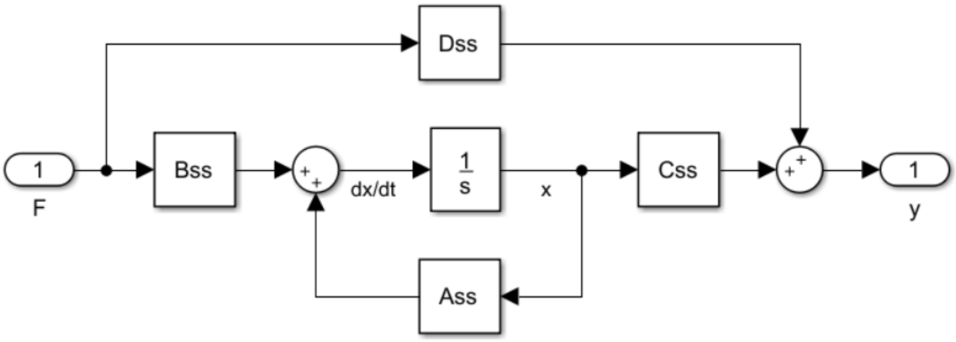

Figure 14 – Block diagram of the state-space continuous time representation.

2.1.3.2 HHT-α and Newmark-β integration methods

The HHT-α generalized structural implicit integration method (HILBER; HUGHES; TAYLOR, 1977) is going to be used in this project, so it will be summarized. This is a generalization of the Newmark-β (NEWMARK, 1959) method, to which is reduced for $\alpha = 0$. The α factor represents a numerical lag in the damping, stiffness and external forces terms of the governing equation:

$$\mathbf{M}\ddot{\mathbf{u}}_{\mathbf{i+1}} + \mathbf{D}\left[\alpha\dot{\mathbf{u}}_{\mathbf{i}} + (1-\alpha)\dot{\mathbf{u}}_{\mathbf{i+1}}\right] + \mathbf{K}\left[\alpha\mathbf{u}_{\mathbf{i}} + (1-\alpha)\mathbf{u}_{\mathbf{i+1}}\right] = \alpha\mathbf{F}_{\mathbf{i}} + (1-\alpha)\mathbf{F}_{\mathbf{i+1}} \tag{2.11}$$

The acceleration is constant between two adjacent time steps.

Being h the time step for the integration, Newmark method uses the following relations for the finite difference approximations:

$$\mathbf{u}_{\mathbf{i+1}} \approx \mathbf{u}_{\mathbf{i}} + h\dot{\mathbf{u}}_{\mathbf{i}} + h^2\left[(1/2-\beta)\ddot{\mathbf{u}}_{\mathbf{i}} + \beta\ddot{\mathbf{u}}_{\mathbf{i+1}}\right] \tag{2.12}$$

and

$$\dot{\mathbf{u}}_{\mathbf{i+1}} \approx \dot{\mathbf{u}}_{\mathbf{i}} + h\left[(1-\gamma)\ddot{\mathbf{u}}_{\mathbf{i}} + \gamma\ddot{\mathbf{u}}_{\mathbf{i+1}}\right] \tag{2.13}$$

This method is at least second-order accurate and unconditionally stable for α within $[0,\ 1/3]$ for $\beta = (1-\alpha)^2/4$ and $\gamma = 1/2+\alpha$. Replacing the position and velocity for the step $i+1$ from equations 2.12 and 2.13 to the acceleration equation 2.11 and grouping terms, we have:

$$\ddot{\mathbf{u}}_{\mathbf{i+1}} = \mathbf{M_1}^{-1}\left[-\mathbf{M_2}\ddot{\mathbf{u}}_{\mathbf{i}} - \mathbf{M_3}\dot{\mathbf{u}}_{\mathbf{i}} - \mathbf{K}\mathbf{u}_{\mathbf{i}} + (1-\alpha)\mathbf{F}_{\mathbf{i+1}} + \alpha\mathbf{F}_{\mathbf{i}}\right] \tag{2.14}$$

with

$$\begin{aligned} \mathbf{M_1} &= \mathbf{M} + h(1-\alpha)\gamma\mathbf{D} + h^2(1-\alpha)\beta\mathbf{K} \\ \mathbf{M_2} &= h(1-\alpha)(1-\gamma)\mathbf{D} + h^2(1-\alpha)(1/2-\beta)\mathbf{K} \\ \mathbf{M_3} &= \mathbf{D} + h(1-\alpha)\mathbf{K} \end{aligned} \tag{2.15}$$

The algorithm of this approach is the recursive application of equations 2.14, 2.12 and 2.13 from $i = 0$ until the desired time step $i = n_t$. a

2.2 Mathematical Model

All the mathematical base to model the 3D vibrational system through FEM using the CUF can be found in (CARRERA et al., 2014). This section will present the mathematical formulation from the basics to the final form of the structural model that is going to be used in the project.

2.2.1 3D Elasticity

In the second chapter of (CARRERA et al., 2014): *Fundamental Equations of 3D Elasticity*, there is a really detailed formulation of the constitutive elasticity equations that is going to be synthesized in this subsection.

Given a certain material, we have the following properties: Young's modulus E, Poisson's ration ν and Shear modulus G. While for the body strains and stresses, the following notation is going to be used: σ_{ii} is the normal stress component in the i direction, σ_{ij} is the shear stress component in the ij plane, ε_{ii} is the axial strain in the i direction and γ_{ij} is the shear strain in the ij plane.

It is important to remember that the strains are related to the displacements $\mathbf{u} = (u_x, u_y, u_z)$ in the following way:

$$\varepsilon_{ii} = \frac{\partial u_i}{\partial i} \text{ and } \gamma_{ij} = \frac{\partial u_i}{\partial j} + \frac{\partial u_j}{\partial i} \text{ for } i, j = x, y, z \tag{2.16}$$

The Hooke's Law gives the physical relation between stress and strain, which are proportional to a stiffness component. In the matrix form:

$$\sigma = \mathbf{C}\varepsilon \tag{2.17}$$

where

$$\sigma = \begin{bmatrix} \sigma_{xx} \\ \sigma_{yy} \\ \sigma_{zz} \\ \sigma_{xz} \\ \sigma_{yz} \\ \sigma_{xy} \end{bmatrix}, \varepsilon = \begin{bmatrix} \varepsilon_{xx} \\ \varepsilon_{yy} \\ \varepsilon_{zz} \\ \gamma_{xz} \\ \gamma_{yz} \\ \gamma_{xy} \end{bmatrix} \text{ and } \mathbf{C} = \begin{bmatrix} C_{11} & C_{12} & C_{12} & 0 & 0 & 0 \\ C_{21} & C_{11} & C_{12} & 0 & 0 & 0 \\ C_{21} & C_{21} & C_{11} & 0 & 0 & 0 \\ 0 & 0 & 0 & C_{44} & 0 & 0 \\ 0 & 0 & 0 & 0 & C_{44} & 0 \\ 0 & 0 & 0 & 0 & 0 & C_{44} \end{bmatrix} \tag{2.18}$$

with $C_{11} = 2G + \lambda$, $C_{12} = C_{21} = \lambda$, $C_{44} = G$, $G = \frac{E}{2(1+\nu)}$ and $\lambda = \frac{\nu E}{(1+\nu)(1-2\nu)}$.

With these equations we can set relations between displacements, strains and stresses in all directions of a 3D body.

2.2.2 Carrera Unified Formulation (CUF)

The approach for the derivation of the finite elements matrices used to describe the structural systems in the numerical simulations is based in the Unified Formulation, which uses the fundamental nuclei (FN): a 3 × 3 array for 1D, 2D and 3D problems. The fifth chapter of (CARRERA et al., 2014): *Introduction to the Unified Formulation*, details the approach that is going to be presented in this subsection.

The main reason for choosing this formulation along this project was the fact that it allows 2D analysis using 1D advanced elements, which means that obtaining the system matrices from this approach reduces significantly the computational costs when compared to 2D elements algorithms. In general lines, CUF transforms the study domain of the structure from 1D or 2D to 3D: in the first case, cross-section expansions along the planes perpendicular to the beam direction are used to discretize the remaining 2 dimensions, while in the second case thickness expansions add the third dimension. Figure 15 shows the graphical representation of the transformations from 1D to 3D.

The finite elements method uses shape functions to describe the displacements in an element. An element composed of n nodes (Bn element) has n shape functions, each one with a value of 1 in one of the nodes and 0 in all of the others. They are usually polynomials and the sum of all shape functions at a given point must be equal to 1.

Let N be the shape function of order N_E and the subscripts i and j associated to the real displacements and virtual variations, respectively. The displacements u_y and virtual variations δu_y in a 1D beam are interpolated by:

$$\begin{aligned} u_y(y) &= N_i u_{y_i} \\ \delta u_y(y) &= N_j \delta u_{y_j} \end{aligned} \tag{2.19}$$

with the beam aligned to the y axis. Using the notation $N_{i,y} = \frac{dN}{dy}$, we have that:

$$\varepsilon = N_{i,y} u_{y_i} \delta\varepsilon = N_{j,y} \delta u_{y_j} \tag{2.20}$$

The 1D FN can be derived from the virtual variation of the internal work:

$$\delta L_{int} = \int_V \delta\varepsilon^T \sigma dV = \delta u_{y_j} k^{ij} u_{y_i} \tag{2.21}$$

where

$$k^{ij} = \int_V N_{j,y} \; E \; N_{i,y} dV \tag{2.22}$$

are the elements that compose the fundamental nucleus matrix of a bar, which is independent to the shape function's order N_E. The stiffness matrix of the 1D element is given by:

$$\mathbf{K} = \begin{bmatrix} k^{11} & \dots & k^{1j} & \dots & k^{1N_E} \\ \vdots & \ddots & \vdots & & \vdots \\ k^{i1} & \dots & k^{ij} & \dots & k^{iN_E} \\ \vdots & & \vdots & \ddots & \vdots \\ k^{N_E1} & \dots & k^{N_Ej} & \dots & k^{N_EN_E} \end{bmatrix} \tag{2.23}$$

Up to this point, it is possible to describe the displacements just in the y direction, being constant in the xz cross-sections. To overcome this limitation, the expansion functions F_τ and F_s are introduced across the xz planes for the displacement and virtual variation, respectively. They work just like the shape function, but in 2D instead:

$$\begin{aligned} u_y(x,y,z) &= F_\tau(x,z)\ u_y(y) = N_i(y)\ F_\tau(x,z)\ u_{y_{\tau i}} \\ \delta u_y(x,y,z) &= F_s(x,z)\ \delta u_y(y) = N_j(y)\ F_s(x,z)\ \delta u_{y_{sj}} \end{aligned} \tag{2.24}$$

Defining matrix $\mathbf{b}$:

$$\mathbf{b} = \begin{bmatrix} \partial/\partial x & 0 & 0 \\ 0 & \partial/\partial y & 0 \\ 0 & 0 & \partial/\partial z \\ \partial/\partial z & 0 & \partial/\partial x \\ 0 & \partial/\partial z & \partial/\partial y \\ \partial/\partial y & \partial/\partial x & 0 \end{bmatrix} \tag{2.25}$$

and updating ε, σ and $\delta\varepsilon$ to the 3D interpolation, we have:

$$\begin{aligned} \varepsilon(x,y,z) &= \mathbf{b}\ N_i(y)\ F_\tau(x,z)\ u_{y_{\tau i}} \\ \sigma(x,y,z) &= \mathbf{C}\ \mathbf{b}\ N_i(y)\ F_\tau(x,z)\ u_{y_{\tau i}} \\ \delta\varepsilon(x,y,z) &= \mathbf{b}\ N_j(y)\ F_s(x,z)\ \delta u_{y_{sj}} \end{aligned} \tag{2.26}$$

From equation 2.21, we can derive the 3D FN associated to the four indexes τ, s, i and j:

$$\mathbf{k}^{\tau sij} = \int_V F_s(x,z)\ N_j(y)\ \mathbf{b}^T\ \mathbf{C}\ \mathbf{b}\ N_i(y)\ F_\tau(x,z)\ dV \tag{2.27}$$

The matrix of the an element is assembled with four loops, one for each index: τ and s varying according to the cross-section discretization while i and j vary according to the nodes discretization in the element. The global stiffness matrix is assembled from

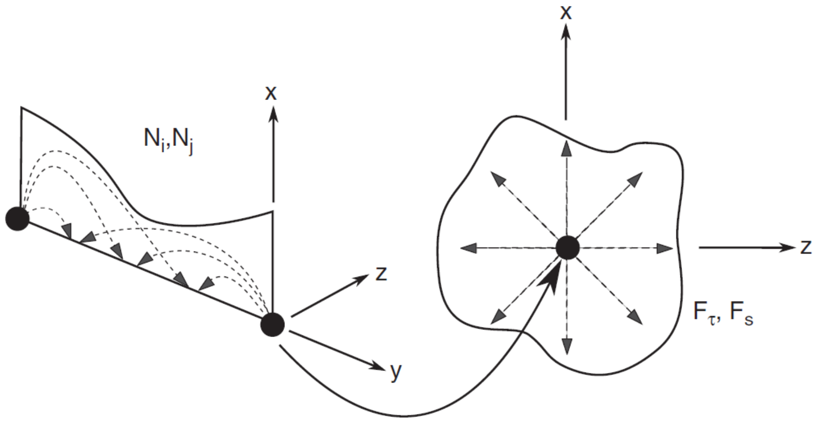

Figure 15 – Graphical representation of the 1D element shape functions N_i and N_j (left) and the 2D cross-section expansion functions F_τ and F_s (right). (CARRERA et al., 2014), page 60.

from the elements matrices, just like in any other finite element method approach. Figure 16 shows the procedure schematic.

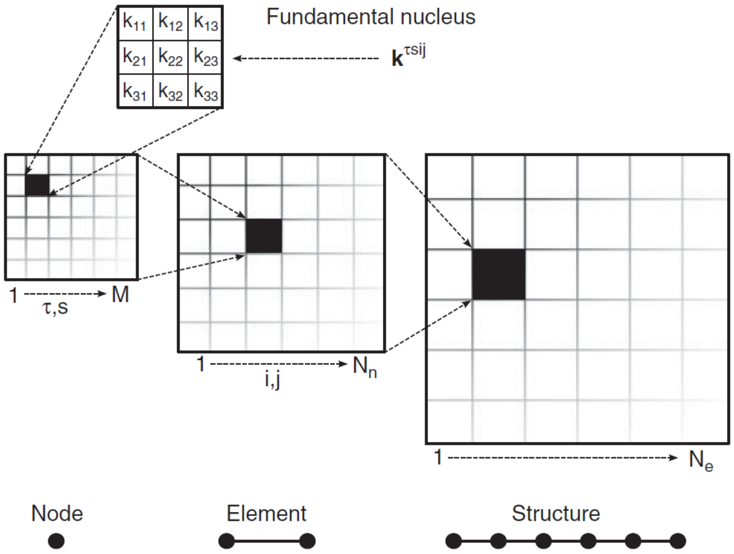

Figure 16 – Global matrix assembly for a 1D element. (CARRERA et al., 2014), page 63.

In an analogue way, we can derive the stiffness matrix for 2D and 3D elements. For a 2D element, N_i is a function of x and y and F_τ is a function of z, while for a 3D element, N_i is a function of x, y and z and $F_\tau = 1$. This way, for 1D, 2D and 3D elements, the displacements will depend on x, y and z, so all problems can be treated the same way.

Even though a panel should be modelled as a 2D structure, CUF turns possible the usage of a 1D model to simulate this kind of structure. We can use the larger dimension of the structure as the beam axis and discretize the long cross-sections with one of the methods that are going to be presented next. This model can provide accurate results to the simulation, as we are going to see in future sections.

2.2.3 Classical Cross-Section Models

The classical reference models for beams under bending were provided by Euler-Bernoulli (Euler, 1744) and Timoshenko (1921, 1922). Below both models will be described and their differences clarified.

2.2.3.1 Euler-Bernoulli Beam Theory (EBBT)

The Euler-Bernoulli beam model are substantiated by some assumptions, represented by figure 17:

1. The cross-sections are perpendicular to the neutral surface during deformation.
2. The cross-sections remain plane during deformation.
3. The cross-sections rotate around the surface, so the neutral surface does not change in length during deformation.

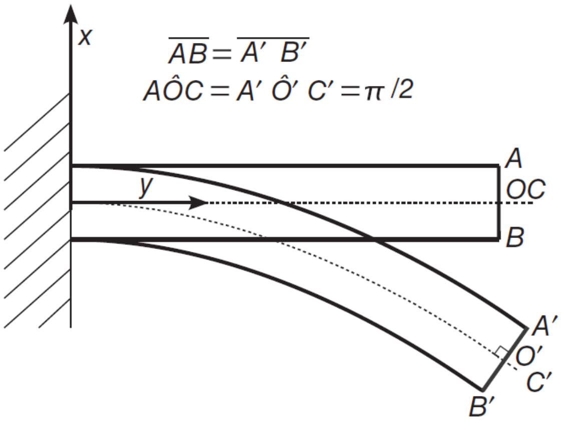

Figure 17 – Euler-Bernoulli beam model. (CARRERA et al., 2014), page 107.

From these assumptions, we have that the x and z coordinates do not affect on the x and z displacements. It means that u_x and u_z are functions of y only and u_y will depend on the neutral surface displacement and on the rotation angles around x and z axes. This theory derivations leads to null shear stresses: $\sigma_{xy} = \sigma_{yx} = 0$.

The governing equations (Euler's elastica) are:

$$\begin{aligned} M &= EI\frac{d^2u_x}{dy^2} \\ Q &= \frac{dM}{dy} \end{aligned} \tag{2.28}$$

where I is the section's inertia moment, M is the bending moment and Q the shear force.

2.2.3.2 Timoshenko Beam Theory (TBT)

The same assumptions made in the previous model remain in Timoshenko's, except that the cross-section is no longer constrained perpendicularlly to the neutral surface. Figure 18 shows the different configuration using TBT for the same example displayed in figure 17 using EBBT.

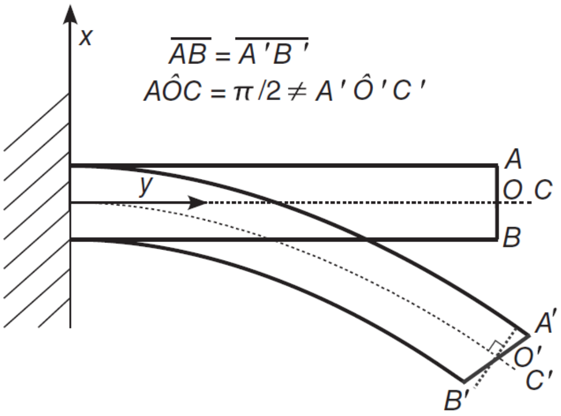

Figure 18 – Timoshenko beam model. (CARRERA et al., 2014), page 109.

In TBT the displacements do not depend on the x and z coordinates, just like EBBT, but the constitutive relations are different: σ_{xy} and σ_{yx} are not null anymore and the normal stress σ_{yy} also differs from the previous model. By solving a problem with both approaches, it is clear that the Timoshenko model results in the same bending contribution from Euler-Bernoulli's added to a shear contribution, which enhances the solution.

2.2.4 Taylor Expansion Class

This subsection will present the N-th order Taylor Expansion to discretize 2D cross-sections of 1D elements, also referred as TE elements. Just like in the previous subsections, all the information presented here is credited to (CARRERA et al., 2014) and can be found in chapter 8 (*One-Dimensional Models with* N*th-Order Displacement Field, the Taylor Expansion Class*) followed by a large number of examples.

As the name suggests, in this class the cross-section expansion functions are originated by the Taylor Expansion until the N-th order term. For $N = 1$:

$$\begin{aligned} u_x &= u_{x_1} + x\ u_{x_2} + z\ u_{x_3} \\ u_y &= u_{y_1} + x\ u_{y_2} + z\ u_{y_3} \\ u_z &= u_{z_1} + x\ u_{z_2} + z\ u_{z_3} \end{aligned} \tag{2.29}$$

which means that $F_1 = 1$, $F_2 = x$ and $F_3 = y$.

If we increase to $N = 2$, we have:

$$\begin{aligned} u_x &= u_{x_1} + x\ u_{x_2} + z\ u_{x_3} + x^2\ u_{x_4} + xz\ u_{x_5} + z^2\ u_{x_6} \\ u_y &= u_{y_1} + x\ u_{y_2} + z\ u_{y_3} + x^2\ u_{y_4} + xz\ u_{y_5} + z^2\ u_{y_6} \\ u_z &= u_{z_1} + x\ u_{z_2} + z\ u_{z_3} + x^2\ u_{z_4} + xz\ u_{z_5} + z^2\ u_{z_6} \end{aligned} \tag{2.30}$$

which means that $F_4 = x^2$, $F_5 = xz$ and $F_6 = z^2$.

We can keep increasing the N value to obtain higher order expansions with a total of $(N+1)(N+2)/2$ terms and expansion functions with binomial coefficients.

Considering a B2 element (formed by two nodes), we can use the following shape functions:

$$N_1 = 1 - \frac{y}{L},\ N_2 = \frac{y}{L},\ \begin{cases} r_1 = 0 \\ r_2 = L \end{cases} \tag{2.31}$$

where the natural coordinate y varies from y_1 to y_2 and correspond to the position of the node. To compute the ε strains we need to calculate the partial derivatives of the displacements with respect to each coordinate, as in equation 2.26. Using a second order TE ($\tau, s = 1, ..., 6$) for the B2 element ($i, j = 1, 2$), we get:

$$\mathbf{F}_\tau = \begin{bmatrix} F_1 \\ F_2 \\ F_3 \\ F_4 \\ F_5 \\ F_6 \end{bmatrix} = \begin{bmatrix} 1 \\ x \\ z \\ x^2 \\ xz \\ z^2 \end{bmatrix} \tag{2.32}$$

therefore

$$\frac{\partial \mathbf{F}_\tau}{\partial x} = \begin{bmatrix} 0 \\ 1 \\ 0 \\ 2x \\ z \\ 0 \end{bmatrix},\ \frac{\partial \mathbf{F}_\tau}{\partial y} = \begin{bmatrix} 0 \\ 0 \\ 0 \\ 0 \\ 0 \\ 0 \end{bmatrix},\ \frac{\partial \mathbf{F}_\tau}{\partial z} = \begin{bmatrix} 0 \\ 0 \\ 1 \\ 0 \\ x \\ 2z \end{bmatrix} \tag{2.33}$$

and

$$\begin{array}{ll} \partial N_1/\partial x = 0 & \partial N_2/\partial x = 0 \\ \partial N_1/\partial y = -1/L & \partial N_2/\partial y = 1/L \\ \partial N_1/\partial z = 0 & \partial N_2/\partial z = 0 \end{array} \tag{2.34}$$

Combining equations 2.26, 2.33 and 2.34 we get that the strain in a generic point $(x, y, z) = (x_p, y_p, z_p)$ can be described by:

$$\begin{aligned} \varepsilon_{xx}(x_p, y_p, z_p) &= 1\ u_{x_{21}} + 2\ x_p\ u_{x_{41}} + z_p\ u_{x_{51}} \\ \varepsilon_{yy}(x_p, y_p, z_p) &= -\frac{1}{L}(1\ u_{y_{11}} + x_p\ u_{y_{21}} + z_p\ u_{y_{31}} + x_p^2\ u_{y_{41}} + x_p z_p\ u_{y_{51}} + z_p^2\ u_{y_{61}}) \\ &\quad + \frac{1}{L}(1\ u_{y_{12}} + x_p\ u_{y_{22}} + z_p\ u_{y_{32}} + x_p^2\ u_{y_{42}} + x_p z_p\ u_{y_{52}} + z_p^2\ u_{y_{62}}) \\ \varepsilon_{zz}(x_p, y_p, z_p) &= 1\ u_{z_{31}} + x_p\ u_{z_{51}} + 2\ z_p\ u_{z_{61}} \end{aligned} \tag{2.35}$$

To make things simpler, we can reduce our model canceling the displacement terms that do not appear in the strain. In this example, if we cancel the terms with u_{x_3}, u_{x_6}, u_{y_5}, u_{z_2} and u_{z_4}, we get the same result with less information processed.

The Euler-Bernoulli and Timoshenko beam theories are obtained as particular cases of the TE expansion with $N = 1$ using the full linear expansion.

2.2.5 Lagrange Expansion Class

Another kind of expansion function that can be implemented through the unified formulation is the Lagrange Expansion, also referred as LE models. This subsection will present and discuss the usage of this kind of expansion for 1D models, as in (CARRERA et al., 2014) (2014), chapter 9 (*One-Dimensional Models with a Physical Volume/Surface-Based Geometry and Pure Displacement Variables, the Lagrange Expansion Class*). The main advantage of this cross-section model is that it reduces considerably the computational costs of the matrices generations.

As the name suggests, Lagrange polynomials are often used as expansion functions for LE models. Quadrilateral and triangular LE elements will be presented with different number of points n and will be called Ln according to this number. The simplest example is the L4 quadrilateral expansion from figure 19.

The corresponding expansion functions to this element is:

$$F_\tau = \frac{1}{4}(1 + \alpha\alpha_\tau)(1 + \beta\beta_\tau), \text{ with } \tau = 1, 2, 3, 4 \tag{2.36}$$

where α_τ and β_τ are the α and β coordinates of each normalized point.

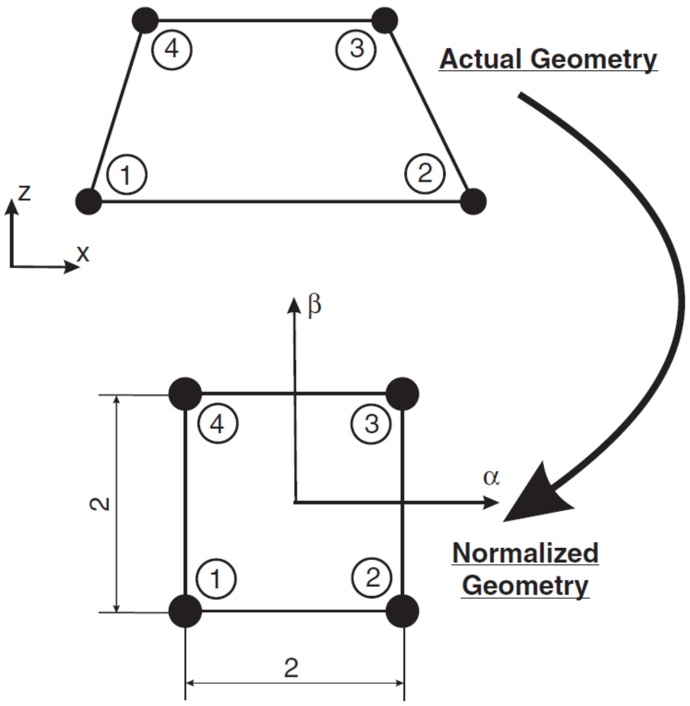

Figure 19 – Actual and normalized L4 element. (CARRERA et al., 2014), page 154.

For the L3 triangular set from figure 20, the polynomials are given by:

$$F_1 = 1 - \alpha - \beta \qquad F_2 = \alpha \qquad F_3 = \beta \tag{2.37}$$

For the L6, are:

$$\begin{aligned} &F_1 = 1 - 3(\alpha + \beta) + 2(\alpha^2 + 2\alpha\beta + \beta^2), && F_2 = 4\alpha(1 - \alpha - \beta) \\ &F_3 = \alpha(2\alpha - 1), && F_4 = 4\alpha\beta \\ &F_5 = \alpha(2\beta - 1), && F_6 = 4\beta(1 - \alpha - \beta) \end{aligned} \tag{2.38}$$

And for the L9, are:

$$\begin{aligned} &F_\tau = \frac{1}{4}(\alpha^2 + \alpha\alpha_\tau)(\beta^2 + \beta\beta_\tau), && \tau = 1,3,5,7 \\ &F_\tau = \frac{1}{2}\beta_\tau^2(\beta^2 + \beta\beta_\tau)(1 - \alpha^2) + \frac{1}{2}\alpha_\tau^2(\alpha^2 + \alpha\alpha_\tau)(1 - \beta^2), && \tau = 2,4,6,8 \\ &F_\tau = (1 - \alpha^2)(1 - \beta^2), && \tau = 9 \end{aligned} \tag{2.39}$$

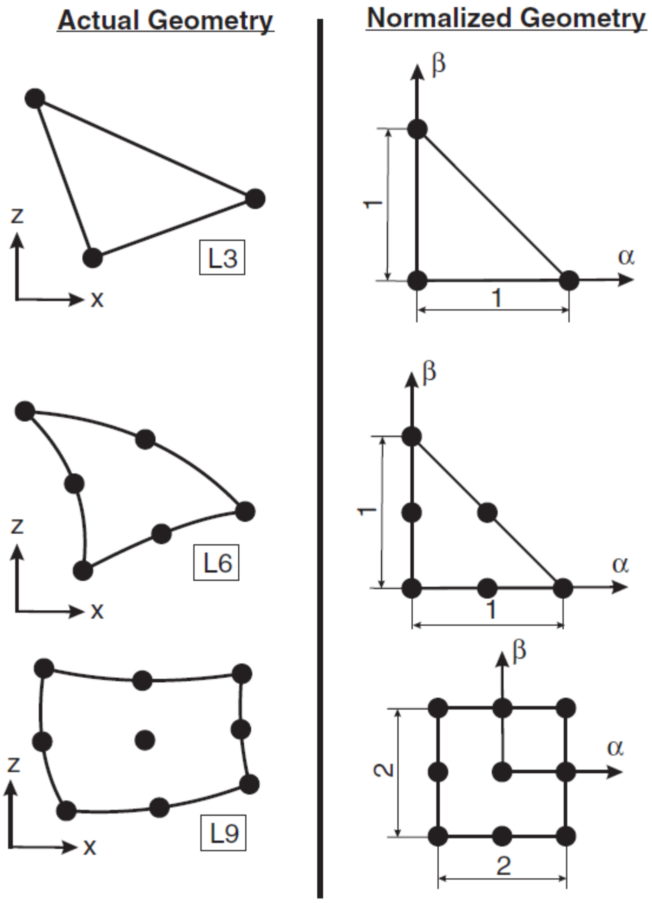

Figure 20 – Actual and normalized L3, L6 and L9 elements. (CARRERA et al., 2014), page 155.

Each point in the LE element has 3 degrees of freedom (DOF) if none of the movements in x, y and z are constrained, it means that L3 has a total of 9 DOF, L4 has 12 DOF, L6 has 18 DOF and L9 has 27 DOF. Just like before, if we derive the displacements with respect to all coordinates we can compute the strain, the virtual work and the fundamental nucleus, respectively.

In the Lagrange expansion model, all cross-sections must be a composition of the four fundamental elements (L3, L4, L6 and L9), giving a better discretization to sections that need higher precision.

To exemplify this statement, let us take three different models for the same hollow square cross-section 21: the first one with 8 L9 elements, the second with 9 L9 and the third with 11 L9 22. The total length of the clamped-clamped beam is 20m, the thickness t is 0.1m and the side of the square h measures 1m. A point load with magnitude of 1N is applied at $(x, y, z) = (0,\ 10\text{ m},\ -0.5\text{ m})$ and the vertical displacement of this point is calculated at table 1 comparing the results for a solid model implemented in MSC Nastran, EBBT, TE with $N = 4,\ 8,\ 11$ and the three LE discretizations. As we can see, the finer LE meshes in the load application point's neighborhood gave closer results to the solid model, as well as the higher order Taylor expansions.

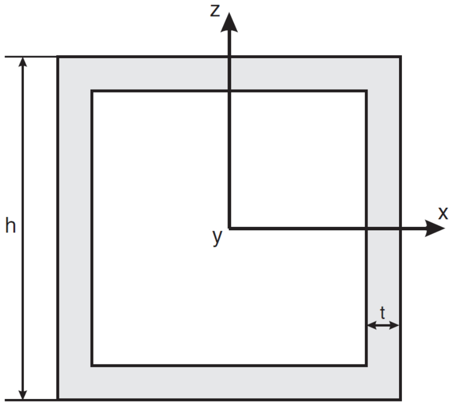

Figure 21 – Cross-section taken from example found in (CARRERA et al., 2014), page 174.

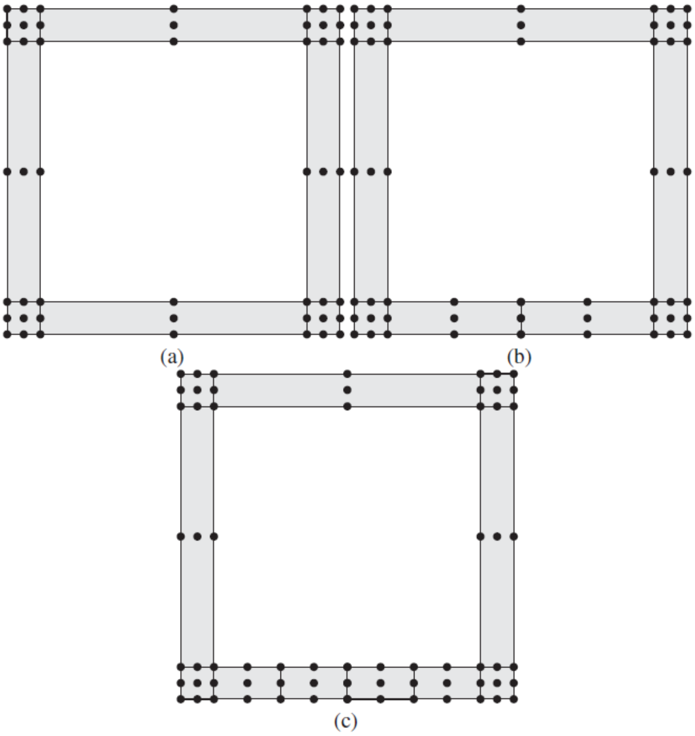

Figure 22 – Cross-section discretizations: (a) 8 L9; (b) 9 L9; (c) 11 L9, as in (CARRERA et al., 2014), page 175.

Model		**DOFs**	$u_z \times 10^8$ (m)
Solid		128952	1.375
TE	EBBT	155	1.129
	$N = 4$	1395	1.209
	$N = 8$	4185	1.291
	$N = 11$	7254	1.309
LE	8 L9	4464	1.277
	9 L9	5022	1.308
	11 L9	6138	1.326

Table 1 – Loaded point vertical displacement for different models. (CARRERA et al., 2014), page 175.

2.2.6 Piezoelectricity Formulation

The introduction of piezoelectric properties in the model demands some addition to the basic structural formulation presented in the previous sections. The formulation described here was presented by Carrera, Zappino and Li (CARRERA; ZAPPINO; LI, 2017).

Including the electric potential ϕ in the generalized displacement vector $\bar{u}$ along with the mechanic displacements $u = (u_x, u_y, u_z)$, we get:

$$\bar{\mathbf{u}} = \begin{bmatrix} u_x \\ u_y \\ u_z \\ \phi \end{bmatrix} \tag{2.40}$$

Updating the differential operator $\mathbf{b}$ to the four DOF formulation operator $\bar{\mathbf{b}}$, we have:

$$\bar{\mathbf{b}} = \begin{bmatrix} \partial/\partial x & 0 & 0 & 0 \\ 0 & \partial/\partial y & 0 & 0 \\ 0 & 0 & \partial/\partial z & 0 \\ \partial/\partial z & 0 & \partial/\partial x & 0 \\ 0 & \partial/\partial z & \partial/\partial y & 0 \\ \partial/\partial y & \partial/\partial x & 0 & 0 \\ 0 & 0 & 0 & \partial/\partial x \\ 0 & 0 & 0 & \partial/\partial y \\ 0 & 0 & 0 & \partial/\partial z \end{bmatrix} \tag{2.41}$$

Hence, defining the electric field vector as the gradient of the electric potential

$\bar{\mathbf{E}} = (E_x, E_y, E_z) = \nabla\phi$ the generalized strain vector $\bar{\varepsilon}$ becomes:

$$\bar{\varepsilon} = \begin{bmatrix} \varepsilon_{xx} \\ \varepsilon_{yy} \\ \varepsilon_{zz} \\ \gamma_{xz} \\ \gamma_{yx} \\ \gamma_{xy} \\ E_x \\ E_y \\ E_z \end{bmatrix} = \bar{\mathbf{b}}\ \bar{\mathbf{u}} \tag{2.42}$$

Defining the permitivy matrix $\bar{\chi}$, the piezoelectric stiffness matrix $\bar{\mathbf{e}}$ and the stiffness matrix $\bar{\mathbf{C}}$ rotated with respect to the z axis in order to align the piezoelectric components pole to the z direction:

$$\bar{\chi} = \begin{bmatrix} \chi_{11} & \chi_{12} & 0 \\ \chi_{21} & \chi_{22} & 0 \\ 0 & 0 & \chi_{33} \end{bmatrix} \tag{2.43}$$

$$\bar{\mathbf{e}} = \begin{bmatrix} 0 & 0 & 0 & e_{14} & e_{15} & 0 \\ 0 & 0 & 0 & e_{24} & e_{25} & 0 \\ e_{31} & e_{32} & e_{33} & 0 & 0 & e_{36} \end{bmatrix} \tag{2.44}$$

$$\bar{\mathbf{C}} = \begin{bmatrix} C_{11} & C_{12} & C_{13} & 0 & 0 & C_{16} \\ C_{21} & C_{22} & C_{23} & 0 & 0 & C_{26} \\ C_{31} & C_{32} & C_{33} & 0 & 0 & C_{36} \\ 0 & 0 & 0 & C_{44} & C_{45} & 0 \\ 0 & 0 & 0 & C_{54} & C_{55} & 0 \\ C_{61} & C_{62} & C_{63} & 0 & 0 & C_{66} \end{bmatrix} \tag{2.45}$$

At last, defining the electric displacement vector $D_e = (D_x, D_y, D_z)$, we can set the constitutive relations of the structure:

$$\begin{gathered} \sigma = \bar{\mathbf{C}}\varepsilon - \bar{\mathbf{e}}^T\bar{\mathbf{E}} \\ \mathbf{D_e} = \bar{\mathbf{e}}\varepsilon + \bar{\chi}^T\bar{\mathbf{E}} \end{gathered} \tag{2.46}$$

Using the generalized stress vector $\bar{\sigma} = \begin{bmatrix} \sigma \\ \mathbf{D_e} \end{bmatrix}$, we can get the relation between the generalized strain $\bar{\varepsilon}$ and the generalized stress $\bar{\sigma}$ (analogue to the Hooke's Law):

$$\bar{\sigma} = \bar{\mathbf{H}}\,\bar{\varepsilon} \tag{2.47}$$

where:

$$\bar{\mathbf{H}} = \begin{bmatrix} \bar{\mathbf{C}} & -\bar{\mathbf{e}} \\ \bar{\mathbf{e}} & \bar{\chi} \end{bmatrix} \tag{2.48}$$

For more details about the rotation of piezoelectric stiffness matrix there are the following references: (KPEKY et al., 2017), (BENJEDDOU; TRINDADE; OHAYON, 1997) and (KAPURIA; HAGEDORN, 2007). Just like before, according to the CUF, the generalized displacement vector depending on all three directions for a beam element is:

$$q(x, y, z) = N_i(y)\ F_\tau(x, z)\ q_{\tau i} \tag{2.49}$$

Analogously to the fundamental nucleus derivation in the mechanical formulation, for the piezo-mechanical it is described by:

$$\mathbf{k}^{\tau sij} = \int_V F_s(x, z)\ N_j(y)\ \bar{\mathbf{b}}^T\ \bar{\mathbf{H}}\ \bar{\mathbf{b}}\ N_i(y)\ F_\tau(x, z)\ dV \tag{2.50}$$

which is a 4 × 4 matrix instead of a 3 × 3, because it includes the electric potential variable as well as the three mechanic displacements.

Regarding to the node-dependent kinematics when modelling structures with embedded or attached piezo-patches, we must discretize the structure with cross-section elements in a way that each element is composed by just one material. If a node belongs to at least one piezo element, then its displacement is given by four variables (u_x, u_y, u_z, ϕ) and the fundamental nucleus associated to this element is 4 × 4. If a node only belongs to non-piezo elements, then its displacement is given by three variables (u_x, u_y, u_z) and the fundamental nuclei of the elements are 3 × 3.

Figure 23 represents a square cross-section divided in 4 L4 elements. Element 1 is compound by nodes *a-b-e-d*, element 2 by nodes *b-c-f-e*, element 3 by nodes *d-e-h-g* and element 4 by nodes *e-f-i-h*. To assemble the finite element matrices, we must follow the CUF rules. Taking $\tau, s = a$, for example, leads us to a single 4 × 4 FN (node *a* is present only in piezo element 1); taking $\tau, s = b$, leads us to the sum of two 4 × 4 FN (node *b* is present in piezo elements 1 and 2); taking $\tau, s = d$, leads us to the sum of a 3 × 3 and a 4 × 4 FN (node *d* is present in piezo element 1 and non-piezo element 3); taking $\tau, s = e$, leads us to the sum of two 3 × 3 and two 4 × 4 FN (node *e* is present in piezo elements 1 and 2 and in non-piezo elements 3 and 4). Following this structure in all indexes loops,

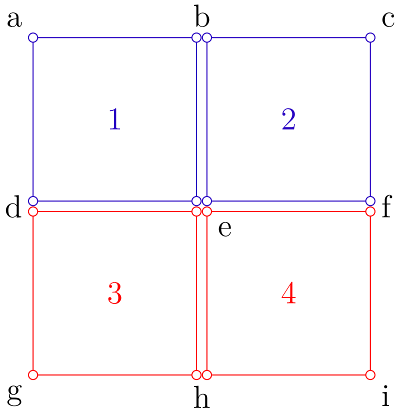

Figure 23 – Piezoelectric cross-section with 4 L4 elements. Blue elements are part of a piezo patch and red elements are purely mechanical.

the global matrix is generated. To enlighten the sum of fundamental nuclei with different sizes, an example is given next:

$$\mathbf{k}_1 = \begin{bmatrix} a_{11} & a_{12} & a_{13} \\ a_{21} & a_{22} & a_{23} \\ a_{31} & a_{32} & a_{33} \end{bmatrix} \text{ and } \mathbf{k}_2 = \begin{bmatrix} b_{11} & b_{12} & b_{13} & b_{14} \\ b_{21} & b_{22} & b_{23} & b_{24} \\ b_{31} & b_{32} & b_{33} & b_{34} \\ b_{41} & b_{42} & b_{43} & b_{44} \end{bmatrix} \tag{2.51}$$

so:

$$\mathbf{k}_{1+2} = \begin{bmatrix} b_{11}+a_{11} & b_{12}+a_{12} & b_{13}+a_{13} & b_{14} \\ b_{21}+a_{21} & b_{22}+a_{22} & b_{23}+a_{23} & b_{24} \\ b_{31}+a_{31} & b_{32}+a_{32} & b_{33}+a_{33} & b_{34} \\ b_{41} & b_{42} & b_{43} & b_{44} \end{bmatrix} \tag{2.52}$$

Considering a beam with $N_E = 4$ B2 elements, all with the same cross-section presented in figure 23. So a total of 5 cross-sections must be considered in the structure, each with 6 piezo nodes and 3 mechanic nodes, which result in a total of $N_p = 30$ piezo nodes and $N_m = 15$ mechanic nodes, totalizing $N_{tot} = 45$ nodes. In terms of DOF, the structure has a total of $30 \times 4 + 15 \times 3 = 165$. So the stiffness matrix of the structure considering the piezoelectricity is 165×165, while the mass matrix is 135×135 ($N_{tot} \times 3 = 135$ and $135 + N_m = 165$). Remembering the governing equation 2.1 of the system, we have:

$$\mathbf{M}\ddot{\mathbf{u}} + \mathbf{D}\dot{\mathbf{u}} + \mathbf{K}\mathbf{u} = \mathbf{F} \tag{2.53}$$

but **M** and **D** sizes do not match **K**. As the potential electric DOF can not be computed in the mass matrix, we can not leave zero values in their positions of the mass matrix, otherwise the system would not have an answer, once that $det(\mathbf{M}) = 0 \Rightarrow \mathbf{M}$ is not invertible. As a possible solution, we can condensate the stiffness matrix for the mechanical simulation and uncondense the results. Writing the static equation 2.3 for a single node with 4 DOF, we have:

$$\begin{bmatrix} \mathbf{K_{uu}} & \mathbf{K_{u\phi}} \\ \mathbf{K_{\phi u}} & k_{\phi\phi} \end{bmatrix} \begin{bmatrix} \mathbf{u} \\ \phi \end{bmatrix} = \begin{bmatrix} \mathbf{F} \\ 0 \end{bmatrix} \tag{2.54}$$

where:

$$\mathbf{K_{uu}} = \begin{bmatrix} k_{xx} & k_{xy} & k_{xz} \\ k_{yx} & k_{yy} & k_{yz} \\ k_{zx} & k_{zy} & k_{zz} \end{bmatrix}, \mathbf{K_{u\phi}} = \begin{bmatrix} k_{x\phi} \\ k_{y\phi} \\ k_{z\phi} \end{bmatrix} \text{ and } \mathbf{K_{\phi u}} = \begin{bmatrix} k_{\phi x} & k_{\phi y} & k_{\phi z} \end{bmatrix} \tag{2.55}$$

From 2.54, we have that:

$$\mathbf{K_{\phi u}u} + k_{\phi\phi}\phi = 0 \Rightarrow \phi = -\frac{1}{k_{\phi\phi}}\mathbf{K_{\phi u}u} \tag{2.56}$$

Replacing ϕ in the first row of 2.54:

$$\mathbf{K_{uu}u} - \frac{1}{k_{\phi\phi}}\mathbf{K_{u\phi}K_{\phi u}u} = \mathbf{F} \tag{2.57}$$

Defining the condensed matrix:

$$\mathbf{K_{cond}} = \mathbf{K_{uu}} - \frac{1}{k_{\phi\phi}}\mathbf{K_{u\phi}K_{\phi u}} \tag{2.58}$$

We can update equation 2.54 to:

$$\begin{cases} \mathbf{K_{cond}}\ \mathbf{u} = \mathbf{F} \\ \phi = -\frac{1}{k_{\phi\phi}}\mathbf{K_{\phi u}u} \end{cases} \tag{2.59}$$

The same algebra can be applied to a global stiffness matrix in order to match the size of the mass matrix. This way we can solve equation 2.1 replacing $\mathbf{K}$ by $\mathbf{K_{cond}}$ and calculating ϕ for every vector u resulted from the solution of the governing matrix differential equation. The usage of the static equation to derive the condensed stiffness matrix does not cause any compatibility problem when using it in the dynamic equation, because the electric potentials do not affect the inertia of the structure, only its stiffness.

To create a more reliable model for a piezo-patches not embedded to the structure found in the market, a metallic layer in the opposite face to the one bonded to the structure representing the electrode can be included. The material of this layer must have the mechanical properties of the chosen metal, no piezoelectric stiffness and high permitivity. This will avoid a misleading heterogeneous voltage distribution on the patch to be measured and calculated and lead to a uniform distribution, as one would expect. This change allows the observation of a single electric degree of freedom for each piezo-patch used as sensor to succesfully control the structure and the application of the control voltage also in a single node.

2.2.7 Damping Matrix

Up to this point damping was not treated, because for large degrees of freedom it is difficult to estimate this matrix analytically. A good alternative is to adopt the Rayleigh Damping Coefficients model, with a detailed formulation referred to (LIU; GORMAN, 1995), experimental methodology to (MOHAMMAD; KHAN; RAMAMURTI, 1995) and specifically computation for large DOF systems (CHOWDHURRY; DASGUPT, 2003).

This model assumes the damping matrix as a linear combination of the mass and stiffness matrices associated to the mechanical DOFs, proportional to the called Rayleigh coefficients α_M and β_K:

$$\mathbf{D} = \alpha_M \mathbf{M_{uu}} + \beta_K \mathbf{K_{uu}} \tag{2.60}$$

These coefficients can be determined by minimizing the following system of equations:

$$2\zeta_i \omega_i = \alpha_M + \beta_K \omega_i^2 \tag{2.61}$$

for the computed natural mode i with frequency ω_i and damping ratio ζ_i, giving higher weights for the first modes, which dynamics prevail. The Trust-Region-Reflective Least Squares fitting algorithm (MORE; SORENSEN, 1983) will be used to minimize the coefficients on equation 2.61, which is possible to be implemented through the *fit* function on MATLAB.

Therefore, the resonance frequency and damping ratio pairs values must be evaluated from experimental data. There are two distinct ways to do so: analyzing the transient response decay in the time domain with the i-th modal shape as initial condition or calculating the resonance peaks height and width in the frequency domain.

For the solution from the first scenario, we start with the differential equation for an unforced single degree of freedom harmonic oscillator that is given by:

$$m\frac{d^2u}{dt^2} + c\frac{du}{dt} + ku = 0 \tag{2.62}$$

which coincides to the governing equation 2.1 when matrices are replace by scalars. The solution for this equation is:

$$u(t) = U_0 \ e^{-\zeta\omega_n} sin(\omega_d t + \phi) \tag{2.63}$$

where U_0 is the initial amplitude, ϕ is the phase delay, $\zeta = c/(2\sqrt{mk})$ is the damping ratio, $\omega_n = \sqrt{k/m}$ is the natural frequency and $\omega_d = \omega_n\sqrt{1-\zeta^2}$ is the damped frequency.

When a structure vibrates freely with one of its modal shapes as initial condition, there is no superposition of modes, that is, the modes are decoupled and only the resonance frequency associated to this modal shape will affect the transient response of the system, which means that every unconstrained point of the structure will vibrate according to function 2.63. It is simple to calculate the damping ratio from this method: one may take the crests from the experimental displacement signal and perform an exponential regression in order to obtain the decaying envelope function $U_0\ e^{-\zeta\omega_n}$ (figure 24). Dividing the exponent by the resonance frequency associate to the oscillation will result in the desired coefficient.

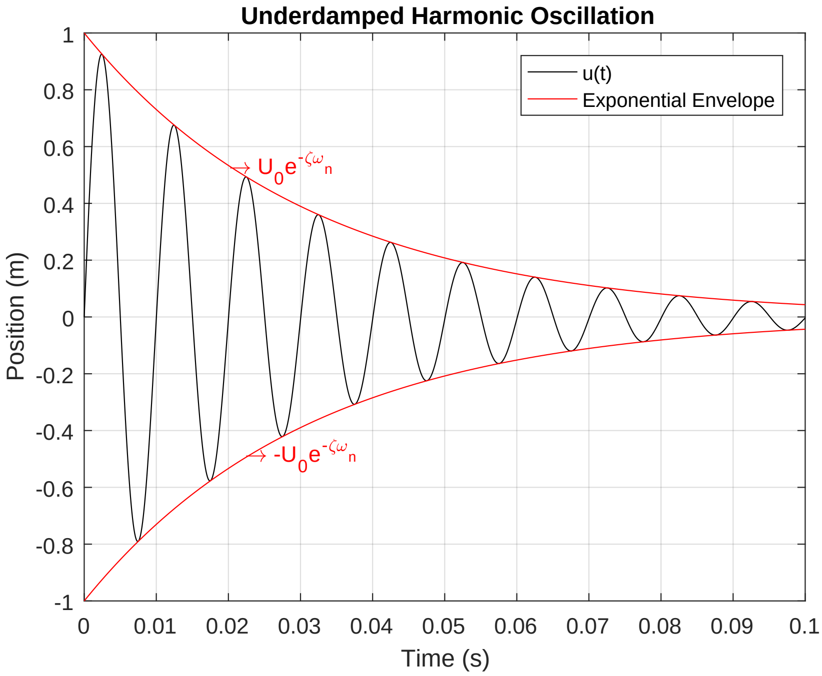

Figure 24 – Underdamped harmonic oscillation with exponential envelope functions for $U_0 = 1$ m, $\phi = 0$, $\zeta = 0.05$, $\omega_n = 200\pi$ rad/s.

For the second scenario, the damping ratio can be obtained from the quality factor parameter $Q = 1/(2\zeta)$ that is calculated from the full width half maximum (FWHM) (figure 25) of the resonant peaks:

$$Q = \frac{\omega_n}{\Delta\omega} \tag{2.64}$$

In other words, the quality factor is equal to the ratio between the resonant frequency itself and the bandwidth for the neighbor frequencies with $1/\sqrt{2}$ times (or -3 dB) the resonant peak gain. (CHOPRA, 2012).

The two distinct ways described above allows us to calculate the damping ratios from different sets of experimental data (in the time or in the frequency domain), so it is possible to make use of redundancy by calculating them from both approaches and, this way, increasing the assertiveness of these values that will be used to estimate the Rayleigh coefficients.

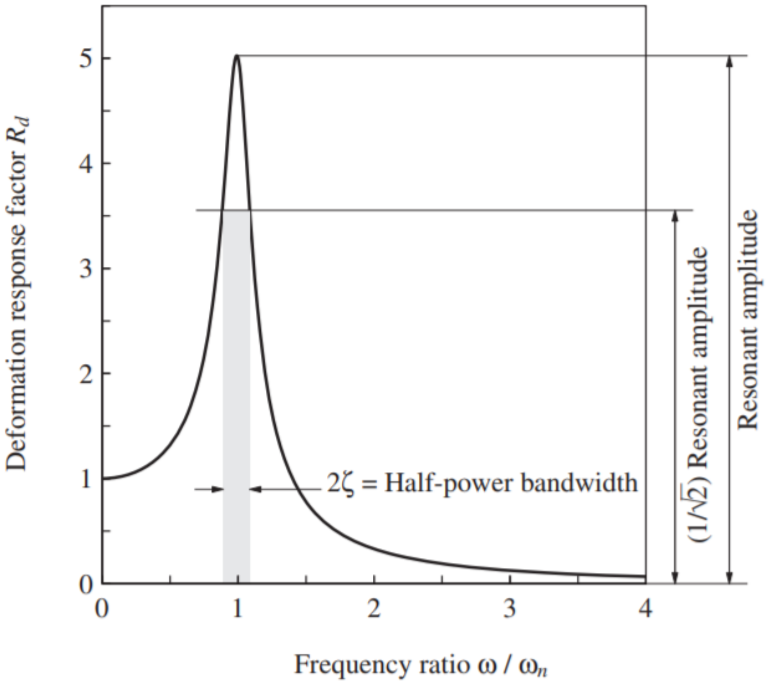

Figure 25 – Definition of half-power bandwidth. (CHOPRA, 2012), page 83

2.3 Active Vibration Control

This section will encompass all the steps performed in the project to generate a controlled signal of the structure motion starting from the piezo-mechanical state-space FEM model. For the controller design, one or more transfer functions must be derived from the state-space model, depending on the kind of control law to be used. For a SISO PID (proportional-integral-derivative) control, for example, only a single transfer function containing the dynamics of a single node voltage used as a sensor as a function of the voltage applied in a piezo-actuator. For a MIMO control, one transfer function is required for each pair of input-output to be controlled. Supposing a situation where three piezo-patches are distributed as actuators and five patches as sensors, to perform an optimal control that minimizes all the sensor signals for each actuator, 15 transfer functions must be taken into account. These are called open loop transfer functions, because there is no feedback connecting output signals to the input. The block diagram of this system was previously presented in the MATLAB implementation subsection (figure 35). Unfortunately it is not possible to simply take the exact transfer functions from the state-space (OGATA, 1995):

$$\mathbf{G}(s) = \mathbf{C}(s\mathbf{I} - \mathbf{A})^{-1} + \mathbf{D} \tag{2.65}$$

because each transfer function of this matrix would have the same amount of poles as the number of degrees of freedom of the structure, which is extremely complex to even be computed by MATLAB. So, in order to make feasible the controller design, an approximation of the model with reduced order is required. The following subsections will deal with the order reduction of the model and the controller design.

2.3.1 Frequency Response

The frequency response of a system is the output steady-state response measurements for the input frequency spectrum injected in it. In other words, if a sinusoidal input is used in the system, we can obtain the gain and the phase lag of the output steady-state response as a function of the input frequency. For a generic transfer function $G(s)$, this is equivalent to calculate the magnitude (M) and phase (Φ) of G for $s = i\omega$ for all frequencies, where i is the imaginary unit and ω is the input frequency measured in rad/s, as clarified in detail by Ogata (OGATA, 1995).

$$G(i\omega) = Me^{i\Phi} = M\underline{/\Phi} \tag{2.66}$$

The graphical representation of the frequency response is called Bode diagram. It is divided in two different plots: the first represents the magnitude M in dB and the second the phase Φ in degrees, both as a function of the frequency ω logarithmically scaled on the x-axis. The representation of the magnitude in dB was originated from methods used to quantify signal power loss in telegraph and telephone circuits. It is represented in tenths of the base-10 logarithm of the signals power ratio. The power of a sinusoidal wave is proportional to the square of its amplitude, so the magnitude in dB is defined as:

$$|G(i\omega)|\ dB = 10\ log_{10}(M^2) = 20\ log_{10}(M) \tag{2.67}$$

A very simple approximation of a Bode diagram of a transfer function can be plotted with its asymptotic lines. If there are no poles or zeros in the origin, an horizontal line comes from the low frequency range at the magnitude equivalent to $|G(s = 0)|$ in decibel. Then, for each zero the magnitude inclination increases 20 dB/decade and for each pole it decreases 20 dB/decade. For the phase plot, for each real zero, 90° must be added and, for each real pole, 90° must be subtracted. The phase transition from one step to another takes 2 decades, centered in the pole frequency. The starting value at low frequency will depend on the sign of $G(s = 0)$, if it is greater than zero, the phase is 0°, otherwise it is 180°.

This approximation does not take into account the resonance peaks that may be contained in second order poles of the system. It is important to highlight that every system order higher than 2 can be split in multiple systems of first and second order, so knowing the peculiarities of systems of order 1 and 2 is enough to describe every system. A second order system can be represented in the following form:

$$H(s) = \frac{\omega_0^2}{s^2 + 2\zeta\omega_0 + \omega_0^2} = \frac{1}{\left(\dfrac{s}{\omega_0}\right)^2 + 2\zeta\left(\dfrac{s}{\omega_0}\right) + 1} \tag{2.68}$$

If the damping coefficient ζ is less than 0.5, not only the decrease of 20 dB/dec must be drawn, but also a peak at ω_0 with the amplitude of $1/2\zeta$ in dB. For complex conjugate zeros instead of poles, the peak amplitude is given by 2ζ in dB. In the phase plot, instead of changing 180° in a single frequency ω_0, the change is performed between $\omega_0/10^{\zeta}$ and $10^{\zeta}\omega_0$. As stated earlier, for real zeros and poles, the transition takes 2 decades, which is equivalent to say that $\zeta = 1$ in those cases.

Despite the impossibility to derive the transfer function directly from the state-space FEM model, it is possible to calculate the frequency response of the system and estimate its transfer function for an order of choice through MATLAB. To generate this Bode diagram, a frequency range of interest must be chosen, as well as the discretization of this range, which can be organized in a frequencies array. A good range should comprise all the significant excitation frequencies to which the model should be subjected, and should be logarithmically spaced, since the representation of the response is in a logarithmic scale. For each frequency of this array, the transfer function evaluation with $s = i\omega$ must be performed and the values divided in magnitude (in dB) and phase (in degrees). Applying the Laplace transform 1.1 in the governing equation 2.1 with the condensation matrices, we get:

$$\left(\mathbf{M_{cond}}s^2 + \mathbf{D_{cond}}s + \mathbf{K_{cond}}\right)\mathcal{L}\{u(t)\} = \mathcal{L}\{F(t)\} \tag{2.69}$$

From the definition of transfer function $Y(s) = \mathbf{G(s)}U(s)$, where $Y(s)$ is the Laplace transform of the output and $U(s)$ is the transform of the input, which in this case are $u(t)$ and $F(t)$ respectively, we can obtain the transfer function for the mechanic degrees of freedom (plant):

$$\mathbf{G_p}(s) = \left(\mathbf{M_{cond}}s^2 + \mathbf{D_{cond}}s + \mathbf{K_{cond}}\right)^{-1} \tag{2.70}$$

Defining the gain matrices related to the actuator $\mathbf{G_act(s)}$ and to the uncondensation $\mathbf{G_{sen}(s)}$, which were referred to as *PiezoPatches* and *Uncondensation* blocks in the block diagram for the open loop system located in the MATLAB implementation subsection (figure 35), the transfer function from the input voltages in the actuator patches to the output voltages in the whole structure can be derived. An output selection matrix $\mathbf{G_{sel}}(s)$ must be created, this will select only the desired electric degrees of freedom to be used as outputs. For the k-th row of this matrix, a value of 1 is placed in the column related to the central node electric degree of freedom located in the measurable face of the k-th patch used as a sensor, while in the rest, a value of 0 is placed. The global open loop transfer function $\mathbf{G_g}(s)$ becomes:

$$\mathbf{G_g}(s) = \mathbf{G_{sel}}(s)\ \mathbf{G_{sen}}(s)\ \mathbf{G_p}(s)\ \mathbf{G_{act}}(s) \tag{2.71}$$

Replacing $\mathbf{G_p}(\mathbf{s})$ from equation 2.70 into equation 2.71 and removing the s dependency from the gain matrices, and using $s = i\omega$ for the frequency response analysis, the global transfer function becomes:

$$\mathbf{G_g}(i\omega) = \mathbf{G_{sel}}\ \mathbf{G_{sen}}\ \left(-\mathbf{M_{cond}}\omega^2 + \mathbf{D_{cond}}i\omega + \mathbf{K_{cond}}\right)^{-1} \mathbf{G_{act}} \tag{2.72}$$

Given this transfer function, to obtain the frequency response of the high order system, one must simply evaluate the magnitude $|G_g(i\omega)|$ and phase $\underline{/G_g(i\omega)}$ for all frequencies contained in the array. In the sequence, the frequency response of the previously introduced example structure will be obtained using the proposed algorithm applied to the G_g transfer function 2.72.

2.3.2 Model Order Reduction

In large-scale dynamical systems, the model order reduction (MOR) is largely used to simplify the system's complexity in order to reduce the computational costs of the simulations or, as in the case of this project, to obtain a simpler and controllable transfer function. The reduced-order model (ROM) is an approximation of the real system, which must be obtained as a balance between accuracy and simulation time. As higher the order, more accurate the approximation as and longer it takes to be evaluated. There are several techniques of MOR. One of the most common ones is the projection-based reduction, which as its name says, reduces the model order by mapping it in a space with lower dimension than the one it belongs to, in a way that the behavior of the MOR is sufficiently close to the original model. The proper orthogonal and generalized decomposition are methods based on this approach widely used in engineering applications. A short review on this method was presented in (CHINESTA; LADEVEZE; CUETO, 2011). An important consequence of this technique that must be verified is the stability preservation, as studied in (SELGA; LOHMANN; EID, 2012). Other techniques and tools specifically used in structural dynamics were summarized in (BENNER; FASSBENDER, 2013).

Fortunately, there is a function implemented in the System Identification Toolbox for MATLAB called *tfest*, that estimates a continuous or discrete time transfer function for a data set, given number of poles and, if specified, zeros. The estimated transfer function

G_{est} for a SISO system is given by the ratio of its numerator $N(s)$ to its denominator $D(s)$:

$$G_{est}(s) = \frac{N(s)}{D(s)} \tag{2.73}$$

If a frequency domain data set with i inputs and a single output is used as parameter to the *tfest* function, it will calculate N_i and D in order to solve the following minimization of the loss function:

$$\underset{N_i,D}{\text{minimize}} \sum_{k=1}^{n_f} \left| W(\omega_k) \left(y(\omega_k) - \sum_{i=1}^{n_u} \frac{N_i(\omega_k)}{D(\omega_k)} u_i(\omega_k) \right) \right|^2 \tag{2.74}$$

where W is a frequency-dependent weight, ω_k is the k-th frequency in the set, y is the output and u_i is the i-th input.

For a single input $(i = 1)$ and leaving the default weight $W = 1$, the nonlinear least-squares problem becomes:

$$\underset{N,D}{\text{minimize}} \sum_{k=1}^{n_f} \left| y(\omega_k) - \frac{N(\omega_k)}{D(\omega_k)} u(\omega_k) \right|^2 \tag{2.75}$$

The problem is solved through S-K iterations, expounded in (DRMAC; GUGERCIN; BEATTIE, 2014), referring to the objective function introduced in (SANATHANAN; KOERNER, 1963).

To assess the quality of the identified model, *tfest* returns some model quality metrics, which compare the estimation to the real data provided by the user. This information can be checked in the MATLAB documentation for the loss function and model quality metrics (MATHWORKS, 2017):

1. **Fitting Percentage:**

   It is the Normalized Root Mean Squared Error expressed as a percentage:

   $$FitPercent = 100 \left(1 - \frac{\| y_{measured} - y_{model} \|}{\| y_{measured} - \overline{y_{measured}} \|} \right) \tag{2.76}$$

   where $y_{measured}$ is the measured output data, $\overline{y_{measured}}$ is its mean and y_{model} is the predicted response of the model. The closer to 100% it is, the more precise the model is in terms of fitting.

2. **Mean Squared Error (MSE):**

   Defined as:

   $$MSE = \frac{1}{N} \sum_{k=1}^{N} e^T(k) e(k) \tag{2.77}$$

   where $e(k)$ is the signal whose norm is minimized for estimation and N is the number of samples in the dataset. The quality of the model can be measured according to how low its MSE is.

3. **Akaike's Final Prediction Error (FPE):**

   Defined as:

$$FPE = det\left(\frac{1}{N}E^T\ E\right)\left(\frac{1+\dfrac{n_f}{N}}{1-\dfrac{n_f}{N}}\right) \tag{2.78}$$

   where n_f is the number of free parameters in the model, N is the size of the dataset and E is the matrix of prediction errors. As lower the FPE of the model is, a better representation of the system it is in term of prediction errors.

Defining n_p the number of poles and n_z the number of zeros in the desired transfer function, the reduced-order is going to match n_p and n_z must be lower than n_p, which can be specified or left as the default value of $n_p - 1$. For each pair of input-output, a transfer function will be estimated and the set of transfer functions will form the reduced-order model.

2.3.3 Feedback Control Loop

Controllers can be classified according to their input signal to be controlled. If this signal comes from the output of the system plant, this is considered an output feedback controller, but if the signal comes from the states of a state-space system, it is considered a state feedback controller. In this subsection, one kind of output feedback controllers will be studied and designed: proportional-integral-derivative (PID). The control loop system is represented by a block diagram in figure 26.

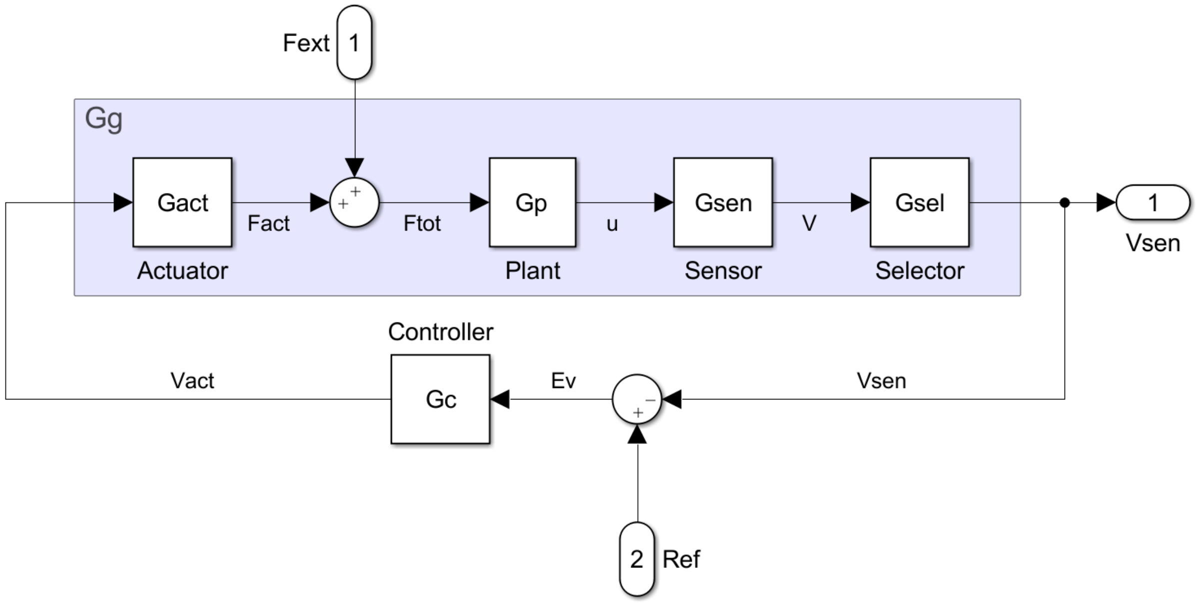

Figure 26 – Block diagram of the closed loop control system of a structure using output feedback control.

The notation used in the figure is the same from equation 2.71, where the blue box represent the high order system G_g, composed by a series of transfer functions. The system works this way: a vector of external mechanical load F_{ext} is applied to the structure and summed to the initially null forces generated by the actuator F_{act}, resulting in the total force F_{tot}; the structure processes the load through the mass, damping and stiffness matrices inside the condensed plant G_p and generates the displacements vector u; the sensor G_{sen} uncondenses the mechanic displacement vector, translating into the voltages distributed along the structure V; the selector G_{sel} chooses only the voltages that will be physically measured in the sensor piezo-patches V_{sen}; this voltages are compared to a reference Ref and the error E_V between them reaches the controller; the controller G_c generates a voltage to be applied in the actuator V_{act} by means of a control law, which is a function of its input and internal states; finally the actuator voltage is translated into mechanic forces and moments when it passes through the actuator G_{act} and closes the cycle.

In a feedback control system, a reference value must be applied to the system. For a servo motor control, for example, a voltage associated to a given angle of the motor axis is used as reference and the controller generates signals that send the angle to the desired position. In a vibration control system, no reference is needed, because the objective is to stop the system motion, that is achieved by setting the reference to zero.

The only problem associated to the usage of G_g to generate the estimation of the system is that the actual disturbance to be applied in the structure is not subjected to the entire system and there is no way to simulate force disturbances during the controller design, only voltage disturbances to be applied before the actuator. Due to the problem linearity, if the system is able to attenuate the voltage at the sensor for input voltage disturbances, it will be also able to control forces, because the poles of both system paths are the same.

In the majority of the applications, a control law based on reference tracking performance is used. The obtained performance does not always consider the attenuation of undesired signals introduced in the loop, for this reason some techniques aiming to increase the system robustness are used. In this project, the control will be focused on the disturbance rejection, so the parameters value of the controller will be chosen in order to optimize the output response for a given disturbance input. The performance of the control is going to consider mainly the settling time and the change in the DC gain.

2.3.4 PID Design

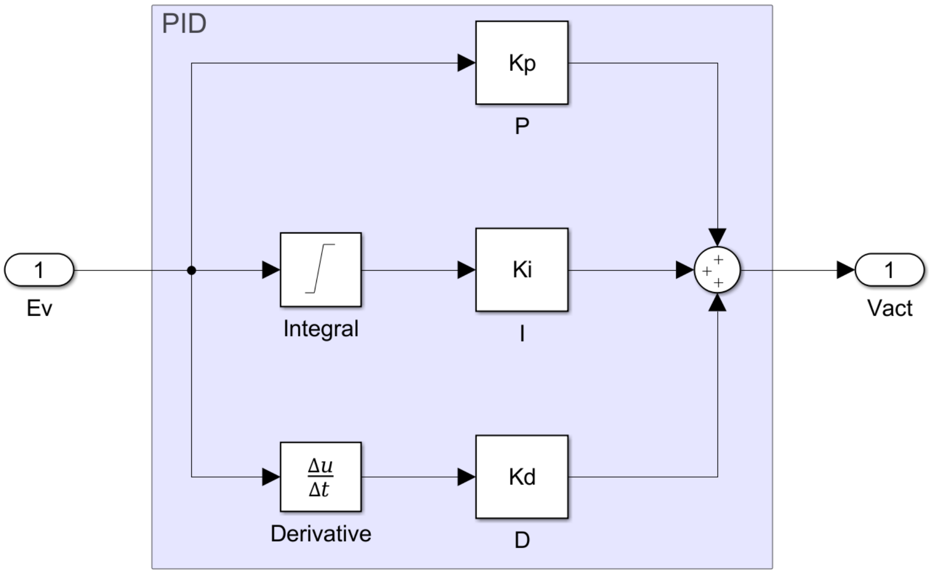

Figure 27 – PID block diagram.

The PID is one of the most basic controllers that can be designed and implemented. At the same time, the majority of controllers in industrial applications are PIDs, because of its simplicity and efficiency.

As the name suggests, the PID controller compensates proportionally the error, its integral and its derivative (figure 27), where the gains K_p, K_i and K_d, respectively, define the sensitivity of the controller to these signals. The proportional term compensates the **present** error, the integral acts on the accumulation of **past** errors and the derivative on the prediction of **future** errors. When any of the gains is set to zero, the controller acronym can be reduced only to the active terms, for example: if $K_d = 0$, we have a PI; if $K_i = K_d = 0$, we have a P; if only $K_i = 0$, we have a PD. Depending on the application, some terms can be useless or even degrade the control.

Control Type	K_P	T_I	T_D
P	$0.5\ K_u$	—	—
PI	$0.45\ K_u$	$T_u/1.2$	—
PD	$0.8\ K_u$	—	$T_u/8$
PID	$0.6\ K_u$	$T_u/2$	$T_u/8$

Table 2 – Ziegler-Nichols tuning parameters.

There are several different techniques for tuning the PID terms. A widely used method is the Ziegler-Nichols (ZIEGLER; NICHOLS, 1942), which sets K_I and K_D to zero, and increases K_P until it reaches the called ultimate gain K_u, which is the stability limit of the system. The parameters are obtained as a function of K_u and the ultimate oscillation period T_u. Table 2 presents the values of K_P, T_I and T_D as function of K_u and T_u, where $K_D = K_P T_D$ and $K_I = K_P/T_D$.

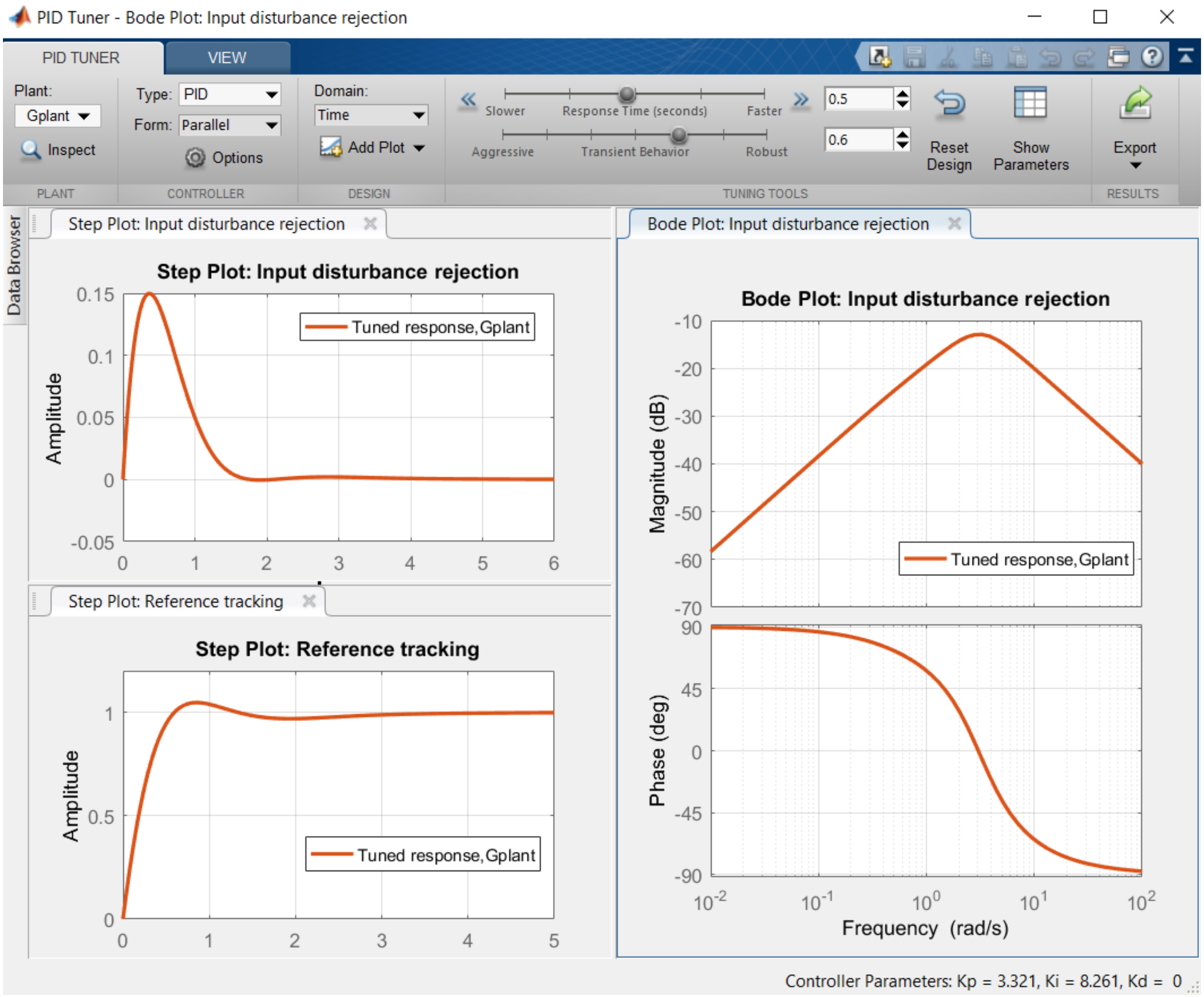

Plant: Gplant

Type: PID

Form: Parallel

Domain: Time

Response Time: 0.5

Transient Behavior: 0.6

Controller Parameters: Kp = 3.321, Ki = 8.261, Kd = 0

Figure 28 – Graphical user interface for *pidTuner* function.

From MATLAB, a graphical user interface (GUI) can be opened by typing the function name *pidTuner* in the command window. From this window, one may choose a system plant to be controlled and set the PID parameters through some slide buttons that change the time and frequency domain performance for reference tracking. Automatically some graphs chosen by the user are plotted, representing the responses for an input or step reference or disturbance in the time or frequency domain. This function does not permit the tuning of each parameter independently, so depending on the application, it is not so efficient. Another function that can be accessed to tune the constants is called *sisotool*. In this function's GUI, one may introduce poles, zeros and change the gain of the controller and obtain the root locus, bode diagram, impulse and step response plots for reference tracking and disturbance rejection, just like *pidTuner*. The only difference is that any controller can be evaluated and obtained through this function, not only PIDs with linked parameters. Figures 28 and 29 show the windows opened when calling these functions through a command line.

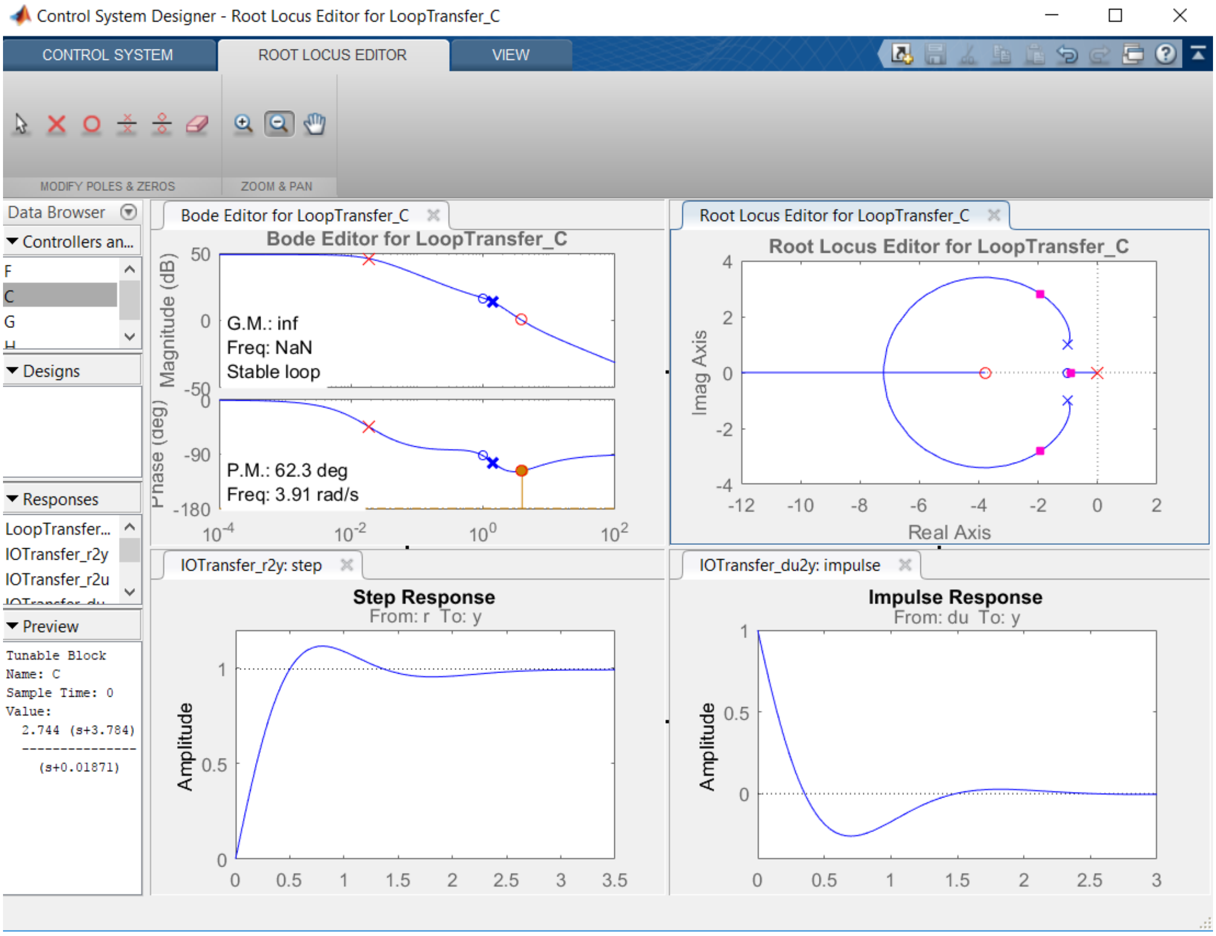

```
G.M.: inf
Freq: NaN
Stable loop
```

```
P.M.: 62.3 deg
Freq: 3.91 rad/s
```

```
Tunable Block
Name: C
Sample Time: 0
Value:
  2.744 (s+3.784)
  ---------------
    (s+0.01871)
```

Figure 29 – Graphical user interface for *sisotool* function.

Each of the terms add a different dynamic to the control loop. Next, a study on the DC gain change of the systems with the use of each type of controller will be shown. The idea is that when a step input is applied to the structure, its static deformation must remain the closest possible to the configuration it would have without control. In other words, for a step input the control voltage should go to zero in the steady-state.

A generic plant $H(s)$ is subjected to a step input $U(s) = \frac{U_0}{s}$. The steady-state response of the structure is calculated using the Final Value Theorem (FVT), which states that if a given time function $f(t)$ has a finite limit when time approaches infinity, then:

$$\lim_{t\to\infty} f(t) = \lim_{s\to 0} sF(s) \tag{2.79}$$

The static position of a degree of freedom, then, can be calculated by:

$$ST_u = \lim_{t\to\infty} y(t) = \lim_{s\to 0} sY(s) = \lim_{s\to 0} sH(s)U(s) = \lim_{s\to 0} \frac{sH(s)U_0}{s} = K_H U_0 \tag{2.80}$$

where K_H is the DC gain of $H(s)$.

The transfer function between a the step input disturbance and the output for a closed loop feedback control system with a controller $G_c(s)$ is:

$$G_{CL}(s) = \frac{H(s)}{1 + H(s)G_c(s)} \tag{2.81}$$

Replacing the plant transfer function $H(s)$ for the closed loop transfer function $G_{CL}(s)$ in equation 2.80, for three different controllers $G_P(s) = K_P$, $G_I(s) = K_I/s$, $G_D(s) = K_D s$, the steady-state displacement becomes:

1. **For $\mathbf{G_c(s) = G_P(s)}$:**

$$ST_P = \lim_{t\to\infty} y(t) = \lim_{s\to 0} \left(\frac{K_H U_0}{1 + K_H K_P}\right) = \frac{K_H U_0}{1 + K_H K_P} = \frac{ST_u}{1 + K_H K_P} \tag{2.82}$$

2. **For $\mathbf{G_c(s) = G_I(s)}$:**

$$ST_I = \lim_{t\to\infty} y(t) = \lim_{s\to 0} \left(\frac{K_H U_0}{1 + K_H \dfrac{K_I}{s}}\right) = 0 \tag{2.83}$$

3. **For $\mathbf{G_c(s) = G_D(s)}$:**

$$ST_D = \lim_{t\to\infty} y(t) = \lim_{s\to 0} \left(\frac{K_H U_0}{1 + K_H K_D s}\right) = K_H U_0 = ST_u \tag{2.84}$$

From this analysis, it is clear that only a pure derivative D controller remain unchanged the steady-state response gain, while P and PD change it by a factor of $1 + K_H K_P$ and any controller with the integral I component will lead to a final value of zero. As the objective of the project is to attenuate the dynamics of vibration instead of leaving null steady-state error, only P, D and PD controllers will be designed.

There is still an important effect that can significantly weaken the control performance, or even make the system unstable: the high frequencies associated to the system. This problems occur when the derivative term D of the controller is used, because the high frequencies generate high derivatives that may unstabilize the loop system. A possible solution to avoid the impoverishment of the response is the addition of a low-pass filter to the control loop, to attenuate the high frequencies from the sensor signals.

2.3.5 Analog Electronic Implementation

The PID controllers designed using the methods from the previous section are going to be implemented as an electronic analog circuit that receives as input the sensor voltage and generates an output voltage for the actuator. The decision on using an analog PID was the fact that it is a low cost solution that can be easily implemented in real applications, without the need of any programming and a microcontroller. The circuit design and simulations will be performed using LTSpice, a free software developed by the semiconductors manufacturer Linear Technology that implements a SPICE simulator (Simulation Program with Integrated Circuit Emphasis).

2.3.5.1 Equivalent RLC

To check the control effectiveness, an oscillator system is necessary, which can be implemented electronically with a resistor, and inductor and a capacitor in series, the so-called RLC series circuit (30).

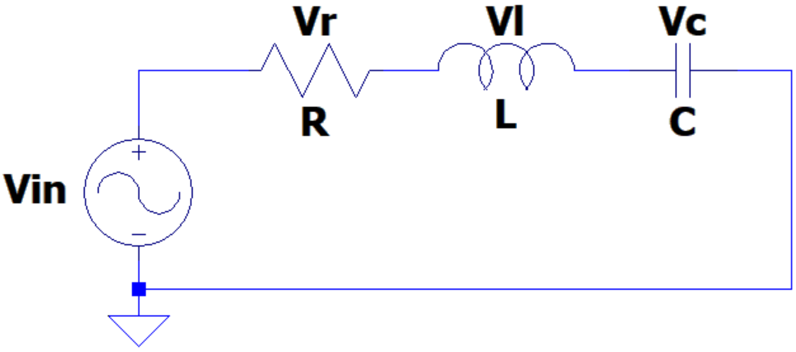

Figure 30 – RLC series circuit.

It is possible to trace an analogy between a mechanical and an electrical oscillating system: the capacitor works as a spring, the inductor as a mass, the resistor as a damper and the electromotive force (EMF) as an external force. The differential equation that represents the system can be obtained by matching the EMF (V_{in}) to the sum of the voltage drops accross each component, that are given by the Ohm's Law (resistor):

$$\Delta V_R = RI, \tag{2.85}$$

the Faraday's Law (inductor):

$$\Delta V_L = L\frac{dI}{dt}, \tag{2.86}$$

and the capacitor constitutive equation:

$$\Delta V_C = \frac{Q}{C} = \frac{1}{C}\int I\ dt. \tag{2.87}$$

Applying the identity $I = C\dfrac{dV_C}{dt}$ to the current results in the following differential equation:

$$V_{in} = LC\frac{d^2V_C}{dt^2} + RC\frac{dV_C}{dt} + V_C \tag{2.88}$$

That can be represented by the following second order transfer function:

$$G_{RLC}(s) = \frac{V_C(s)}{V_{in}(s)} = \frac{\frac{1}{LC}}{s^2 + \frac{R}{L}s + \frac{1}{LC}} \tag{2.89}$$

with a natural frequency given by $\omega_n = \sqrt{\dfrac{1}{LC}}$ and the damping ratio $\zeta = \dfrac{R}{2}\sqrt{\dfrac{C}{L}}$.

Higher order systems are obtainable by adding RLC systems, so it is possible to design an electronic circuit equivalent to a reduced order model used to design the controller. This circuit will be used to represent the prototype on LTSpice and to be controlled by the analog PID implemented in the software.

For summing the voltages, it is possible to use an Operational Amplifier (op-amp) as an inverting voltage adder. An ideal op-amp has infinite open-loop gain, infinite input impedance R_{in} (zero input current), zero input offset voltage and zero output impedance R_{out} (figure 31), as explained in (SEDRA; SMITH, 1997).

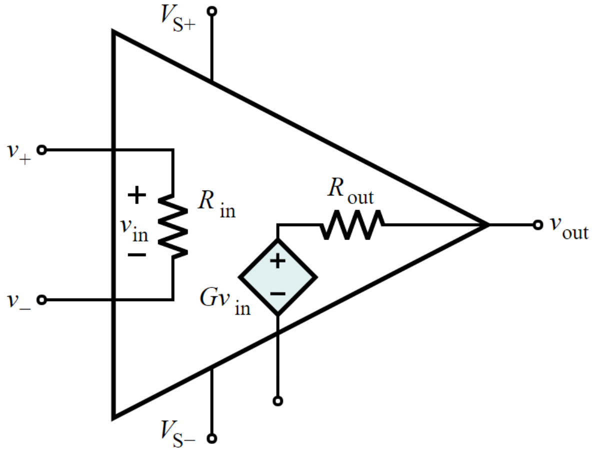

Figure 31 – Ideal operational amplifier equivalent circuit (WIKIMEDIA, 2009).

Therefore, the output summed voltage from the circuit in figure 32 is obtained by matching the input currents to the output:

$$I_F = \sum_{i=1}^{n} I_i = -\sum_{i=1}^{n} \frac{V_i}{R_i} \tag{2.90}$$

so, applying the Ohm's Law to transform currents into voltages:

$$V_F = -\sum_{i=1}^{n} \left(V_i \frac{R_F}{R_i}\right) \tag{2.91}$$

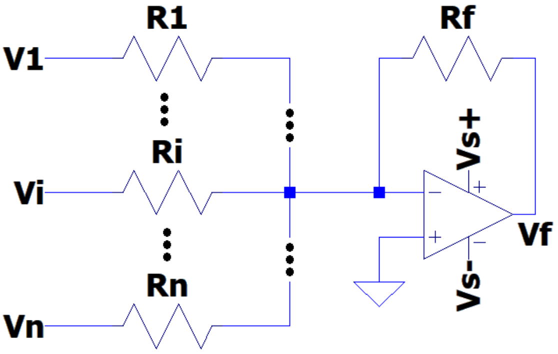

Figure 32 – Inverting adder circuit.

It is important to mention that there is a saturation for the output voltage, which means that it is always bounded between the supply voltages V_s+ and V_s-. The ratio between the input and feedback resistances can represent the dc gain of each vibration mode of the reduced model.

2.3.5.2 Operational Amplifier PID Circuit

Besides summing, it is possible to compute the derivative and the integral of a signal using amp-ops. Each term of a PID controller can be implemented with an amp-op, so the error signals can be summed and multiplied by -1 with a last amp-op to track the reference. As only proportional and derivative control is going to be used in this project, the integrator circuit will not be presented.

To calculate a proportional error, the inverting adder circuit from figure 32 may be used with a single output. So the proportional error signal V_p is:

$$V_p = -V_i \frac{R_F}{R_i} \tag{2.92}$$

For the derivative, a differentiator circuit is introduced in figure 33 with an optional filtering capacitor with capacitance C_F.

Matching the currents and using Ohm's law and the capacitor constitutive equation to work with voltage variables, we get that:

$$Cd\frac{dV_i}{dt} = -R_F V_d - C_F \frac{dV_d}{dt} \tag{2.93}$$

as $C_F << R_F$, we have that:

$$V_d \approx -R_F C_d \frac{dV_i}{dt} \tag{2.94}$$

The transfer function between the output and the input is:

$$\frac{V_d(s)}{V_i(s)} = \frac{-C_d s}{R_F + C_F s} \tag{2.95}$$

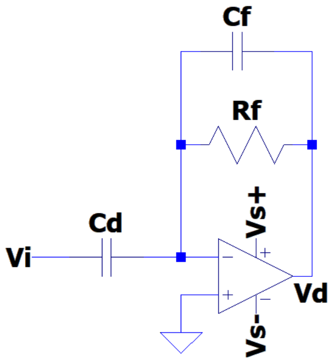

Figure 33 – Inverting differentiator circuit.

which could be obtained using the complex impedance $Z = 1/(sC)$ in the proportional amplifier equation for the input capacitor and the equivalent parallel impedance for the feedback resistor and capacitor.

The differentiator may introduced undesired high frequency oscillations to the output derivative error that can unstabilize the system. For this reason, it is sometimes necessary to filter this signal. In this work, passive low-pass filters of 1st and 2nd orders are going to be used to eliminate these frequencies, which are composed by one and two stages, respectively (figure 34).

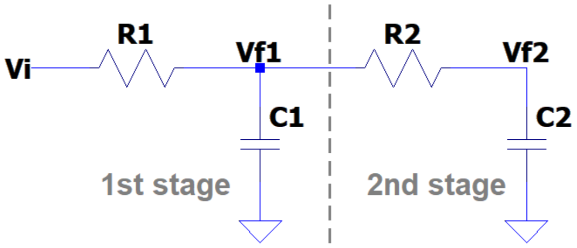

Figure 34 – Low-pass RC passive filters with one or two stages.

The first order filter contains a single pole, which means that it attenuates 20dB/decade after its cut-off frequency, while the second order one attenuates 40dB/decade. At the same time, the first order introduces a lower phase shift than the second one, so there is a trade off between rejection and phase shift when designing a passive filter in a circuit. The cut-off frequency for a first order RC filter is:

$$f_c = \frac{1}{2\pi R_1 C_1} \tag{2.96}$$

while for the second order:

$$f_c = \frac{1}{2\pi\sqrt{\sum_{i=1}^{n} R_i C_i}} \tag{2.97}$$

2.4 Numerical Implementation

The mathematical base given by the formulations provided in the previous sections is enough to start the numerical implementation of the system. The finite elements matrices are going to be generated by a Fortran application developed by MUL2 group and saved in a pre-determined work directory as text files. Then they will be imported to MATLAB, where all the dynamic simulation and control of the structures are going to be implemented.

2.4.1 MUL2 Fortran Application

The application is an executable file that was built through Microsoft Visual Studio and was coded in the Fortran programming language by MUL2 research group. This language is especially suited to numeric computation and was originally developed by IBM in the 1950s for scientific and engineering applications. The name Fortran means Formula Translation, because it translates mathematical formulas into computational algorithms.

The application can generate output text files with the mass and stiffness sparse matrices for structures with and without piezoelectric materials, 3D model files showing diverse physical quantities distribution along the mesh and other simulation parameters and outputs according to the analysis type. The application reads the inputs provided by the user through text files in an specified directory, being really versatile and allowing us to simulate numerous entirely different problems.

The code is constantly being update to later versions with more features to give a better freedom for the user and more robustness in the responses. The application allows you to choose between five different kinds of analysis:

1. **Static Analysis - Mechanical Problem:** this kind of analysis is used to generate the stiffness matrix of a purely mechanic problem and to solve the static equation 2.3, allowing us to see in a 3D model the deformed configuration of the mesh for given input loads applied.

2. **Free Vibration Analysis - Mechanical Problem:** this analysis is used to generate the mass matrix of any problem, because the thermal and piezo terms do not affect the structure inertial. It also solves the kinematic equation 2.5, returning a number of natural frequencies chosen by the user and allowing us to see in a 3D model the modal deformations of the mesh for each natural frequency.

3. **Static Analysis - Piezo-Mechanical Problem:** this is just like the mechanical static analysis, but it also considers the piezoelectric parameters and properties. Fixed voltages can be applied to the model in order to simulate it statically.

4. **Static Analysis - Thermo-Mechanical Problem:** analogously to the previous type, this analysis is like the mechanical analysis, but considers thermal properties and parameters, allowing the insertion of fixed temperatures to the model.
5. **Static Analysis - Piezo-Thermo-Mechanical Problem:** as the name suggests, this is the union of piezo-mechanical and thermo-mechanical analysis.

For beam elements, the program allows you to choosen up to 20 elements between B2, B3 and B4 (linear, quadratic or cubic shape functions), while the two dimensional cross-sections, can be composed of Taylor expansions of any order up to 19 (including Euler-Bernoulli and Timoshenko) or Lagrange expansions composed by L4 and L9 quadrilateral elements (triangular L3 and L6 and quadrilateral L16 expansions were under development when this thesis was initiated). It is possible to use 2D elements with 1D "sections" or even 3D solid elements with this application. The limit of degrees of freedom permitted to solve the structure is 10,000.

Regarding boundary conditions, we can constrain the mechanical displacement in any direction to a desired value, as well as the electrical and thermal variables. The constrained region can be given by a plane or can be specified to each desired point. Punctual mechanical loads can be also specified in all three directions. In terms of the system matrices, the boundary conditions change them in order to set the unknowns to the desired constrained values. For example: if one of the rows of the stiffness matrix of a 3 DOF system is $\begin{bmatrix} 1 & 2 & -1 \end{bmatrix}$, the second DOF can be set to 2 by inserting a value of 2 in the second position of the load input vector and changing the stiffness matrix row to $\begin{bmatrix} 0 & 1 & 0 \end{bmatrix}$, resulting in the simple equation $0\ u_1 + 1\ u_2 + 0\ u_3 = u_2 = 2$. If the DOF must be set to zero, we can set the row to $\begin{bmatrix} 0 & k & 0 \end{bmatrix}$, where k is a significantly high number (order of magnitude around 20) to make displacement u_2 small enough to be considered zero regardless of the force vector value.

Concerning the materials, isotropic and orthotropic can be chosen for the mechanical properties. Isotropic materials have the same properties in all directions, while orthotropic material's properties differ along the orthogonal axes. Additional properties can be specified: thermal expansion, specific heat, thermal conductivity, piezo coupling constant, electric permeability, magnetic permeability, *etc.* The lamination direction of the material can be determined too in order to provide more accurate constitutive relations.

Let us take a cantilever beam with piezo-patches attached to it and a force applied in the free extremity as an example to be simulated by the application. It is needed to perform two different kinds of analysis in order to obtain the system matrices: first a piezo-mechanic static and then a free vibration mechanic analysis. For both we should define two different materials and its properties, one lamination for each material, a discretization along the beam axis and an expansion along the cross-sections. The first will provide the stiffness matrix with all unknowns (mechanic and electric) that will be condensed. The second must be performed in order to obtain the mass matrix related only to the mechanic displacement, so unlike the first, it should not include the applied load.

2.4.2 MATLAB

Once the matrices are generated in their respective text files, we are able to move on and simulate the system through MATLAB. By importing the sparse mass and stiffness matrices, the force vector and the connectivity file, that associates each row and column in the matrices to the coordinates of that node, we can start the files manipulation.

The first step is to clean the constrained DOFs in $\mathbf{M}$ and $\mathbf{K}$ matrices, in order to avoid problems coming from the high values used to constrain some displacements, that can reach orders of magnitude over 20. As this degrees are constrained to zero, the removal of their dynamics will not affect the rest of problem, and their position can be inserted after all the computation.

Next, the condensation of the stiffness matrix is applied by listing all the nodes with piezoelectric properties and combining their electric unknowns to the mechanics by means of equation 2.54. Being N_{dof} the total number of DOF of the problem, N_{mec} the number of non-piezo DOFs that are not constrained, N_{pie} the number of non-constrained piezo nodes and N_{con} the number of constrained DOFs, we have the following relations:

$$\begin{aligned} &N_{dof} = N_{mec} + N_{pie} + N_{con} \\ &N_{\mathbf{K_{cond}}} = N_{\mathbf{M}} = N_{mec} \\ &N_u = N_{mec} \\ &N_\phi = N_{pie} \end{aligned} \tag{2.98}$$

between the degrees of freedom and the matrices dimensions of $\mathbf{K_{cond}}$ and $\mathbf{M}$ and the vector lengths of u and ϕ. This relations are important to organize the programming loops that are going to be used through all the implementation.

The open loop block diagram of the uncontrolled system is shown in figure 35. The first input, F, is the vector of external loads and its length is equal to N_{mec}, while the second, V, is the vector of external voltages applied to the piezo-patches with length N_{pat} (number of piezo-patches in the structure). The *PiezoPatches* block is a matrix that converts the applied voltages in mechanical forces with size $N_{mec} \times N_{pat}$, the *Plant* block comprises the dynamics of the condensed problem and the *Uncondensation* block is a the matrix that converts the mechanical displacements to the electric potentials with size $N_{pie} \times N_{mec}$ and described by equation 2.56.

The matrix represented by *PiezoPatches* block has its columns composed by force vectors associated to the application of 1V in one of the piezo-patches without any other

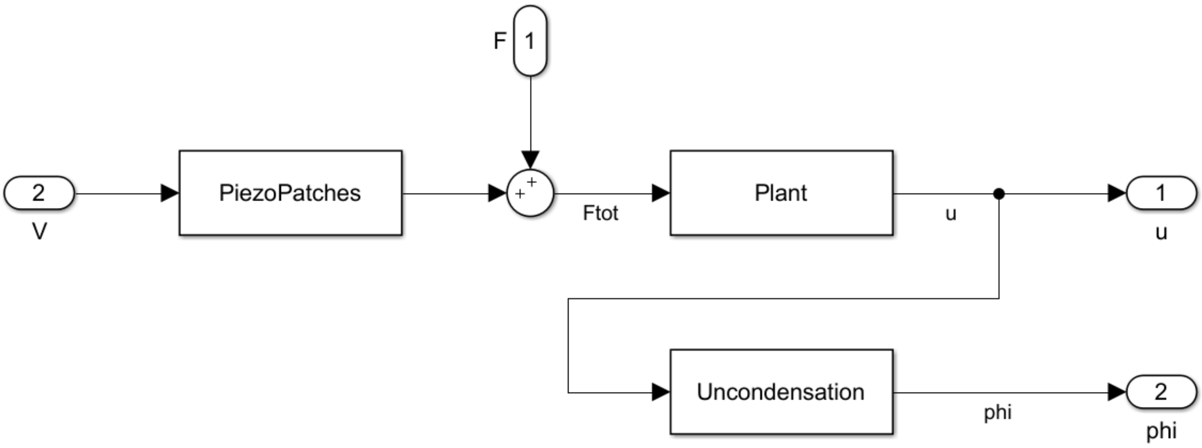

Figure 35 – Block diagram of an open loop system of a structure with piezo-patches.

inputs. Each column represent a different patch and must be generated by running the MUL2 application in piezo-mechanic static mode and taking the output force vector with the application of the voltage. This solution is valid because the system is linear, so it accepts the superposition principle.

The *Plant* block represents the discretization of the continuous state-space system defined by equations 2.9 and 2.10. It is important to emphasize that it is not necessary to invert the mass matrix in order to calculate the state-space matrices, which would require high computational costs for large matrices as the ones that are going to be used. Instead, we can use the backslash operator or the *mldivide* function in MATLAB, that solves a generic system of linear equations $\mathbf{A}x = \mathbf{B}$ for x in using the Lower Upper (LU) decomposition for square matrices. The detailed algorithm can be found in (BUNCH; HOPCROFT, 1974).

With the displacement and electric potential vectors obtained through the MATLAB script and the connectivity file from the Fortran application, the structure can be graphically represented for each time instant using *plot3* and *surf* functions and a suitable displacement multiplier, otherwise the displacements would not be visible to the naked eye.

For the static and free vibration analysis, applying the equations and algorithms describe in the *Governing Equation* section using MATLAB is enough to get the displacement vector, natural frequencies and modal shapes, which can be compared to the ones provided by the Fortran executable file.

2.5 Prototypes

The prototype definition is the first step towards the experimental implementation of the methodology presented previously, initially applied to a FEM model using computational simulation. This section will contemplate the materials selection, the prototype design, dimensioning, manufacturing and assembly. Some of these items were based on Ruben Salas' work (SALAS, 2017), which allowed him to earn his doctorate degree supervised by Prof. Dr. Emilio Carlos Nelli Silva as well.

The decision was to manufacture three prototypes through the same processes, in order to compare the results in each one of them and avoid misleading conclusions if any of them provide us improper outcomes due to manufacturing flaws. The main idea of this approach is that the second structure is confronted to the first in order to assess the results. If they differ, the third is used to check whether the first or the second contains the imperfection that reproduced the deceptive effect.

2.5.1 Design

The structural prototype is divided in two main materials: a metallic one for the substrate and a ceramic with piezoelectric characteristics to be used as actuator and sensor for the system, one bonded above and the other below the substrate. The elected materials were aluminum, due to its low mass density and relative low stiffness compared to other metals, and lead zirconate titanate (Navy Type II: PZT-5H), that yields higher charge sensitivity than Navy Type I (PZT-4), but also implies a higher dielectric heating (ST, 2018). The aluminum alloy sheet used for the prototype was the same used in (SALAS, 2017), where isotropic properties were considered (table 4), while the piezoceramic patches were the same used in (SALAS et al., 2017), where orthotropic properties were considered (table 3).

Property	**Symbol**	**Value**	**Unit**
Elastic Constants	C_{22}	81.3	GPa
	C_{12}	81.3	
	C_{13}	64.5	
	C_{33}	64.5	
	C_{44}	64.5	
Piezoelectric Constants	e_{32}	-0.442	C/m^2
	e_{33}	11.61	
	e_{25}	18.10	
Permitivity Constants	χ_{22}	16.5	($\times 10^{-9}$) F/m
	χ_{33}	7.24	
Density	ρ	7511	kg/m^3

Table 3 – PZT-5H orthotropic properties (SALAS et al., 2017).

Property	Symbol	Value	Unit
Young's Modulus	E	69.489	GPa
Poisson's Ratio	ν	0.307	-
Density	ρ	2520.110	kg/m^3

Table 4 – Isotropic aluminum alloy properties (SALAS, 2017).

The most appropriate design for the objectives of this project is a structure whose thickness order of magnitude is much lower than its length and width. The remaining two dimensions must be slightly different so that the prototype can be considered a plate (2D), but at the same time the advanced beam elements (1D) can be used to simulate it properly. The usage of this modeling method implies that both parts that compose the prototype must be rectangular with fixed thickness, even though rounded formats are sometimes more efficient in some applications. In optimization problems the resulting formats are usually irregular, to they could not be properly modeled using this methodology.

The baseline for the dimensions were the sheet metal and the PZT-5H patches available at the laboratory for the manufacturing of the prototypes. The nominal thickness of the aluminum sheet was 1 mm, while the piezoceramic patches nominal dimensions were 60 × 60 × 0.5 mm. Both sides of the available ceramics are covered with a very thin layer of a silver alloy (a few Ångströms thick), that works as an electrode, ensuring an equipotential distribution along each face of the patch. Among the available machinery that could be used in this project were a laser and a waterjet cutter, so it was decided that the aluminum would be cut through waterjet and the piezoceramics would be used without cutting, once that the waterjet could break them due to their fragility and the laser would make the surface reach temperatures higher than the Curie point ($T_C \approx 195$ ºC), depolarizing the material in the vicinity of the cut edge and making it lose its piezoelectric properties.

The scope of the project aims only the control of bending modes along the length direction of the beam elements, so, in order to avoid unpredicted actuation along the width direction of the structure, the substrate and the patches width must coincide. Another consideration taken into account during the design stage of the prototype was the fact that the position along the beam elements direction of the piezoceramic used as actuator and the one used as sensor should be equal, this way the actuation would affect directly the signals provided by the sensor.

Therefore, the thickness and width of the prototype were already set, remaining the length of the substrate and the piezoceramics positions to be determined. From previous experiences, the laboratory staff recommended that around 20 mm of the length would be necessary to clamp the structure, so this was the distance from the fixed extremity of the plate that the patches were placed. The length of the unconstrained portion of the prototype was defined as 100 mm: an equilibrium between the feasibility of simulating the structure numerically with the beam elements and the possibility of considering it as a plate with the majority of its length covered by the piezoceramics, resembling a sandwich structure.

2.5.2 Manufacturing

From the design described in the previous subsection, a blueprint prototype was created and shown in figure 36.

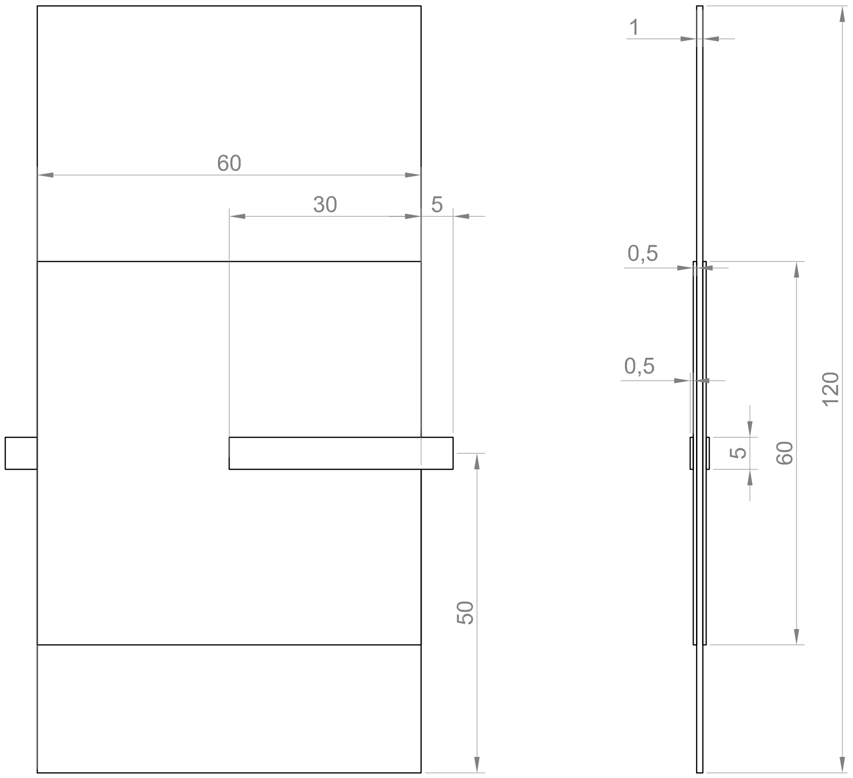

Figure 36 – Prototype blueprint.

Next, the manufacturing processes used to obtain the designed prototype are listed.

1. **Cutting and Sanding:** As explained previously, the only part that required to be cut was the aluminum substrate. This process was performed at LMR (PMI-USP) using their waterjet cutting machine and placing a sacrifice wooden board below the metal sheet. Then the three aluminum plates to be used in the prototypes were detached from the wooden board and the tape residues were removed using alcohol. To eliminate burrs and sharp edges, all edges were sanded initially using 220 grit sandpaper and finishing with a 600 grit.

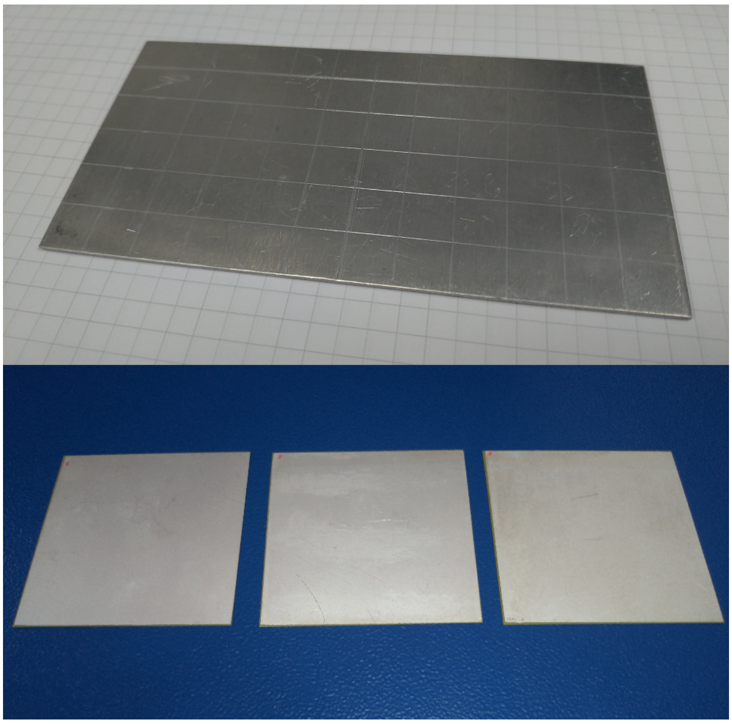

Figure 37 – Top: Aluminum substrate for one of the prototypes after cutting and sanding processes. Bottom: Piezoceramic patches before attached to the substrate.

2. **Bonding and Curing:** For the piezoceramics attachment to the substrate, a professional epoxy adhesive (Araldite® Profissional) was used. Following the preparation instructions contained in the adhesive data sheet (TEKBOND, 2017), the metal surfaces were polished using 600 grit sandpaper and cleaned with alcohol. The piezoceramics faces to be bonded were also cleaned, but not polished, otherwise the electrode layer would be removed. The area of application was measured and delimited with crepe tape to protect the rest of the surface from the spread glue and avoid a wrong positioning. The epoxy bond mixture was prepared with the aid of two syringes, that guaranteed the correct volumetric proportion between the hardener and the resin and finally applied to the aluminum with a paint-brush. A bench vise was used to apply enough pressure to fix the parts, but not excessive, in order avoid buckling. The initial idea was to use the vacuum pump at LADIN-USP during the curing period to eliminate air bubbles between the substrate and the patches, but it was unavailable at that time. This adhesive takes around 90 minutes to dry and requires 24 hours for a complete cure, so the parts were left untouched for a whole day. At the end of the process, the crepe tape was removed and one last stage of fine sanding (600 grit) was required to remove the excess of dried glue that was spread.

3. **Measuring:** After polishing and cleaning the surfaces, the geometric characterization of the aluminum-ceramic sets was obtained after computing the mean value

of measures taken from different points. Table 5 shows the measures from figure 38 for each of the three prototypes. The measurement tools used to obtain the final dimensions of the prototypes were a micrometer with 0.01 mm resolution (A, B, F) and a caliper with 0.05 mm resolution (C, D, E).

Measurement	**Prot. 1**	**Prot. 2**	**Prot. 3**	**Prot. Mean**
A	120.70	120.70	120.75	**120.72**
B	60.00	60.85	60.80	**60.55**
C	0.53	0.49	0.48	**0.50**
D	0.07	0.06	0.08	**0.07**
E	1.03	1.03	1.04	**1.03**
F	8.65	8.05	8.10	**8.27**

Table 5 – Mean value of measured lengths in milimeters by prototype for each measurement from figure 38 and mean between prototypes.

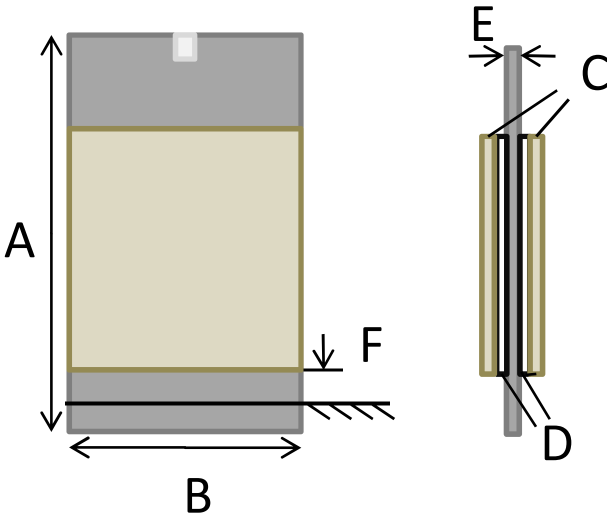

Figure 38 – Graphical representation of considered measurements: A) plate length; B) plate width; C) piezoceramic thickness; D) epoxy layer thickness; E) aluminum sheet thickness; F) distance between clamp and piezoceramic.

4. **Electrical Connections:** For the electrical connections some alternative conductive materials were required to avoid unintended effects in the signals transmitted. The first problem faced was again related to the Curie point, once that welding a wire directly to the piezoceramic would result in the depolarization of a small area around the point. The solution found was the usage of a copper tape from Eletrofitas, bonded to the center of the piezoceramic with the conductive silver epoxy adhesive CW2400 (CHEMTRONICS, 2013) and welding a wire to it outside the ceramic surface. The second problem was that using a common wire for electronic applications would significantly impact in the experimental results due to its inertia when subjected

to vibration, so the solution was to use a very light wire. Consulting the american logarithmic stepped standardization wire gauge (AWG) (LUND, 2018), the 34 AWG size was chosen (⌀ 0.16 mm) after evaluating the effects of its linear resistance (856 mΩ/m) and linear density (0.18 g/m) when using around 1 m of wire for each of the two connections. The enamel that covers was removed from the extremities using a utility knife and finally it was welded to the copper tape with a tin/lead (Sn/Pb) solder.

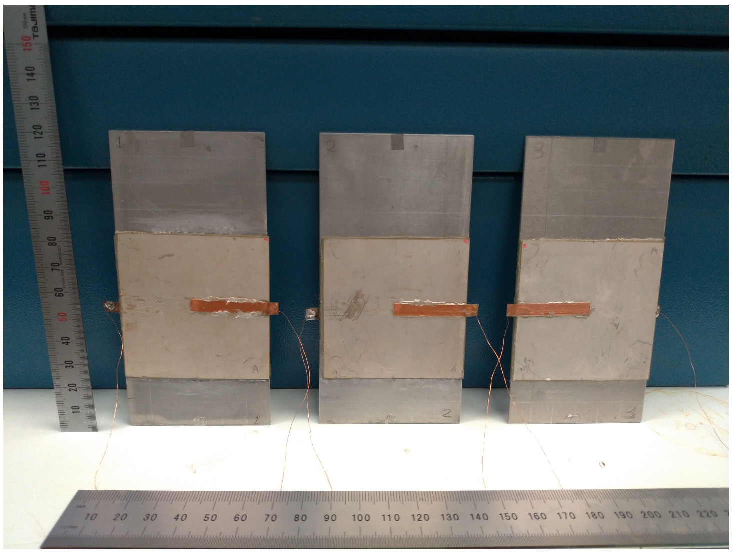

Figure 39 – Finished prototypes.

2.6 Experimental Characterization

This section will give a detailed explanation on the experimental methodology used to perform the obtainment of the system behavior for different inputs and to effectively perform the vibration suppression of the prototypes. The system response to disturbances will initially be acquired in order to improve the numerical results introducing uncertainties and losses to the model used for simulation and, after designing the controller with a more realistic model, the experimental control will be presented. The instrumentation in this project was based in some works from the literature, as (RAHMAN; ALAM, 2012), (ZHANG et al., 2014), (VASQUES; RODRIGUES, 2007) and, mainly, in (SALAS, 2017), once that most of the instruments used by Salas was available for using in this project and his previous experiences were extremely helpful to avoid possible flaws in the data acquisition procedures.

All of the instruments and their connections are represented in a diagrammatic view in figure 40. Next, the role of each block present in the diagram will be explained

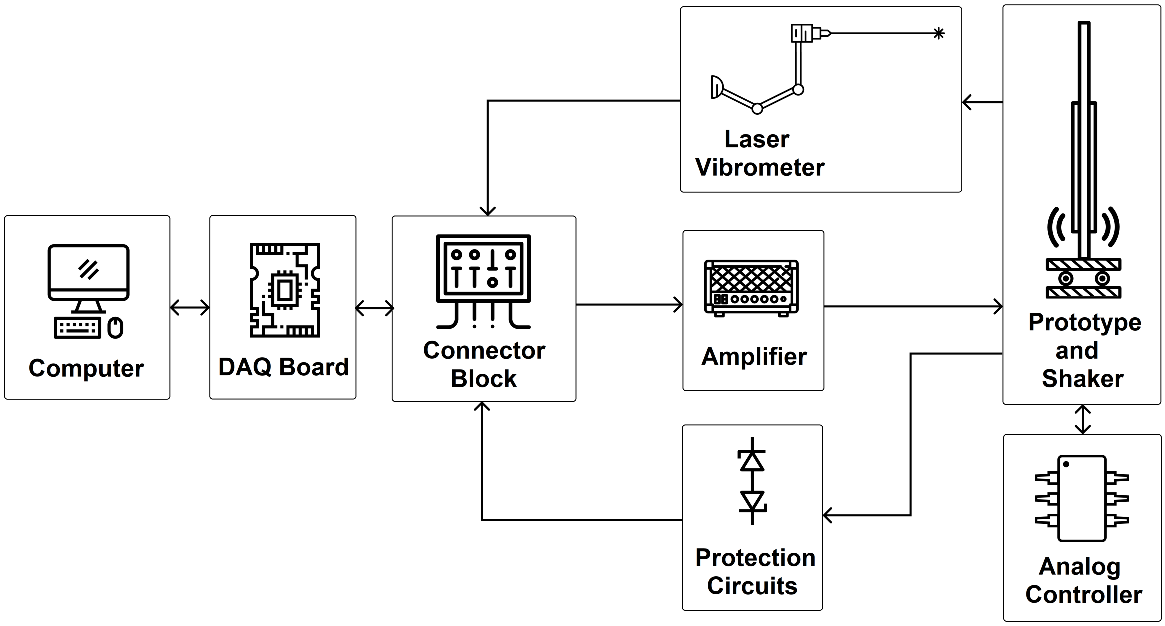

Figure 40 – Experimental characterization diagram.

2.6.1 Signals Acquisition

1. **Excitation signal:** In order to impose vibration to the structures that will be studied, an excitation signal is necessary. To generate this signal, the following equipment was used: a computer with MATLAB license, input/output multifunction board installed to the computer (NI PCIe-6341 X) used for data aquisition (DAQ)/signal generation, a terminal block with input and output BNC connectors (NI BNC 2110, shown in figure 41) used as interface between the DAQ board and the external analog signals and an amplifier module (Taramp's TL-600) with bandpass between 50Hz and 50kHz and 2 channels (only one of the channels was used). This devices are represented by **Computer**, **DAQ Board**, **Connector Block** and **Amplifier** blocks on the diagram from figure 40.

   Initially, the signal was created programmatically as an unidimensional array of double precision numbers inside MATLAB environment. This series of values is then sent to the DAQ board, that contains an interface compatible to MATLAB, and to the terminal block, that sends the excitation signal via BNC cables. The PCI board output voltages are bounded between -10V and +10V due to its limitations. When the signal is transmitted to the actuator, the piezoceramic is directly connected to the terminal block, while when it is used as input to the shaker, the range of -10V/+10V is not enough no produce significant displacements to the base that fixes the prototype, so the signal must be amplified. A power supply with nominal values of 12VDC and 20A (Nodaji) is used to power the amplifier and a an electric transformer

Figure 41 – Terminal block BNC 2110, National Instruments.

is connected to the output to increase the voltage that will feed the shaker (figure 42). An approximate gain of 100 was identified in the set amplifier-transformer connected, it was necessary when evaluating the feasibility of the experiment, but is not going to be included in the modeled system, once that the input disturbance considered for the problem is the displacement on the base of the shaker, that is going to be measured.

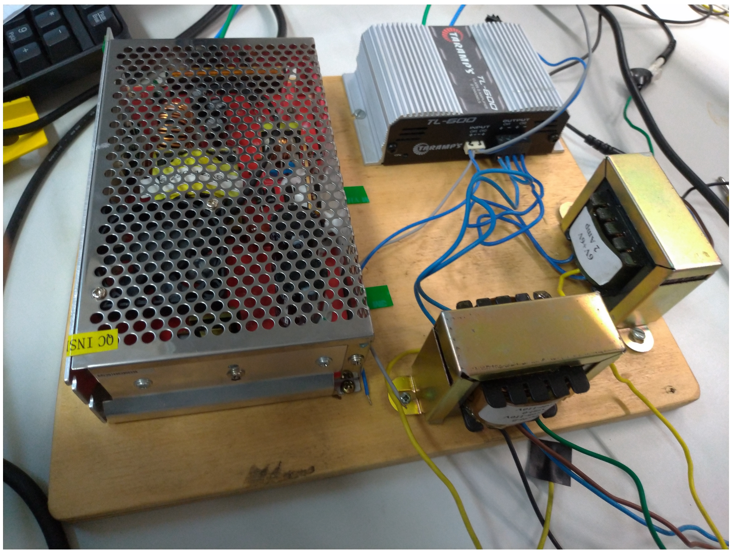

Figure 42 – Set composed by power supply, amplifier and transformers connected to both output channels.

2. **Velocity signal:** One of the main information for the system identification is the displacement signal of the base and the free extremity of the prototype during the vibrations. The movement is induced by the disturbance signal that enters the mechanical shaker and produces current in its internal coils. The change in this current creates a magnetic field and attraction and repulsion forces to the internal permanent magnet, which moves the base, where the prototype is clamped to (LANG; SNYDER, 2011). This process is represented by the **Prototype and Shaker** block on the diagram from figure 40.

   To measure the tip velocity of the plate, a laser vibrometer is used (Polytec OFV-5000, figure 43, block **Laser Vibrometer** on diagram 40). There is the possibility of measuring displacement or velocity from the vibrometer, but both are based on the same working principle, which is based on Doppler Effect: a laser beam is emitted directly to a reflective tape bonded to the surface to be measured and reflected with a frequency shift, from which the surface velocity is calculated. The displacement that can be provided by the instrument is generated after an internal integration that introduces some degradation to the signal, so it was decided to acquire only the velocity and integrate it numerically using MATLAB. A BNC cable connects the velocity signal from the vibrometer to the terminal block, that will be received to the computer from the acquisition board.

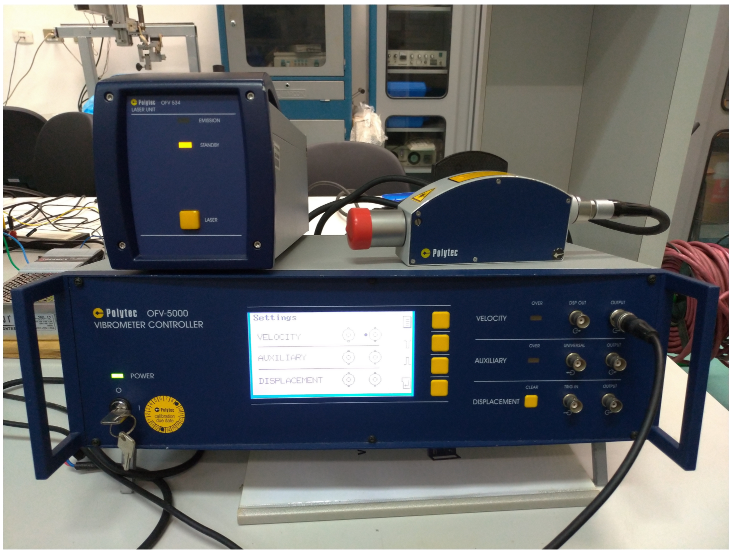

Figure 43 – Polytec OFV-5000 laser vibrometer.

   To ensure precise measurements, the shaker and the laser emitter must be horizontally aligned and the laser beam perpendicular to the surface. A professional photographer tripod was used to fix the laser head and to facilitate the alignment. The distance between the plate and the emitter was kept at 300mm for every measurement, guaranteeing constant conditions and reducing uncertainties associated to the processes.

Before start acquiring the data from the vibrometer, a suitable resolution (m/V/S) is chosen and the emitter is manually focused. Figures 44 and 45 show the alignment preparation before a measurement and the process itself, respectively.

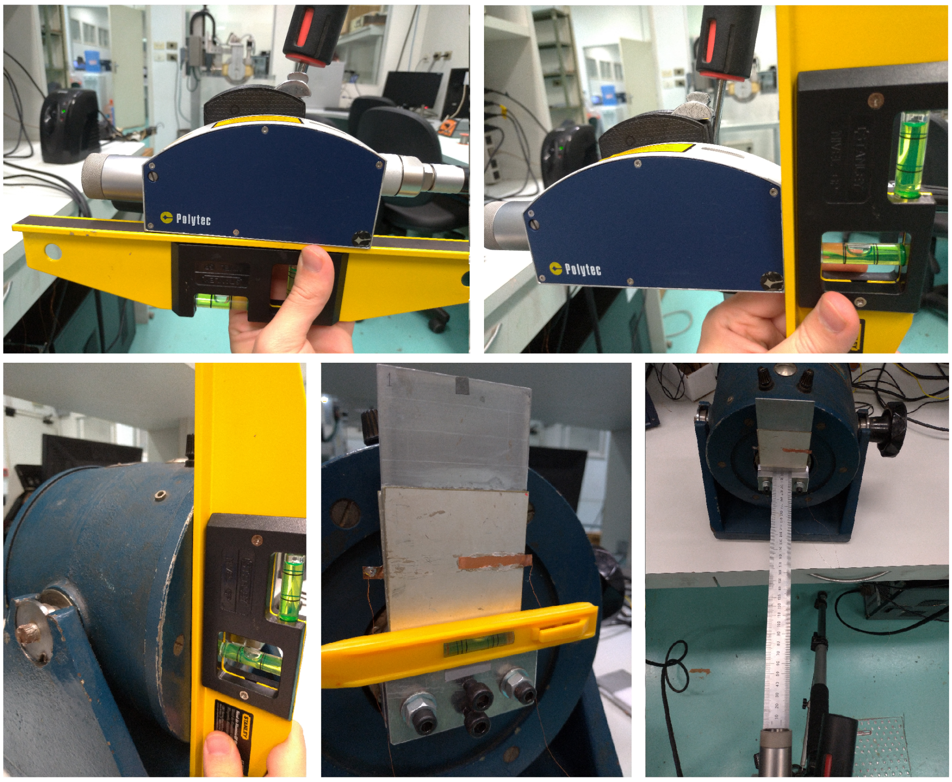

Figure 44 – Alignment preparation before vibrometer measurement.

Figure 45 – Shaker and laser head positioned for a measurement.

3. **Sensor Voltage Signal** Due to the symmetry on the model, the choice of the patch to be used as sensor or actuator is arbitrary, once that ideally the actuator/sensor response should be the same if their roles were inverted. To maintain a coherence, the piezoceramic attached to the side that faces the laser is going to be the actuator for all of the prototypes.

   The sensor signal will also be received as an input for the DAQ board but a protection is needed in order to avoid overvoltage damage to the board, once that it can read only analog signals in the range -10V/+10V. For this reason, a protection circuit based on 9.8V Zener diodes was designed and its output was used to feed the terminal block. The circuit is presented on figure 46 (block **Protection Circuits** on diagram 40): each Zener blocks the conduction in a direction when the input voltage is below the reverse conduction voltage (9.8V), leaving the output equals to the input, but when the voltage amplitude exceeds this value, the Zeners will conduct, creating a voltage drop on the resistor and leaving the output as the sum of the reverse voltage of one diode and the direct voltage of the other. The reference potential will be set as the one on the aluminum substrate.

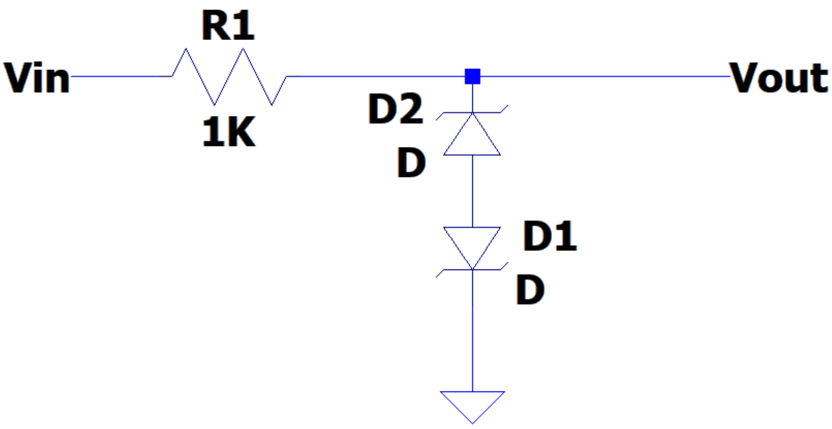

Figure 46 – Schematics for Zener diodes protection circuit.

4. **Actuator Voltage Signal** Finally, the actuator voltage will be generated by the controller circuit introduced previously, using the sensor voltage as input. For these reason, the block **Analog Controller** has a two way communication to the prototype (actuation/sensing) on the diagram 40. Just like the sensor voltage, a protection circuit will be used in order to send the actuation signal to the data acquisition board.

2.6.2 Experimental Curves

The experimental data used to attain the characteristic curves of the studied system is obtainable through the processes described above. This subsection will focus in the conditions and data processing used for each experimental curve needed in this project.

2.6.2.1 Transient Response (Time Domain)

In order to check if a reduction in the oscillation of a signal was successfully obtained, one may usually evaluate and compare the controlled and uncontrolled transient signals in the time domain. This way, with both plots on the same graph and axis, it is easy to notice a reduction in the overshoot and in the settling time. For the uncontrolled system, the transient response will depend on the external disturbances dynamics and the modal behavior of the structure. Fortunately, it is possible to decouple the response by manipulating the external interference and processing the time domain data obtained from the analysis for a given frequency.

Any free vibration dynamic response can be interpreted as a linear combination of the modal shapes of the structure, which means that setting one of the modal shapes as initial condition for the structure and letting it vibrates freely uncouples the modes, so the time domain response will be composed by a single frequency. This also occurs when applying an harmonic excitation with a frequency matching the resonance of the structure. For impulses and step inputs, the response will be a composition of the natural modes and frequencies. Last, for a harmonic forcing term with any frequency that does not match a natural frequency of the structure, the transient response will take into account the forcing and natural frequencies of the system.

Therefore, to obtain a decoupled transient response of the system, two different approaches may be used:

1. Acquire data for a free vibrating structure with a modal shape as initial condition, which is obtainable by tuning a forcing disturbance frequency to match one of the resonances of the structure and removing it when the system reaches the steady state.
2. Apply a load that does not change in time after its application (step or impulse) and filter the acquired data to remove every frequency, except the desired one. The filtering process will be explained next.

The data acquired through one of these methods can be used to evaluate the damping ratio for the desired vibrating mode as explained in the Damping Matrix section, once that the response will have the behavior from the graph presented in figure 24.

2.6.2.2 Harmonic Response (Frequency Domain)

The frequency response curves of the system are extremely necessary for understanding the characteristics of the outputs of a system for any kind of input introduced in it. In this work, two different curves will be used:

- **Shaker disturbance:** the oscillations of the central point of the free extremity of the aluminum substrate for an harmonic displacement of the shaker.
- **Actuator input:** the voltage measured on the face of the piezoceramic attached to the back of the aluminum substrate (sensor) for an harmonic voltage signal applied to the face of the front ceramic (actuator).

The idea of the project is to suppress the vibration in the structure by controlling the sensor voltage by the application of a voltage signal to the actuator. The verification of the suppression will be done by analyzing the free extremity central node oscillations with and without vibration for disturbances introduced as displacements to the base of the shaker. For this reason, it is important to know the behavior of the observable input to the disturbance that is going to be introduced. The second curve is necessary to know the behavior of the output that is going to be controlled when a forcing term is introduced to the input actuator, this way the controller can be properly designed. Both curves will compared to the frequency response of the FEM numerical model and used to improve the realism of the model by introducing damping, losses and uncertainties in some aspects, as the boundary conditions, for instance. Consequently, the control quality will be improved as well, once that the controller design will be performed on the FEM model.

Reaching a frequency response curve experimentally is far more complex than reaching a time response because it is not possible to sweep the frequency range of interest with a single signal. In order to achieve it, several time domain curves must be obtained for different frequencies that discretize the range of interest. The following steps are necessary to raise the harmonic response curves:

1. The approximated resonance peaks are identified by changing the input frequency dichotomically;
2. A frequency array is defined with a high discretization close to the peaks and logarithmically spaced values far from them;
3. The time domain data is acquired for each forcing frequency;
4. The initial and final intervals corresponding to the transient response of the system are cut, leaving only the steady-state;
5. A band-pass infinite impulse response (IIR) filter is applied to the signal in order to eliminate undesired frequencies;
6. The crests and troughs are identified and the mean amplitude is calculated;
7. The gain magnitude and phase shift between the input and output are calculated.

In the cases that the displacement is necessary, the velocity signal obtained by the laser vibrometer is integrated by the trapezoidal numerical integration method, which approximates the function to be integrated as a set of line segments between two consecutive points. The band-pass IIR filter used in the fifth step is implemented through the zero-phase digital filtering MATLAB function (*filtfilt*).

3 Results and Discussion

In this chapter, the designed and manufactured structure presented previously will be modeled through the FEM and the numerical results for the model will be compared to the experimental results in order to increase the reliability of the model and, therefore, improve the vibration control system that is going to be designed numerically and implemented experimentally as an electronic circuit. All of these steps will follow the methodologies described in the previous chapter with the objective to reduce the transient and the harmonics of the vibration.

The structure that is going to be studied is presented in figure 47. The aluminum substrate is clamped at $y = 0$, with length $L = 108$ mm, width $b = 60$ mm and thickness $h_c = 1$ mm. The piezoceramics are located at a distance $L_1 = 8$ mm from the fixed side, with a thickness $h_p = 0.5$ mm. As the patches are squared and their width match the substrate's width, their length is $L_2 = 60$ mm. The reference adopted is the aluminum substrate electric potential. The material properties considered in the model were presented in the prototype section (tables 4 and 3).

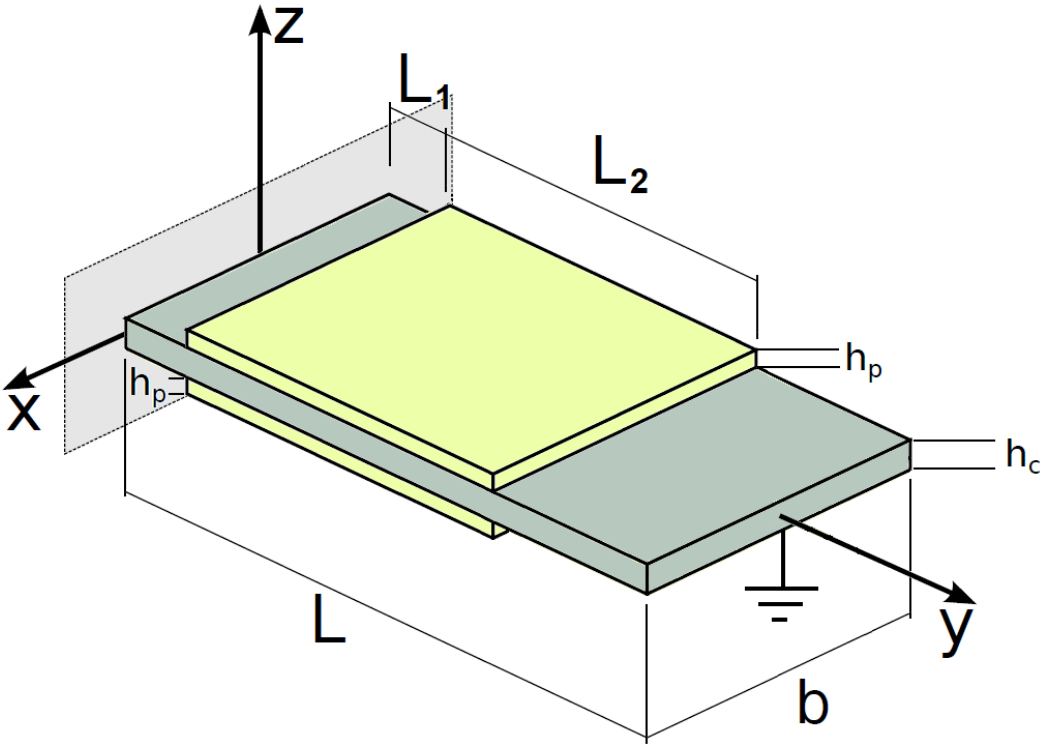

Figure 47 – Structure to be controlled.

3.1 Finite Element Model

The theory and formulation behind the FEM and the CUF are presented in the methodology chapter of this text. These methods will be used to model the structure that is presented in this chapter (figure 47) and from which the stiffness and mass matrices will be obtained, as well as the actuator gain vector. The model will be performed using beam elements with bidimensional cross-section discretization.

The FEM model for this structure will be divided in 11 B3 elements, resulting in 23 nodes along the y-axis. The first element goes from $y = 0$ to $y = 8$ mm and from the second to the eleventh, all elements have the same length of 1 cm. The cross-section will be discretized by L9 expansions that are 10 mm long along the x-axis each, each layer containing six expansions. So the cross sections without the piezoceramics will be composed by 6 L9 expansions and the ones containing the patches by 18 L9 for. The boundary conditions applied to the model are the fixed plane at $y = 0$ and the reference potential planes at $z = 0.5$ mm and $z = -0.5$ mm. The total number of nodes in this mesh is 1573, totalizing 5733 DOFs. In figure 48, the 3D mesh representation generated by the GMSH software is shown.

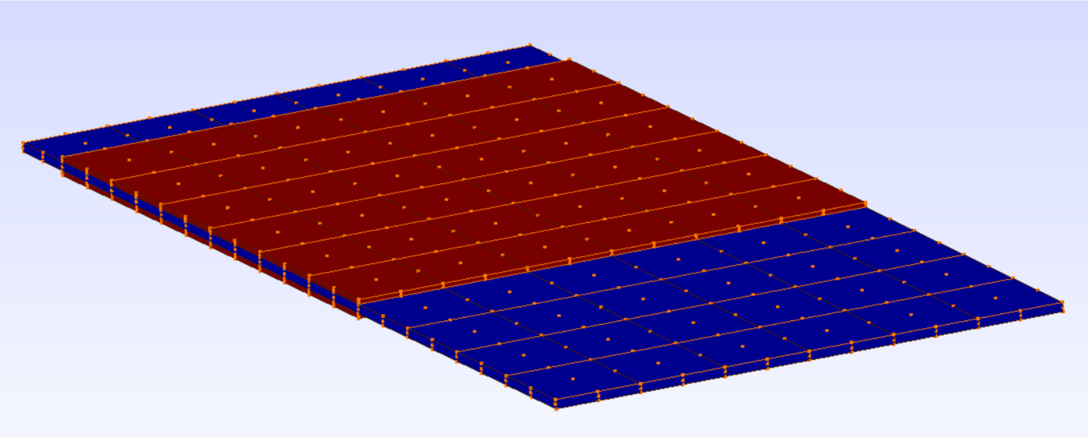

Figure 48 – Mesh representation as a GMSH 3D model.

After obtaining the mass matrix $\mathbf{M}$ and condensing the stiffness matrix $\mathbf{K}$ created by the MUL2 application, the eigenvalues of the system are calculated and the resonance frequencies and modal shapes obtained in MATLAB. The results for the first bending modes are compared to a free vibration analysis performed through the Fortran application on table 6 and the modal shapes are presented on figures 49, 50 and 51.

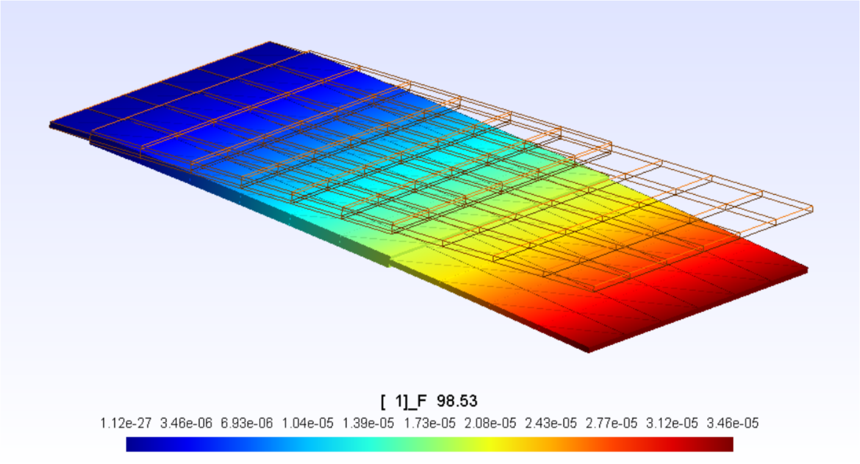

Figure 49 – First bending modal shape of the model.

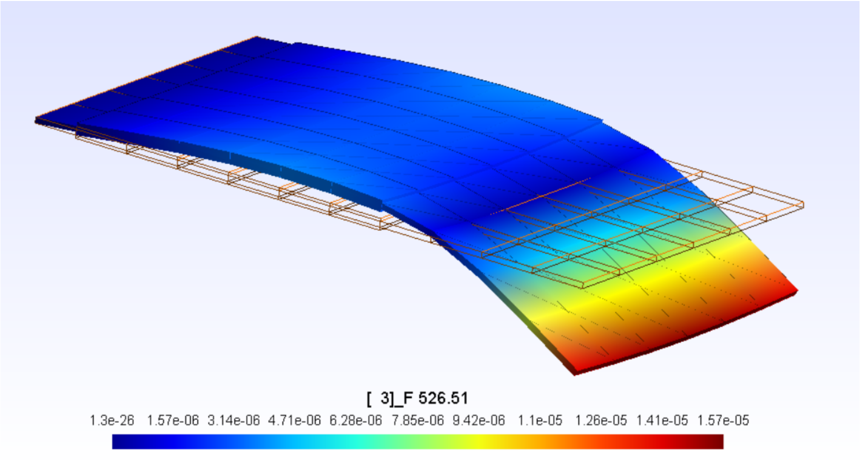

Figure 50 – Second bending modal shape of the model.

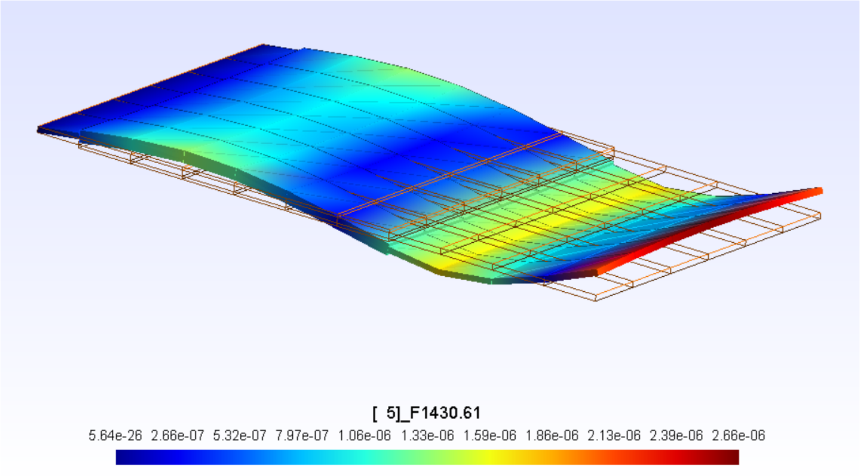

Figure 51 – Third bending modal shape of the model.

Mode	**Natural Frequency (Hz)**		**Difference** $(\times 10^{-5}\%)$
	MUL2	MATLAB	
1	98.53	98.53	-1.491
2	526.5	526.5	-0.3062
3	1430.6	1430.6	-0.2997

Table 6 – Three first natural frequencies associated to bending of the FEM model obtained through MUL2 and MATLAB codes.

In order to characterize the system, the forces distribution coming from a potential applied to the actuator's electrode is required. This distribution is obtainable by setting 1V to the actuator as a boundary condition when performing a static analysis through MUL2 application (figure 52). The resultant force vector applied to the mechanical nodes will be used as the actuator gain G_{act} from figure 26, where:

$$\mathbf{F_{act}} = \mathbf{G_{act}} V_{act} \tag{3.1}$$

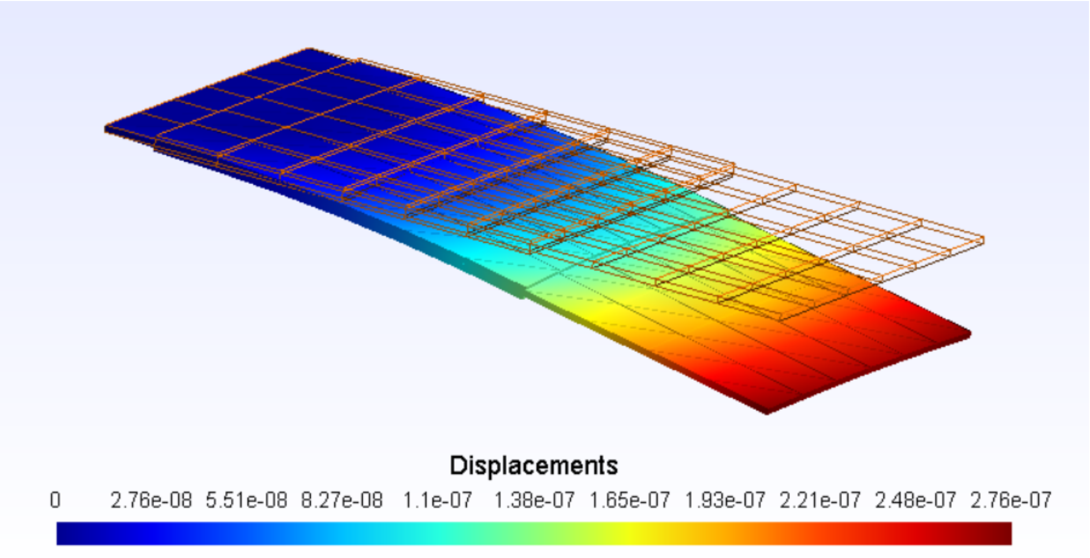

Figure 52 – Resultant structural static deformation due to the application of 1V to the actuator.

From the forces distribution it is expected that the third bending mode is not so well controllable with a single actuator. Usually a larger number of patches is necessary to control higher frequencies, once that the modal shape is composed by more than a single rotation around the fixed side of the structure. To compensate the modal shapes that visually resemble waves with more than one node and one anti-node (as the one from figure 51), it is necessary to have more actuators bonded along the y direction of the structure with interspersed voltage polarities applied to them.

3.2 Frequency Response

In this section, the frequency response curves obtained numerically and experimentally will be presented.

3.2.1 Numerical Curve

The only numerical curve to be raised in this project is the sensor voltage response due to an harmonic input voltage to the actuator. The frequency response $G_g(i\omega)$ for this system is obtained by evaluating the function from equation 2.72 to the desired frequency band and calculating the magnitude and phase for all values.

The structural matrices used to evaluate the function for every frequency are the condensed stiffness matrix $\mathbf{K_{cond}}$ obtained from equation 2.58, the mass matrix $\mathbf{M_{cond}} = \mathbf{M}$ due the non existence of inertial terms associated to the electric DOFs, and $\mathbf{D_{cond}} = \mathbf{0}$, once that the Rayleigh damping coefficients have not yet been estimated, so $\alpha_M = \beta_K = 0$. The necessary gain matrices are the output selection matrix $\mathbf{G_{sel}}$, the sensor gain $\mathbf{G_{sen}} = -K_{\phi\phi}^{-1} K_{\phi u}$ obtained from the uncondesation equation 2.59, and the actuator gain $\mathbf{G_{act}}$ from the previous section (equation 3.1).

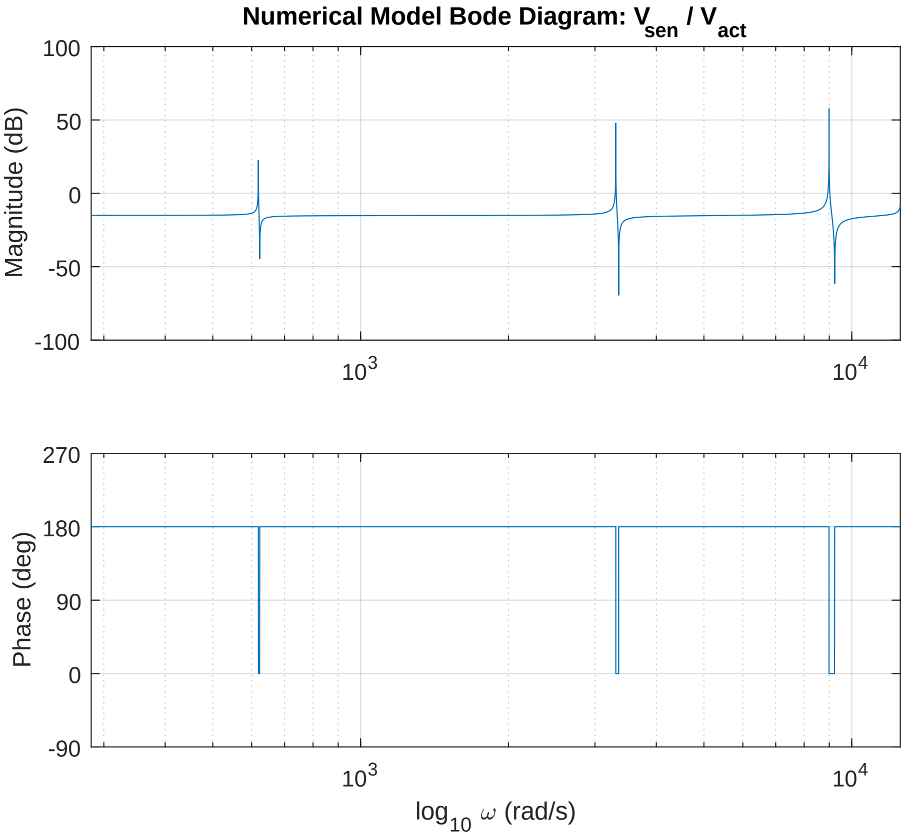

Figure 53 – Frequency response for the actuator/sensor system from the numerical FEM model.

The decision was to bound the frequency range between 45 Hz and 2kHz, once that the known resonance frequencies to be studied are contained in this interval and that the amplifier module that is going to be used in the experimental part does not work with lower frequencies. Figure 53 shows the Bode Diagram after calculating the complex frequency response for 2,000 frequency values logarithmically spaced within the range.

From this diagram, one may observe that the first three resonance and antiresonance peaks of the system associated to the same frequencies obtained in table 6. As there was no introduction of damping to the model, the peaks have really high gains, which will be corrected after the adjustment from the experimental curves.

3.2.2 Experimental Curves

As explained previously at the end of the Experimental Characterization section from the *Methodology* chapter, two different curves are required to characterize the model: the displacement of the free extremity of the structure due to disturbances applied by the shaker and the sensor voltage due to an actuator input, as in the numerical curve. The steps taken to acquire and process the experimental data have also been describe in that section.

The first step is to estimate the resonance frequencies for each prototype by applying a sinusoidal input, changing its frequency and looking for local maxima in the amplitude of the output signal. For this estimation, an oscilloscope (Agilent DSO3062A) and a function generator (Agilent 33220A) are used. The approximate resonance frequencies for each of the three prototypes are shown in table 7. The prototypes are numbered in the same order they were manufactured, so, from the comparison between their estimated resonance frequencies to the numerical model values, we can see that the prototype's quality has increased after each repetition of the manufacturing processes.

Prot.	**Natural Frequency (Hz)**		
	Mode 1	**Mode 2**	**Mode 3**
1	67.9	498	1164
2	81.5	514	1307
3	85.4	516	1374

Table 7 – Resonance frequencies estimated for each prototype before acquiring experimental data.

From the estimated frequencies, the frequency arrays were defined for each prototype. All of the arrays started at 45 Hz and ended at 2 kHz. The discretization was finer close to the resonance peaks and almost logarithmically spaced between peaks, totalizing 1,000 distinct values of frequencies for each prototype. In order to guarantee the steady-state stabilization for each forcing frequency, 200 cycles were applied as input and the acquisition finished only 2 seconds after the input cessation, assuring that the system was at rest before initiating a new acquisition. Each session took around 100 minutes to acquire data for all 1,000 frequencies.

For the frequency response to the shaker disturbance, the experiment was executed twice for each prototype: in the first are acquired the sensor voltage and the free extremity velocity, and in the second are acquired the sensor voltage and the base velocity. This decision was taken because there is only one laser vibrometer available and two different velocity signals are necessary. The sensor voltage is acquired on both sessions in order to assure that both experiments are executed in the same conditions, so if the sensor voltage frequency response presents different offset values, the velocity signals are corrected with the offset difference. The base velocity was used to normalize the free extremity displacement response between prototypes. As already explained, the displacement signals were calculated by integrating the velocities through the trapezoidal method.

Figure 54 presents the sensor voltage curves used for offset correction for prototype 2 and figure 55 the base displacement curve for normalization between prototypes. The sensor voltage correction curves for prototypes 1 and 3 followed the same behavior as the one illustrated for prototype 2. As the conditions were the same for every experiment, the final frequency response curves were almost left unchanged, as one may notice by the almost coincident offset levels between the correction and normalization curves.

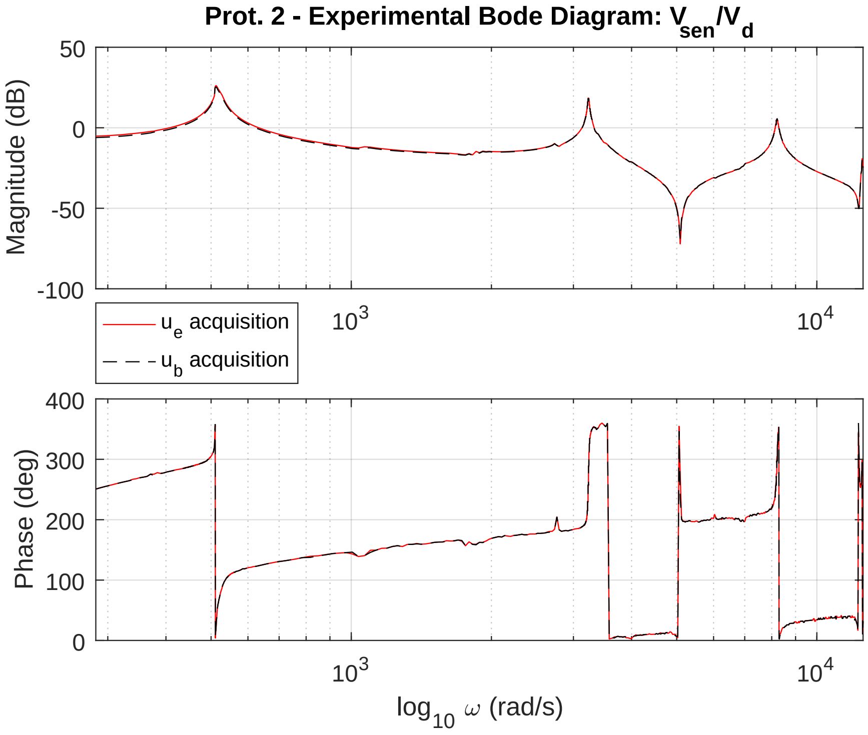

Figure 54 – Experimental frequency response for the sensor voltage/shaker voltage disturbance system (V_{sen}/V_d) for prototype 2 used for correction.

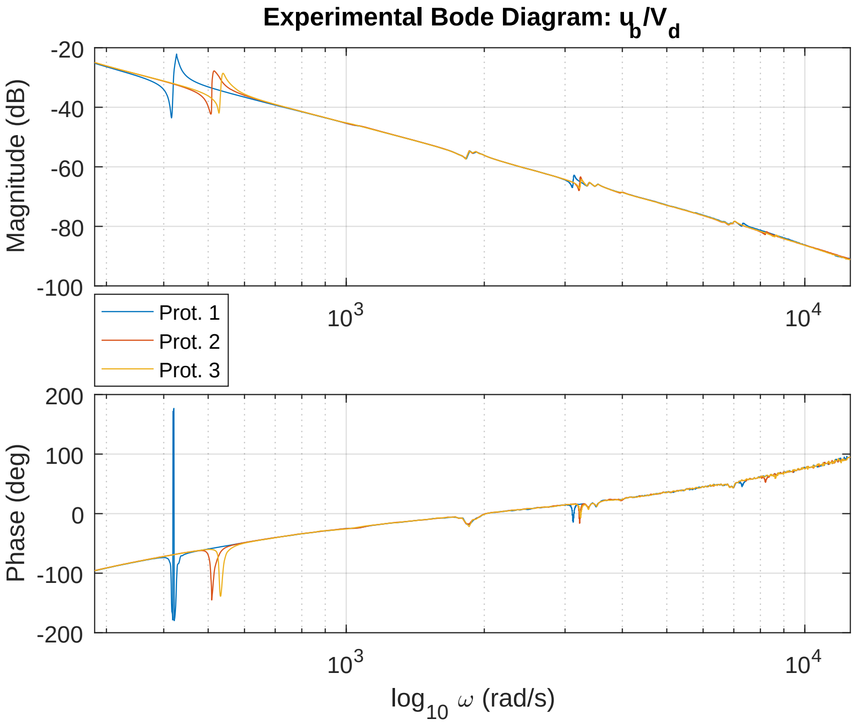

Figure 55 – Experimental frequency response for the base displacement/shaker voltage disturbance system (u_b/V_d) for each prototype used for normalization.

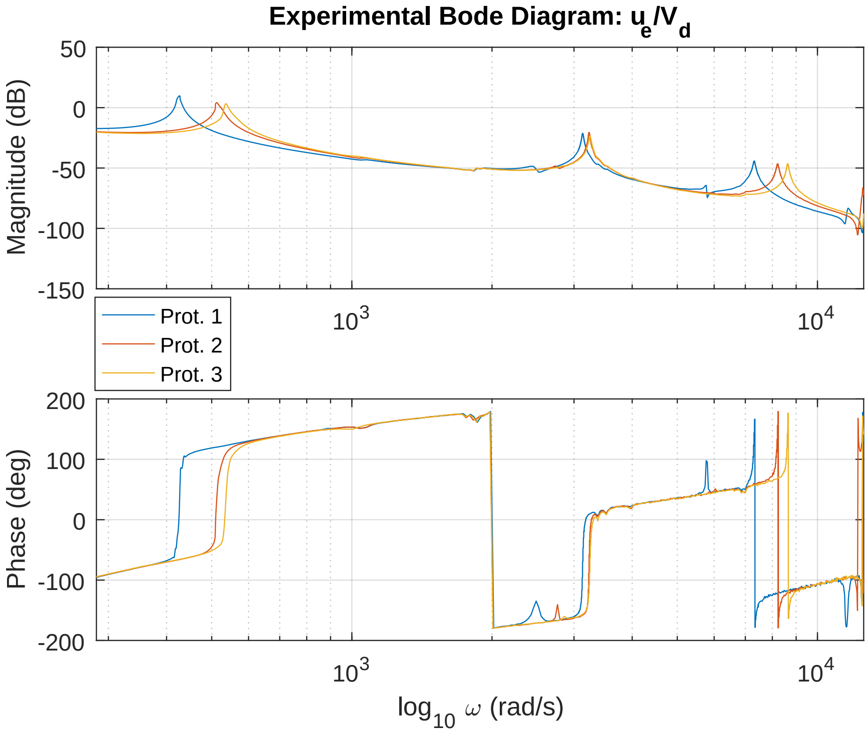

Figure 56 – Experimental frequency response for the free extremity displacement/shaker voltage disturbance system (u_e/V_d) for each prototype.

When processing the oscillatory signals used to calculate the complex response for the frequency associated to it, the cutting and filter parameters were defined by trial and error. The initial 25% of the signals were cut and the final 50 cycles in order to eliminate the transient and let only the steady-state response remain. The digital band-pass IIR filter applied to the signals was of 10th order, had the same sample rate of the acquired signal of 1 μs, with a band-pass width of 5% the frequency to be maintained f, given by $[0.975f,\, 1.025f]$.

The input signals and the laser vibrometer resolution were previously bounded in order to assure that the acquisition signals did not exceed the 10V limit that could damage the board. The input amplitude generated for the actuator was 1V and 300mV for the shaker, before passing through the amplifier. The laser resolution used was 50(mm/s)/V. The resulting Bode Diagrams for the three prototypes are presented in figures 56 and 57.

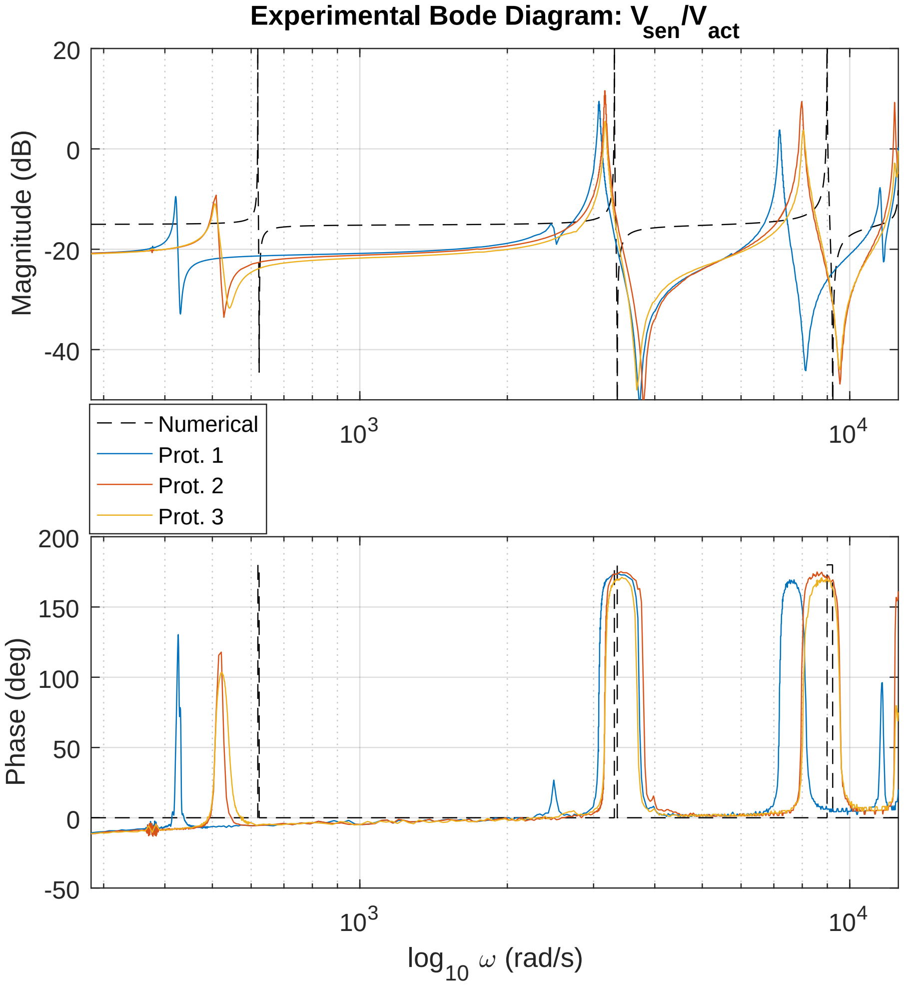

Figure 57 – Numerical and experimental frequency response for the actuator/sensor system (V_{sen}/V_{act}) for each prototype.

It is clear that the actuator/sensor curves obtained experimentally differs from the one obtained numerically. The following section will deal with these differences.

3.3 Numerical Model Adjustment

The numerical model presented in the first section of this chapter did not take some important considerations that a non-ideal system require. This section will be focused in this considerations and in the adjustment of the initially ideal numerical model to a more realistic based on the experimental data. Some hypothetical adaptations were raised as good candidates to affect the frequency response curve of the model towards the experimental model but did not impact significantly on it. Among them were the implementation of the epoxy layer and the silver electrode layer. Only the adjustments that successfully changed the numerical results, making it more trustworthy by comparing to the experimental frequency response, were added to the model and will be described in the next subsections. After describing each change made to the final numerical model, the frequency response comparison between the numerical model and the experimental data will be shown.

3.3.1 Boundary Conditions

The first relevant ideality assumed as premise in the numerical model was the perfect fixation of the cantilever structure. In real applications, it is really important to know relatively well the boundary conditions to which the system is subjected, because they are the only connections between the isolated system to the external world. For this reason, it was decided not to simulate the structure with total displacement constraint to every node at plane $y = 0$. Instead, several combinations were tested and the resonance frequencies compared to the ones obtained experimentally with the prototypes. The boundary conditions that better reproduced the experimental results were the constraining of the nodes contained in the plane $y = 0$ where $x \in \{0, 15, 30, 45, 60\}$ mm. This way, only the nodes closer to the bolts that were used to fix the structure to the shaker were constrained. The change in the resonance frequencies of the structure and its comparison to the ones measured for each prototype are shown in table 8

Model	**Natural Frequency (Hz)**		
	Mode 1	**Mode 2**	**Mode 3**
Ideal	98.5	526.5	1430.6
Adjusted	82.3	511.8	1362.3
Prot. 1	67.9	489.5	1163.9
Prot. 2	81.5	514.4	1307.5
Prot. 3	85.4	516.5	1374.3

Table 8 – Boundary conditions adjustment impact on natural frequencies.

The reference potential distribution along the aluminum structure was measured with the aid of a multimeter. As the electrical resistance is insignificant for such short distances, it was not necessary to adapt the boundary condition that sets $V = 0$ to the planes containing the piezoelectric faces bonded to the aluminum substrate.

3.3.2 Rayleigh Damping Coefficients

The methodology associated to the estimation of the Rayleigh Damping coefficients α_M and β_K can be found at the second chapter of this text. These coefficients will improve the frequency response of the numerical modal by including mechanical damping proportional to the inertia and the stiffness of the structure. It is important to recall that this adjustment compensates only mechanical losses associated to the system, which means that the electrical losses are not contemplated in this analysis.

The estimation of the coefficients will be performed for each of the three prototypes in three different steps: the damping estimation due to the resonance peaks attenuation observed in the harmonic analysis, due to the transient sinusoidal response decay associated to the natural frequencies of interest, and a final fine adjustment of the coefficients by effectively applying them to the system.

For the harmonic analysis, the damping ratios were estimated by evaluating the quality ratio from the full width half maximum (equation 2.64) for each resonance peak in the frequency response curve of the model. Table 9 shows the obtained values for each mode and prototype.

Prototype	**Mode**	f_i (Hz)	Gain (dB)	Q_i	ζ_i (10^{-3})
Prot. 1	1	67.0	-9.4	87.1	5.74
	2	489.7	9.4	104.3	4.80
	3	1145.0	3.8	85.0	5.88
Prot. 2	1	81.0	-9.2	44.0	11.38
	2	503.6	11.6	124.6	4.01
	3	1270.1	9.4	88.3	5.66
Prot. 3	1	80.5	-10.9	34.6	14.47
	2	504.0	5.5	83.7	5.98
	3	1279.9	3.7	63.9	7.83

Table 9 – Quality factor Q_i and damping ratio ζ_i estimation for the first three natural bending frequencies f_i of each prototype. Obtained from the harmonic response curves.

For the transient analysis, the decay exponent of the response was estimated by applying equation 2.63 to the transient signals with only the resonance frequencies of interest activated. For decoupling the modes, a sinusoidal excitation in the desired frequency was used as input to the actuator until the system reach the steady-state and then the input was removed, leaving the structure vibrating only in the excitation mode. From the exponent, the damping ratios were calculated and presented in table 10.

Prototype	**Mode**	f_i (Hz)	a_i	ζ_i (10^{-3})
Prot. 1	1	67.6	2.2	5.25
	2	492.6	16.5	5.33
	3	1149.4	42.5	5.89
Prot. 2	1	80.6	4.8	9.48
	2	500.0	11.9	3.79
	3	1282.1	41.0	5.09
Prot. 3	1	82.0	5.5	10.68
	2	505.1	20.5	6.46
	3	1288.6	81.5	10.07

Table 10 – Decay exponent $a_i = 2\pi f_i \zeta_i$ and damping ratio ζ_i estimation for the first three natural bending frequencies f_i of each prototype. Obtained from the transient response curves.

From the damping ratios estimated through both analyses, the Rayleigh coefficients were obtained by applying the least squares method described in the methodology chapter to equation 2.61, that correlates the coefficients to pairs of damping ratio and natural frequency. The mean coefficients values obtained from the experimental data are $\alpha_M = 9.07$ and $\beta_K = 1.69 \times 10^{-6}$ and the detailed results for each mode and prototype are presented on table 11. The mean value for the coefficients were used as initial values to implement to the numerical model and compare to the experimental modal curves. By tuning these two parameters, the optimized implementation of the damping matrix was reached after several simulations. The last row of table 11 contains the final values used in the adjustment.

Analysis	**Prototype**	α_M	β_K (10^{-6})
Harmonic	1	4.66	1.71
	2	11.29	1.26
	3	14.29	1.81
Transient	1	4.32	1.77
	2	9.37	1.16
	3	10.50	2.42
Implementation		4.5	2.25

Table 11 – Rayleigh damping coefficients α_M and β_K estimated by each kind of analysis for each prototype.

3.3.3 Additional Considerations

Even after adjusting the boundary conditions, damping coefficients, implementing additional layers of initially ignored materials, the numerical curve will not perfectly fit the experimental data. There are many reasons that may be responsible for this difference, among which are the stiffness and damping differences between applying effectively a voltage to the actuator and applying equivalent forces to the structure that are created from this voltage, the flaws associated to the manufacturing processes applied to generate the prototypes, the inefficiencies associated to the efficiency and power transfer of the system, and the dielectric losses in the piezoceramics. These three effects will be described in the following paragraphs.

It is not easy to identify the flaws associated to the manufacturing processes that influenced the final characteristics of the system. Some hypotheses raised that could explain the divergences in the distances between the resonance and antiresonance frequencies for the experimental models are the epoxy layer elasticity and the presence of microbubbles in it, which could be removed with a vacuum pump that, unfortunately, was not available to use during the manufacturing period of this project. Mass and stiffness changes in the structure affect the spacing between resonance and antiresonance peaks, as experimentally demonstrated in (WAHL; SCHIMIDT, 1999) and further explained in (HANSON et al., 2007).

The efficiency and power transfer in the system was studied in a similar application in (SALAS, 2017). It associates an equivalent electrical circuit that includes the mechanical and electrical inertia, stiffness and damping to the maximum power transfer capacity according to the impedance of the external system coupled to the structure.

One of the main responsible for the dielectric losses is the relation between the capacitive reactance of the piezoceramic and its equivalent series resistance (ESR). This ratio is called tangent loss factor $tan(\delta)$ and it is given by:

$$tan(\delta) = \frac{1}{Q} = ESR\omega C = \frac{Re(Z)}{|Im(Z)|} \tag{3.2}$$

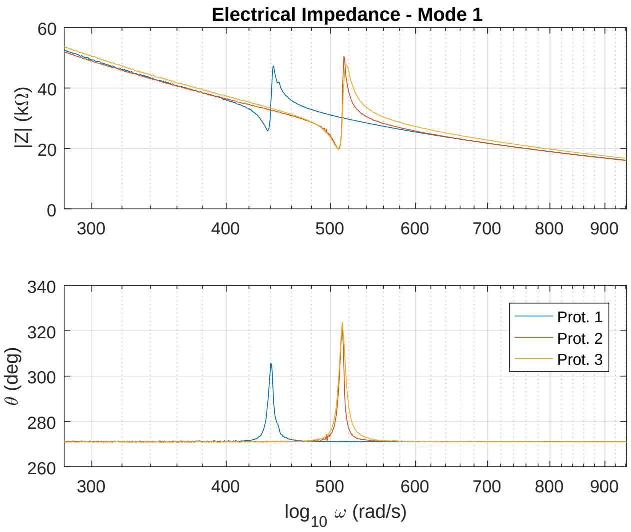

Figure 58 – Complex electrical impedance around the first mode for the three prototypes.

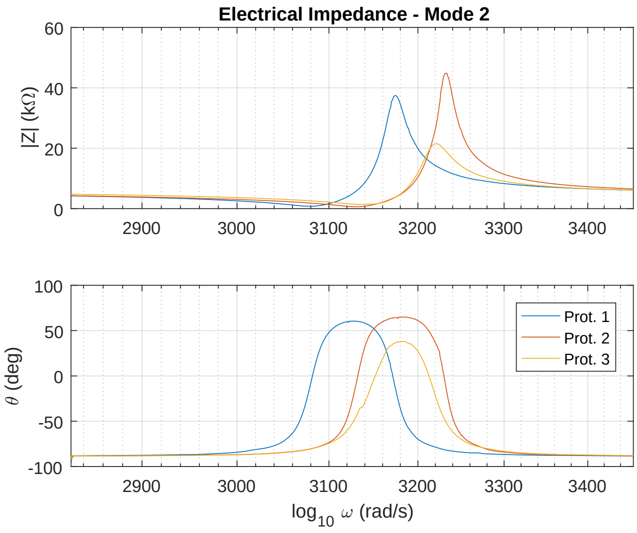

Figure 59 – Complex electrical impedance around the second mode for the three prototypes.

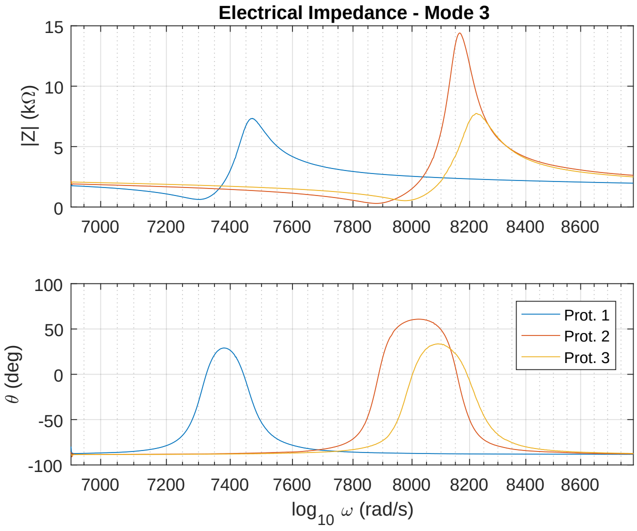

Figure 60 – Complex electrical impedance around the third mode for the three prototypes.

It is very useful when characterizing piezoceramics, as explained in details in (PEREZ et al., 2016), (DEANGELIS; SCHULZE, 2015), and (SALAS, 2017). This relation is easily obtained by using and impedance analyzer, which sweeps a frequency range of interest and returns the complex impedance in this range. The Agilent 4294A Precision Impedance Analyzer was used in this project in order to evaluate the electric impedance of the system. The resulting curves for each of the prototypes are shown in figures 58, 59 and 60. The loss factor value for each frequency is the tangent of the phase shifts θ from the presented curves. The impedance could be also used to obtain the resonance frequencies of the system, which are located at the local minima of the curves, once that the output gain is inversely proportional to the impedance.

In order to compensate not only the elements described along this subsection, but possible other effects not taken into account until now, a proportional and exponential correction to the numerical frequency response curve will be applied according to:

$$|H'(j\omega)| = (a|H(j\omega)|)^b \tag{3.3}$$

where H is the original model and H' is the adjusted through coefficients a and b. After tuning a and b several times, a sufficient fitting was obtained for $a = 2.37$ and $b = 2.8$.

The resulting frequency response curve after all of the adjustments introduced in this section is presented in figure 61. Certainly more adaptations could be applied to improve the model, specially in the peaks bandwidth, however the corrections implemented were considered enough for the scope of this work.

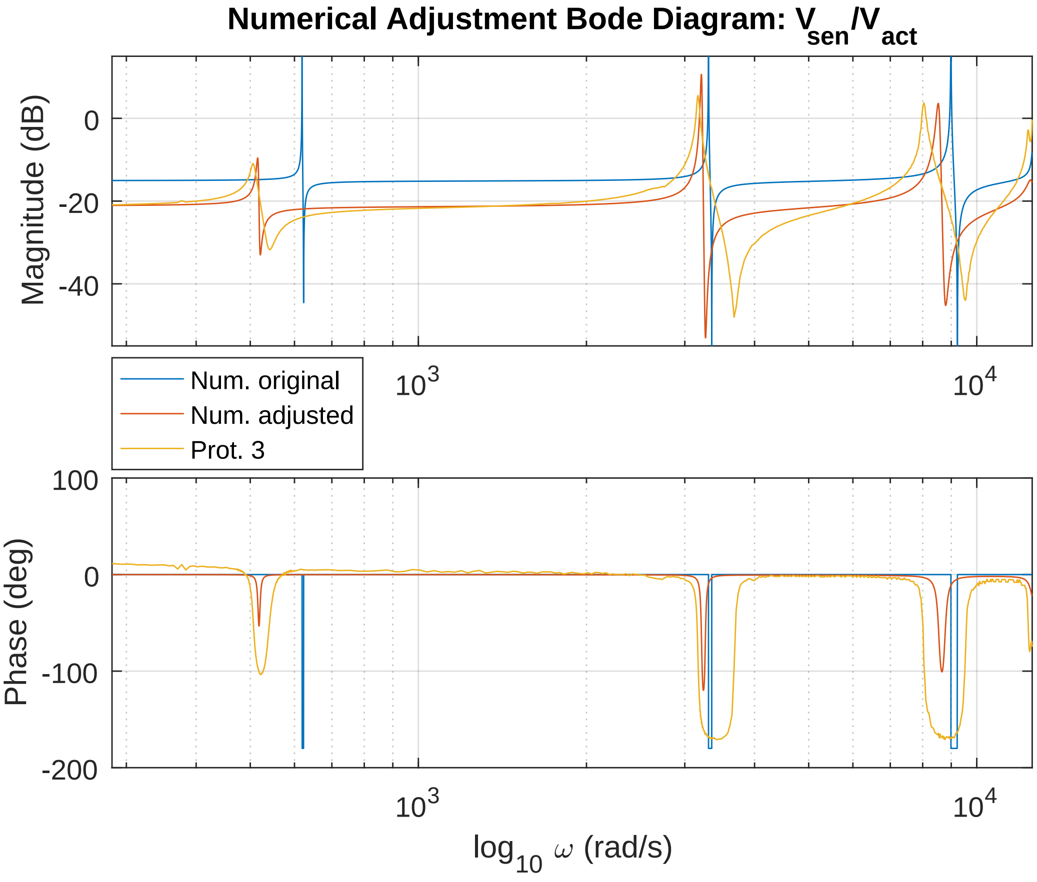

Figure 61 – Frequency response for the adjusted numerical model.

3.4 Model Order Reduction

The emphasis of this section is the order reduction of the FEM model that is initially of order 5,733 (number of DOFs). The reduced model will be represented in terms of a continuous time transfer function and of an equivalent RLC circuit, as exposed in the methodology chapter. In order to consider at least the three first modes, a minimum of 3 pairs of poles is necessary.

3.4.1 Transfer Function

The low order transfer functions were estimated for each of the three prototypes experimental frequency response data using the MATLAB function *tfest*, represented by equation 2.75, with 3, 4 and 5 pairs of poles ($n_p = 6,\ 8,\ 10$) and one pair less of zeros $n_z = n_p - 2$. The magnitude Bode diagram and the quality metrics associated to the estimations are presented on figure 62 and table 12.

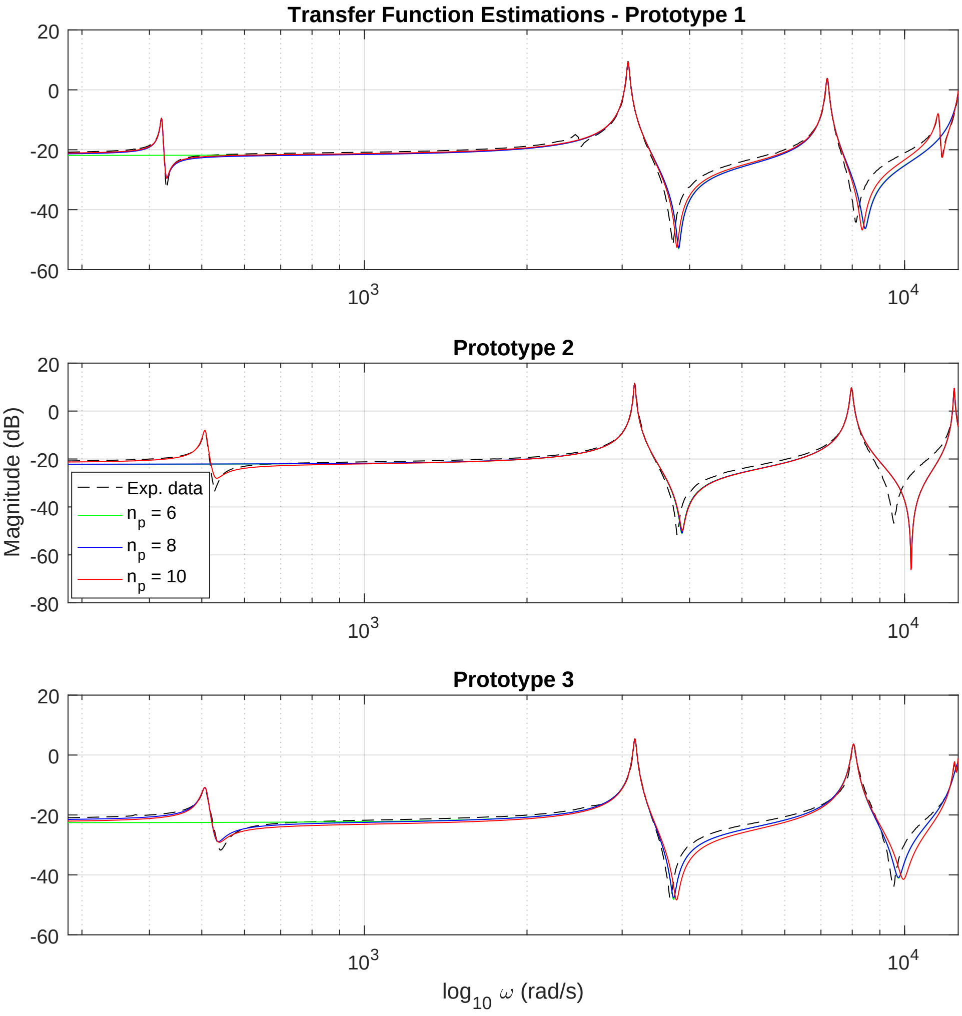

Figure 62 – Magnitude Bode diagram comparison between experimental data and estimations.

n_p	Prot. 1		Prot. 2		Prot. 3	
	Fit (%)	MSE (10^{-3})	Fit (%)	MSE (10^{-3})	Fit (%)	MSE (10^{-3})
6	91.78	7.067	91.90	13.00	82.56	3.425
8	92.91	6.067	92.09	10.36	89.48	1.323
10	94.15	5.079	92.52	9.842	91.18	0.7683

Table 12 – Quality metrics for estimated transfer functions with 6, 8 and 10 poles for each prototype experimental data.

From the estimations frequency response data (FRD), it is possible to see that with 4 pairs of poles all of the desired resonance frequencies are encompassed. Since the third prototype is closer to the numerical model than the other two and that the eighth order transfer function estimated from its data has reasonable fitting values, it was chosen as the reduced order model. Therefore, in its zero-pole-gain (*zpk*) form, the estimated plant G_{est} that is going to be used is:

$$\begin{aligned} K &= 5.801 \times 10^6 \\ F_{z,1}(s) &= s^2 + 24.37s + 2.816 \times 10^5 \\ F_{z,2}(s) &= s^2 + 68.23s + 1.395 \times 10^7 \\ F_{z,3}(s) &= s^2 + 321.4s + 9.477 \times 10^7 \\ F_{p,1}(s) &= s^2 + 13.96s + 2.585 \times 10^5 \\ F_{p,2}(s) &= s^2 + 39.83s + 1.004 \times 10^7 \\ F_{p,3}(s) &= s^2 + 141.1s + 6.476 \times 10^7 \\ F_{p,4}(s) &= s^2 + 406.4s + 1.584 \times 10^8 \\ G_{est}(s) &= K\left(\prod_{i=1}^{3} F_{z,i} \bigg/ \prod_{j=1}^{4} F_{p,j}\right) \end{aligned} \tag{3.4}$$

The decomposition of this transfer function into partial fractions is possible by calculating the residues to each of the four pair of poles. The residues, resonance frequencies and damping ratios associated to G_{est} are found in table 13.

Mode	r (10^{-3})	$\omega_n (rad/s)$	ζ (10^{-3})
1	6.73	508.4	13.73
2	26.7	3,168.8	6.284
3	23.5	8,047.6	8.765
4	24.2	12,587	16.15

Table 13 – Residues r, resonance frequencies ω_n, and damping ratios ζ for the four pair of poles of G_{est}.

3.4.2 Equivalent RLC

From the decomposition of the reduced order transfer function into partial fractions, it is possible to transform obtain equivalent RLC circuits for each pair of poles (equation

2.89). By choosing an initial value for the capacitor, the inductor and resistor can be calculated from the natural frequency and the damping of i-th mode of the system:

$$L_i = \frac{1}{C_i \omega_{n,i}^2} \text{ and } R_i = \frac{2\zeta_i}{C_i \omega_{n,i}} \tag{3.5}$$

The output variable for this system is the voltage drop across the capacitor, so to couple the modes, this voltages must be summed through an inverting op-amp adder, as previously demonstrated in equation 2.91. By setting a value to the feedback resistor R_F, the input resistors $R_{k,i}$ are evaluated from the partial fractions residues r_i:

$$R_{k,i} = \frac{R_F}{r_i} \tag{3.6}$$

The chosen capacitance values for the RLC circuits are $C_1 = 5\mu$F and $C_2 = C_3 = C_4 = 1\mu$F and the feedback resistor $R_F = 1$kΩ. The equivalent circuit is presented in figure 63.

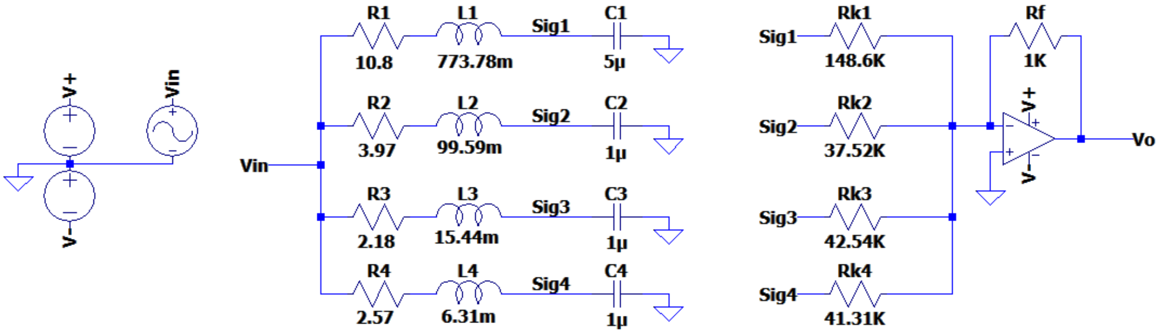

Figure 63 – Eighth order RLC circuit representing the structural system.

By applying a long unitary pulse to the input voltage V_{in} with negative voltage, a transient response similar to the G_{est} unity step response obtained through the command *step* in MATLAB. The negative potential is required due to the inverting adder that sums the capacitor voltages. The signal obtained by LTSpice solver was imported to MATLAB for this comparison, that is shown in figure 64 for three different time resolutions. Both signals have the same dynamics, with a small difference in their offset, which is given by the additional output offset provided by the op-amp.

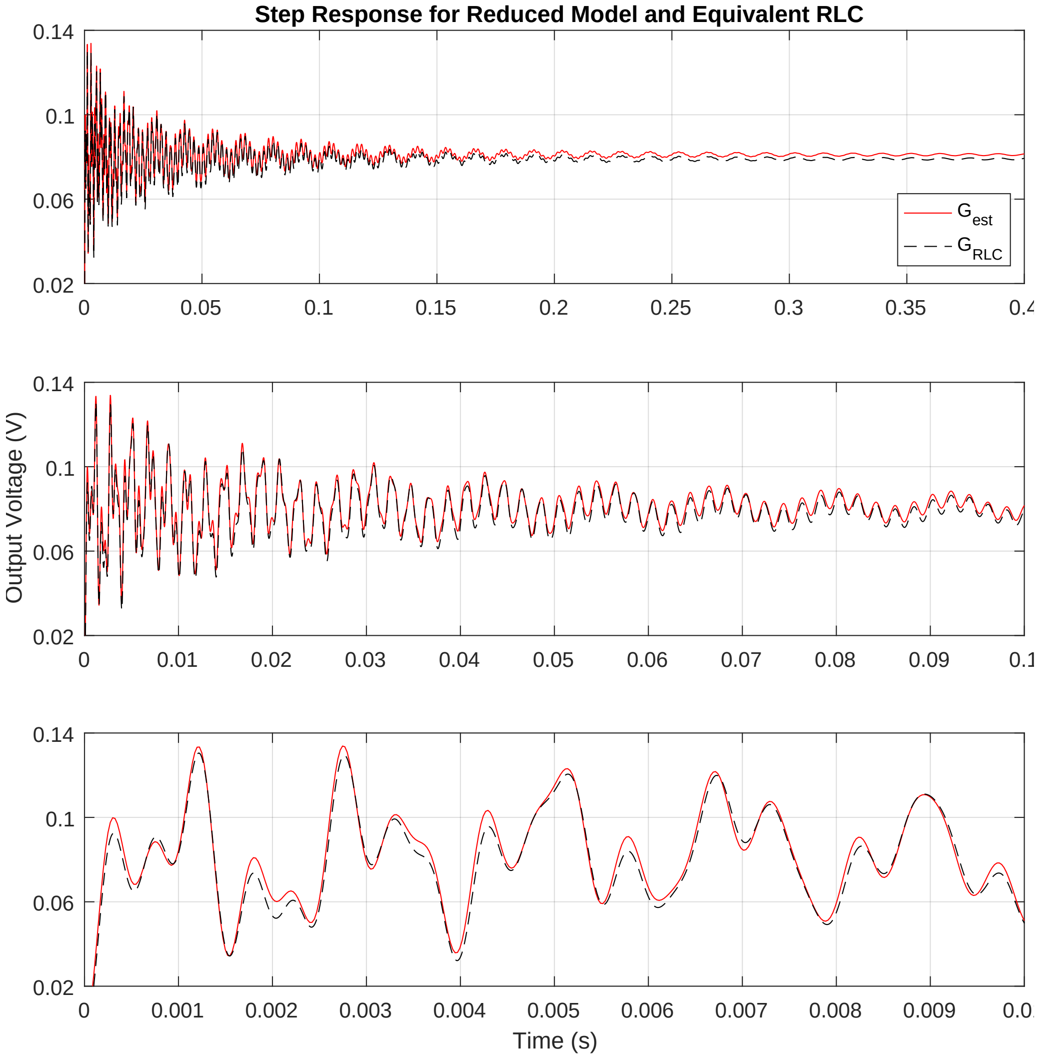

Figure 64 – Unit step response for the eighth order transfer function G_{est} and the equivalent RLC system G_{RLC}.

3.5 Controller Design

This section will be responsible for the controller design taking into account only the transfer function dynamics that represents reduced model. As stated in the methodology chapter, PID controllers are going to be implemented, which can be shown diagrammatically on figure 27. There are different methods for tuning the proportional, integrative and derivative parameters, but initially the Ziegler-Nichols method will be used in order to estimate initial values that will later be finely tuned.

The proportional gain K_P is given as function of the ultimate (or critical) gain K_u, which is reached when the system reaches the marginal stability. This requires a study on the stability of the system, which will be performed by analyzing the stability gain and phase margins of the uncontrolled plant and the Nyquist plot of the system.

For a closed loop system with a single gain in the feedback, the poles can be obtained by solving the characteristic equation $1 + G_p(s) = 0$, where $G_p(s)$ is the plant open loop transfer function. Therefore, the stability margins are given as the distance from the frequency response plot to the value of -1, which is equivalent to a response with a gain of 0 dB and a phase of 180°. Figure 65 may provide misleading information about stability margins, once that it shows an infinite gain margin and a relatively high phase margin of 37.2°. Actually, the system is closer to instability that it seems in the second, third and fourth peaks. The phase plot is almost vertical close to the 0 dB crossover frequencies associated to the second and third peaks, which means that it approaches 180° with small changes in the frequency. Furthermore, the delay margin is very low: 203μs and 98μs for the second and third peaks, respectively, once that they are located at high frequencies. Additionally, the last peak has a gain magnitude of -2.48 dB and the correspondent phase also changes drastically towards the unstable 180°. Lastly, the system presents an asymptotic approximation to 180° phase for high frequencies and, once that it never reaches this value, the gain margin is infinite. Given this aspects, the real system may become unstable for small changes and uncertainties in its gain, in the response delay, in the poles location and for disturbance injection in the closed loop.

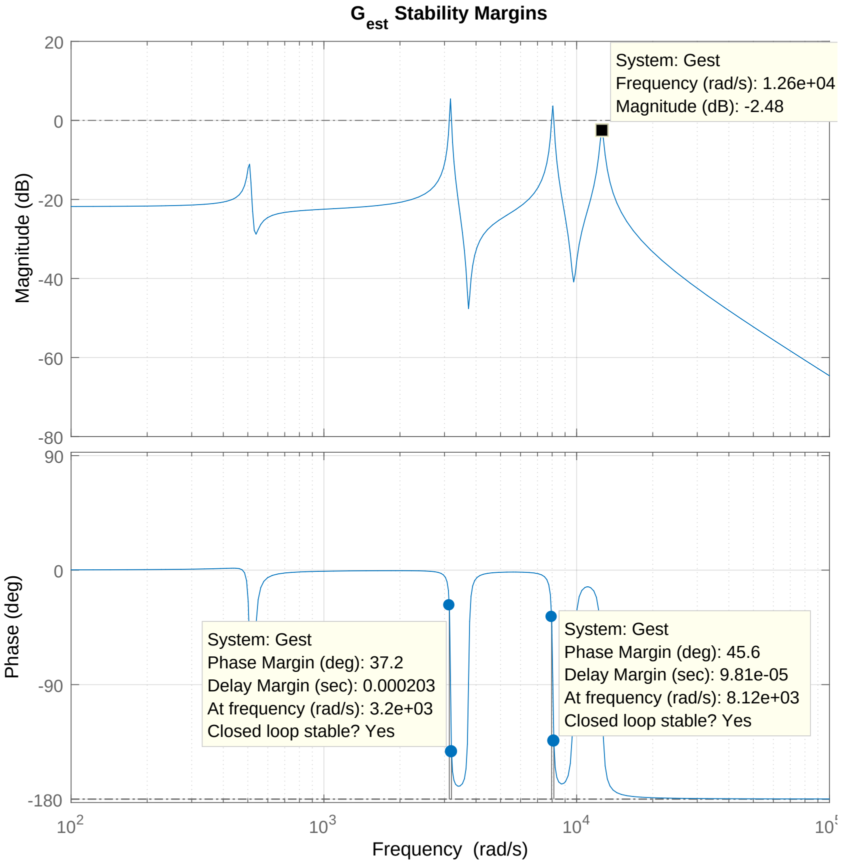

Figure 65 – Stability margins for the reduced order model $G_{est}(s)$.

The lack of robustness when closing the loop for this system can be easily observed from the peaks in the sensitivity function $S(s) = (1 + G_p(s))^{-1}$ from figure 66. As the sensitivity function is the inverted characteristic equation, the distances from the -1 in the Nyquist plot are the radii $1/M_i$, where M_i is the absolute magnitude gain for each peak of the sensitivity function S (figure 67). The values associated to each peak are found in table 14.

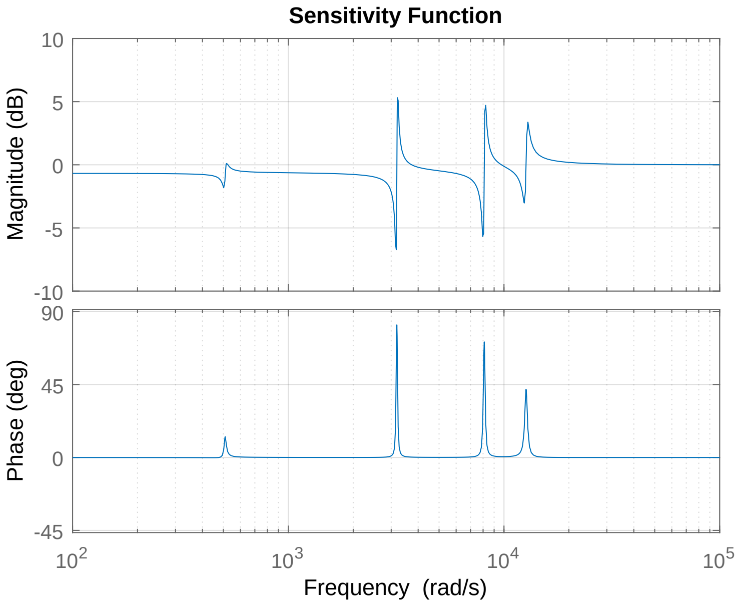

Figure 66 – Sensitivity function $S(s)$ Bode diagram.

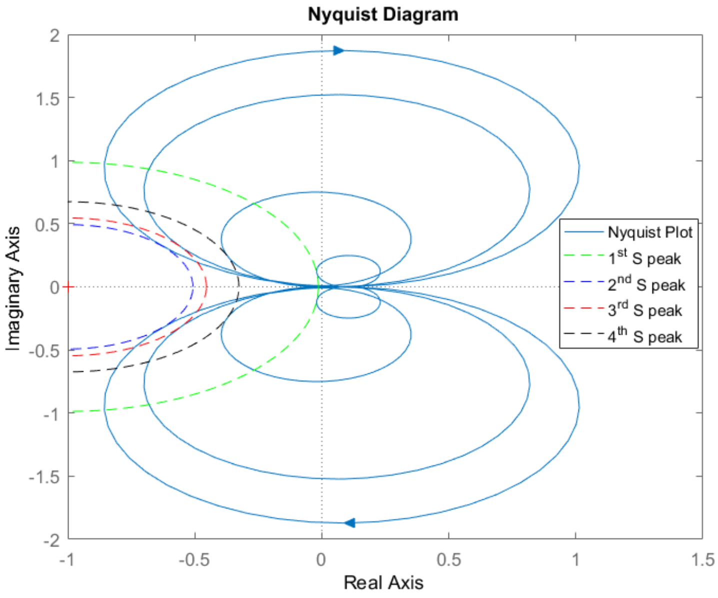

Figure 67 – Nyquist plot and robustness margins for each sensitivity peak.

Peak	Frequency (rad/s)	Magnitude (dB)	Radius ($1/M_i$)
1	518	0.12	0.99
2	3,213	6.15	0.49
3	8,192	5.26	0.55
4	12,9872	3.43	0.67

Table 14 – Sensitivity peaks characteristics.

As there is no value for the critical gain K_u, once that the gain margin is infinite for the system, the decision is to choose a limit gain that takes the system very close to the instability. For this system, the choice is where the phase margin reaches 3°, which happens for $K_u = 16.52$. The crossover frequency associated to the minimum phase margin is 2872 Hz, therefore, the ultimate oscillation period to be used is $T_u = 348.2\mu$s. From the Ziegler-Nichols parameters table 2, we get: for the P controller $K_P = 8.26$, and for the PD controller $K_P = 12.22$ and $T_d = 43.5\mu$s. So the controllers become:

$$G_{c,P}(s) = 8.26 \text{ and } G_{c,PD} = 13.22 + 5.75 \times 10^{-4}s \tag{3.7}$$

The PD controller $G_{c,D}$ is a non-causal system (more zeros than poles), which means that it is not realizable. In real applications, a pole with very high time constant is added with the derivative zero, being fast enough not to influence the dynamics of the closed loop system. For a pure D controller $G_{c,D}$ the same happens: a high frequency pole and a very low proportional gain are added in order to make the system feasible. For the transfer functions analyses on MATLAB the ideal non-causal controllers will remain unchanged.

The argument for not using the integral parameter K_I in the controller was already determined previously, but it is reinforced here due to the instabilities that it may introduce in a system that is already not robust initially. The derivative parameter K_D for the pure derivative controller will be the same from the PD: $G_{c,D}(s) = 5.75 \times 10^{-4}s$.

From the block diagram from figure 68, the output response y due to the reference r and the disturbance d inputs is given by:

$$Y(s) = D(s)\frac{G_p(s)}{1 + G_c(s)G_p(s)} + R(s)\frac{G_c(s)G_p(s)}{1 + G_c(s)G_p(s)} \tag{3.8}$$

The reference signal for this system is always zero, so in order to obtain the equivalent closed loop transfer function $G_{CL}(s)$ between the disturbance and the output:

$$\frac{Y(s)}{D(s)} = G_{CL}(s) = \frac{G_p(s)}{1 + G_c(s)G_p(s)} \tag{3.9}$$

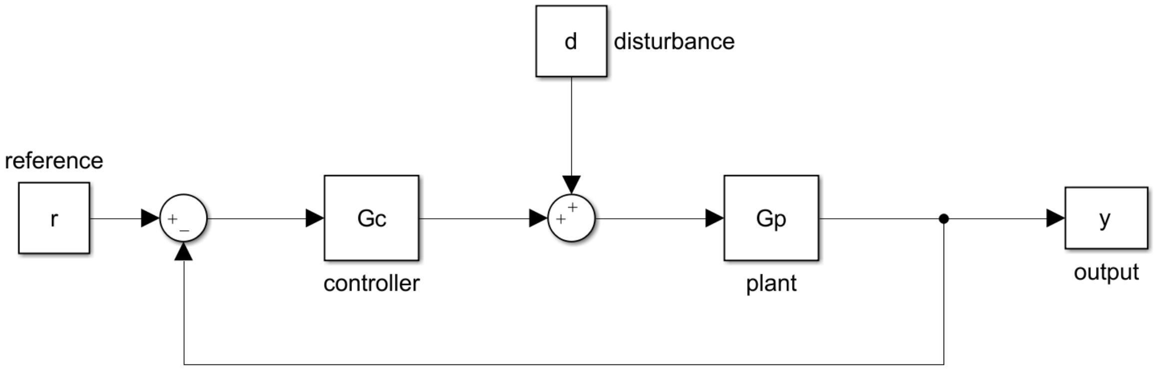

Figure 68 – Control loop for the plant transfer function $G_p(S)$ and the controller transfer function $G_c(s)$ with inputs from the reference r and disturbance d.

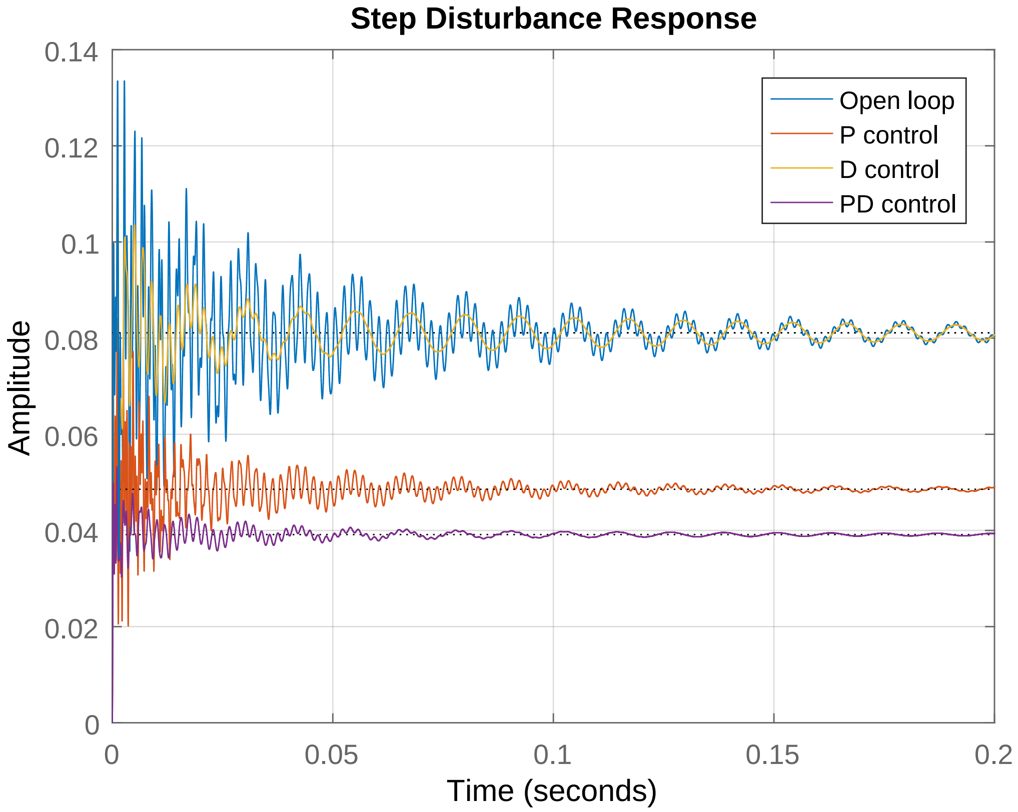

Figure 69 – Output transient response for disturbance step input for different controllers.

For the open loop response $G_c(s) = 0$, so the equivalent transfer function is simply $G_p(s)$. Figure 69 shows the differences between the uncontrolled and the controlled systems for each kind of controller when applying a unit step disturbance to the actuator voltage.

As expected and described during the methodology chapter, the low frequency DC gain of the closed loop system changes when the proportional parameter is applied (for P and PD). The derivative term influences more in the higher oscillation frequencies, but leaves the lower almost unchanged in this system, while the proportional affects the low frequency response and does not change much the higher frequency oscillations. Therefore, the PD control gives a better transient response by acting on all frequencies of the signal, which is clear from the lower settling time that can be observed in the step response. In the frequency domain, it is also possible to see the attenuation by changing the gain of the system for the whole spectrum of frequencies and by increasing active damping to the resonance peaks, as presented in figure 70.

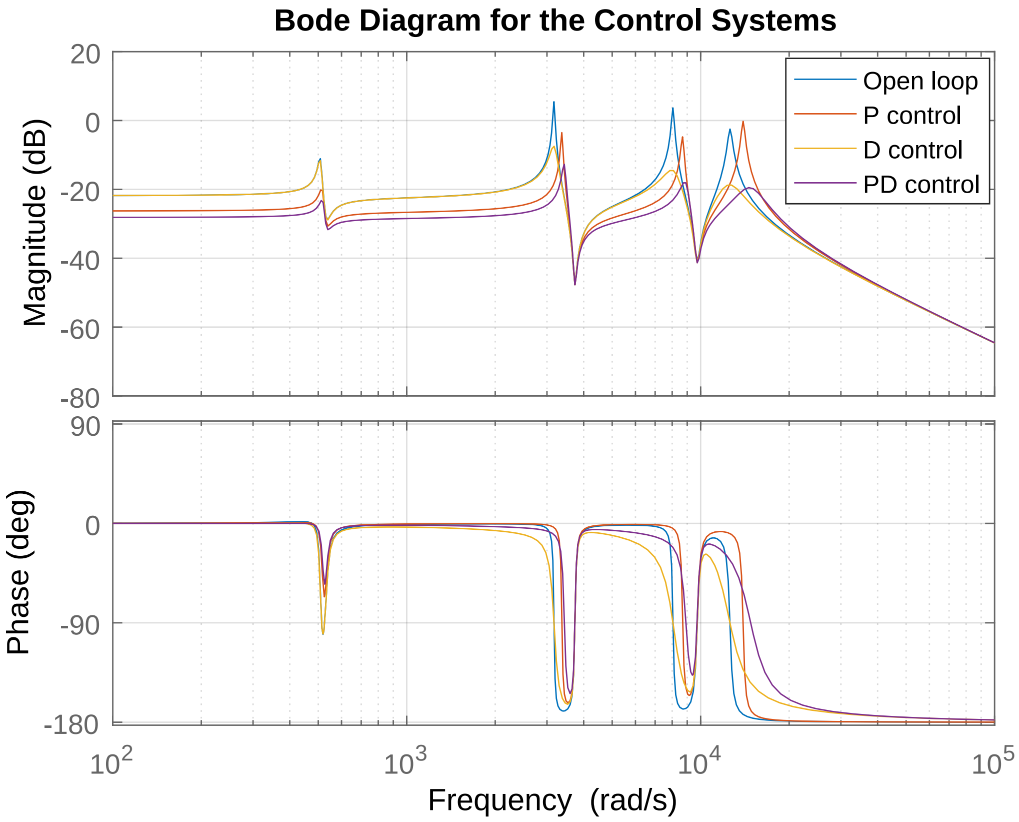

Figure 70 – Bode diagram for open loop, P, D and PD control systems.

Next, the parameters will be increased in order to show that, given the infinite gain margin, the proportional term will never unstabilize the system. However, later will be proved that for the real system it does not happen. Using the *pidTuner* and *sisotool* interface in MATLAB, the proportional and derivative gains were tuned for obtaining a settling time below 1ms and a disturbance DC gain close to 10^{-3}, resulting in the controller $G_c(s) = 750 + 0.085s$. Figures 71 and 72 present the disturbance unit step response and the bode diagram for this unrealizable controller, respectively.

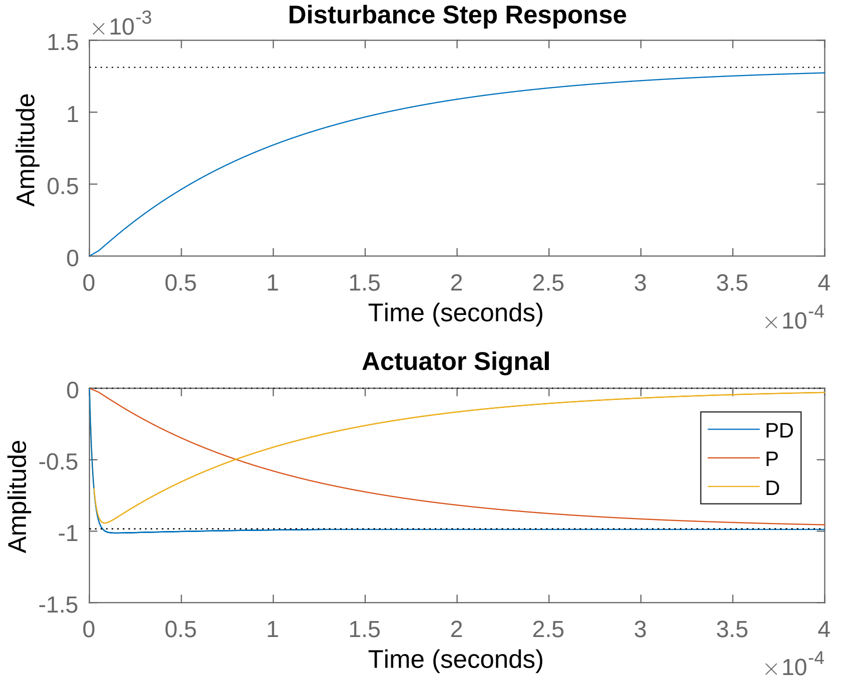

Figure 71 – Output response for unit step disturbance with an ideal high gain PD controller and the respective P, D and PD actuation signals.

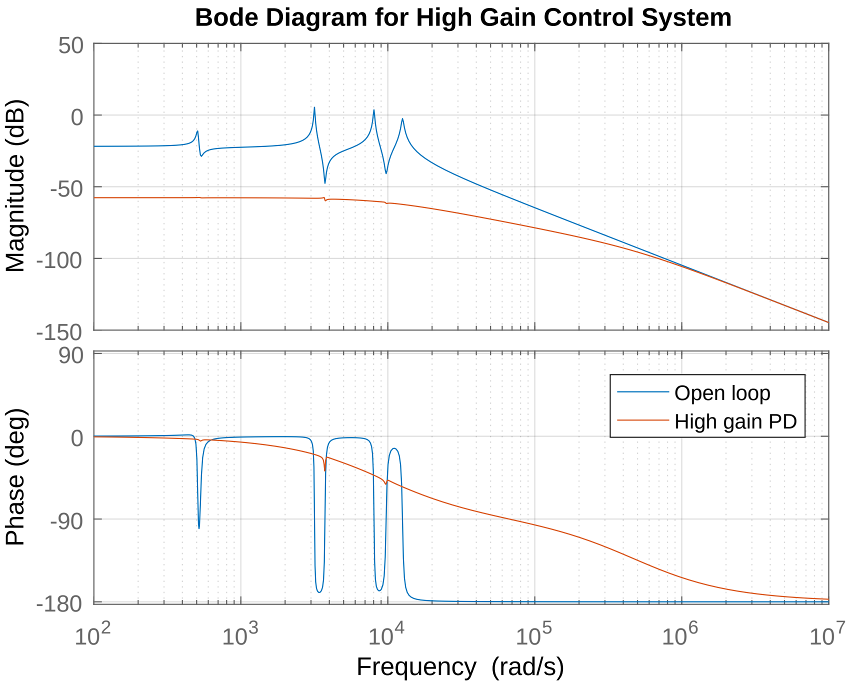

Figure 72 – Bode diagram comparison between the open loop and the ideal high gain PD control system.

3.6 Control Loop Implementation

This section will focus on how the control loop is implemented: numerically, through MATLAB and LTSpice, and experimentally, using electronic components. Also, the final results for the controlled system in each case is going to be presented and discussed.

3.6.1 LTSpice Control

The analog controller is implemented using general purpose operational amplifiers in feedback circuits. These integrated circuits can be also used as comparators for a wide variety of applications, where the output saturates to the supply voltage values according to the electric potential difference between the inverting and the non-inverting input. The choice of an op-amp depends on the power required for the application in which it is inserted. Usually, for precise piezo driving in robust systems, high voltages are necessary, so an amplifier is often needed. The main goal of this project is to show that it is possible to control the structure with an analog circuit having as start point the design for an unconventional numerical model. Therefore, extremely low overshoots and settling times are not in the control requirements of the work, so such high voltages will not be needed. Consequently, a family of op-amps that accept supply voltages ranging from -5V/+5V to -18V/+18V was chosen, the TL07X, once they provide enough to actuate on the structure with low requirements. This family is composed by TL071, TL072 and TL074, where the first is packaged with a single op-amp, the second with dual and the third with quad. Four different amplifiers will be needed, so the TL074 is going to be used. These integrated circuits will be supplied with symmetric power supplies of 12V each, that can be easily found in the market.

Figure 73 presents the circuit that implements a proportional-derivative controller, according to the methodology presented in the second chapter. The supply voltages V_+ and V_- are connected to the TL074 supply pins and each amplifier U_i of the packaging plays a different role in the cascade circuit: U_1 implements the inverted proportional gain $-K_P$ as an inverting amplifier, U_2 implements the inverted derivative gain $-K_d$ as an inverting differentiator, U_3 sums the proportional V_{pro} and the derivative signal V_{der} as an inverting adder, and U_4 sums the actuation voltage V_{act} to the disturbance input signal V_{in}.

The value of 10kΩ is chosen for the fixed resistors in order to maintain the same magnitude order of the system impedance $|Z|$ (figures 58, 59 and 60). For the capacitors in the differentiator the value of 3.3nF is chosen, resulting in a low-pass filter with cutting frequency depending on the feedback resistor value: $f_c = (2\pi C_f R_d)^{-1} = 4.82 \times 10^7/R_d$. The free parameters R_p and R_d will determine the controller gains K_P and K_D.

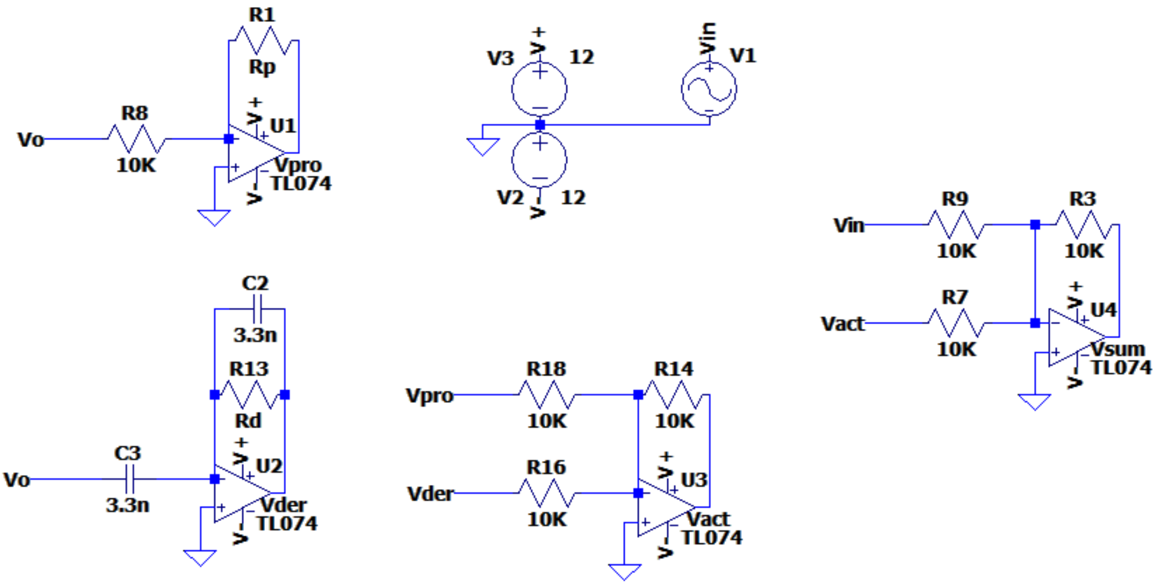

Figure 73 – PD controller implemented on LTSpice.

The signal received by the RLC circuit is given by:

$$V_{sum} = -(V_{in} + V_{act}) \tag{3.10}$$

where:

$$V_{act} = -(V_{pro} + V_{der}) \tag{3.11}$$

The separated actuation voltages are:

$$V_{pro} = -\frac{R_p}{R_{in}} V_o \tag{3.12}$$

and:

$$V_{der} = -C_d R_d \frac{dV_o}{dt} \tag{3.13}$$

So, applying the Laplace transform, the RLC input signal V_{sum} from equation 3.10 as a function of the RLC output signal V_o becomes:

$$V_{sum} = -V_{in} - (K_P + K_D s)V_o \tag{3.14}$$

where $K_P = R_p/R_{in}$, $K_D = C_d R_d$, R_{in} =10kΩ and C_d =3.3nF.

In order to simulate the system's response in the same conditions that resulted in the transient from figure 69, the chosen resistances must match the K_P and K_D calculated through the Ziegler-Nichols tuning method. Their values can be found in table 15. After choosing V_{in} as a negative unit step, once that V_{sum} inverts the input sign, the simulations for each controller are performed and presented in figure 74, using a maximum time step $T_{max} = 5\mu$s and a total simulation time $T_f = 0.25$s in the LTSpice transient solver. These results show that the changes in the dynamics of the system associated to the proportional term are almost equivalent to that presented when simulating through the transfer function, while the derivative term did not attenuate the vibration as much as expected from the previous simulation.

Controller	K_P (10^{-4})	K_D	R_p (kΩ)	R_d (kΩ)
P	8.26	—	82.6	—
D	—	5.75	—	174.2
PD	13.22	5.75	132.2	174.2

Table 15 – Controller parameters implemented in LTSpice.

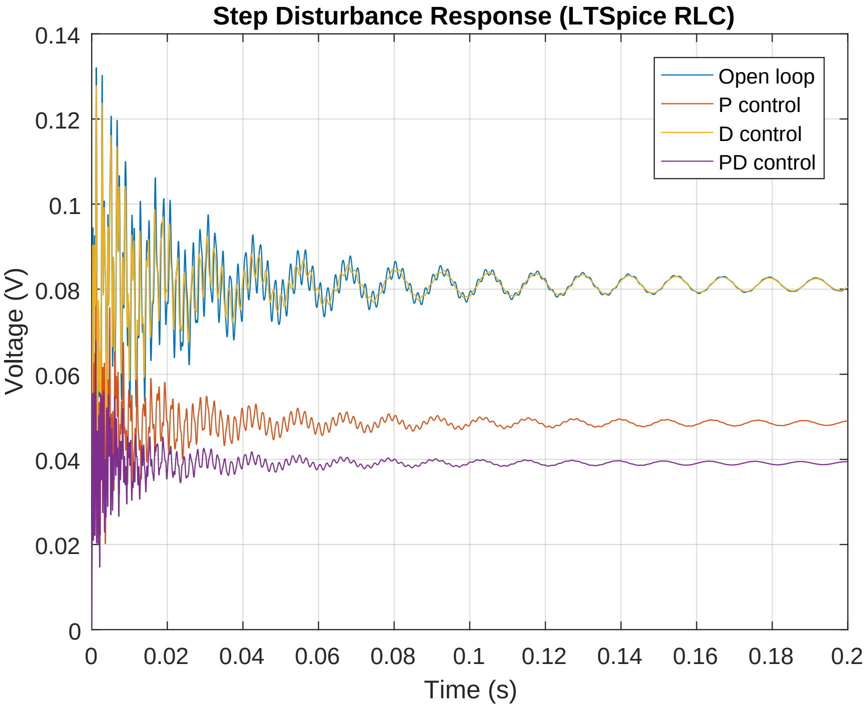

Figure 74 – Output transient response for disturbance step input for different controllers implemented in LTSpice.

A positive point when simulating the control of the RLC equivalent circuits on LTSpice is the fact that it is possible to check the impact of the controller in each parallel RLC, which represent the effects of that controller in each mode of the structure. Figure 75 shows exactly these effects in each mode. From that, it is possible to identify that the derivative controller almost does not impact on the first and fourth modes, however it increases more significantly the damping for the second and third modes. On the other hand, the proportional control reduces the DC gain for every mode and introduces new frequencies to the second, third and fourth equivalent RLC circuits.

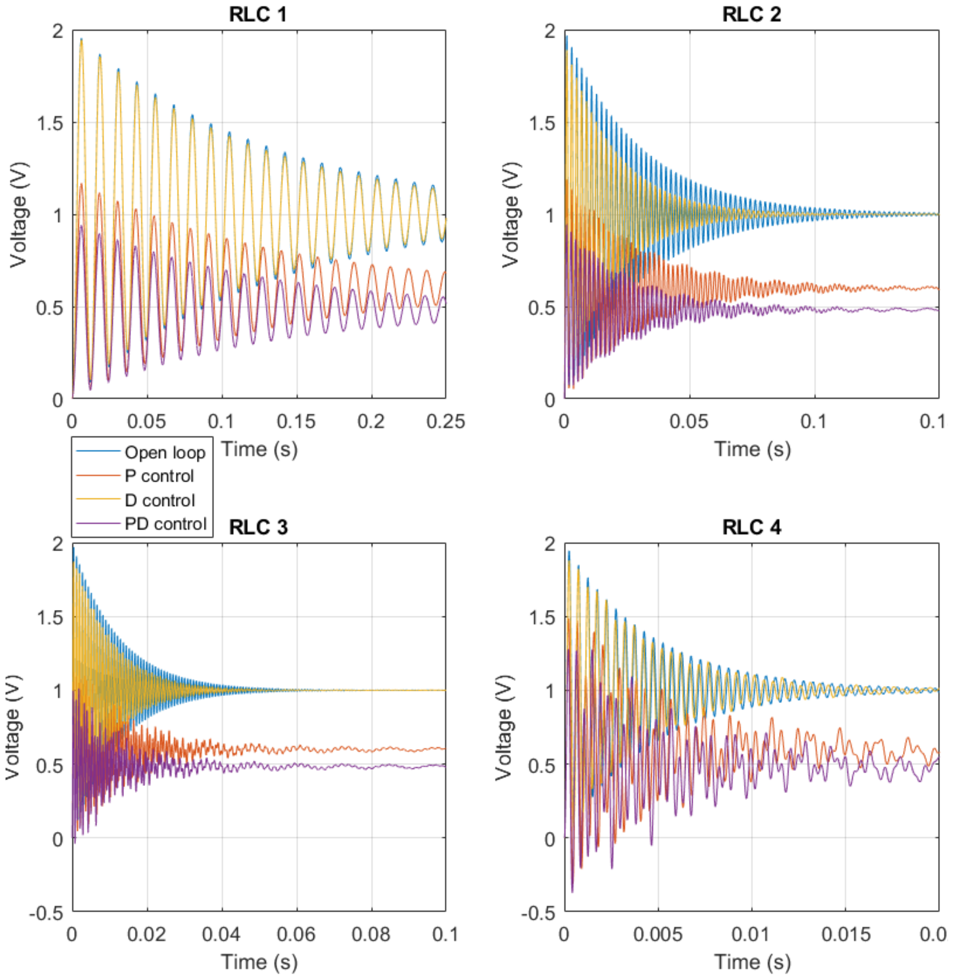

Figure 75 – Decoupled signals for each RLC circuit equivalent to a vibration mode.

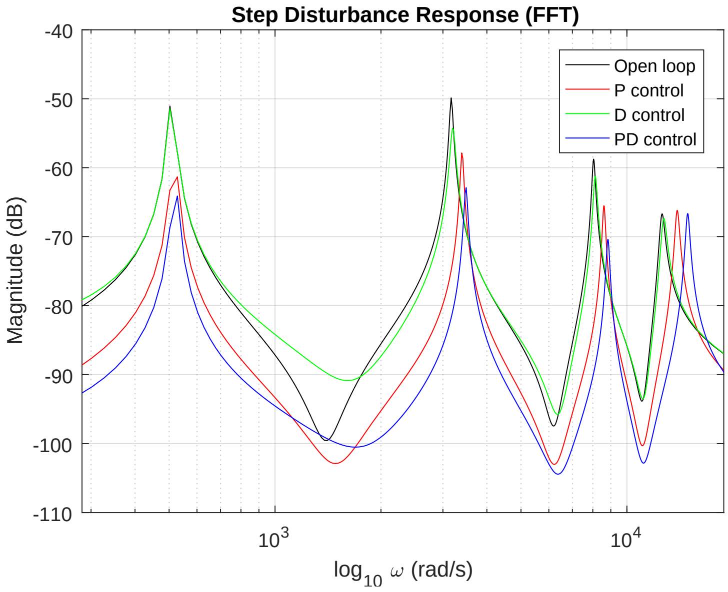

Figure 76 – Fast Fourier transform for the disturbance step with P, D and PD control.

There is still another way of checking the effectiveness of the control in each case, by means of the fast Fourier transform (FFT) of the transient signals. Figure 76 shows the signal composition in the frequency domain, which reiterates the conclusions obtained from the time domain signals.

As already expected, the high gain controller presented in the controller design section of the results chapter destabilizes the electronic system. By tuning the gains on LTSpice, the critical gain $K_u = 36.53$ is obtained with a period of $T_u = 342.4\mu\text{s}$. The new Ziegler-Nichols controllers parameters are presented in table 16. Figure 77 compares the step response results for $G_c(s)$ and $G'_c(s)$ controllers. The derivative parameter had no visible effect on the response, while the new proportional slightly improved damping, but increased the number of oscillations by introducing a higher frequency to the system. Therefore, the new controller reduces the settling time and the DC gain, while increasing the cycles to which the structure is subjected and taking the system closer to instability.

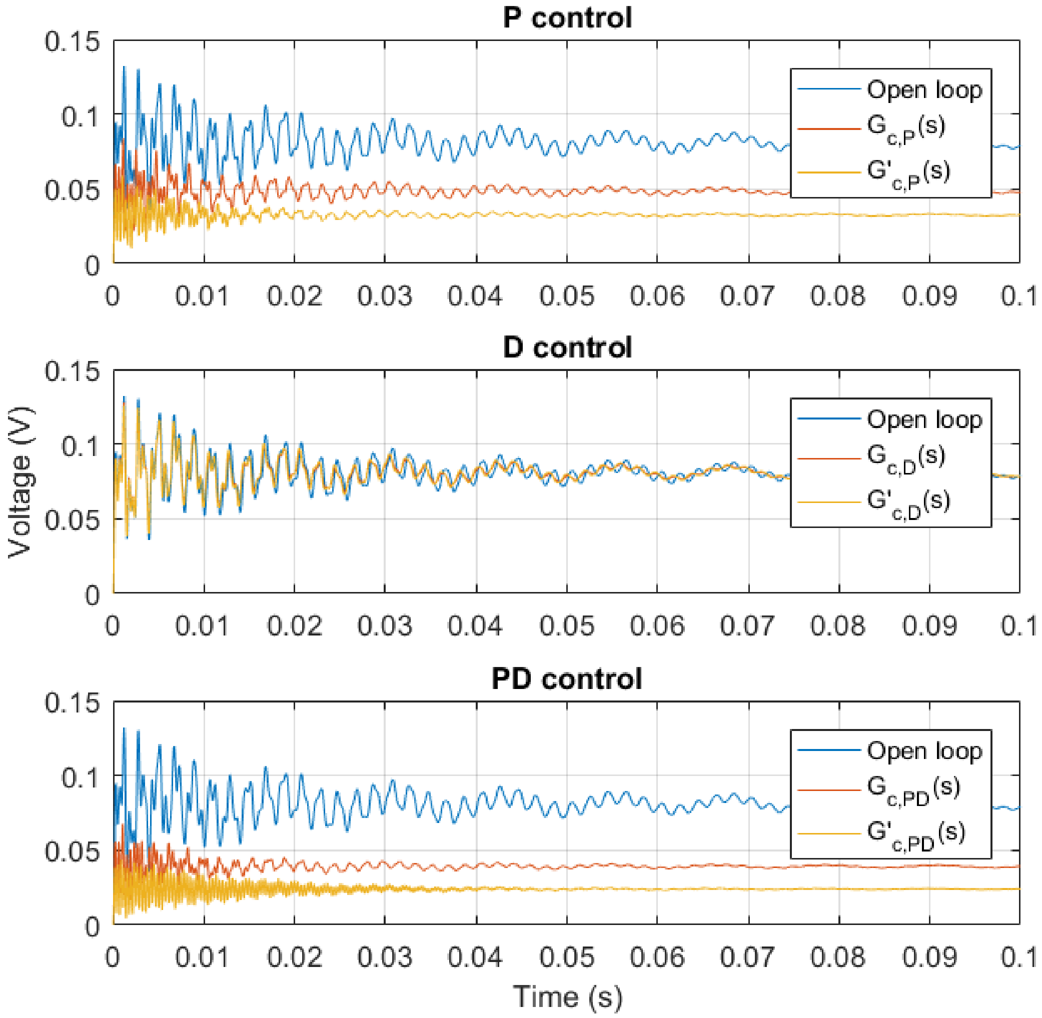

Figure 77 – Disturbance step response comparison between $G_c(s)$ and $G'_c(s)$ controllers implemented in LTSpice.

Controller	K_P	K_D (10^{-3})	R_p (kΩ)	R_d (kΩ)
P	18.27	—	182.7	—
D	—	1.25	—	378.8
PD	29.22	1.25	292.2	378.8

Table 16 – New controller parameters implemented in LTSpice.

The FFT for the new controllers are presented in figure 78. As concluded from the transient signals in the time domain, the derivative term change did not affect much on the damping, while the proportional term increased the damping for the first three modes and reduced for the fourth.

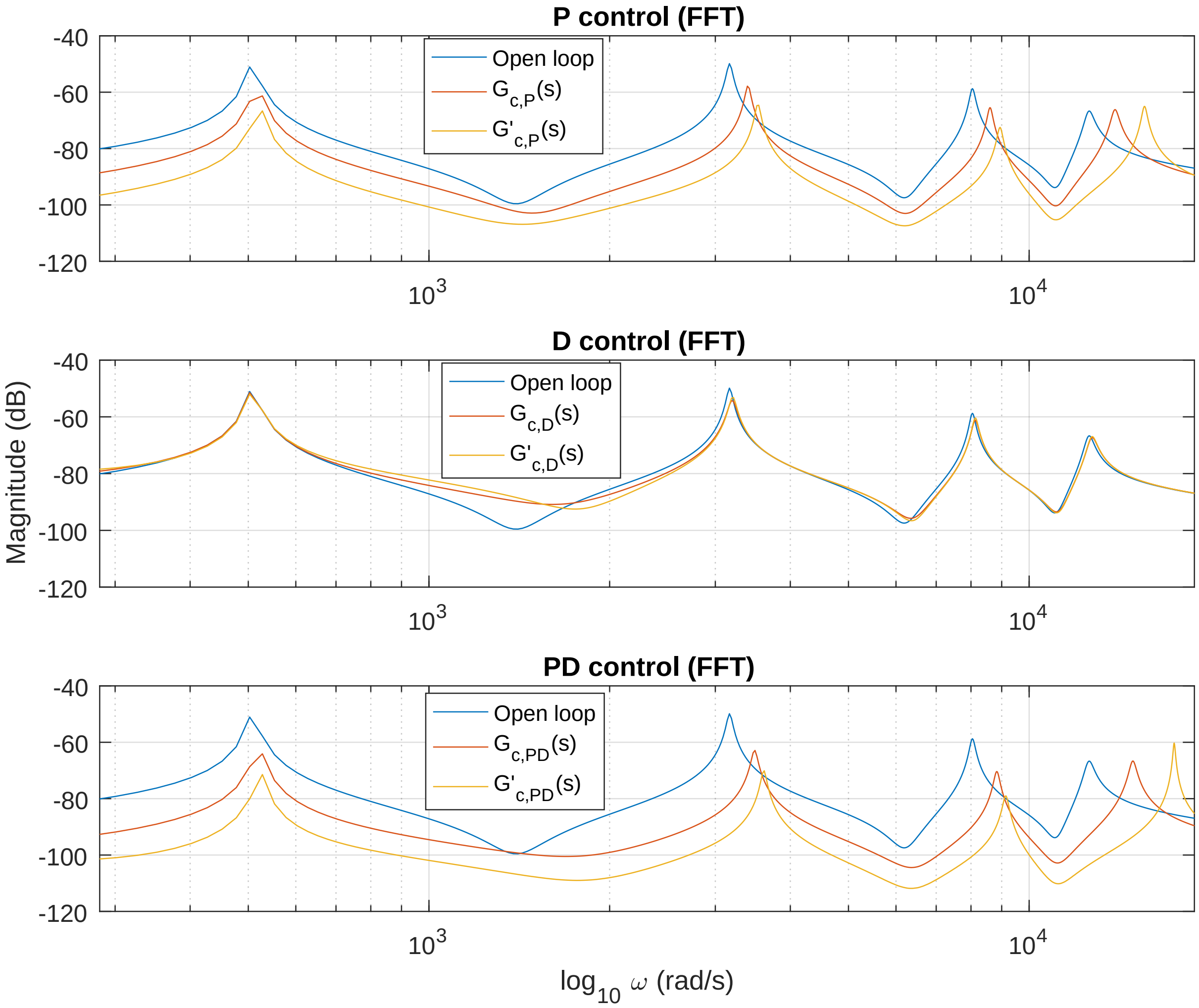

Figure 78 – Fast Fourier transform for the disturbance step control for controllers G_c and G'_c.

3.6.2 Experimental Control

The experimental implementation of the control loop follows the circuits presented along the section that explains the implementation on LTSpice. For supplying power to the active components, two power symmetric supplies with nominal 12VDC/500mA are enough, once that the impedance of the system is high, as shown in the Impedance Analyzer curves previously. The power transferred to the structure is also bounded according to the operational amplifiers characteristics. Taking into account the necessary power to drive the piezoelectric actuator such that relevant loads are applied to the structure, the TL074 integrated circuit from STMicroelectronics, which contains four op-amps in the same package, is a reasonable choice.

Usually, when designing an electronic circuit, one must consider that the common resistors and capacitors found in the market have standard values. An alternative to the common resistors with a fixed resistance value are the potentiometers: variable resistors with a sliding or rotating contact that allow their resistance to be adjusted. Therefore, by replacing the feedback resistor in the amplifier or differentiator circuit by a potentiometer, the freedom for tuning the controllers gains increases drastically.

Two different control experiments will be presented in the following pages: first the harmonic control of the system to sinusoidal inputs and then the transient control for step inputs.

3.6.2.1 Harmonic Control

In this first experiment, the proportional (P) controller is going to be implemented and its gain K_P tuned, starting from zero, with a potentiometer with maximum 50kΩ. Sinusoidal signals with 5V amplitude will be sent from the DAQ board to the Taramp's amplifier, in order to generate harmonic disturbances to the constrained nodes of the structure. The forcing frequencies are in the vicinity of the three known resonances of the system, so it will be possible to check the best gain to control each mode. Positive and negative gains will be tested, once that the phase frequency response of the system is not uniform to all modes, which means that a positive disturbance may excite a frequency in one direction and another in the opposite direction.

The optimal suppression for the first mode was using the inverting amplifier with a feedback resistance $R_f = 17\text{k}\Omega$, which results in $K_{P,1} = -1,7$, given the input resistor $R_{in} = 10\text{k}\Omega$. For the second and third modes, the control signal was inverted twice with the first feedback resistors adjusted to 50kΩ, the second to 44kΩ and both input resistors fixed at 10k$R_{in} = 10\text{k}\Omega$, resulting in $K_{P,2} = K_{P,3}$ =22. From this experiment, the harmonic analysis of the controlled system is performed and the frequency response for each of the three modes is raised and compared to the open loop system on figures 79, 80 and 81.

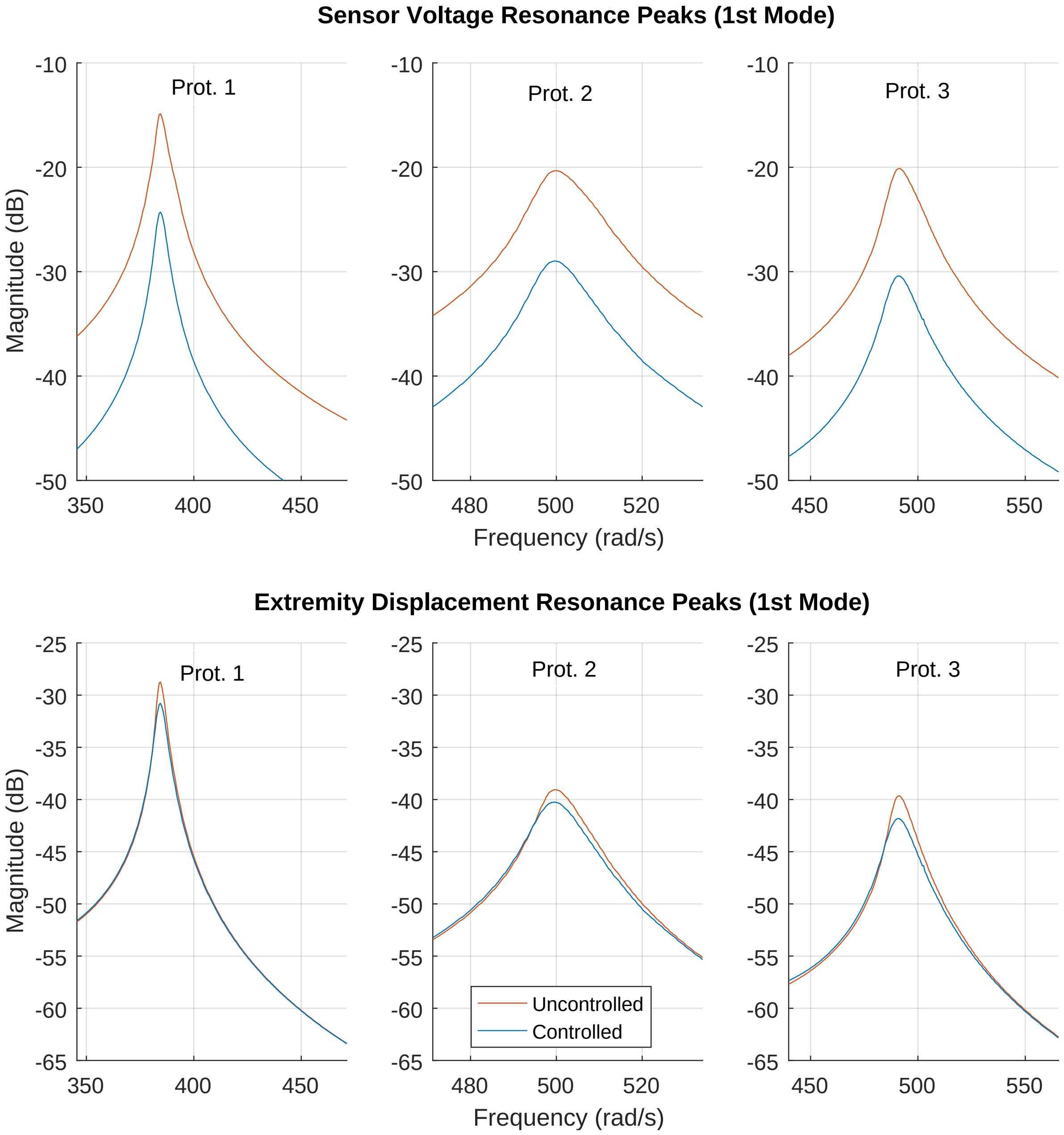

Figure 79 – Resonance peaks damping for the harmonic control of the first mode.

The damping associated to the first mode resonance peak for the uncontrolled system differed considerably between the different prototypes, being the first one with the lowest damping and the second with the highest. When applying the control, slightly changes are observed in the free extremity responses, that become more smooth, but almost no changes in the magnitudes outside the peak. In the other hand, the frequency response curves for the sensor voltage are vertically moved, which implies in changes in the system gain, but not introducing active damping. As the main objective of the controller was to reduce the sensor voltage, which was expected to influence directly in the tip displacement, it is correct to say that it efficiently reduced the amplitudes of the signal under control. However, the influence to the displacement is not significant, which could be foreseen from the modal shapes of the structure obtained previously: the electric stiffness of the system influences from the second bending mode on, once that the first is mostly structural (figures 49, 50 and 51).

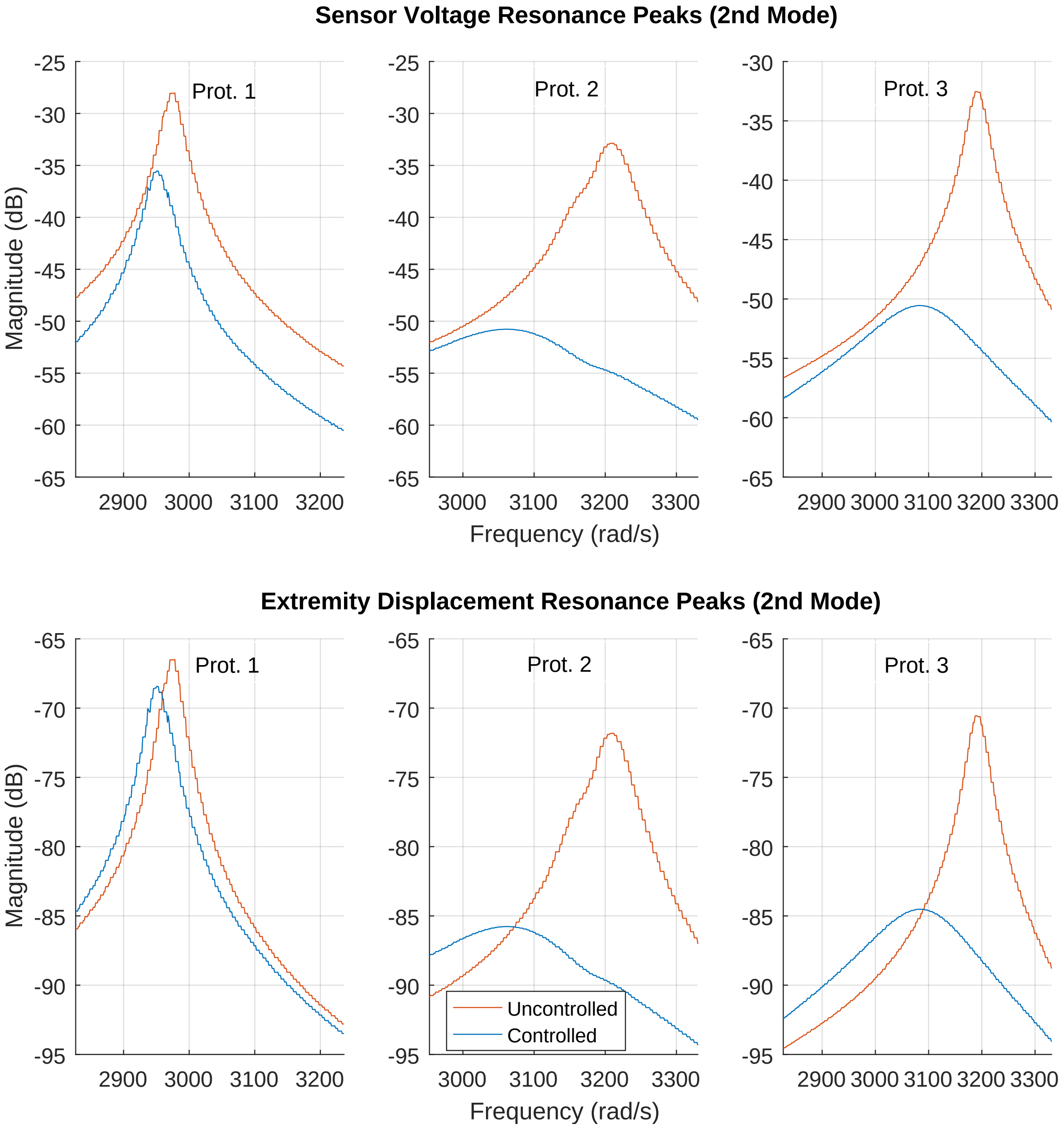

Figure 80 – Resonance peaks damping for the harmonic control of the second mode.

The influences of the sensor voltage control in the extremity displacement for the second and third modes are undoubtedly more clear than in the first mode. Analyzing the second mode active damping injection to the second and third prototypes, the maximum magnitudes were greatly reduced and the the resonance frequencies moved to the left. In terms of damping ratio, the second prototype attenuation was increased in almost 4 times, and the third in almost 6 times both for the voltage and the displacement, as shown in tables 17 and 18. For the first prototypes, the results were not so satisfactory, with an increase of approximately 25% for the sensor and 11% for the extremity. As this was the first prototype to be manufacture, it possibly presents more flaws than the other two. It was already noticed when the resonance frequencies for each prototype were calculated, being the second and third much closer to the numerical results than the first one. For the third mode, the first prototype presents better responses, with about 2 times the initial damping, while the second prototype kept the increase of 4 times and the third multiplied by 3 the open loop damping.

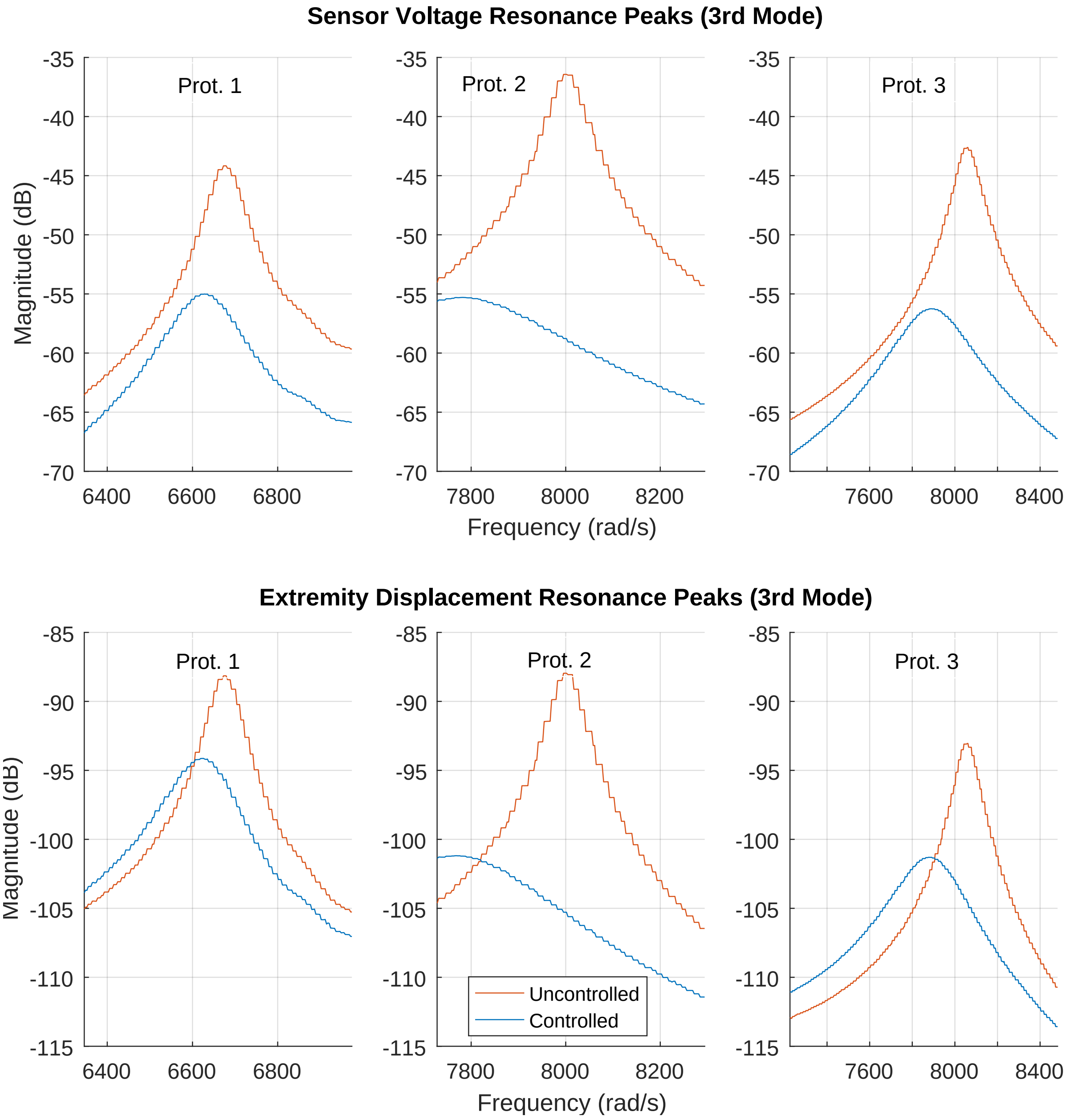

Figure 81 – Resonance peaks damping for the harmonic control of the third mode.

Mode	K_P	Prot.	ζ_i (10^{-3})	f_i (Hz)	$\lvert H\rvert$ (dB)	ζ_i' (10^{-3})	f_i' (Hz)	$\lvert H'\rvert$ (dB)
1	-1.7	1	7.35	61.2	-14.9	7.35	61.2	-24.3
		2	14.5	79.5	-20.3	13.2	79.5	-29.0
		3	14.7	78.2	-20.1	15.3	78.2	-30.4
2	22	1	5.49	474.0	-28.0	6.81	469.6	-35.5
		2	8.61	511.2	-32.9	34.7	487.6	-50.8
		3	5.62	507.3	-32.5	34.6	490.5	-50.6
3	22	1	5.64	1063	-44.2	12.3	1056	-55.0
		2	3.93	1273	-36.4	15.7	1238	-55.3
		3	7.60	1283	-42.6	22.1	1256	-56.3

Table 17 – Harmonic control results for the sensor voltage signal. Comparison between the uncontrolled system parameters (ζ_i, f_i and $|H|$) and the controlled ones (ζ_i', f_i' and $|H'|$).

Mode	K_P	Prot.	ζ_i (10^{-3})	f_i (Hz)	$\lvert H\rvert$ (dB)	ζ_i' (10^{-3})	f_i' (Hz)	$\lvert H'\rvert$ (dB)
1	-1.7	1	5.72	61.2	-28.8	8.17	61.2	-30.8
		2	11.3	79.5	-39.1	12.6	79.5	-40.2
		3	11.5	78.2	-39.6	15.4	78.1	-41.8
2	22	1	6.12	474.0	-66.5	6.81	469.6	-68.4
		2	8.61	511.2	-71.8	35.5	487.6	-85.8
		3	5.62	507.3	-70.6	34.6	490.5	-84.5
3	22	1	6.59	1063	-88.1	11.6	1054	-94.1
		2	3.93	1273	-88.0	14.2	1237	-101.2
		3	7.60	1283	-93.1	22.1	1254	-101.3

Table 18 – Harmonic control results for the extremity displacement signal. Comparison between the uncontrolled system parameters (ζ_i, f_i and $|H|$) and the controlled ones (ζ_i', f_i' and $|H'|$).

3.6.2.2 Transient Control

The second and most important experiment aims the transient control of the structure with the PID type controllers. In order to check the effectiveness of the disturbance rejection of the system, known disturbance inputs must be introduced. The simplest input that makes studying the transient signal possible is a step, because this kind of excitation simply moves the system from the initial rest to a new rest position almost instantaneously. This activates multiple natural modes of the structure and generates a transition signal between the initial position and the new one. And the oscillation of this signal before reaching the steady state is exactly what must be reduced. One problem may be associated to the fact that the step forcing term goes from zero to the final value in a really short time interval, which is called the rise time. If it is too steep, the derivatives of the input seen by the system become discontinuous and uncontrollable modes of the structure that may destabilize the controlled variable are activated.

Before implementing the control loop, the input signal that generates the shaker disturbance is acquired. As a result of the modal shaker dynamics not considered in the project, which are modeled and presented by (MARTINO; HARRI, 2018), the input signal is degraded and the high level voltage that the pulse should keep constant is not maintained. An alternative to circumvent this problem is the introduction of the disturbance signal through the electronic circuit that implements the controller, more specifically as an additional summing term to the amplifier that generates the effort signal to the actuator. This action is the same that was taken to produce the disturbance signal in LTSpice, which used the U_4 op-amp from figure 73 to sum the input to the actuation signal. An additional problem associated to the inputs that could be diagnosed during these initial tests was the presence of noise with predominantly 60 Hz coming from the electrical network to which the system was connected. For this reason, these experiments are all performed during the times of the day when the minimum number of electrical equipment is connected to the network.

Proportional (P), derivative (D) and hybrid (PD) controllers are applied for the purpose of controlling the transient response of the system. The gains for each parameter were initially set to zero, so it could be possible to obtain the uncontrolled response taking the passive electronics component in the system into account as well. Then the gains were increased gradually, again with potentiometers, and the data for each prototype was collected until the values were high enough to make the system unstable. In total, 82 performed experiments are considered, where the time domain signals for the free extremity velocity, and the sensor and actuator voltages are acquired for an step disturbance of 8V to the actuator. The most attenuated signals for each controller and prototype are compared to the uncontrolled system in figures 82, 83 and 84. The parameters associated to each controlled signal from the figures are presented in table 19.

Prot.	Controller	K_P	K_D (10^{-4})	R_p (kΩ)	R_d (kΩ)	C_d (nF)
1	P	2	—	20	—	—
	D	—	6.6	—	100	6.6
	PD	1	6.6	10	100	6.6
2	P	3	—	30	—	—
	D	—	3.3	—	100	3.3
	PD	1	6.6	10	100	6.6
3	P	1.5	—	15	—	—
	D	—	3.3	—	100	3.3
	PD	1	6.6	10	100	6.6

Table 19 – Controller parameters with best results for each prototype.

It is not possible to reach the proportional and derivative gains that are tuned from the Ziegler-Nichols methods because the ultimate gain K_u associated to the real system is significantly lower than the ones obtained from the estimated transfer function

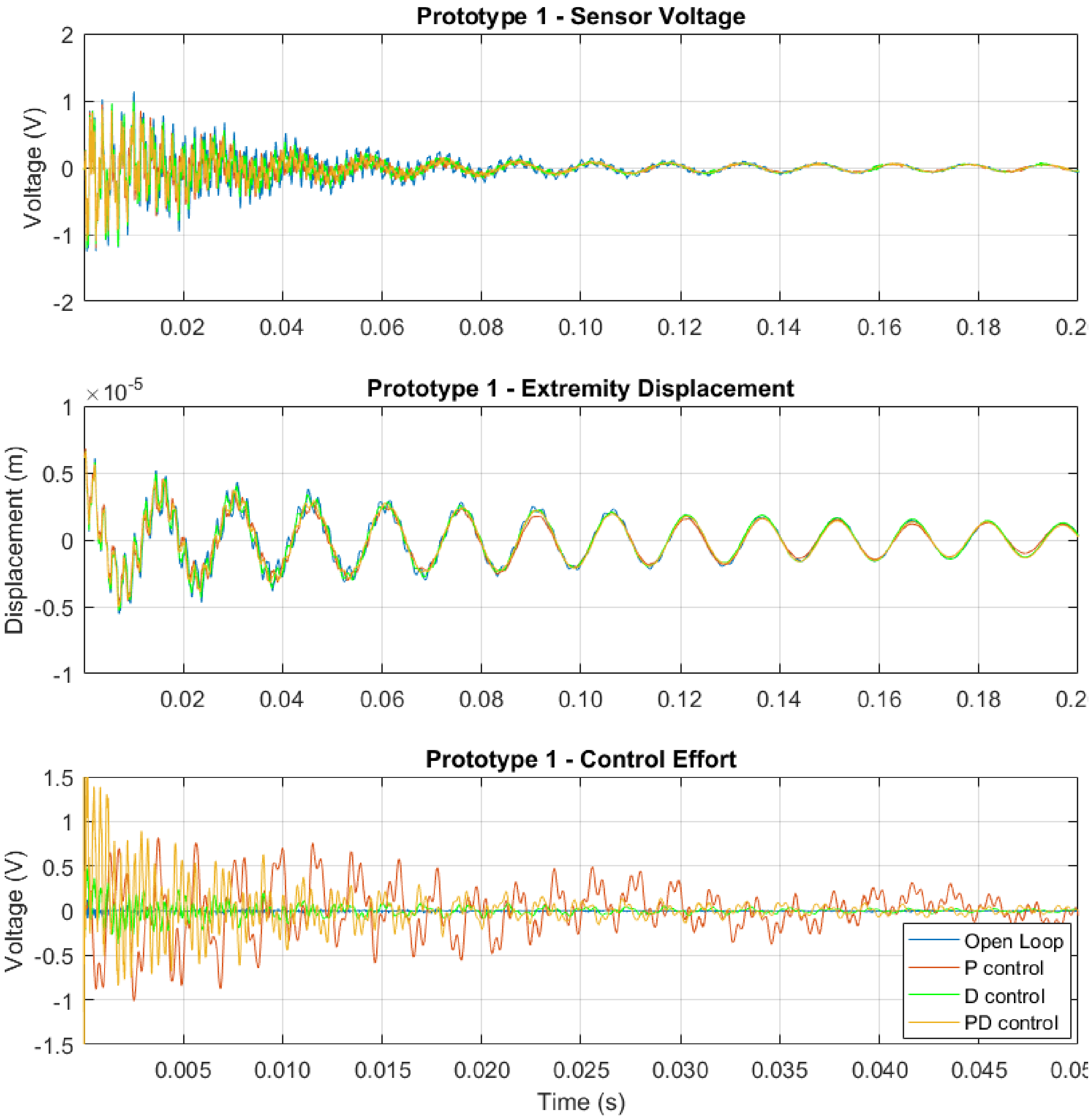

Figure 82 – Prototype 1: sensor voltage, tip displacement and control effort for open loop system and closed loop systems with P, D and PD control.

and from the equivalent circuits in the Controller Design and LTSpice Control sections, respectively. Prototypes 1 and 3 reached the marginal stability for $K_P = 2.5$, while prototype 2 remained stable until $K_P = 4$. These differences may be associated to more than a single inconsiderate effect. Among them, is the fact that higher frequencies that are strongly excited from noise coming from the electronic circuit are not modeled in the estimations. In addition, an ideal derivative controller is unrealizable, because when a zero is added to a causal system, a pole is also introduced, which is also ignored in the modelling stage for not being dominant. One last fact that is not considered is the shaker coil circuit, which interacts to the system when electromotive forces are induced from the base movements.

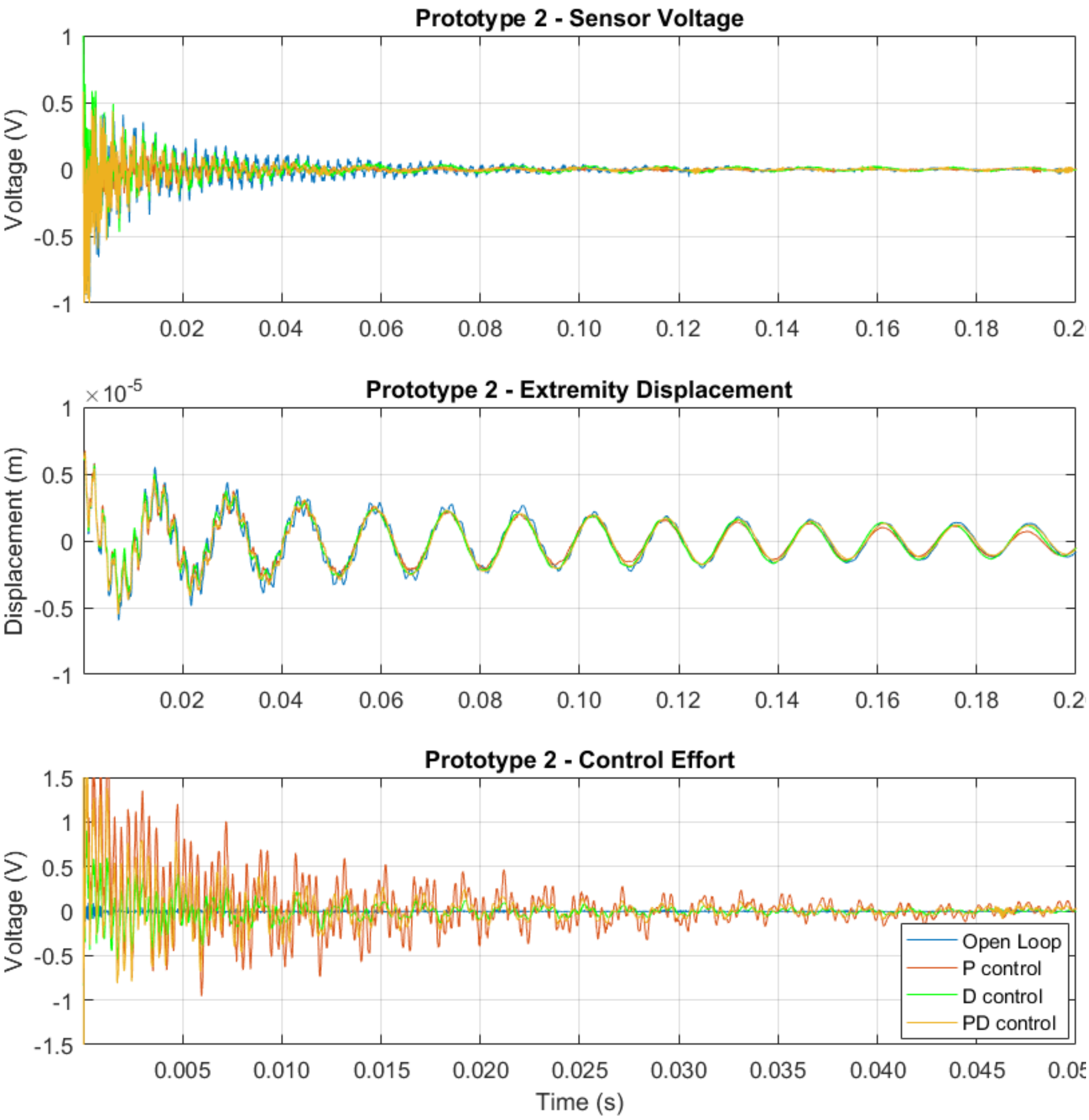

Figure 83 – Prototype 2: sensor voltage, tip displacement and control effort for open loop system and closed loop systems with P, D and PD control.

As the sensor voltage is the control variable of the system, it is easier to observe the vibration suppression directly to this signal. Besides that, the voltage amplitudes associated to the second and third modes are higher than the one on the first mode, while for the extremity displacement signal, the first mode is a lot more significant. In the previous experiments, it is shown that the positive gain controllers are not able to control the lowest resonance frequency of the structure, due to two main reasons: the phase response associated to this frequency and the fact that this vibration mode suffers almost no direct influence from the voltages in the actuator. However, the first mode is still activated when a step is introduced as disturbance due to the superposition of modes that are contained in this kind of signal and to the tendency of the purely mechanical system to oscillate in this frequency.

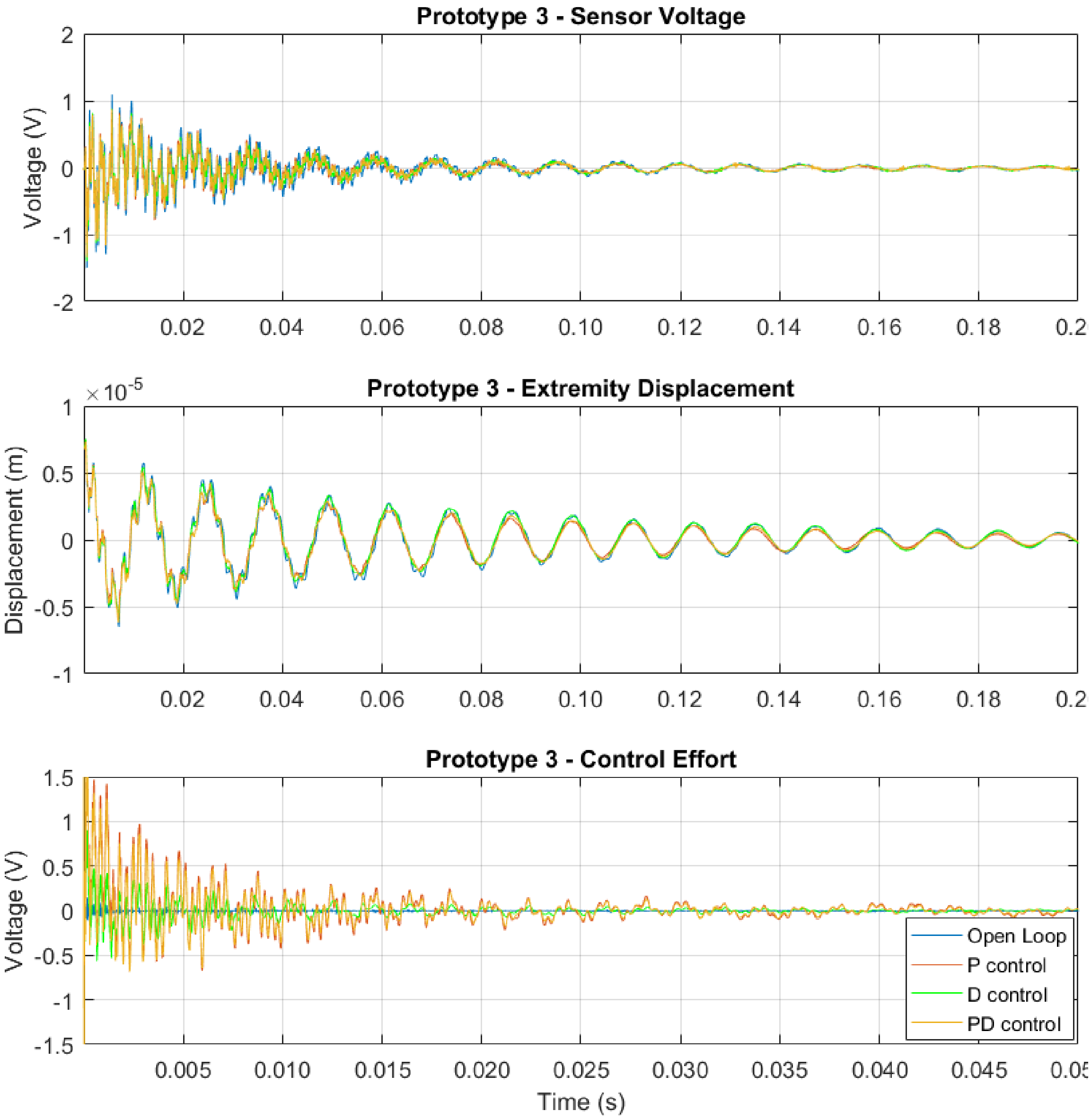

Figure 84 – Prototype 3: sensor voltage, tip displacement and control effort for open loop system and closed loop systems with P, D and PD control.

The inefficiency in controlling the low frequency mode is easily noticed from the transient response signals in the closed loop systems, which makes the higher frequencies control difficult to visualize. In order to clarify the efficiency for the second and third modes, a sixth order high pass IIR filter with bandpass frequency of 200 Hz is applied to the displacement signals and the filtered results are presented in figure 85. In real applications, this low frequency rejection can be generated from passive control: electrically, using passive electrical components or mechanically, applying materials that absorb vibration to the structure, as viscoelastic materials, for instance. These new transient displacements verify the successful control of the two next modes.

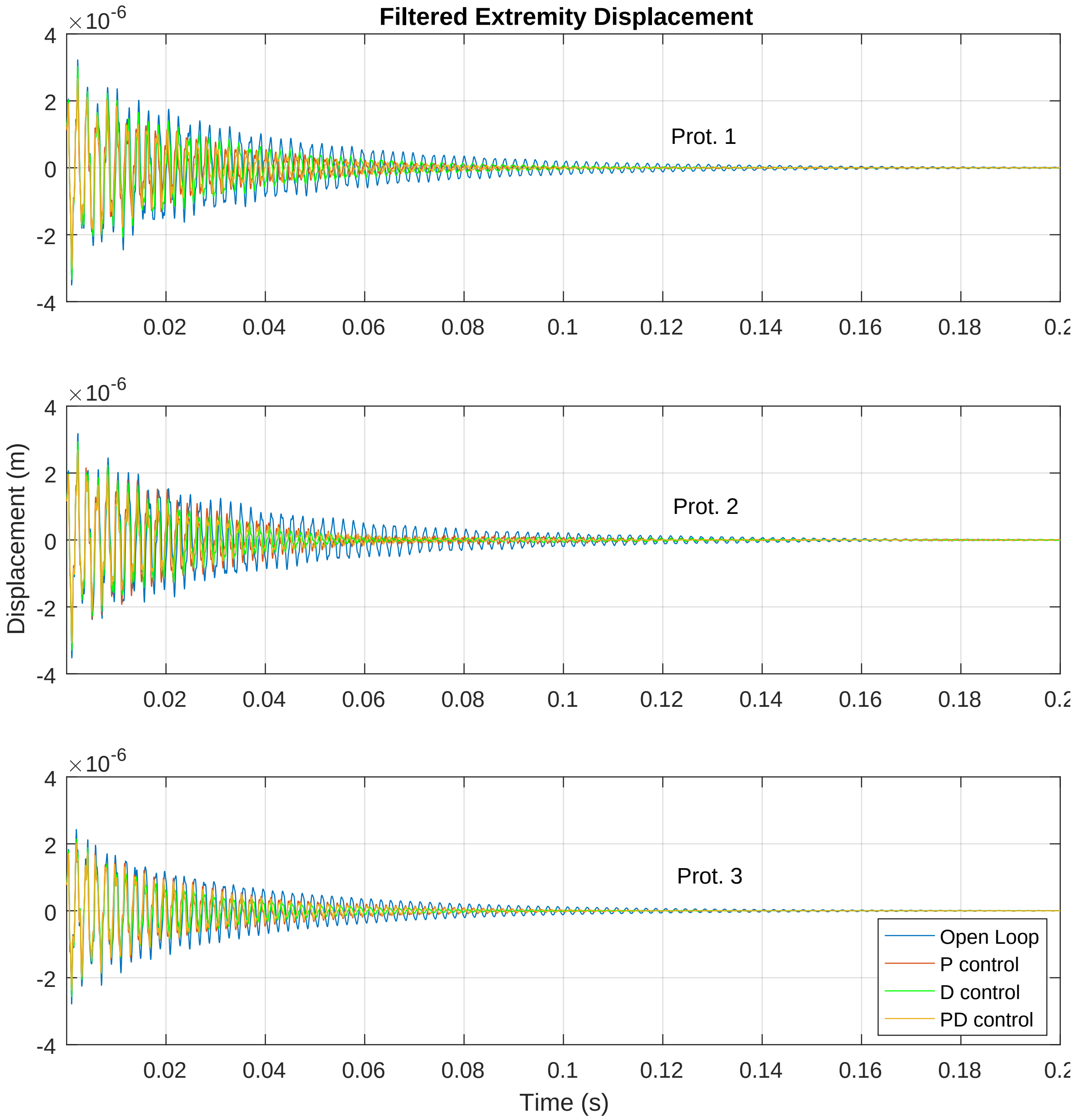

Figure 85 – Filtered tip displacement signals for the three prototypes.

Another way of verifying and, principally, quantifying the active damping introduced to the system for each type of control, is by means of the FFT of the signal. From these diagrams, the quality factor Q of the signal is estimated through equation 2.64 and, consequently, the damping ratio ζ evaluation becomes possible. The FFT of each controlled signal presented for the transient experiments are shown in figures 86, 87 and 88. The resonance peaks amplitudes, frequencies and estimated damping ratios for each case presented are presented in tables 20 and 21.

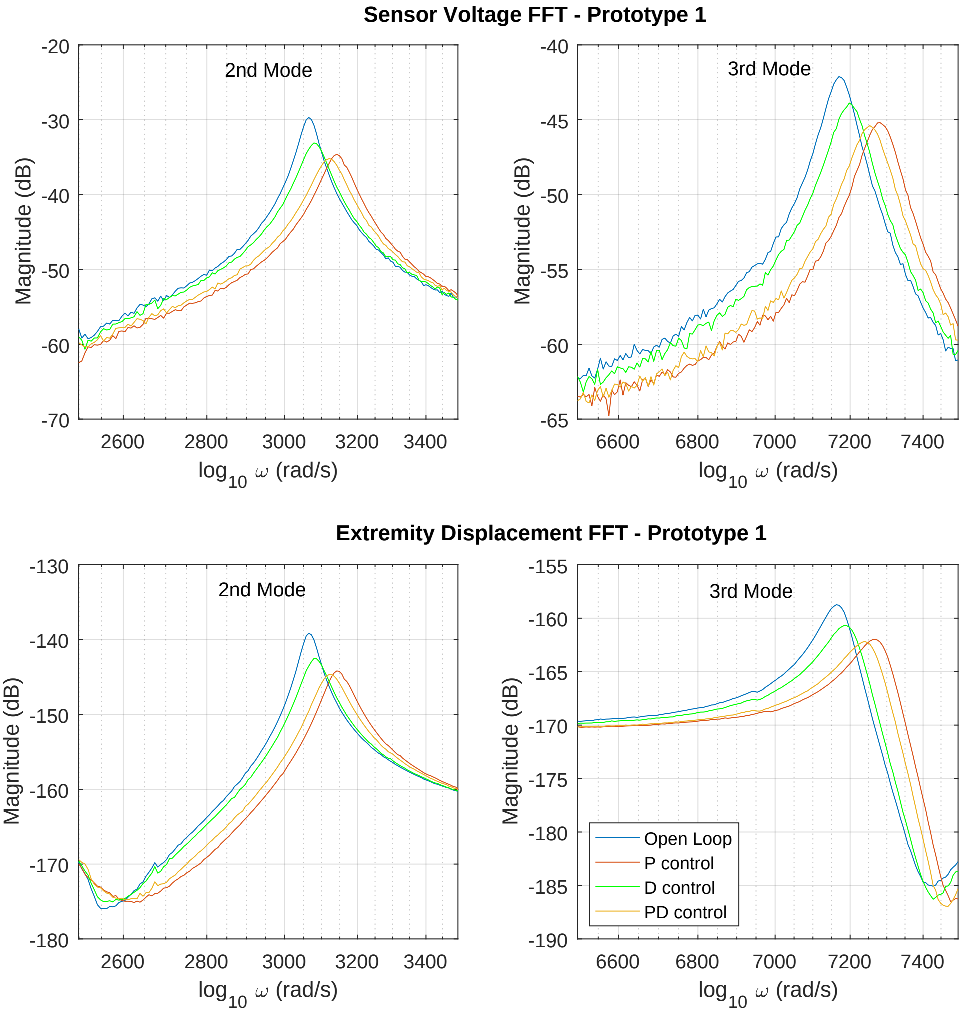

Figure 86 – Prototype 1: FFT for the second and third resonance peaks in the sensor voltage and extremity displacement signals.

Prot.	**Type**	**2nd Mode**			**3rd Mode**		
		$\|H\|$ (dB)	ζ (10^{-3})	f (Hz)	$\|H\|$ (dB)	ζ (10^{-3})	f (Hz)
1	Open loop	-29.9	9.11	487.8	-42.0	6.33	1141
	P	-34.9	13.3	500.0	-45.0	7.67	1159
	D	-33.3	11.3	490.0	-43.8	7.76	1146
	PD	-35.4	13.4	496.7	-45.2	8.18	1154
2	Open loop	-39.9	8.01	485.5	-51.1	10.1	1151
	P	-50.2	20.3	492.2	-57.2	10.0	1164
	D	-45.0	19.1	493.3	-52.7	12.0	1162
	PD	-46.2	15.8	492.2	-53.7	13.3	1167
3	Open loop	-32.3	9.87	506.7	-44.8	9.40	1300
	P	-36.0	11.9	513.3	-47.4	10.5	1327
	D	-37.1	15.3	508.9	-48.6	13.1	1314
	PD	-36.8	14.1	513.3	-48.0	11.8	1323

Table 20 – Peak magnitude $|H|$, damping ratio ζ and frequency f for the second and third resonance of the sensor voltage signal.

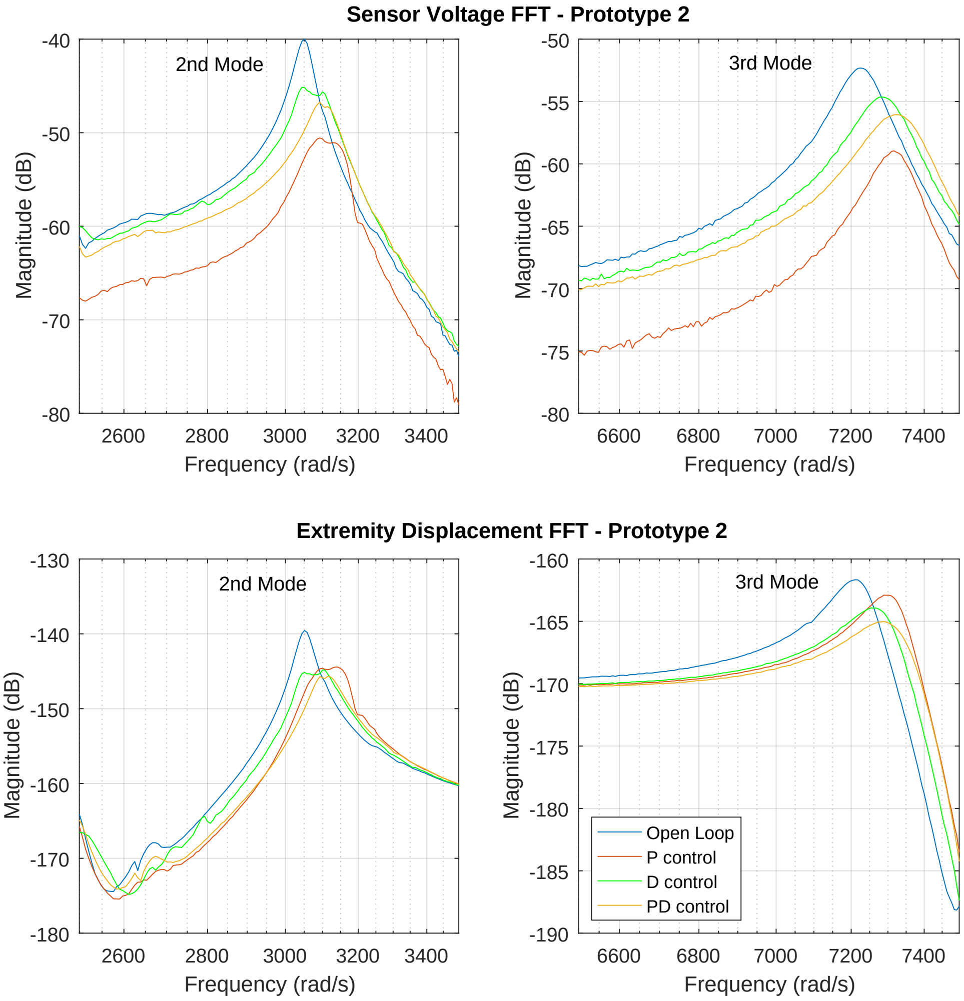

Figure 87 – Prototype 2: FFT for the second and third resonance peaks in the sensor voltage and extremity displacement signals.

Prot.	**Type**	**2nd Mode**			**3rd Mode**		
		$\lvert H\rvert$ (dB)	ζ (10^{-3})	f (Hz)	$\lvert H\rvert$ (dB)	ζ (10^{-3})	f (Hz)
1	Open loop	-139.4	7.97	487.8	-158.7	6.82	1140
	P	-144.4	13.3	500.0	-161.9	9.13	1157
	D	-142.7	12.5	490.0	-160.6	8.75	1143
	PD	-144.9	14.5	496.7	-162.1	9.64	1152
2	Open loop	-139.8	8.01	485.5	-161.6	11.1	1148
	P	-144.7	20.0	500.0	-162.8	12.4	1162
	D	-145.0	20.3	493.3	-163.8	14.9	1157
	PD	-145.9	15.7	495.6	-164.9	18.7	1160
3	Open loop	-142.0	8.77	506.7	-162.8	12.0	1297
	P	-145.6	11.9	514.4	-165.4	16.0	1320
	D	-146.6	15.3	508.9	-166.6	24.7	1307
	PD	-146.4	14.1	513.3	-166.0	18.1	1318

Table 21 – Peak magnitude $|H|$, damping ratio ζ and frequency f for the second and third resonance of the free extremity displacement.

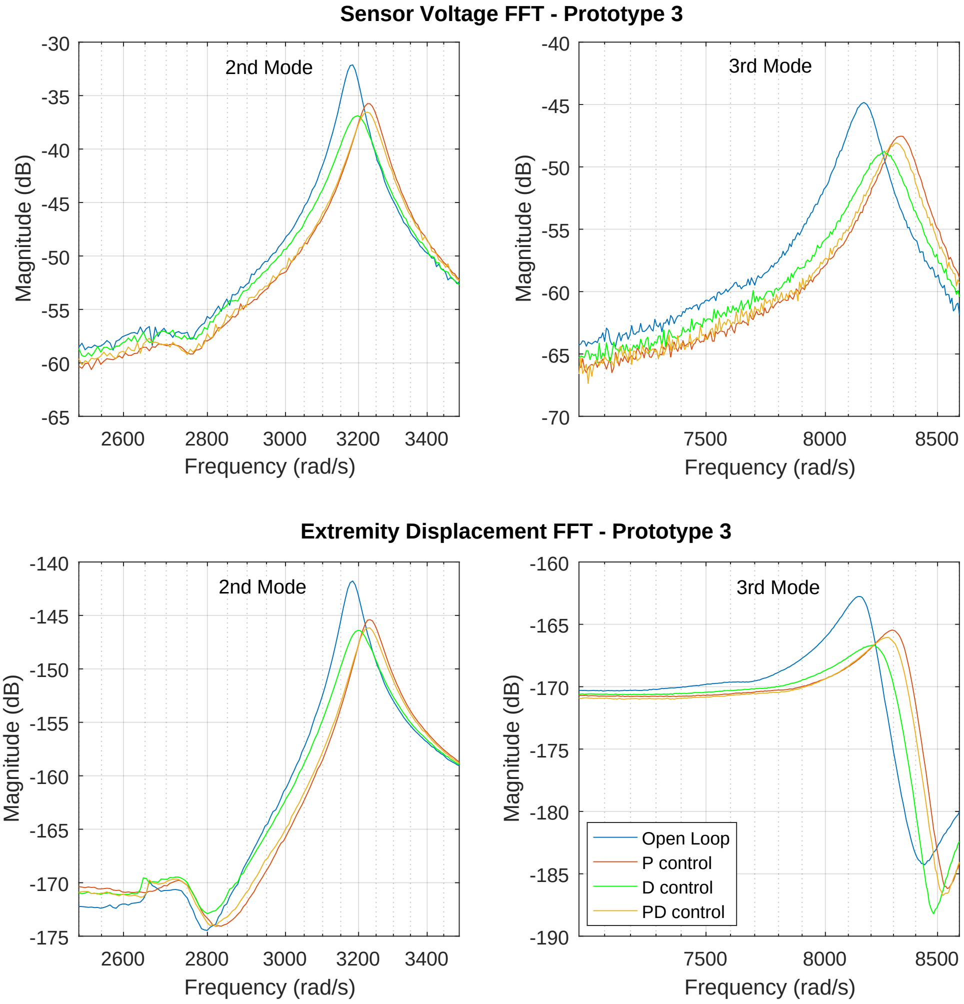

Figure 88 – Prototype 3: FFT for the second and third resonance peaks in the sensor voltage and extremity displacement signals.

Both modes are considerably damped when the control loop is closed, being the second mode more affected than the third. This difference in the results are related to the fact that the second modal shape (figure 50) is similar to the static deformation when the structure is under action of a static voltage in one of the piezoceramics (figure 52). It means that the load distribution, which is used as the actuator gain for the numerical model, can effectively compensate the second mode deformation. In order to obtain better results for the third modal shape (figure 51), two actuators would be required with inverted voltage signals and in specific locations, in a way that their resultant deformation would get closer to the third modal shape of the structure.

From the time domain transient signals, it is possible to obtain additional information that may be used quality metrics for the control. Two of them are the settling time t_s and the mean square error (MSE). The settling time is defined as the time taken by the measured variable to reach the equilibrium value within a predetermined deviation. The mean square error, which was already used to verify the estimation error for the reduced order model, is given by the mean squared difference between the variable value at a given instant and the equilibrium value. These two quantities are presented for each transient control experiment in table 22. For the sensor voltage the deviation limit to calculated the settling time is 70mV and for the filtered tip displacement it is 0.3μm.

Prot.	**Type**	**Sensor Voltage**		**Tip Displacement (filt)**	
		t_s (ms)	MSE (10^{-4} V^2)	t_s (ms)	MSE (10^{-12} m^2)
1	Open loop	171	94.3	174	7.03
	P	141	57.9	122	3.47
	D	156	69.5	120	4.61
	PD	141	56.4	104	3.40
2	Open loop	55.5	15.1	169	6.43
	P	33.2	5.89	133	4.34
	D	79.8	78.6	139	3.96
	PD	33.2	11.2	93.4	3.09
3	Open loop	127	71.7	148	4.28
	P	114	51.5	107	2.57
	D	114	50.4	86.7	2.43
	PD	114	49.7	100	2.38

Table 22 – Time domain quality metrics for each transient control experiment.

From the time domain metrics it is possible to choose the best control method according to the project requirements to which it is going to be implemented. In most of the experiments, a pure proportional or pure controller reduced considerably the amount of time taken to stabilize the second and third modes of the structure, but still a PD combined presented overall better results. The PD better performance can be attributed to the fact that it combines the error compensation performed by the proportional parameter, which acts directly in the present error, and the compensation from the derivative parameter, which acts directly in future errors or, more strictly, in the error variation rate.

3.6.2.3 Shaker Disturbance Control

After the conclusion that the PD controller is the most efficient when closing the loop for the real system, it will be used as an attempt to control the shaker disturbance when a 0.5V step input in sent from the DAQ board to the amplifier and, finally, to the modal shaker. The resulting degraded voltage signal between the shaker terminals is presented by figure 89.

The modal shaker operates according to the induction principle from Faraday's Law, which means that for constant voltages there is no change in the magnetic flux and, therefore, the signal presents a spike in the discontinuity, which starts decreasing until reaching the equilibrium point. The resulting signal resembles a wide impulse and contains a frequency close to 20kHz during the whole interval that is low pass filtered in the figure to improve its visibility.

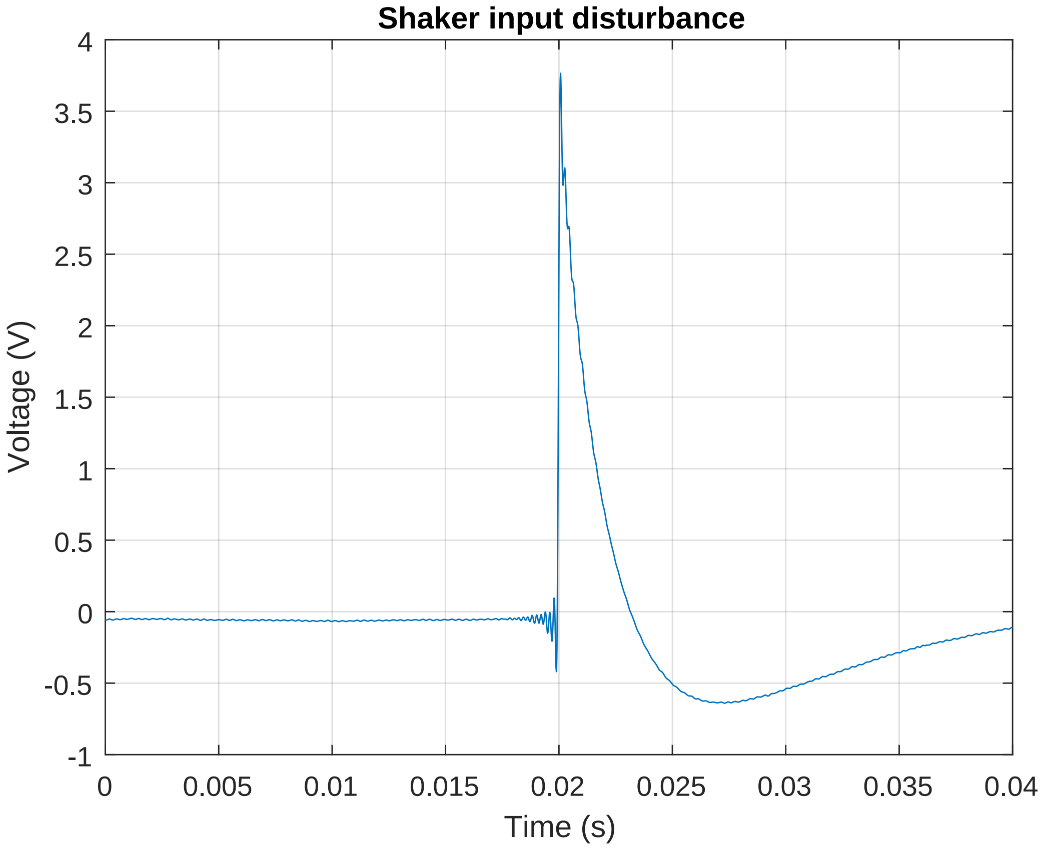

Figure 89 – Resulting filtered voltage signal when a step signal is sent to the modal shaker.

Figure 90 shows, for each prototype, the free tip motion comparison between the open loop and the closed loop system with the PD controller implemented previously. For the three prototypes, the main mode which is activated by the shaker input disturbance is the first. For this reason, the control is inefficient and causes minimal changes to the displacement transient response. Through the application of the FFT to the output signals, it is possible to evaluated the maximum magnitude for the first natural peak of the response. Table 23 presents these values in dB.

Prototype	**1st Peak Magnitude** (dB)	
	Open Loop	Closed Loop (PD)
1	-21.5	-22.1
2	-23.5	-23.9
3	-30.9	-31.4

Table 23 – Shaker disturbance: gain magnitude for the first peak of the transient response FFT in open and closed loop systems.

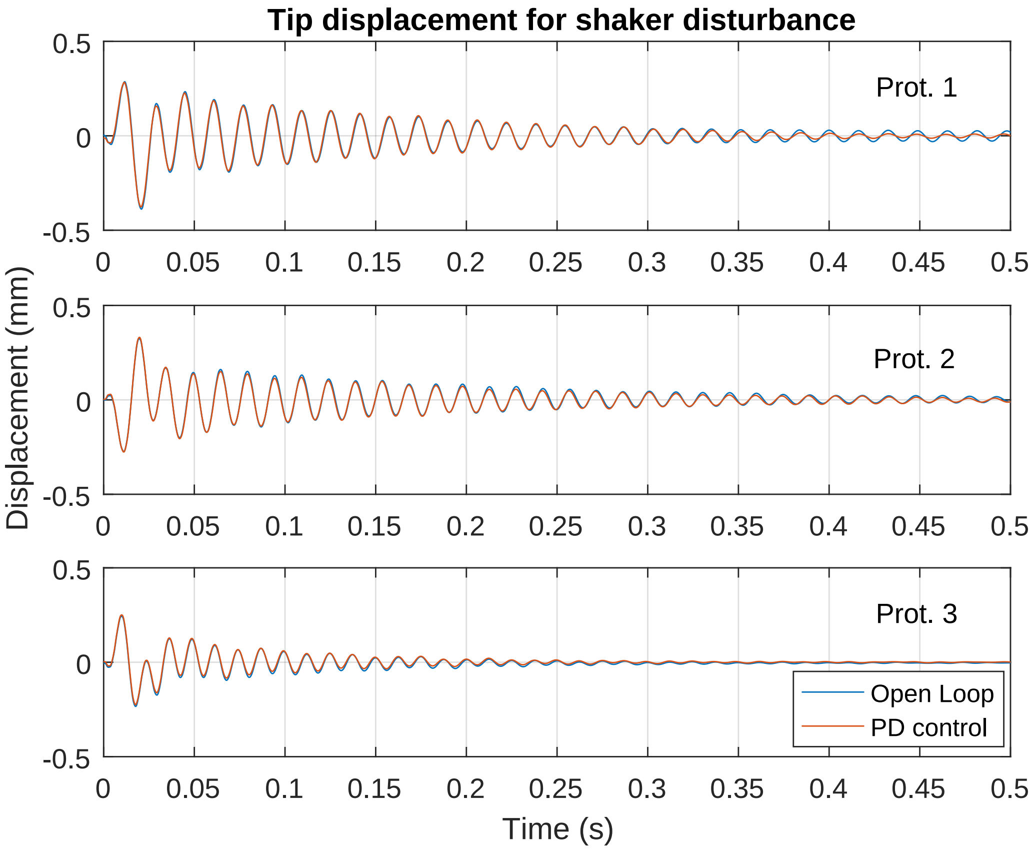

Figure 90 – Free extremity motion comparison between controlled and uncontrolled system for a shaker disturbance.

3.6.3 Numerical Model Control

The numerical dynamic simulations of the system are performed through the HHT-α implicit integration method from equation 2.14. For fine meshes the algorithm implemented in MATLAB is very costly. For this reason, 5 different meshes with distinct discretizations are used to be compared in performed static, modal and simple dynamic analyses in table 24. From these results, the better choice is mesh 4, which gives close results to the more refined mesh 5, while almost 85% less execution time for dynamic simulations.

Mesh	**DOF**	u_e (10^{-7} m)	f_1 (Hz)	f_2 (Hz)	f_3 (Hz)	t_{run} (s)
1	351	-2.76	91.76	500.5	1,589	2.760
2	945	-2.74	97.56	519.6	1,454	14.33
3	1701	-2.69	98.44	525.4	1,440	64.34
4	2835	-2.67	98.60	526.4	1,433	186.8
5	5733	-2.62	98.53	526.5	1,431	1,120

Table 24 – Mesh comparison for: static analysis with 1V applied to the actuator (extremity displacement u_e), modal analysis (frequencies f_i), and step response dynamic analysis for 400 time steps (execution time t_{run}).

In order to simulate the real controller properly, a low pass filter that works like the parallel capacitors in the analog circuit must be introduced. To guarantee that the three first frequencies of the structure will not be affected by the filter, a cutting frequency of 2kHz is used. The transfer function for the first order filter is:

$$G_f(s) = \frac{1}{1 + s/\omega_c} = \frac{4000\pi}{s + 4000\pi} \tag{3.15}$$

The step frequency for the simulations is 50kHz, which translates into a time step T_s =20μs. Converting the filter from continuous to discrete time, using the zero-order-hold (ZOH) method:

$$G_f(z) = \frac{Y_f(z)}{Y(z)} = \frac{0.22}{z - 0.78} \Longrightarrow y_f(k) = 0.22\; y(k-1) + 0.78\; y_f(k-1) \tag{3.16}$$

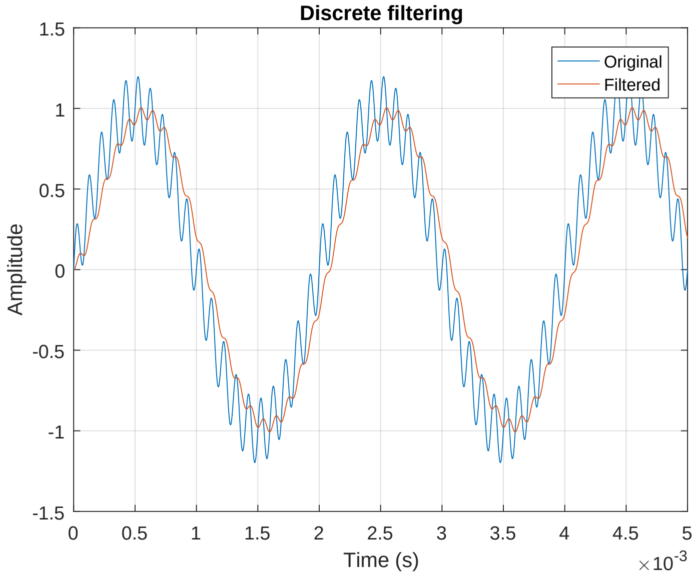

Figure 91 – Signal containing 500Hz and 10kHz frequencies filtered by first order low pass discrete filter.

The difference equation is implemented in the integration loop, so the high frequencies are attenuated, avoiding an instability from the derivative controller. Figure 91 shows the discretized G_f filter applied to a sampled signal containing two frequencies: 500Hz and 10kHz. A higher order could be used to increase the attenuation, but this would introduce more delay to the filtered response, which could take the closed loop system to an unstable state.

The PD control signal is implemented in the iteration loop as a function of the filtered error signal e_f and its derivative, obtained from the finite differences:

$$V_{act}(k) = K_P \; e_f(k-1) + K_D \; \frac{e_f(k-2) - e_f(k-1)}{T_s} \tag{3.17}$$

For pure P or pure D control, one of the gains in equation 3.17 is simply set to zero. The first controllers that are going to be implemented numerically are the P, D and PD designed and adjusted after the implementation in LTSpice (table 16). Their transfer functions are:

$$\begin{aligned} \text{P (design)}: \quad & G_c(s) = 18.27 \\ \text{D (design)}: \quad & G_c(s) = 1.25 \times 10^{-3} s \\ \text{PD (design)}: \quad & G_c(s) = 29.22 + 1.25 \times 10^{-3} s \end{aligned} \tag{3.18}$$

The numerical integration in this case will be performed for unit step disturbance in the actuator, keeping the time step T_s =20μs. The mean duration for each simulation between instants $t_{initial} = 0$ and $t_{final} =$ 200ms, containing 10,000 time steps, was approximately 1h15min. The results for the sensor voltage and free extremity displacement transient responses, as well as the signals filtered by the same high pass IIR filter presented in the previous section (sixth order, bandpass frequency of 200Hz) that eliminate the uncontrollable first mode, are presented in figure 92. The FFT of the signals are also evaluated and presented in figure 93. Last, the frequency domain parameters for the second and third modes, such as resonance peak magnitude, estimated damping ratio and resonance frequency are shown in table 25.

From the plots presented, it is possible to notice that the damping associated to the first mode of the numerical model is lower than the values obtained experimentally. Again, the effects of the unmodeled epoxy resin layer of the prototypes on the system's dynamics are the stiffness reduction and the damping increase. Consequently, the time domain response differences become apparent.

From both the time domain and frequency domain curves, the better performance of the PD controller is highlighted. Like in the experimental implementation, the combination of the present and past errors gives the improved responses for this type of controller. Despite the worse performances, the pure proportional and derivative controllers still managed to introduce significant active damping to the system. Analyzing the damping ratios for the displacement variable, increases of approximately 160%, 50% and 380% are computed in the second resonance for the P, D and PD controllers, respectively. For the third mode, the increases are even higher: close to 550%, 180% and 660%, respectively.

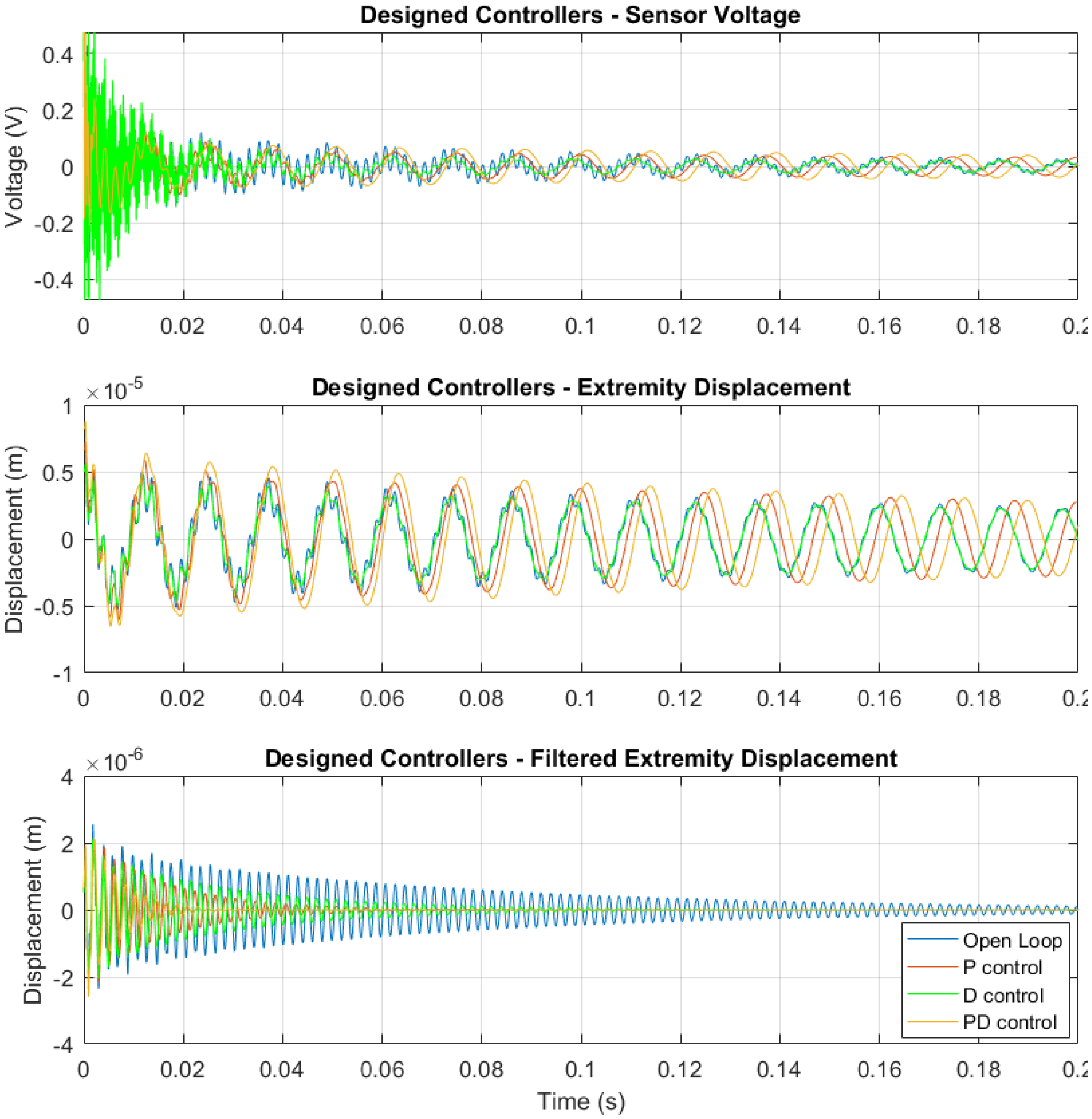

Figure 92 – Numerical implementation of the designed controllers: sensor voltage and tip displacement (original and filtered) for open loop system and closed loop systems with P, D and PD control.

As it is not possible to keep the real system stable with the controllers used in the first wave of simulations, a second wave will be performed for the higher gain controllers that kept the prototypes' oscillation stable during the experimental control section. The gains used for second prototype are chosen, once that this is the model with the higher critical gain, which should result in better performance.

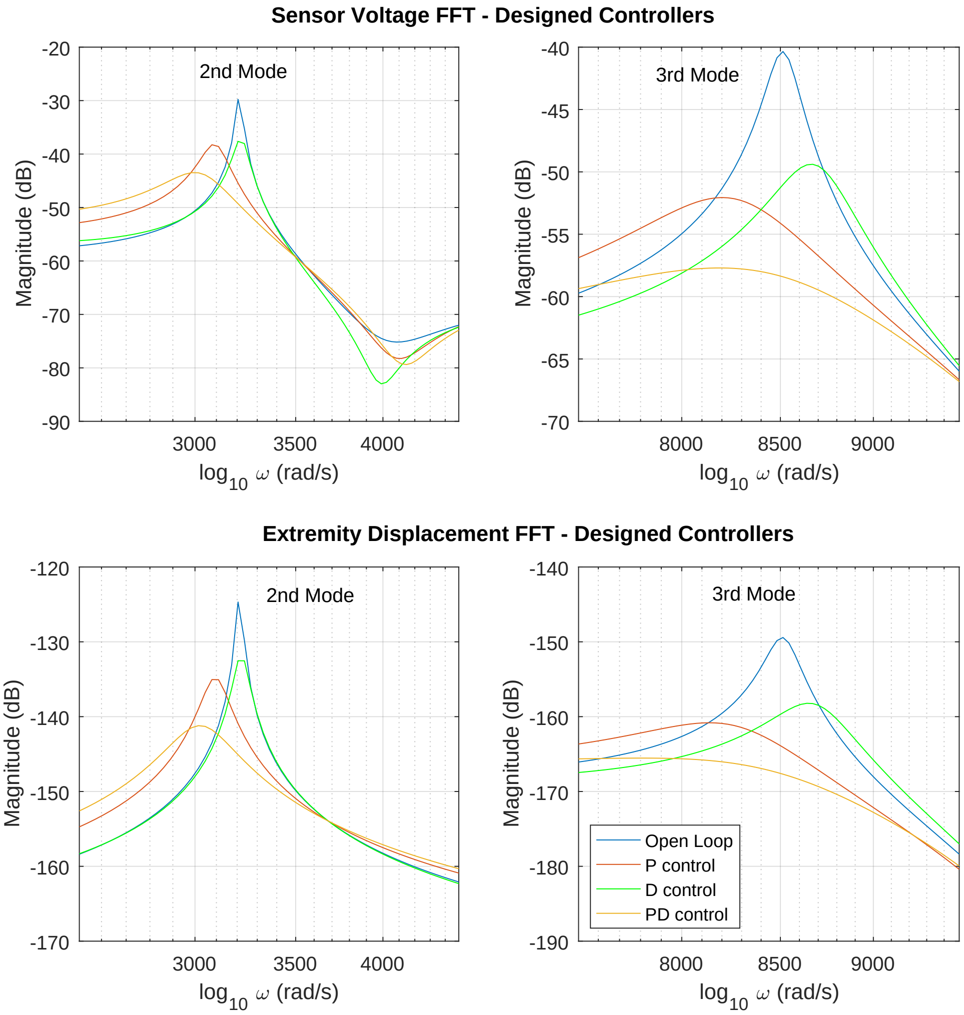

Figure 93 – FFT for the second and third modes using controllers designed in LTSpice.

Signal	**Type**	**2nd Mode**			**3rd Mode**		
		$\lvert H\rvert$ (dB)	ζ (10^{-3})	f (Hz)	$\lvert H\rvert$ (dB)	ζ (10^{-3})	f (Hz)
Sen. Volt.	Open loop	-29.8	9.80	510.0	-40.3	11.1	1,355
	P	-38.3	20.4	490.0	-52.1	51.7	1,305
	D	-37.6	14.7	510.0	-49.4	23.6	1,380
	PD	-43.5	52.6	475.0	-57.7	82.4	1,305
Ext. Disp.	Open loop	-124.7	9.80	510.0	-149.4	9.23	1,355
	P	-135.0	25.5	490.0	-160.8	59.8	1,305
	D	-132.5	14.7	510.0	-158.2	25.5	1,380
	PD	-141.2	46.9	475.0	-165.5	70.3	1,305

Table 25 – Frequency domain quality metrics for the second and third resonance modes for the controllers designed in LTSpice.

The transfer functions for the P, D and PD controllers are:

$$\begin{aligned} \text{P (exper.)}: &\quad G_c(s) = 3 \\ \text{D (exper.)}: &\quad G_c(s) = 3.3 \times 10^{-4}s \\ \text{PD (exper.)}: &\quad G_c(s) = 1 + 6.6 \times 10^{-4}s \end{aligned} \tag{3.19}$$

To make comparisons feasible, the input for the simulations will be the same disturbance used in the experimental applications: a step with amplitude of 8V. Other than that, the system gain will be increased accordingly to the adjustment coefficient $a = 2.37$, estimated from equation 3.3.

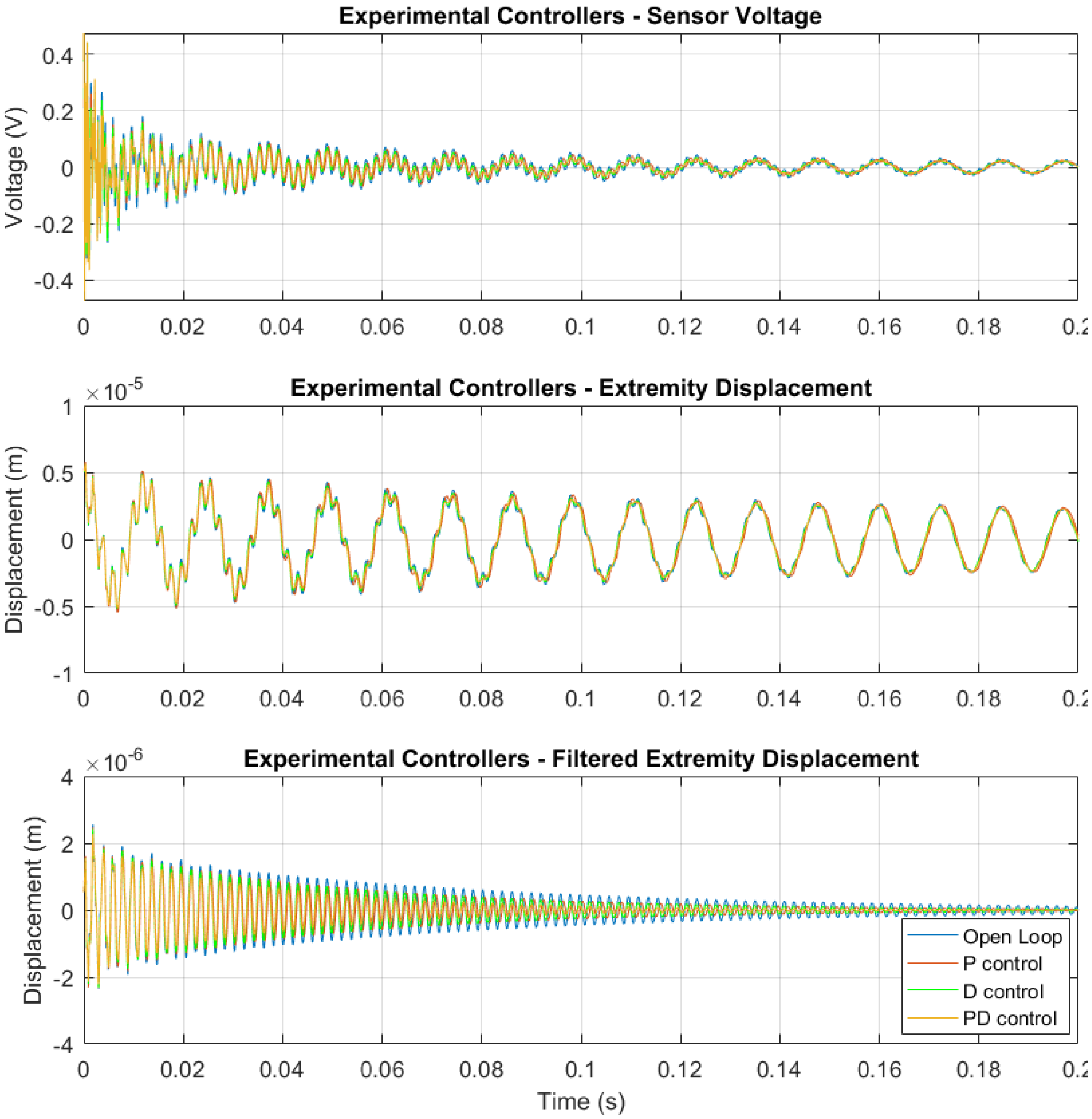

Figure 94 – Numerical implementation of the controllers obtained experimentally: sensor voltage and tip displacement (original and filtered) for open loop system and closed loop systems with P, D and PD control.

The time domain responses are shown in figure 94, the FFT in figure 95 and the frequency domain resonance parameters in table 26.

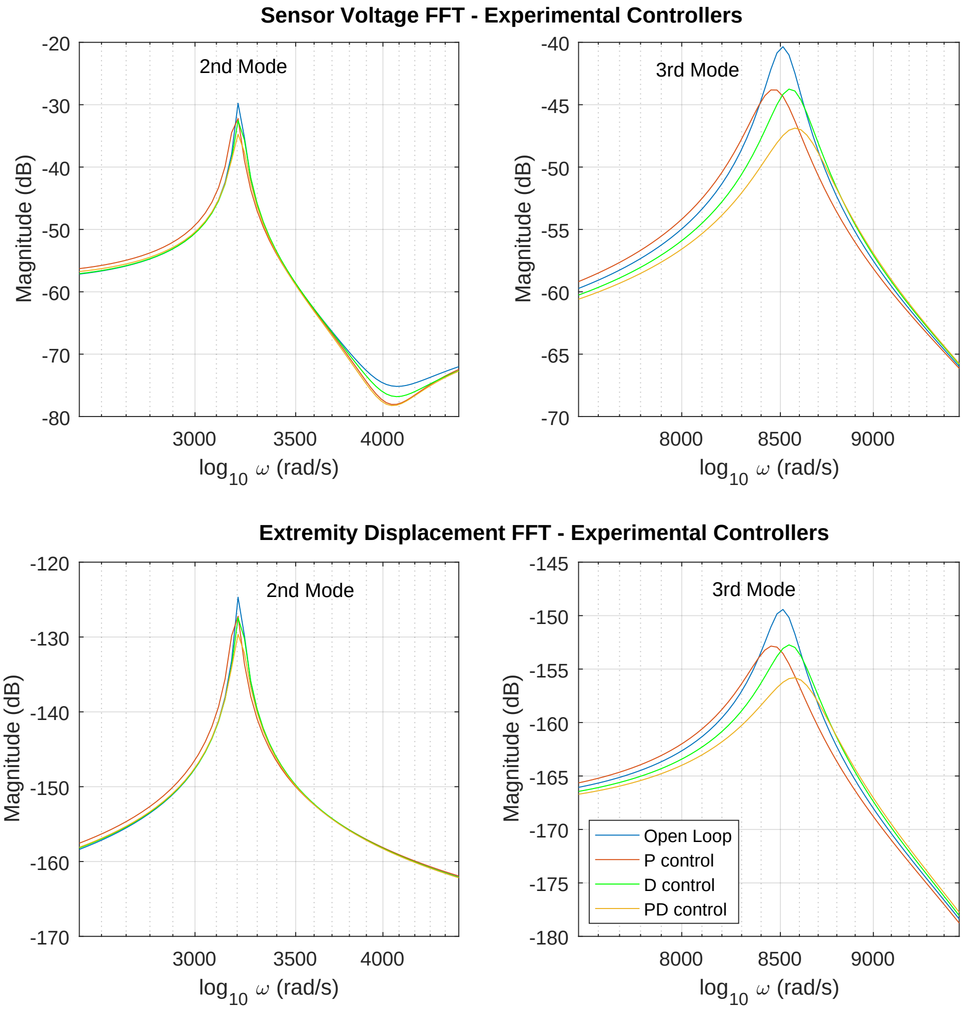

Figure 95 – FFT for the second and third modes using controllers obtained experimentally.

Signal	Type	2nd Mode			3rd Mode		
		$\lvert H\rvert$ (dB)	ζ (10^{-3})	f (Hz)	$\lvert H\rvert$ (dB)	ζ (10^{-3})	f (Hz)
Sen. Volt.	Open loop	-29.8	9.80	510.0	-40.3	11.1	1,355
	P	-32.2	9.80	510.0	-43.8	14.9	1,345
	D	-32.5	9.80	510.0	-43.7	14.7	1,360
	PD	-34.7	9.80	510.0	-46.9	20.1	1,365
Ext. Disp.	Open loop	-124.7	9.80	510.0	-149.4	9.23	1,355
	P	-127.2	9.80	510.0	-152.8	14.9	1,345
	D	-127.4	9.80	510.0	-152.7	14.7	1,360
	PD	-129.6	9.80	510.0	-155.8	20.1	1,365

Table 26 – Frequency domain quality metrics for the second and third resonance modes for the controllers obtained experimentally.

Given that the numerical model can handle more gain than the real system, one may expect that the control performance is worse using the experimentally obtained controller gains than using the gains optimized through LTSpice. It is confirmed by confronting the results between the two waves of simulation. A fact that becomes visible by comparing the estimated damping ratios from the new frequency domain curves is the constant values for the second mode. It is a result of the low time resolution used for the integration, once that the frequency resolution from the FFT curves is low and it is directly proportional to the number of samples of the signal. The zero padding technique could be used with the objective of improving this resolution. Unfortunately, for these signals, the introduction of ripple to the signal leads to worse results than the one presented. For the second mode, an increase of approximately 60% for P and D control and 120% for the PD, which is a lot lower than the evaluated values for the first wave. Table 27 presents additional comparison between the designed and experimentally obtained controllers through the settling time t_s and the mean squared error (MSE).

Controller	**Type**	**Sensor Voltage (filt)**		**Tip Displacement (filt)**	
		t_s (ms)	MSE (10^{-4} V^2)	t_s (ms)	MSE (10^{-14} m^2)
—	Open loop	167	17.6	174	32.0
Design	P	44.8	8.97	41.8	10.9
	D	65.5	27.5	68.4	12.4
	PD	22.1	8.23	18.9	5.80
Exper.	P	121	13.6	124	24.1
	D	118	13.4	123	22.7
	PD	85.2	11.3	89.1	16.5

Table 27 – Time domain quality metrics for the controllers designed in LTSpice (*Design*) and obtained experimentally (*Exper.*).

4 Final Considerations

The conclusive chapter of this text will be responsible for the comparison and hypothetical explanations in the similarities and differences between the experimental and numerical results. In addition, the chapter will comprise a brief confrontation between the results found in the articles presented during the literature review and the outcomes of the present work. In the end, possible continuations that could fit as direct extensions of this project will be suggested.

4.1 Conclusions

The main goal of the developed project was to actively control thin structures experimentally and numerically modeled through the finite elements method with the Carrera Unified Formulation employing piezoelectric materials. In order to accomplish this objective, manufacturing techniques had to be applied for obtaining the prototypes, as well as a series of MATLAB scripts had to be developed to send, acquire and process experimental data, and to handle and shape the numerical system matrices. These matrices are obtained through the MUL2 Fortran application according to the requirements of the project and the numerical model curves are adjusted in accordance to the real prototypes, which are used to design the control loop of the system. The designed controllers are later implemented numerically and experimentally conforming the stability limitations of each system.

Regarding the system characterization, it was possible to create an adjusted numerical model that represented well the prototypes, but that still did not contain certain uncertainties present in the real structural system. For the vibration suppression, positive results were obtained both experimentally and for the numerical model. However, it was not possible to apply the optimized controllers evaluated from the reduced order model due to the lack of robustness and the high sensitivity of the system when the loop was closed. Instead, controllers that provide not so good performance had to be implemented to the real model.

During the *Results and Discussion* chapter, the optimized controllers obtained from the implementation on LTSpice and the controllers limited experimentally by the real model were applied to the numerical model. Figures 96 and 97 allows drawing final conclusions on the quality of the numerical model by comparing the time and frequency domain responses between the numerical simulations and the experimental data acquired for the open loop systems and the closed loop systems with the same PD controller.

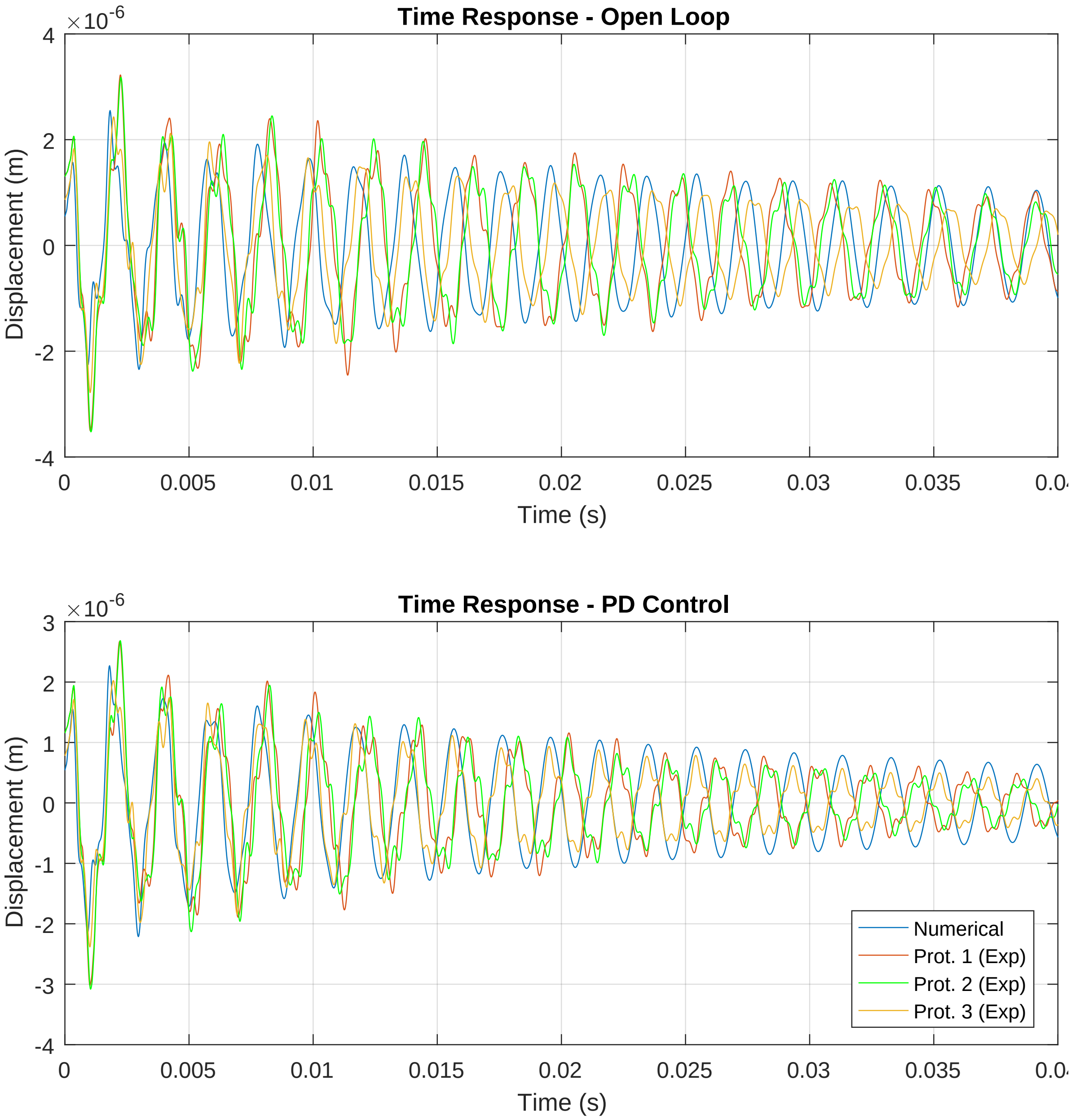

Figure 96 – Filtered tip displacement Time response comparison between numerical model and experiments executed with each prototype.

From both figures, it is possible to observe that the damping in the second mode for the numerical model is slightly lower than for the real system, while for the third mode the experimental values are closer to the model. There is more than one reason to which this fact may be attributed. First, the epoxy layer added to the prototypes for bonding the piezoceramics to the metallic substrate is not considered in the numerical model. This affects the system not only increasing its damped response, but also reduces the stiffness of the whole system due to non ideal load transmission between different layers. This can be one of the causers of the gain difference observed between the numerical and the experimental models.

The second reason for the differences associated to the damping is that the Rayleigh coefficients model is based in many assumptions and does not perfectly match the nonlinearities present in real systems. Making the damping matrix proportional to the mass and stiffness gives only two degrees of freedom to the problem, so it is not possible to match the damping ratios obtained experimentally for three or more resonance frequencies, but estimate them by minimizing the errors when using the data to linearly fit this classical viscous damping model. Actually, the effective damping contains radiation damping at the supports of the structure, which can usually be better represented by a set of mass-spring-damper at the supports of the structure. Last, the modal damping model violates the structural equilibrium by unbalancing the internal reaction forces of the structure. These considerations are further explained in chapter 19 of (WILSON, 2002): *Linear Viscous Damping*.

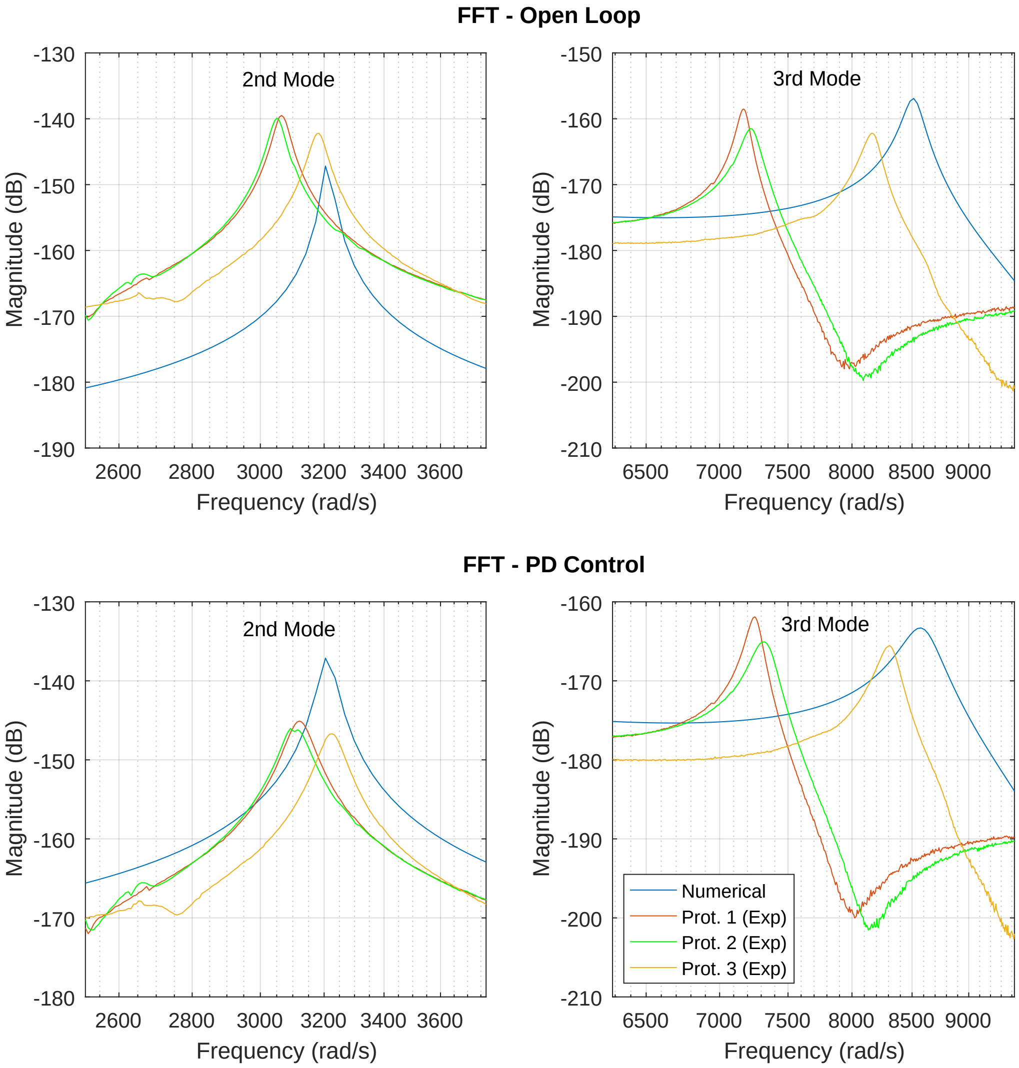

Figure 97 – Tip displacement FFT comparison between numerical model and experiments executed with each prototype.

Next, control results from papers found at the *Literature Review and State of the Art* of the introductory chapter will be presented and confronted to the ones obtained using the methods of this assignment.

One of the problems found in the literature (RAHMAN; ALAM, 2012) is the transient control of an aluminum cantilever beam, named (b) in the article, with dimensions 180x27x2mm. The sensor and actuator are PZT-5H patches with dimensions 15x15x0.5mm located at the clamped side of the structure. A digital PID controller was implemented in the LabView environment, which receives the sensor voltage through a DAQ board. The actuation voltage is amplified and the resulting signal is saturated between -200V/+200V. The uncontrolled and controlled results are shown in figure 98. Due to the high controller gains and the high voltage saturation, it is possible to properly suppress the vibration with small patches far from the extremity. This way, the sensor and actuator do not influence significantly in the natural modes of the structure, which allows the first mode to be compensated. The results obtained in the present project could be improved by using a digital controller, amplifying the actuation voltage and reducing the actuator and sensor lengths. Furthermore, it is important to notice that the problem in the literature controls a beam, which makes the system less sensible in the torsional modes and guarantees better performance.

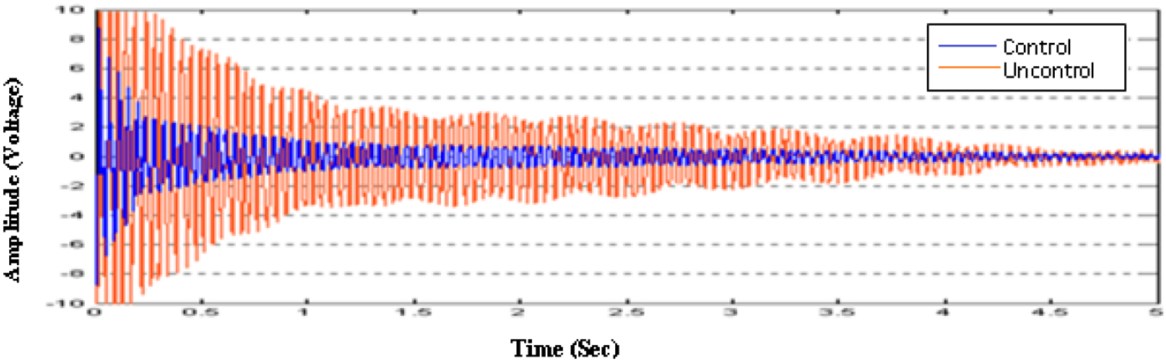

Figure 98 – Experimental open-loop vs. closed-loop vibration response of beam (b); (RAHMAN; ALAM, 2012).

Another problem was presented in (VASQUES; RODRIGUES, 2007): an aluminum cantilever beam with dimensions 400x15x2mm and piezoceramics of 30x15x1mm used as actuator. The pure proportional controller is implemented with a high gain and high saturation voltage operational amplifier and the control is performed for the tip velocity signal obtained by a laser vibrometer. Figure 99 shows the tip velocity time domain response for the open loop and the closed loop systems. Again, the high voltage availability and the almost unidimensional structure permits the usage of an actuator far from the measured displacements. Additionally, this control loop senses directly the variation rate of the displacement and proportionally compensates it, which is equivalent to apply an analog derivative controller to the desired signal. For this problem, the results for a gain of 80 are closer to the responses found in the present work, but for higher gains the performance is highly improved. It means that, with a less sensible closed loop system, better results could be obtained even with an analog controller.

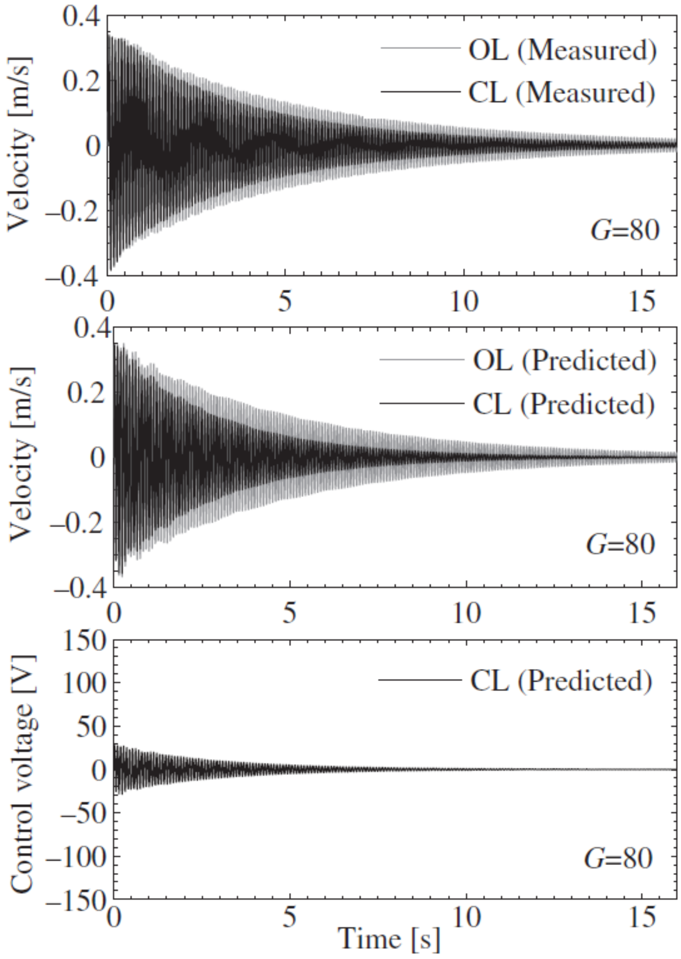

Figure 99 – Free vibration response of the open-(OL) and closed-loop (CL) systems and control voltage with filtered velocity feedback control; (VASQUES; RODRIGUES, 2007).

The last problem used as comparison is found at (QIU et al., 2006). In this article, a plate with 1.5mx0.5mx1.78mm is controlled with multiple pairs of PZT sensor/actuator of dimensions 50x15x1mm optimally positioned. The system is studied with a PD and a positive position feedback (PPF) controller closing the loop. The open loop and closed loop response for the PD controller are shown in figure 100. From this example, it is possible to observe that using multiple smaller patches to sense the vibration and suppress it can increase the performance if well positioned. Therefore, a possible evolution for the results obtained in the present project could be obtained by increasing the controller order, which would even make possible the control of higher order modes, and optimally designing the sensors and actuators.

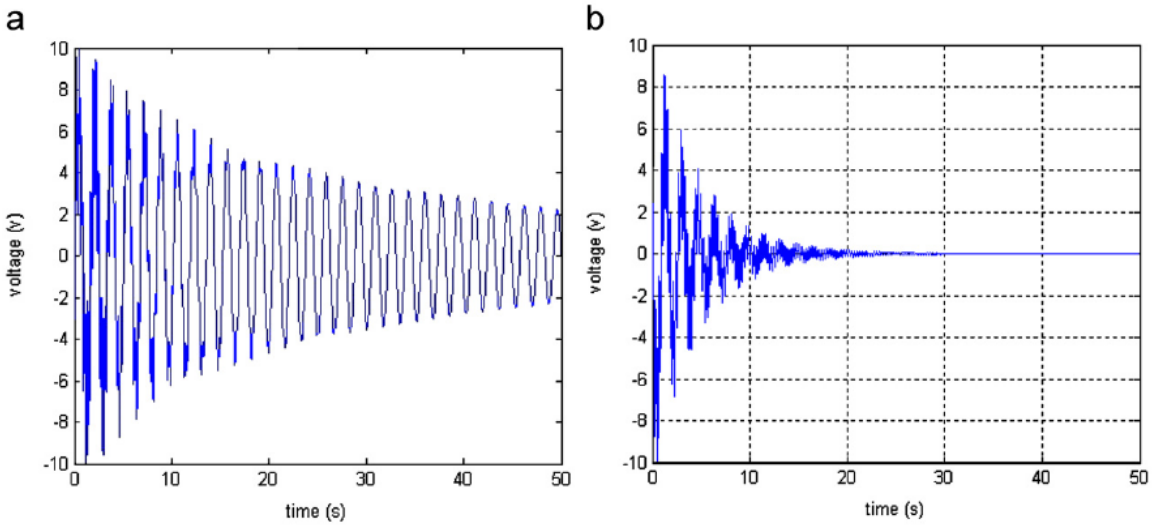

Figure 100 – Sensor voltage for the first two bending modes: (a) without control; (b) PD control; (QIU et al., 2006).

The positive results presented on the *Results and Discussion* chapter indicate that the objective of this work was fulfilled by merging studies developed with knowledge from the fields of Solid Mechanics, Vibration, Computational Mechanics, Numerical Calculus, Materials Science, Analog Electronics, Manufacturing, Signal Processing and Control Theory. As a graduation project in Mechatronics Engineering, it fitted perfectly, since the knowledge acquired through all the years of higher education was heavily needed and applied to this project. In addition to that, deepening in the structural mechanics combined to the computational mechanics field has definitely provided an enrichment to all of the background provided by the course.

4.2 Suggestions for Future Works

There are many ramifications of this thesis that, if explored, would make this project much wider and complete. Unfortunately it is outside of the scope of this work for a undergraduate project, but some possible continuations to the work developed in this thesis, based on CUF, that could become themes for other specialization thesis or academic researches, are presented next.

1. **Patches placement and design optimization:**

   The sensor and actuator positioning were chosen based on some papers and finely adjusted by trial and error. A study aiming the optimal response for a given set of sensors and actuators could be of high relevance and importance. The approaches describe in the articles that can be found at the second section of the first chapter (*Literature Review and State of the Art*) of this thesis could be validated and implemented for FEM/CUF models. A good option is using the Topology Optimization Method, which would allow an optimal design and positioning of the sensors and actuators used in the active control.
2. **Hybrid control:**

   The control performance could be improved by adding passive components that could reduce even more the vibration of the modes of the structure that are already controllable and, additionally, suppressing the first mode that could not be controlled in this project. The passive control can be implemented by adding layers of viscoelastic materials to the structure or connecting passive electric components between the piezoceramics in such a way that the damping of the whole system is increased. The performance of a hybrid control is presented numerically in (TRINDADE; BENJEDDOU; OHAYON, 2001).
3. **Free vibration control:**

   Instead of the response to step disturbance inputs, the system could be controlled without external loads applied for an initial displacement. Setting the initial configuration as one of the modal shapes of the structure leads to a decoupled activation of that mode. This way, it is possible to easily check the control effectiveness for each mode independently in the time domain. Numerically it is a simple task: the modal analysis of the system is performed and the initial displacement to be set is given by the eigenvector associated to the eigenvalue that represents the desired activation frequency. In the other hand, setting the initial configuration as a modal shape experimentally is way more complicated. One of the possible solutions is to apply an harmonic disturbance matching exactly the desired resonance frequency of the structure and taking off the input smoothly, in a way that no other modes are activated.
4. **Different control design approaches:**

   A continuation project vould cover a wider range of control design approaches, including additional output feedback and new state feedback controllers, that could be implemented digitally.

   Regarding the output feedback, H-∞ could be implemented in order to improve the system robustness, because it is based in a mathematical optimization problem that directly changes the system sensitivity to disturbances. The mathematical complexity and the difficult to handle with non linear constraints such as saturation are some cons of this method.

From the state feedback controllers, the Linear-Quadratic Regulator (LQR) is a good candidate to control the system, given the fact that it allows multiple sensor signals to be controlled by each actuator. This approach calculates an optimal gain matrix for a MIMO controller, minimizing a quadratic cost function that is solved by the continuous time Riccati differential equation. A problem associated to the usage of state feedback controllers is the need of systems that observe the states of the state-space model. In a real application, the states would not be directly obtainable just by the sensor voltages of the patches, which would require a state observer or a kalman estimator to estimate these quantities.

Being this one of my first academic researches, I felt that there is a lack of publications that would be completely clear for a novice researcher. That is the reason for all the detailing along the report of this assignment. This way this documentation is much more friendly for everyone that is unfamiliarized to the arguments of this project. With such a text, it is easier to reproduce and evolve the simulations and experiments presented in this project.

Bibliography

AHMAD, S.; UPADHYAY, C.; VENKATESAN, C. Electro-thermo-elastic formulation for the analysis of smart structures. *Smart Materials and Structures*, v. 15, n. 2, p. 401, 2006. Cited on page 32.

ALKHATIB, R.; GOLNARAGHI, M. Active structural vibration control: A review. *The Shock and Vibration Digest*, v. 35, n. 5, p. 367–383, 2003. Cited on page 34.

ALMA, M. et al. Design and tuning of reduced order H-infinity feedforward compensators for active vibration control. *IEEE Transactions on Control Systems Technology*, v. 20, n. 2, p. 554–561, 2012. Cited on page 34.

ASN. *Aviation Safety Network: de Havilland DH-106 Comet 1*. United States: Flight Safety Foundation, 2018. <http://aviation-safety.net/database/record.php?id=19540110-1>. Accessed: 2018-09-23. Cited on page 37.

BAILEY, T.; UBBARD, J. Distributed piezoelectric-polymer active vibration control of a cantilever beam. *Journal of Guidance, Control, and Dynamics*, v. 8, n. 5, p. 605–611, 1985. Cited on page 34.

BALAMURUGAN, V.; NARAYANAN, S. Shell finite element for smart piezoelectric composite plate/shell structures and its application to the study of active vibration control. *Finite Elements in Analysis and Design*, v. 37, n. 9, p. 713–738, 2001. Cited on page 34.

BEHESHTI-AVAL, S. et al. A refined sinus finite element model for the analysis of piezoelectric laminated beams. *Journal of Intelligent Material Systems and Structures*, v. 22, n. 3, p. 203–219, 2011. Cited on page 32.

BENJEDDOU, A.; TRINDADE, M.; OHAYON, R. A unified beam finite element model for extension and shear piezoelectric actuation mechanisms. *Journal of Intelligent Material Systems and Structures*, v. 8, n. 12, p. 1012–1025, 1997. Cited on page 56.

BENNER, P.; FASSBENDER, H. *Encyclopedia of Systems and Control - Model Order Reduction: Techniques and Tools*. London, UK: Springer London, 2013. 1-10 p. Cited on page 64.

BILLAH, K.; SCANIAN, R. Resonance, Tacoma Narrows bridge failure, and undergraduate physics textbooks. *American Journal of Physics*, v. 59, n. 2, p. 118, 1990. Cited on page 24.

BUNCH, J.; HOPCROFT, J. Triangular factorization and inversion by fast matrix multiplication. *Mathematics of Computation, American Mathematical Society*, v. 28, n. 125, p. 231–236, 1974. Cited on page 79.

BUSH, E. *75 years ago: Famous clip of Galloping Gertie not accurate, study says*. Seattle, WA, United States: Seattle Times, 2015. <http://www.seattletimes.com/seattle-news/75-years-ago-famous-clip-of-galloping-gertie-not-accurate-study-says/>. Accessed: 2018-09-23. Cited 2 times on pages 11 and 26.

CARDINAL, D. *Tech wrecks: Lessons from some of the biggest hardware screw-ups: Square windows that changed the aviation industry – de Havilland Comet*. United States: Extreme Tech, 2012. <https://www.extremetech.com/extreme/129764-tech-wrecks-lessons-from-some-of-the-biggest-hardware-screw-ups/3>. Accessed: 2018-09-23. Cited 2 times on pages 11 and 37.

CARRERA, E. Theories and finite elements for multilayered, anisotropic, composite plates and shells. *Archives of Computational Methods in Engineering*, v. 10, n. 3, p. 215–296, 2002. Cited on page 32.

CARRERA, E.; BÜTTNER, A.; NALI, P. Mixed elements for the analysis of anisotropic multilayered piezoelectric plates. *Journal of Intelligent Material Systems and Structures*, v. 21, n. 7, p. 701–717, 2010. Cited on page 33.

CARRERA, E. et al. *Finite Element Analysis of Structures through Unified Formulation*. United Kingdom: John Wiley & Sons Ltd., 2014. Cited 13 times on pages 11, 17, 32, 43, 44, 46, 47, 48, 50, 51, 52, 53, and 54.

CARRERA, E.; FAGIANO, C. Mixed piezoelectric plate elements with continuous transverse electric displacements. *Journal of Mechanics of Materials and Structures*, v. 2, n. 3, p. 421–438, 2007. Cited on page 33.

CARRERA, E.; ROBALDO, A. Hierarchic finite elements based on a unified formulation for the static analysis of shear actuated multilayered piezoelectric plates. *Multidiscipline Modeling in Materials and Structures*, v. 6, n. 1, p. 45–77, 2010. Cited on page 33.

CARRERA, E.; ZAPPINO, E.; LI, G. An analysis of beams with piezo-patches by node-dependent kinematic finite element method models. *Journal of Intelligent Material Systems and Structures*, v. 29, n. 7, p. 1379–1393, 2017. Cited 3 times on pages 31, 33, and 54.

CERAMTEC. *Piezo-ceramics for Sensor Technology: Piezo-ceramic Sensors and Sensor Applications*. Germany: CeramTec, 2018. <https://www.ceramtec.com/applications/piezo-applications/sensor-technology/>. Accessed: 2018-09-23. Cited 2 times on pages 11 and 31.

CHEMTRONICS. *Technical Data Sheet: CircuitWorks Conductive Epoxy CW2400*. GA, United States: CHEMTRONICS, 2013. <https://www.chemtronics.com/content/msds/Cw2400tds.pdf>. Accessed: 2018-10-13. Cited on page 84.

CHINESTA, F.; LADEVEZE, P.; CUETO, E. A short review in model order reduction based on proper generalized decomposition. *Archives of Computational Methods in Engineering*, v. 18, n. 4, p. 395–404, 2011. Cited on page 64.

CHOPRA, A. *Dynamics of structures: Theory and applications to earthquake engineering*. University of California at Berkeley, United States: Prentice Hall; 4th edition, 2012. Cited 3 times on pages 12, 60, and 61.

CHOWDHURRY, I.; DASGUPT, S. Computation of Rayleigh damping coefficients for large systems. *Electronic Journal of Geotechnical Engineering*, v. 8, n. 0, p. 1–11, 2003. Cited on page 59.

CHUNG, J.; HULBERT, G. A time integration algorithm for structural dynamics with improved numerical dissipation: the Generalized-α Method. *Journal of Applied Mechanics*, v. 60, n. 2, p. 371–375, 1993. Cited on page 33.

CINEFRA, M.; VALVANO, S. A variable kinematic doubly curved MITC9 shell element for the analysis of laminated composites. *Mechanics of Advanced Materials and Structures*, v. 23, n. 11, p. 1312–1325, 2016. Cited on page 32.

CINEFRA, M.; VALVANO, S.; CARRERA, E. Heat conduction and thermal stress analysis of laminated composites by a variable kinematic mitc9 shell element. *Curved and Layered Structures*, v. 2, n. 1, 2015. Cited on page 32.

COLGREN, R. *Efficient Modeling and Control of Large-Scale Systems*. United States: Springer US, 2010. Cited on page 33.

COURANT, R. Variational methods for the solution of problems of equilibrium and vibrations. *Bulletin of the American Mathematical Society*, v. 49, n. 1, p. 1–23, 1943. Cited on page 32.

CRAWLEY, E.; ANDERSON, E. Detailed models of piezoceramic actuation of beams. *Journal of Intelligent Material Systems and Structures*, v. 1, n. 1, p. 4–25, 1990. Cited on page 32.

CRAWLEY, E.; LUIS, J. D. Use of piezoelectric actuators as elements of intelligent structures. *American Institute of Aeronautics and Astronautics*, v. 25, n. 10, p. 1373–1385, 1987. Cited on page 32.

DEANGELIS, D.; SCHULZE, G. The effects of piezoelectric ceramic dissipation factor on the performance of ultrasonic transducers. *Physics Procedia*, v. 63, p. 28–36, 2015. Cited on page 108.

DRMAC, Z.; GUGERCIN, S.; BEATTIE, C. Quadrature-based vector fitting for discretized h2 approximation. *SIAM Journal on Scientific Computing*, v. 37, n. 2, p. 625–652, 2014. Cited on page 65.

ERTURK, A.; INMAN, D. An experimentally validated bimorph cantilever model for piezoelectric energy harvesting from base excitations. *Smart Materials and Structures*, v. 18, 2009. Cited on page 34.

GAVIN, H. *Numerical Integration in Structural Dynamics*. NC, United States: Department of Civil & Environmental Engineering, Duke University, 2016. Cited on page 33.

GOLDSCHMIDTBOEING, F.; WOIAS, P. Characterization of different beam shapes for piezoelectric energy harvesting. *Journal of Micromechanics and Microengineering*, v. 18, 2008. Cited on page 34.

GUO, N.; CAWLEY, P. Transient response of piezoelectric discs to applied voltage pulses. *Ultrasonics*, v. 29, n. 3, p. 208–217, 1991. Cited on page 40.

GUO, N.; CAWLEY, P.; HITCHINGS, D. The finite element analysis of the vibration characteristics of piezoelectric discs. *Journal of Sound and Vibration*, v. 159, n. 1, p. 115–138, 1992. Cited on page 40.

HANAGUD, S.; OBAL, M.; CALISE, A. Optimal vibration control by the use of piezoceramic sensors and actuators. *Journal of Guidance, Control, and Dynamics*, v. 15, n. 5, p. 1199–1206, 1992. Cited on page 34.

HANSON, D. et al. The role of anti-resonance frequencies from operational modal analysis in finite element model updating. *Mechanical Systems and Signal Processing*, v. 21, p. 74–97, 2007. Cited on page 107.

HE, X. A FEM model for the active control of curved FGM shells using piezoelectric sensor/actuator layers. *International Journal for Numerical Methods in Engineering*, v. 54, n. 6, p. 853–870, 2002. Cited on page 34.

HEYLIGER, P.; RAMIREZ, G.; SARAVANOS, D. Coupled discrete-layer finite elements for laminated piezoelectric plates. *International Journal for Numerical Methods in Biomedical Engineering*, v. 10, n. 12, p. 971–981, 1994. Cited on page 32.

HILBER, H.; HUGHES, T.; TAYLOR, R. Improved numerical dissipation for time integration algorithms in structural dynamics. *Earthquake Engineering and Structural Dynamics*, v. 5, n. 3, p. 283–292, 1977. Cited 2 times on pages 33 and 42.

HRENNIKOFF, A. Solution of problems of elasticity by the framework method. *Journal of Applied Mechanics*, v. 8, n. 4, p. 169–175, 1941. Cited on page 32.

HUANG, B.; KIM, H.; YOON, G. Modeling of a partially debonded piezoelectric actuator in smart composite laminates. *Smart Materials and Structures*, v. 24, n. 7, 2015. Cited on page 32.

ISO. *ISO 2631-1: Mechanical vibration and shock – Evaluation of human exposure to whole-body vibration – Part 1: General requirements.* Geneva, Switzerland: International Organization for Standardization, 1997. Cited on page 36.

ISO. *ISO 2631-2: Mechanical vibration and shock – Evaluation of human exposure to whole-body vibration – Part 2: Vibration in buildings (1 Hz to 80 Hz.* Geneva, Switzerland: International Organization for Standardization, 2003. Cited on page 36.

JOVANOVIC, M. et al. Experimental studies on active vibration control of a smart composite beam using a PID controller. *Smart Materials and Structures*, v. 22, n. 11, 2013. Cited on page 34.

KAPURIA, S.; HAGEDORN, P. Unified efficient layerwise theory for smart beams with segmented extension/shear mode, piezoelectric actuators and sensors. *Journal of Mechanics of Materials and Structures*, v. 2, n. 7, p. 1267–1298, 2007. Cited on page 56.

KERSCHEN, G. et al. The method of proper orthogonal decomposition for dynamical characterization and order reduction of mechanical systems: An overview. *Nonlinear Dynamics*, v. 41, n. 1, p. 147–169, 2005. Cited on page 33.

KPEKY, F. et al. Linear and quadratic solidshell finite elements SHB8PSE and SHB20E for the modelling of piezoelectric sandwich structures. *Mechanics of Advanced Materials and Structures*, v. 25, n. 7, p. 559–578, 2017. Cited on page 56.

KUMAR, K.; NARAYANAN, S. Active vibration control of beams with optimal placement of piezoelectric sensor/actuator pairs. *Smart Materials and Structures*, v. 17, n. 5, 2008. Cited on page 34.

LANG, G.; SNYDER, D. Understanding the physics of electrodynamic shaker performance. *Sound D. Vibration*, Shock & Vibration Symposium, 2011. Cited on page 88.

LIN, S.-M. PD control of a rotating smart beam with an elastic root. *Journal of Sound and Vibration*, v. 312, n. 1-2, p. 109–124, 2007. Cited on page 34.

LIU, M.; GORMAN, D. Formulation of Rayleigh damping and its extensions. *Computers & Structures*, v. 57, n. 2, p. 277–285, 1995. Cited on page 59.

LUND, M. W. *American Wire Gauge table and AWG Electrical Current Load Limits.* [S.l.]: PowerStream Technology, 2018. <https://www.powerstream.com/Wire_Size.htm>. Accessed: 2018-10-13. Cited on page 85.

LUO S. XIE, X. Z. Y. Vibration control of honeycomb sandwich panel using multi-layer piezoelectric actuator. *Computers & Structures*, v. 86, n. 7-8, p. 744–757, 2008. Cited on page 34.

MARTINO, J.; HARRI, K. The shaker parameters estimation, a first step to virtual testing. *MATEC Web of Confereces*, v. 148, 2018. Cited on page 131.

MATHWORKS. *System Identification Toolbox: User's Guide (R2017b).* [S.l.]: Mathworks, 2017. <https://it.mathworks.com/help/ident/ug/model-quality-metrics.html>. Cited on page 65.

MOHAMMAD, D.; KHAN, N.; RAMAMURTI, V. On the role of Rayleigh damping. *Journal of Sound and Vibration*, v. 185, n. 2, p. 207–218, 1995. Cited on page 59.

MORE, J.; SORENSEN, D. Computing a trust region step. *Journal on Scientific and Statistical Computing*, v. 3, p. 553–572, 1983. Cited on page 59.

MUL2. *MUL2 Research Group website.* Turin (TO), Italy: Flight Safety Foundation, 2018. <http://www.mul2.com/>. Accessed: 2018-09-23. Cited on page 35.

NASA. *Compact Active Vibration Control System: Active damping of flexible structures using a simple and compact actuator, sensor, and control system.* United States: NASA Technology Transfer Program, 2011. Cited on page 34.

NEGRUT, D. et al. On an implementation of the Hilber-Hughes-Taylor method in the context of index 3 differential-algebraic equations of multibody dynamics. *Journal of Computational and Nonlinear Dynamics*, v. 2, n. 1, p. 73–85, 2006. Cited on page 33.

NEWMARK, N. A method of computation for structural dynamics. *Journal of the Engineering Mechanics Division*, v. 85, n. 3, p. 67–94, 1959. Cited 2 times on pages 33 and 42.

OGATA, K. *Discrete time control systems.* NJ, United States: Englewood Cliffs: Prentice Hall; 2nd edition, 1995. Cited 4 times on pages 30, 33, 61, and 62.

OGATA, K. *System Dynamics.* NJ, United States: Upper Saddle River: Prentice Hall; 4th edition, 2005. Cited 4 times on pages 11, 24, 25, and 33.

OGATA, K. *Modern control engineering.* NJ, United States: Upper Saddle River: Prentice Hall; 5th edition, 2010. Cited 2 times on pages 30 and 33.

PALAZZOLO, A. *Vibration theory and applications with finite elements and active vibration control*. TX, United States: Texas A&M University, 2016. Cited 3 times on pages 23, 34, and 36.

PEREZ, N. et al. Numerical characterization of piezoceramics using resonance curves. *Materials*, v. 9, n. 2, p. 71, 2016. Cited on page 108.

PUSHKAR, R. *Comet's Tale: A half century ago, the first jet airliner delighted passengers with swift, smooth flights until a fatal structural flaw doomed its glory*. United States: Simithsonian Magazine, 2002. <http://www.smithsonianmag.com/history/comets-tale-63573615/>. Accessed: 2018-09-23. Cited on page 37.

QIU, Z. et al. Optimal placement and active vibration control for piezoelectric smart flexible cantilever plate. *Journal of Sound and Vibration*, v. 301, n. 3-5, p. 521–543, 2006. Cited 4 times on pages 15, 34, 153, and 154.

RAHMAN, N.; ALAM, M. Active vibration control of a piezoelectric beam using PID controller: Experimental study. *Latin American Journal of Solids and Structures*, v. 9, n. 6, p. 657–673, 2012. Cited 4 times on pages 15, 34, 85, and 152.

ROBBINS, D.; REDDY, J. Analysis of piezoelectrically actuated beams using a layer-wise displacement theory. *Computers & Structures*, v. 41, n. 2, p. 265–279, 1991. Cited on page 32.

ROGACHEVA, N. *The theory of piezoelectric shells and plates*. United States: CRC press, 1994. Cited on page 32.

SALAS, R. *Projeto Dinâmico de Estruturas Piezocompósitas Laminadas (EPLA) Utilizando o Método de Otimização Topológica (MOT)*. São Paulo, Brazil: Doctoral Dissertation, Escola Politécnica da USP, 2017. Cited 7 times on pages 17, 34, 80, 81, 85, 107, and 108.

SALAS, R. et al. A topology optimization formulation for transient design of multi-entry laminated piezocomposite energy harvesting devices coupled with electrical circuit. *International Journal for Numerical Methods in Engineering*, v. 113, n. 8, 2017. Cited 2 times on pages 17 and 80.

SALAS, R. et al. Optimized dynamic design of laminated piezocomposite multi-entry actuators considering fiber orientation. *Computer Methods in Applied Mechanics and Engineering*, v. 335, p. 223–254, 2018. Cited on page 33.

SANATHANAN, C.; KOERNER, J. Transfer function synthesis as a ratio of two complex polynomials. *IEEE Transactions on Automatic Control*, v. 8, n. 1, p. 56–58, 1963. Cited on page 65.

SEDRA, A.; SMITH, K. *Microelectronic Circuits*. New York, United States: Oxford University Press, Inc.; 4th edition, 1997. Cited on page 73.

SELGA, R.; LOHMANN, B.; EID, R. Stability preservation in projection-based model order reduction of large scale systems. *European Journal of Control*, v. 18, n. 2, p. 122–132, 2012. Cited 2 times on pages 33 and 64.

SHUNQI, R. S. Z.; XIANSHENG, Q. Active vibration control of piezoelectric bonded smart structures using PID algorithm. *Chinese Journal of Aeronautics*, v. 28, n. 1, p. 305–313, 2015. Cited on page 34.

ST. *Navy Type PZT Classifications*. Canada: Sensor Technology LTD, 2018. <https://sensortechcanada.com/technical-notes/articles/navy-type-pzt/>. Accessed: 2018-10-09. Cited on page 80.

STOYKOV, S.; MARGENOV, S. *Innovative Approaches and Solutions in Advanced Intelligent Systems: Finite Element Method for Nonlinear Vibration Analysis of Plates*. Switzerland: Springer International Publishing, 2016. Cited on page 33.

TEKBOND. *Ficha Técnica: Araldite Profissional*. SP, Brazil: Tekbond, 2017. <http://www.tekbond.com.br/images/produtos/arquivos/tds/tds_FICHA_TECNICA_ARALDITE_PROFISSIONAL_rev_10_18.pdf>. Accessed: 2018-10-13. Cited on page 83.

TEO, Y.; FLEMING, A. Active damping control using optimal integral force feedback. *2014 American Control Conference*, Portland, Oregon, USA, 2014. Cited on page 34.

TIERSTEN, H. *Linear piezoelectric plate vibrations*. United States: Springer US, 1969. Cited on page 32.

TIMOSHENKO, S. *Vibration Problems in Engineering*. New York, NY, United States: D. Van Nostrand Company, Inc.; 2nd edition, 1937. Cited on page 32.

TIMOSHENKO, S.; GERE, J. *Mechanics of Materials*. London, UK, England: Nelson Thornes Ltd., 1991. Cited on page 32.

TORII, A.; MACHADO, R. Structural dynamic analysis for time response of bars and trusses using the generalized finite element method. *Latin American Journal of Solids and Structures*, v. 9, n. 3, p. 1–31, 2012. Cited on page 33.

TRINDADE, M.; BENJEDDOU, A.; OHAYON, R. Piezoelectric active vibration control of damped sandwich beams. *Journal of Sound and Vibration*, v. 246, n. 4, p. 653–677, 2001. Cited 2 times on pages 34 and 155.

TZOU, H.; GADRE, M. Theoretical analysis of a multilayered thin shell coupled with piezoelectric shell actuators for distributed vibration controls. *Journal of Sound and Vibration*, v. 132, n. 3, p. 433–450, 1989. Cited on page 32.

VASQUES, C.; RODRIGUES, J. Active vibration control of smart piezoelectric beams: Comparison of classical and optimal feedback control strategies. *Computers & Structures*, v. 84, n. 22-23, p. 1402–1414, 2006. Cited on page 34.

VASQUES, C.; RODRIGUES, J. Active vibration control of a smart beam through piezoelectric actuation and laser vibrometer sensing: simulation, design and experimental implementation. *Smart Materials and Structures*, v. 16, p. 305–316, 2007. Cited 5 times on pages 15, 34, 85, 152, and 153.

VATANSEVER, D.; SIORES, E.; SHAH, T. *Global Warming - Alternative Resources for Renewable Energy: Piezoelectric and Photovoltaic Smart Structures*. United Kingdom: IntechOpen; Chapter 10, 2012. Cited 2 times on pages 11 and 31.

WAHL, F.; SCHIMIDT, G. On the sifnificance of antiresonance frequencies in experimental structural analysis. *Journal of Sound and Vibration*, v. 219, n. 3, p. 379–394, 1999. Cited on page 107.

WIKIMEDIA. *Op-Amp Internal*. [S.l.]: InductiveLoad, 2009. <https://commons.wikimedia.org/wiki/File:Op-Amp_Internal.svg>. Accessed: 2018-10-21. Cited 2 times on pages 12 and 73.

WILSON, E. *Three-Dimensional Static and Dynamic Analysis of Structures: A Physical Approach With Emphasis on Earthquake Engineering*. Berkeley, California, USA: Computers and Structures, Inc.; 3rd ddition, 2002. Cited on page 151.

XIAOJIN, Z. et al. Analysis of active vibration control for piezoelectric intelligent structures by ANSYS and MATLAB. *International Conference on Computer Application and System Modeling*, 2010. Cited on page 34.

ZAPPINO, E.; CARRERA, E. Thermo-piezo-elastic analysis of amplified piezo-ceramic actuators using a refined one-dimensional model. *Journal of Intelligent Material Systems and Structures*, 2017. Cited on page 33.

ZHANG, H.; SHEN, Y. Vibration suppression of laminated plates with 1–3 piezoelectric fiber-reinforced composite layers equipped with interdigitated electrodes. *Composite Structures*, v. 79, n. 2, p. 220–228, 2007. Cited on page 34.

ZHANG, T. et al. Experimental verifications of vibration suppression for a smart cantilever beam with a modified velocity feedback controller. *Shock and Vibration*, 2014. Cited on page 85.

ZIEGLER, J.; NICHOLS, N. Optimum settings for automatic controllers. *ASME Journal of Dynamic Systems, Measurement, and Control*, v. 115, n. 2, p. 220–222, 1942. Cited on page 68.

ZIENKIEWICZ, O.; TAYLOR, R. *The Finite Element Method*. Woburn, MA, United States: Butterworth-Heinemann; 5th edition, 2000. Cited on page 32.

ZUO, G.; WONG, L. A review on recent active vibration control techniques. *Computing Research Repository*, 2016. Cited on page 33.